Physics of Atomic Nuclei, Vol. 65, No. 11, 2002, pp. 1931–1932. Translated from Yadernaya Fizika, Vol. 65, No. 11, 2002, pp. 1987–1988.

80th Anniversary of Yuriĭ Georgievich Abov

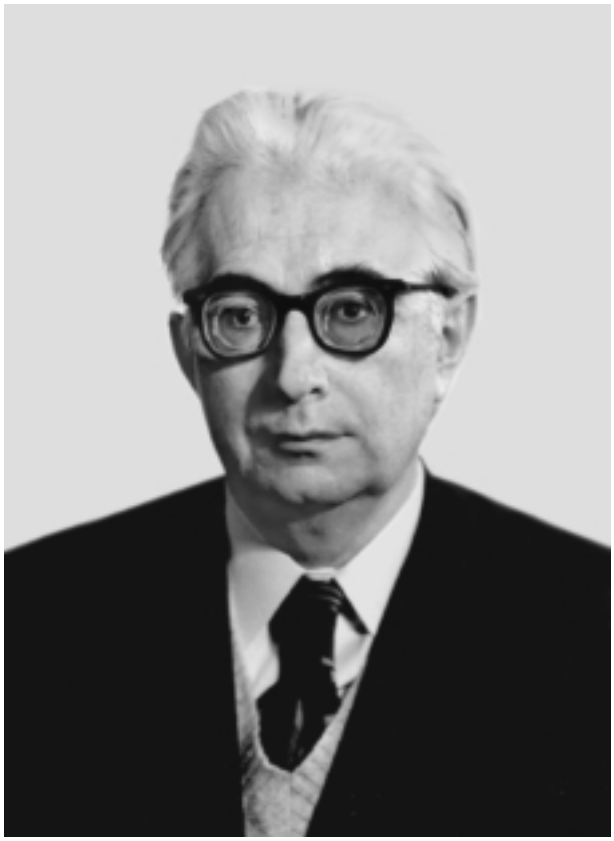

On November 7, 2002, Yuriĭ Georgievich Abov, a Corresponding Member of the Russian Academy of Sciences, Editor in Chief of the journal *Yadernaya Fizika*, which is known in the English-speaking world as *Physics of Atomic Nuclei*, celebrated his 80th birthday.

Every reader of this journal knows that its contents cover all basic lines of contemporary physics that are associated with the structure of matter at the most profound level—from the fundamental problems of quantum field theory and elementary-particle physics to macroscopic phenomena accompanying nuclear processes in matter. Even those who do not have the privilege of personally knowing Yuriĭ Georgievich (over 60 years of his activities in various realms of physics, the range of his friends, colleagues, and disciples includes a few hundred physicists) can easily imagine what a personality and what a physicist one must be in order to head the Editorial Board of our journal.

Yuriĭ Georgievich belongs to the generation of researchers whose scientific career began in the hard postwar years at the Institute of Theoretical and Experimental Physics (ITEP—at that time, Laboratory no. 3 at the USSR Academy of Sciences) and who were in charge of reviving the military potential of the Soviet Union and of creating its atomic industry. He took an active part in the commissioning of the first experimental heavy-water nuclear reactor in the Soviet Union. For the contribution that he made in the late 1940s and 1950s to the technologies of heavy-water reactors, Abov was later decorated with a "Badge of Honour" order.

With all his energy and enthusiasm, Abov then joined the work on creating the first neutron diffractometer in the Soviet Union and actively participated in experiments devoted to neutron structural analysis. Yuriĭ Georgievich is still nourishing keen interest in this field—he is head of the "Neutron Optics" group that performs measurements in one of the beams of the reactor installed at the Moscow Engineering Physics Institute (MEPI).

Abov and his colleagues were the first in the Soviet Union to develop and apply, in physics investigations, the procedure of polarized thermal neutrons. Their monograph on the subject is still an indispensable handbook for all those who employ neutron beams. In 1964, an experiment that was performed under the supervision of Abov and with his direct participation resulted in observing the asymmetry of gamma-ray emission in radiative polarized-neutron capture. This demonstrated that there is parity-nonconserving weak interaction between nucleons in a nucleus. For the discovery of this phenomenon, Abov, together with V.M. Lobashev, P.A. Krupchitsky, and V.A. Nazarenko, was awarded the USSR Lenin Prize of 1974 in physics.

Together with F.L. Shapiro (Joint Institute for Nuclear Research, Dubna) and J. Connors (USA), Abov and his colleagues from ITEP were the founding fathers of the spectroscopy of magnetic resonance and relaxation of polarized beta-active nuclei, a new fundamental method for studying matter. A number of fundamental physical results were obtained with the aid of this method, which possesses an extremely high sensitivity. In particular, the properties of defects arising in crystals upon radiative thermal-neutron capture by nuclei were studied at the ITEP; in addition,

1063-7788/02/6511-1931$22.00

precision investigations into basic spin-kinetics processes, such as phase nuclear relaxation, multispin magnetic resonance, and spin diffusion in disordered media, were also performed there on the basis of the same method.

Under the supervision of Abov, a beam of ultracold neutrons was obtained at the ITEP reactor and a magnetic trap for their long-term storage was constructed for the first time.

Scientific publications of Abov always arouse keen interest and give impetus to further investigations. Throughout the past 25 years, Professor Abov has delivered lectures at the Faculty of Experimental and Theoretical Physics at MEPI, and many students have had the unique opportunity of acquiring knowledge from a man of high erudition who possesses the unfading talent of researcher and teacher.

Yuriĭ Georievich inherited the chair of the Editor in Chief of the journal *Physics of Atomic Nuclei* from his outstanding predecessors V.I. Veksler and V.V. Vladimirsky. This was not only a gratifying but also a difficult heritage in our times. In the Soviet Union, the period spanning the 1960s to the 1980s covered the years of maturity of physics centers known all over the world, of organization of new institutions for nuclear research, and of generous state funding of nuclear-physics investigations. The contents of the journal at that time were second to none, especially as the authorities executed strict control over the publications of Soviet physicists abroad. The present-day situation concerning the high costs of experimental physics is well known. Nevertheless, the journal *Physics of Atomic Nuclei* still exists and continues publishing excellent articles having a high quotation index. Every year, the best studies are awarded prizes from the publishing house.

Yurii Georgievich Abov is a wise man and a charming personality, and it is a real pleasure for people of all ages and views to associate with him.

The present issue of the journal prepared by Abov's colleagues and disciples for the 80th anniversary of his birth is a tribute of respect and admiration to their friend and teacher.

Dear Yuriĭ Georgievich, your colleagues, friends, and disciples wish you good health, happiness, and many years of creative activities in your favorite realms.

Physics of Atomic Nuclei, Vol. 65, No. 11, 2002, pp. 1933–1979. Translated from Yadernaya Fizika, Vol. 65, No. 11, 2002, pp. 1989–2035.

REVIEWS

Dynamical Neutron Diffraction on Perfect Crystals

Yu. G. Abov[1)], N. O. Elyutin[1)], and A. N. Tyulyusov

Institute of Theoretical and Experimental Physics,
Bol'shaya Cheremushkinskaya ul. 25, Moscow, 117218 Russia

Received March 29, 2002

Abstract—The theory of phenomena occurring in the interaction of a thermal-neutron beam with a regular periodic set of nuclei, which represents a perfect crystal, and the results of relevant experimental investigations of such phenomena are described. The development of studies in these realms has led to the emergence of new fields of investigations in neutron optics, such as neutron interferometry and neutron topography. Neutron crystal spectrometers that possess a high angular and a high energy resolution and which serve for studying small-angle and diffuse scattering have been created. The possibilities for developing new theoretical descriptions of dynamical neutron diffraction and for performing new experiments with neutron beams are discussed. © *2002 MAIK "Nauka/Interperiodica"*.

1. INTRODUCTION

The present review article is devoted to considering the modern status of the theory and experiment in the realms of neutron diffraction in perfect crystals. Thermal-neutron scattering on perfect crystals represented as regularly arranged scattering centers—that is, on atomic nuclei forming a perfect (undisturbed) three-dimensional lattice—is described by the dynamical theory of scattering. By this term, one usually means a theory that takes into account the interaction of the entire set of waves arising in the irradiated crystal under the effect of the incident wave, which is plane in the simplest case. Waves that arise in the crystal are coherent; being interrelated, they form a unified neutron field. The wave components (transmitted and reflected ones) exchange neutrons, which permanently go over from one direction to the other. As a result, nuclei in the lattice are subjected to the effect of a unified wave field, so that their interaction with neutrons differs from the interaction of free nuclei with free neutrons.

Over the first period of investigations into neutronography, neutron diffraction was described by analogy with x-ray diffraction. The foundations of the theory of dynamical x-ray diffraction were laid in the studies of Ewald [1], Darwin [2], and von Laue [3]. Later on, the approach of Ewald became the most popular. Below, we will touch upon this version of the theory as applied to neutron diffraction (not to x-ray diffraction). Darwin proposed a different method for describing the interaction of waves in a crystal; we will also briefly consider this method in the present article. The approach of Darwin seems more promising in developing the theory of dynamical diffraction for weakly deformed crystals.

A modern exposition of the theory of x-ray diffraction can be found in a number of excellent monographs, including that of James [4] and that of Pinsker [5]. A theory of dynamical neutron scattering with allowance for the nature of neutron–nucleus interaction was first presented by Goldberger and Seitz [6]. It was further developed in the studies of Kagan and Afanas'ev [7]. A modern account of the theory is given by Sears [8] and by Rauch and Petrascheck [9]. Despite slight errors in some formulas presented in [9], the exposition in that study is clear and straightforward, which is quite an appealing feature. From the mathematical point of view, the theory of x-ray diffraction is similar to the theory of neutron diffraction. This is because the conditions of scattered-wave coherence have the same form in the two cases being discussed—in either case, they are determined by the requirement of Bragg's law. Nonetheless, it should be borne in mind that the interaction of x rays and neutrons with matter are of different origins. We emphasize that the scattering of neutron waves in a perfect crystal is coherent not only in the case of potential scattering but also in the case of resonance scattering, despite enormously long (on nuclear scales) lifetimes of the compound state [7]. Approaches to describing neutron-optics phenomena in nearly perfect crystals were developed in [10, 11], and it turned out once again that neutron optics is similar to x-ray optics.

The similarity of phenomena in neutron and x-ray optics dictates the similarity of equipment used in relevant experimental investigations (diffractometers,

[1)]Moscow State Engineering Physics Institute (Technical University), Kashirskoe sh. 31, Moscow, 115409 Russia.

1063-7788/02/6511-1933$22.00

interferometers, etc.). At the same time, we would like to note that the advent of neutron interferometers made it possible not only to perform a precision measurement of the neutron–nucleus scattering length but also to study the physical properties of the neutron itself—for example, its gravitational properties—and to confirm Einstein's equivalence principle at the microscopic level [12]. It is natural that, in the present article, attention is given primarily to the results of experiments with a germanium crystal obtained by the present authors, which weakly absorbs neutrons, and to the procedure that they developed and are employing in their investigations performed at the reactor of the Moscow Engineering Physics Institute (MEPI).

2. KINEMATICAL AND DYNAMICAL SCATTERING

To a considerable extent, the elastic scattering of radiation by a crystal is determined by the volume where the scattering process is strictly coherent—that is, by the volume where the crystal represents a perfect three-dimensional diffraction grating. In accordance with this, crystals can be classified as mosaic and perfect ones; there are also those that belong to the class that is intermediate between these two.

In mosaic crystals, a perfect lattice of atoms is realized only within blocks of characteristic linear dimension in the range 10^{-5}–10^{-4} cm. The diffraction properties of such crystals are described by the kinematical theory of diffraction [4, 10], where the attenuation of the incident wave due to the excitation of scattered waves can be disregarded in view of the smallness of a block of a mosaic. This kinematical (geometric) theory of diffraction is applicable as long as the attenuation of the incident beam is weak within a single block.

On the contrary, the interaction of the incident primary wave with excited secondary waves is of crucial importance for the diffraction process if one is dealing with diffraction processes in perfect crystals, where there are large regions (of volume about a few mm^3) of a rigorously periodic arrangement of atoms whose nuclei scatter coherently. Here, diffraction effects are described by a dynamical theory where it is assumed that the interaction of waves is mediated by a unified wave field throughout the crystal volume. Although the position of the diffraction maximum is well reproduced by either theory, the intensity and interference effects for perfect crystals are described only by the dynamical theory of diffraction.

There is no full theory that would describe the diffraction properties of crystals in the intermediate region (between that of a perfect and that of a mosaic structure), but many problems of diffraction in this region of crystallite dimensions were considered in the monograph of Krivoglaz [10].

Basic equations of the theory of dynamical diffraction are written in a general form where the number of partial plane waves constituting the unified wave field that is formed over the crystal volume is not bounded; moreover, all nodes of the reciprocal lattice—that is, all systems of atomic planes—can in principle contribute to reflection or create new reflexes. However, only in the two-wave approximation, where two beams—a reflected and a directly transmitted one—are fixed at the exit of the crystal, were the relevant theoretical calculations reliably performed in practice. This is because the majority of experimentally observed phenomena can be explained within the theory of the two-ray approximation; in view of this, it is precisely this approximation that was adopted as a starting point in writing the basic equations formulated for the cases of a plane and a of spherical radiation wave in a perfect crystal. The absorption of neutrons in matter is usually weak in a perfect crystal; therefore, there are two wave fields within the crystal that are close in amplitude and which lead to characteristic interference phenomena. The effect of absorption somewhat changes this pattern and calls for a dedicated consideration, especially if one is dealing with resonance neutron absorption.

In connection with the development of semiconductor technologies, there appeared large (of dimension about 10 cm^3) high-quality crystals of Si, Ge, GaAs, InSb, and CdS, which are necessary for experiments with neutron beams. This made it possible to observe effects described by the dynamical theory of neutron diffraction [7–9]. A significant distinction between the dynamical theory of x-ray diffraction and the dynamical theory of neutron diffraction is due to a strongly localized character of neutron–nucleus interaction, which is specified in the form of the point-like Fermi pseudopotential. In view of this, thermal neutrons (of energy 0.001–0.01 eV) are scattered on a nuclear potential of zero orbital angular momentum (S-wave scattering), in which case there is no angular dependence. X rays are scattered on atomic electrons, whose distribution extends over the radiation wavelength. This leads to the emergence of a strong angular dependence in the amplitude for scattering even on an individual atom (atomic form factor). For the nuclear scattering of thermal neutrons, the form factor is equal to unity, since their wavelength is five orders of magnitude longer than the nuclear size. That the neutron has a nonzero magnetic moment leads to its interaction with the magnetic moments of atoms. This interaction is close in magnitude to nuclear interaction and also features an angular dependence characteristic of x rays. That an electrically neutral particle has a distributed charge (form factor)

causes its electrostatic interaction with atomic electrons; however, ne interaction is rather modest and can usually be disregarded. Because of a relatively weak absorption and because of the smallness of the amplitude for scattering by nuclei, dynamical effects in neutron diffraction manifest themselves at significant crystal thicknesses (of about a few millimeters); at the same time, the majority of x-ray experiments employ thinner samples (of thickness about 10^3 μm).

Taking into consideration the aforesaid, we now proceed to expound the dynamical theory of neutron diffraction, the results obtained by experimentally testing this theory, and some of its applications. In doing this, our lines of reasoning will be similar to those adopted in the review articles of Rauch and Petrascheck [9] and of Bonse and Rauch [12], in the monograph of Pinsker [5], in the articles of Shull [13, 14], in the textbook by Abov and Elyutin [15], and in some original studies.

3. BASIC EQUATIONS OF THE DYNAMICAL THEORY OF NEUTRON DIFFRACTION

In the majority of actual crystals, a perfect crystal structure exists only within small blocks of a mosaic, but it becomes necessary to take into account the interaction of the incident and the diffracted beam if the dimensions of a block increase and if there arise large regions (of dimension about a few mm^3) of coherent scattering. The wave function for thermal neutrons in a relatively large perfect crystal satisfies the Schrödinger equation

$$\left[-\frac{\hbar^2}{2m}\nabla^2 + V(\mathbf{r})\right]\Psi(\mathbf{r}) = E\Psi(\mathbf{r}), \qquad (1)$$

where $V(\mathbf{r}) = V(\mathbf{r}+\mathbf{R}_n)$ is the periodic potential of the interaction between neutrons and nuclei forming the crystal lattice, $\mathbf{R}_n$ is the translation vector in this lattice, and E is the total energy of neutrons in the crystal. This total energy is equal to their kinetic energy in a vacuum, $E_n = (\hbar^2/2m)k^2$. According to the Bloch theorem, a solution to Eq. (1) can be sought in the form [16]

$$\Psi_{\mathbf{k}}(\mathbf{r}) = U_{\mathbf{k}}(\mathbf{r})\exp(i\mathbf{K}\cdot\mathbf{r}), \qquad (2)$$

where $U(\mathbf{r})$ is a periodic function whose periodicity reproduces the periodicity of the lattice, $\mathbf{K}$ is the wave vector of a partial Bloch wave, and the subscript $\mathbf{k}$ labels neutron wave fields in the crystal. Physically, this means that, within a perfect crystal, a neutron state is described by a wave function that is a superposition of plane waves constituting a unified wave field. By using the periodicity of the lattice, we can expand the functions $V(\mathbf{r})$ and $U(\mathbf{r})$ in a Fourier series in the reciprocal-lattice vectors $\mathbf{B}_n$; that is,

$$U(\mathbf{r}) = \sum_{\mathbf{B}} U(\mathbf{B})\exp(i\mathbf{B}\cdot\mathbf{r}), \qquad (3)$$
$$V(\mathbf{r}) = \sum_{\mathbf{B}} V(\mathbf{B})\exp(i\mathbf{B}\cdot\mathbf{r}),$$

where $\mathbf{B} = \mathbf{B}_n = \mathbf{B}_{hkl} = h\mathbf{b}_1 + k\mathbf{b}_2 + l\mathbf{b}_3$ is a reciprocal-lattice vector; $\mathbf{b}_i = (2\pi/v_{\mathrm{coh}})[\mathbf{a}_j \times \mathbf{a}_k]$ are basis vectors of the reciprocal lattice of the crystal, whose unit cell formed by the basis vectors $\mathbf{a}_i$ has the volume v_c; and hkl are Miller indices. Substituting (2) and (3) into (1), we obtain the set of equations of the dynamical theory of neutron diffraction:

$$((\hbar^2/2m)(\mathbf{K}+\mathbf{B})^2 - E)U(\mathbf{B}) \qquad (4)$$
$$= -\sum_{\mathbf{B}'} V(\mathbf{B}-\mathbf{B}')U(\mathbf{B}').$$

The set of Eqs. (4) is an infinite homogeneous set of linear equations with respect to $U(\mathbf{B})$. Prior to seeking solutions for the simplest single-wave case and for the two-wave case, which is the most popular and which is of importance in practice, we will make some assumptions concerning the form of the interaction potential $V(\mathbf{r})$.

The interaction of neutrons with nuclei of crystal atoms is described by the Fermi pseudopotential (the ab initio substantiation of the use of the Fermi pseudopotential can be found in [8])

$$V(\mathbf{r}) = 2\pi\frac{\hbar^2}{2m}\sum_{i,d} b_{\mathrm{coh}}^{(d)}\delta(\mathbf{r}-\mathbf{R}_i-\mathbf{r}_d). \qquad (5)$$

Here, we consider nonmagnetic systems and unpolarized neutron beams, thereby implying that the wave functions involved are scalar quantities. The vector $\mathbf{R}_i$ specifies the position of a unit cell, while $\mathbf{r}_d$ is a basis vector that indicates the position of an atom in a unit cell. By the symbol $b_{\mathrm{coh}}^{(d)}$, we denote the amplitude for coherent scattering on a nucleus having a mass m_A and occurring at the position d in the unit cell specified by the index i: $b_{\mathrm{coh}}^{(d)} = a_{\mathrm{coh}}(m_A + m_n)/m_A$, with a_{coh} being the amplitude for coherent scattering on a free nucleus. The temperature dependence is taken into account through the well-known Debye–Waller factor W in such a way that $b_{\mathrm{coh}} = b_{\mathrm{coh}}^{(d)}\exp(-2W)$. Performing the Fourier transformation (5) to the momentum space according to the rule

$$V(\mathbf{B}) = (1/V)\int V(\mathbf{r})\exp(-i\mathbf{B}\cdot\mathbf{r})d^3r$$

and considering that $V = v_c N_c$, where N_c is the number of unit cells in the crystal being considered, we can

Table 1. Features of thermal-neutron scattering by silicon and germanium crystals

Feature	Lattice constant D, 10^{-8} cm	Coherent amplitude b_{coh}, 10^{-12} cm	Number of nuclei N, 10^{22} cm^{-3}	Mean potential $V(0)$, 10^{-8} eV	$\frac{V(0)}{E_n}$, 10^{-6}	One-wave thickness D_λ, μm	Extinction length Δ_0, μm $(hkl) = (111)$	Region of total reflection $\Delta\theta_B$, angular seconds
Si	5.43	0.41	4.98	5.32	2.60	154	102	1.25
Ge	5.66	0.81	4.42	9.29	4.54	88	58	2.3

show that, upon the expansion in a Fourier series in reciprocal-lattice vectors, the potential $V(\mathbf{r})$ chosen in the form (5) takes the form

$$V(\mathbf{B}) = \frac{2\pi\hbar^2}{m_n v_c} F_N(\mathbf{B}), \qquad (6)$$
$$F_N(\mathbf{B}) = \sum_d b_{\mathrm{coh}}^{(d)} \exp(-i\mathbf{B}\cdot\mathbf{r}_d),$$

where F_N is the structural nuclear factor for reflections from (hkl) planes. Summation in (6) is performed over nuclei within a unit cell. The structural nuclear factor $F_N(0)$ can be replaced by the scattering amplitude b_{coh} multiplied by the structural geometric factor $F(0)$: $F_N(0) = b_{\mathrm{coh}}F(0)$; the latter in turn is related to the number N of atoms in a unit cell by the equation $N = F(0)/v_c$. Therefore, the ratio of the interaction potential averaged over the medium to the kinetic energy E_n of neutrons can be represented as

$$\frac{V(0)}{E_n} = 2\pi\left(\frac{\hbar^2 b_{\mathrm{coh}} N}{m_n}\right). \qquad (7)$$

Some characteristic parameters of the interaction of thermal neutrons (whose wavelength is $\lambda_n = 2$ Å) with semiconductor silicon and germanium crystals, which readily form a perfect lattice of nuclei, are given in Table 1, where it is considered that $|V(220)| = \sqrt{2}|V(111)| = V(0)$ and that the Debye–Waller factor is virtually equal to unity.

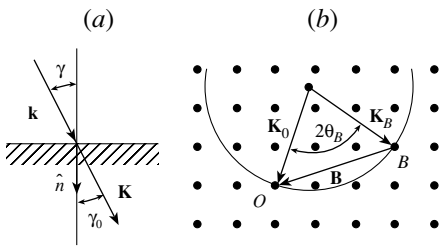

Fig. 1 [9]. (*a*) Refraction of a neutron beam at the crystal surface in the one-ray approximation, in which case only one point O is on the Ewald sphere; (*b*) Ewald diagram for the two-ray approximation (neutron diffraction).

From Table 1, it can be seen that the interaction of thermal neutrons with nuclei of the medium is weak: $V(0)/E_n \sim 10^{-5}$–10^{-6}. This makes it possible to find some useful approximate solutions to the set of Eqs. (4)—it is hardly possible to solve these equations exactly. It will be shown below that, from the fact that the strength $V(0)$ of neutron interaction with the medium is small, it follows that the neutron wave vector $\mathbf{K}$ within the crystal differs only slightly from the neutron wave vector $\mathbf{k}$ in a vacuum (Fig. 1*a*).

It is obvious that only those solutions to the set of Eqs. (4) are nontrivial that, on the left-hand side, have a coefficient of the same order of smallness as the interaction itself. This leads to the condition

$$|(\mathbf{K}+\mathbf{B})^2 - \mathbf{k}^2| \sim \left|\frac{2mV(0)}{\hbar^2}\right|. \qquad (8)$$

Let us consider the case where this condition is satisfied only at $\mathbf{B} = 0$. One can then disregard all other values of the wave functions $U(\mathbf{B} \neq 0)$ and reduce the set of Eqs. (4) to the single equation

$$((\hbar^2/2m)\mathbf{K}^2 - E)U(0) = -V(0)U(0), \qquad (9)$$

where $K \simeq k(1 - V(0)/2E_n)$. This approximation is referred to as the one-ray approximation. With the aid of the Ewald diagram (Fig. 1), the condition in (8)

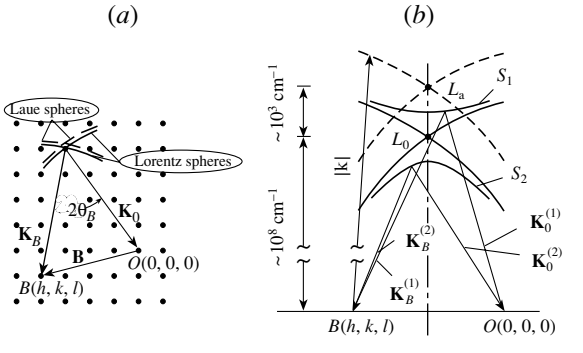

Fig. 2 [17]. (*a*) Dispersion-surface diagram for the two-ray case of diffraction at (hkl) planes; (*b*) enlarged region of the intersection of the Laue and Lorentz spheres (L_a and L_0 are, respectively, the Laue and the Lorentz point).

can be illustrated in the following way: only the reference point O in the reciprocal space lies near the Ewald sphere of radius k. Physically, this approximation corresponds to the refraction of a neutron wave as a discrete unit with the refraction factor $n^2 = 1 - V(0)/E_n$—that is, to a phenomenon that is in perfect analogy with that which occurs in the optics of visible light. From the condition requiring that the tangential components of the vector $\mathbf{K}$ be continuous (see Fig. 1*a*), it follows that

$$\mathbf{K} = \mathbf{k} - [k(V(0)/2E)\cos\gamma]\hat{n}, \qquad (10)$$

where $\hat{n}$ is a unit vector normal to the crystal surface. In the one-ray approximation being discussed, this makes it possible to describe the refraction of the incident neutron beam in terms of the refraction factor n_λ,

$$n_\lambda = \sin\gamma/\sin\gamma_0 = |\mathbf{K}|/|\mathbf{k}| \cong 1 - V(0)/2E_n. \qquad (11)$$

The refraction factor for neutrons belonging to the thermal spectrum is almost always different from unity by a value not greater than about 10^{-6}. In just the same way as in the optics of visible light, one can define here the one-wave plate thickness D_λ as the length over which there arises the phase difference 2π because of the different neutron-optic densities of the vacuum and the medium. The value of this length is deduced from the condition $(K - k)D_\lambda = 2\pi$. The result is

$$D_\lambda = 2\pi/(\lambda_n N b_{\mathrm{coh}}). \qquad (12)$$

For the case of silicon and germanium crystals, the numerical values of D_λ are given in Table 1. They are positive for all media where $b_{\mathrm{coh}} > 0$.

4. TWO-RAY APPROXIMATION IN DYNAMICAL THEORY

In the kinematical theory of diffraction, the width of the diffraction maximum is inversely proportional, in order of magnitude, to the number of reflecting planes [4]—for example, it is about $0.01''$ for a crystal of thickness of about 1 mm. In the dynamical theory [8, 9], the width of the maximum is much larger—it is about a few units of angular seconds. We note that the width of the maximum is determined by the limiting deviation of the angle from that which is specified by Bragg's law, in which case there is a significant reflection of neutrons from atomic planes.

According to (4), all nodes of the reciprocal lattice may contribute to reflection, but the shorter the distance from the Ewald sphere to the nodes, the greater the amplitudes of the waves; therefore, the multiwave approximation, which takes into account the contribution of all $U(\mathbf{B}_n)$ to the wave field of neutron radiation, is the most general and rigorous. This approximation becomes important at short wavelengths of incident neutron radiation because, in this case, the radius of the Ewald sphere (R_{E}) becomes large ($R_{\mathrm{E}} \sim K_0 \sim 1/\lambda_n$), so that a considerable number of nodes of the reciprocal lattice are situated near its surface.

However, the case where, in addition to the point O, yet another point—for example, B—occurs near the Ewald sphere (Fig. 1*b*) is of greatest importance from the practical point of view. In this case, radiation reflected by the set of (hkl) planes begins to propagate in the direction of $\mathbf{K}_B = \mathbf{K} + \mathbf{B}$ and the set of Eqs. (4) reduces to a set of two linear equations

$$\begin{cases} [(\hbar^2/2m)\mathbf{K}^2 - E + V(0)]U(0) + V(-\mathbf{B})U(\mathbf{B}) = 0, \\ V(\mathbf{B})U(0) + [(\hbar^2/2m)(\mathbf{K}+\mathbf{B})^2 - E + V(0)]U(\mathbf{B}) = 0. \end{cases} \qquad (13)$$

This is the set of fundamental equations of the dynamical theory of scattering in the two-ray approximation. These equations describe neutron fields in a perfect crystal for the most important and a relatively simple case of the formation of two beams, that which is directly transmitted (incident, refracted, primary) and that which is reflected (diffracted, scattered, secondary) at the angle $2\theta_B$ (see Figs. 1*b*, 2*a*). The deviation of reciprocal-lattice vectors from the Ewald sphere is characterized by the quantity ε, which is usually referred to as an excitation error and which is on the same order of magnitude as $V(0)/E_n \sim 10^{-5}$–10^{-6}:

$$2\varepsilon = K^2/k^2 - 1 \text{ or } K^2 = k^2(1 + 2\varepsilon). \qquad (14)$$

We recall that $\mathbf{K}$ is the neutron wave vector within the crystal and that $\mathbf{k}$ is its counterpart in a vacuum; taking into account (11), we therefore have $K^2/k^2 = 1 + 2\varepsilon \sim n_\lambda^2$. In order to determine the excitation error ε, it is necessary to introduce additionally the quantity α, which is an angular measure of the deviation of the node B from the reflection sphere (Ewald sphere) having a radius $|\mathbf{k}|$ and passing through the node O—in other words, a measure of the deviation of the wave vector $\mathbf{k}$ of the incident wave from the Bragg direction. This can be done with the aid of the cosine theorem, whence we obtain

$$(1 + \alpha)k^2 = B^2 + k^2 \cdot 2(\mathbf{K}\cdot\mathbf{B}), \qquad (15)$$
$$\alpha = 2(\theta - \theta_B)\sin 2\theta_B.$$

By using, as in the one-ray approximation, the continuity of the tangential components, we find, for the transmitted beam, that

$$\mathbf{K} = \mathbf{k} + (k\varepsilon\cos\gamma)\hat{n}, \tag{16}$$

where $\cos\gamma = (\mathbf{k}_0 \cdot \hat{n})$, and, for the reflected beam, that

$$(\mathbf{K} + \mathbf{B})^2 = k^2(1 + 2\varepsilon/\beta + \alpha), \tag{17}$$

where $\beta = \cos\gamma/\cos\gamma_B$ with $\cos\gamma_B = (\mathbf{k}_B \cdot \hat{n})$. Substituting (14), (16), and (17) into the set of Eqs. (13) and equating its determinant to zero,

$$\begin{vmatrix} 2\varepsilon + \dfrac{V(0)}{E_n} & \dfrac{V(-\mathbf{B})}{E_n} \\ \dfrac{V(\mathbf{B})}{E_n} & \dfrac{2\varepsilon}{\beta} + \alpha + \dfrac{V(0)}{E_n} \end{vmatrix} = 0, \tag{18}$$

we obtain the analytic expression for ε in the form

$$\varepsilon_{1,2} = \frac{1}{4}\left\{-\alpha\beta - (1+\beta)\frac{V(0)}{E_n} \pm \sqrt{\left[\alpha\beta - (1-\beta)\frac{V(0)}{E_n}\right]^2 + 4\beta\frac{V(\mathbf{B})V(-\mathbf{B})}{E_n}}\right\}. \tag{19}$$

From Eq. (19), which is a corollary of the two-ray approximation, one can obtain the important result that the incident wave Ψ_j splits into two components for both propagation directions O and B (see Fig. 2*b*). Specifically, we arrive at

$$\Psi_0^{(1,2)} = U_{1,2}(0)\exp(i\mathbf{K}^{(1,2)} \cdot \mathbf{r}), \tag{20}$$
$$\Psi_B^{(1,2)} = U_{1,2}(\mathbf{B})\exp(i(\mathbf{K}^{(1,2)} + \mathbf{B}) \cdot \mathbf{r}),$$

where the wave vectors $\mathbf{K}^{1,2} = \mathbf{k} + (\mathbf{k}\varepsilon_{1,2}\cos\gamma)\hat{n}$ differ only slightly both in absolute value and in direction. The quantities $U_{1,2}(0)$ and $U_{1,2}(\mathbf{B})$ determine the functions $U_{1,2}(\mathbf{r})$ according to Eq. (3). From the basic set of Eqs. (13), one can find that the wave amplitudes satisfy the relation

$$\chi_{1,2} = \frac{U_{1,2}(\mathbf{B})}{U_{1,2}(0)} = -\frac{2\varepsilon_{1,2} + V(0)/E}{V(-\mathbf{B})/E}. \tag{21}$$

Two independent solutions to the Schrödinger Eq. (1) that obey the Bloch theorem (2) are obtained as a superposition of the partial Bloch waves (20) in the form

$$\Psi^{(1,2)} = \Psi_0^{(1,2)} + \Psi_B^{(1,2)}, \tag{22}$$

which refer to the wave fields 1 and 2 (see Fig. 2*b*). In place of two waves that we had in the kinematical theory of diffraction [1]—one that propagates in the direction of incidence $(\mathbf{K}_0, \Psi_0)$ and the other that propagates in the Bragg direction $(\mathbf{K}_B, \Psi_B)$—there is therefore, in a dynamical treatment performed in the two-ray approximation, the splitting of each wave of neutron radiation into two waves: $(\mathbf{K}_0, \Psi_0)$ splits into $(\mathbf{K}_0^{(1)}, \Psi_0^{(1)})$ and $(\mathbf{K}_0^{(2)}, \Psi_0^{(2)})$, while $(\mathbf{K}_B, \Psi_B)$ splits into $(\mathbf{K}_B^{(1)}, \Psi_B^{(1)})$ and $(\mathbf{K}_B^{(2)}, \Psi_B^{(2)})$. This splitting, which is the result of dynamical exchange between the transmitted neutron beam and the radiation emitted in the Bragg direction, can be illustrated graphically.

Thus, one can see that, if only one primary ray is incident on a crystal, a sphere having a center at the point O and the radius $|\mathbf{K}_0| = n_\lambda k$, where n_λ is the refraction factor, which is determined by formula (11), appears to be its dispersion surface. According to the reciprocity theorem, the reflected wave can also be considered as a primary wave; assuming that it is the only strong wave, one can then construct the dispersion surface for it. For this surface, we will then again have a sphere of radius $|\mathbf{K}_0|$, but its center will be at the point B. Both these surfaces are referred to as Lorentz spheres (see Fig. 2*a*), while the point of intersection of their projections that lies in the plane spanned by the vectors $\mathbf{K}_0$ and $\mathbf{B}$ is referred to as the Lorentz point L_0, since it arises upon taking into account refraction at the vacuum–crystal interface. Similarly, one can construct two spheres of radius $|\mathbf{k}|$ around the points O and B. These spheres are referred to as Laue spheres, while the point of their intersection is referred to as the Laue point L_a. It is clear that the radii of Lorentz and Laue spheres differ by $(1 - n_\lambda) \sim 10^{-5}$–$10^{-6}$; it follows that, depending on the sign of $(1 - n_\lambda)$, one of these is embedded into the other.

Naturally, the region that is close to the points L_a and L_0 is of particular interest, since it is the region where the two waves coexist. But this region must be depicted on an enlarged scale (see Fig. 2*b*); for this reason, the spherical surfaces in the vicinities of L_a and L_0 should be replaced by tangential planes, while the lines of their intersection with the plane spanned by the vectors $\mathbf{K}_0$ and $\mathbf{K}_B$ should be replaced by straight lines. A hyperbolic cylinder that intersects the plane of the vectors $\mathbf{K}_0$ and $\mathbf{K}_B$ along the two hyperbolas represented in Fig. 2*b* by solid lines (S_1 and S_2) is the locus of points where the transmitted and the reflected wave that form the neutron field in the crystal are coupled. The Lorentz point L_0 is the center of the hyperbolas, the tangents to the Lorentz spheres being their asymptotes.

A further discussion of processes occurring in a perfect crystal in neutron diffraction requires introducing specific boundary conditions and additional parameters in the description of these processes. The boundary conditions are determined, in particular, by the relative orientation of the vectors specifying the

incident and the reflected radiation and of the normals to reflecting planes and to the crystal surface.

Let us introduce some parameters facilitating the description of dynamical neutron diffraction (see Table 1):

(i) The efficiency of the transfer of the neutron-radiation energy from one direction to the other is determined by the coherent amplitude for neutron scattering on bound nuclei of a crystal, b_{coh}.

(ii) The probability of a change in the beam direction in a crystal is affected by the neutron wavelength λ_n (or E_n).

(iii) The so-called extinction length Δ_0 defined as the crystal-thickness value at which the energy of the transmitted wave is fully converted into the energy of the reflected wave,

$$\Delta_0 = \frac{\pi v_c \sqrt{\cos\gamma_0 \cos\gamma_B}}{\lambda_n |F_n| e^{-2W}}, \qquad (23)$$

is yet another quantity that appears in the dynamical theory of diffraction and which characterizes the interference of Bloch waves in a crystal.

(iv) The reduced crystal thickness $A = \pi t/\Delta_0$, where t is the geometric crystal thickness, is also an important parameter.

(v) Instead of the angle of incidence of a neutron beam on a perfect crystal, it is convenient to use the parameter

$$y \equiv \frac{\alpha\beta - (1-\beta)V(0)/E_n}{\sqrt{|\beta|}\sqrt{V(\mathbf{B})V(-\mathbf{B})}/E_n}, \qquad (24)$$

which characterizes the orientation of the vectors $\mathbf{K}_0$ and $\mathbf{K}_B$ with respect to the crystal surface. In introducing the parameter y, the quantity $(\theta - \theta_B)$ (measured in rad) is multiplied by a value of about 10^5, which takes into account specific conditions of the problem being considered—that is, the values of b_{coh}, λ_n, (hkl), and $\beta = \cos\gamma/\cos\gamma_B$.

With allowance for the above parameters, it is straightforward to write specific expressions for the excitation error $\varepsilon_{1,2}$ and for the wave vectors in the crystal, $\mathbf{K}^{(1,2)}$, whereby we arrive at the appropriate representations for formulas (16) and (19); that is,

$$\mathbf{K}^{(1,2)} = \mathbf{k} + (\pi/\Delta_0)(-y \pm \sqrt{y^2 + \mathrm{sgn}\beta})\hat{n} - \frac{kV(0)}{\cos\gamma \cdot 2E}\hat{n}, \qquad (25)$$

$$\varepsilon_{1,2} = \frac{\pi\cos\gamma}{k\Delta_0}\left(-y \pm \sqrt{y^2 + \mathrm{sgn}\beta} - \frac{V(0)}{2E}\right). \qquad (26)$$

The sign of β is of considerable importance for expressions (25) and (26). This sign specifies the relative positions of the crystal surface and reflecting atomic planes. For $\beta > 0$, the case of Laue geometry is realized if the planes are approximately orthogonal to the surface and if the reflected beam is on the other side of the reflecting crystal plate. If, in addition, the reflecting planes are strictly orthogonal to the plane crystal surface, the scattering process is referred to as symmetric Laue diffraction. For $\beta < 0$, we have the case of Bragg geometry if the incident and the reflected beam are on the same side of the crystal plate and if the reflecting crystal planes are approximately parallel. Analogously, the scattering process is referred to as symmetric Bragg diffraction if the crystal surface is strictly parallel to atomic planes. We further consider each of these cases individually.

5. DYNAMICAL SCATTERING IN LAUE GEOMETRY

For the case of Laue geometry at $\beta > 0$, we will discuss here what occurs to the neutron field within a crystal plate in response to changes in the angular position of a perfect crystal with respect to the incident neutron wave specified by the wave vector $\mathbf{k}$. In this case, the rotation of a crystal in actual space is equivalent to the motion of the normal $\hat{n}$ in the plane of Fig. 3*a* within the image of the crystal surface on the y axis. Therefore, the position of the normal is determined by the angle of incidence of the vector $\mathbf{k}$. As the continuation of the normal approaches the point L_0 (this occurs for angles of incidence that tend to the exact value of θ_B), the normal intersects the hyperbolas S_1 and S_2 at the points D_1 and D_2, which are points of coupling of the wave fields and which are defined as $(\mathbf{K}_0^{(1)}, \mathbf{K}_B^{(1)})$ and $(\mathbf{K}_0^{(2)}, \mathbf{K}_B^{(2)})$. A superposition of these fields exists in a crystal over the entire range of angles of incidence, but the amplitudes of these waves vary in inverse proportion to the distances from the points D_1 and D_2 to the tangent T_B^0 to the Lorentz surface (see Fig. 3*a*). The ratios of the amplitudes for all waves within the crystal to the incident-wave amplitude $\mathbf{k}$ are displayed in Fig. 3*b* versus y. It can be seen that, as soon as the normal reaches the point L_0, the transmitted-wave amplitudes $U_1(0)$ and $U_2(0)$ become equal, whereupon $U_2(0)$ asymptotically tends to unity, while $U_1(0)$ asymptotically tends to zero. The reflected-wave amplitudes $U_{1,2}(\mathbf{B})$ behave differently: the absolute values of the two amplitudes remain equal over the entire region of the maximum, which is symmetric with respect to zero values of y (exact value of the Bragg angle).

Thus, a superposition of four neutron wave fields whose vector coupling can be seen in Fig. 2*b* is formed in a perfect crystal, provided that Bragg's conditions are strictly satisfied. These fields differ by the

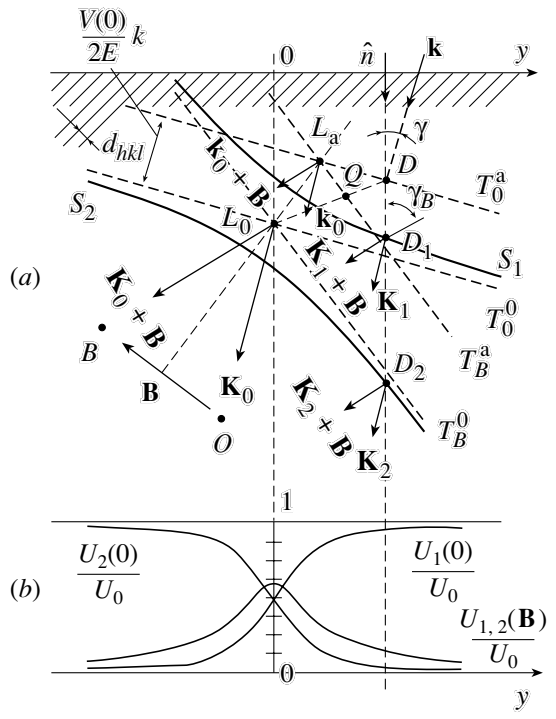

Fig. 3 [5]. Diffraction in Laue geometry: (*a*) dispersion surfaces in asymmetric reflection and (*b*) changes in the wave-function amplitudes within a crystal versus $y \sim (\theta - \theta_B) \times 10^5$.

directions of the corresponding wave vectors and by amplitudes. This corresponds to the conclusions that were drawn from the above analytic consideration [see formulas (20)–(22)]. For the case of Laue geometry, we now present the pattern of field distributions in a plane-parallel plate of a perfect single crystal (Fig. 4) where atomic planes are strictly orthogonal to the crystal surface. If Bragg's law ($\theta = \theta_B$) is strictly satisfied, four waves of wave vectors ($\mathbf{K}_0^{(1)}$, $\mathbf{K}_B^{(1)}$ and $\mathbf{K}_0^{(2)}$, $\mathbf{K}_B^{(2)}$) and different amplitudes propagate in two directions that are symmetric with respect to reflecting planes. During the propagation through the crystal, fields carrying identical superscripts, $\mathbf{K}_0^{(1)}$ and $\mathbf{K}_B^{(1)}$ (accordingly, $\Psi_0^{(1)}$ and $\Psi_B^{(1)}$), on one hand, and $\mathbf{K}_0^{(2)}$ and $\mathbf{K}_B^{(2)}$ ($\Psi_0^{(2)}$ and $\Psi_B^{(2)}$), on the other hand, exchange running waves that have the wave vectors $(\mathbf{K}_0^{(1)} + \mathbf{K}_B^{(1)})$ and $(\mathbf{K}_0^{(2)} + \mathbf{K}_B^{(2)})$, respectively, and which travel strictly along the reflecting planes, their frequency being determined by the neutron wavelength λ_n.

Further, the neutron radiation being considered reaches the opposite surface of the plane-parallel crystal (see Fig. 4), whereupon the neutron field splits into two components: Ψ_0 (of wave vector $\mathbf{K}_0$),

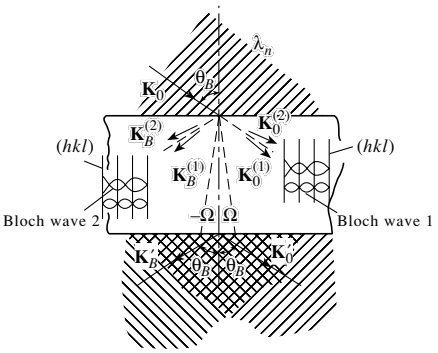

Fig. 4 [15]. Schematic representation of neutron waves in a perfect crystal under the conditions of reflection in Laue geometry.

which propagates in the direction of incidence, and $\Psi_B(\mathbf{K}_B)$, which is radiation traveling in the Bragg (reflection) direction. The pairs of the wave vectors that existed in the crystal disappear; however, the neutron beams that have the wave vectors $\mathbf{K}_0$ and $\mathbf{K}_B$ and which escape from the crystal into a free space became coherently coupled.

In the Laue case ($\beta > 0$), which is discussed in this section, the amplitude of the diffracted wave vanishes at the front surface of the crystal (see Fig. 4), where $(\mathbf{n} \cdot \mathbf{r}) = 0$ and where one has the boundary conditions

$$U_1(0) + U_2(0) = U_0, \quad U_1(\mathbf{B}) + U_2(\mathbf{B}) = 0. \quad (27)$$

With allowance for expressions (21), (25), and (26), this makes it possible to represent the amplitudes for the diffracted and the transmitted wave at the exit of the crystal as

$$U_{1,2}(0) = \frac{U_0}{2}\left(1 \pm \frac{y}{\sqrt{1+y^2}}\right), \quad (28)$$

$$U_{1,2}(\mathbf{B}) = \frac{U_0}{2}\sqrt{\beta}\frac{V(\mathbf{B})}{\sqrt{V(\mathbf{B})V(-\mathbf{B})}}\frac{\mp 1}{\sqrt{1+y^2}}. \quad (29)$$

As might have been expected on the basis of a geometric consideration (see Fig. 3), one of these functions, $U_{1,2}(0)$ (28), is asymmetric with respect to the point $y \sim (\theta - \theta_B) \times 10^5$, while the other, $U_{1,2}(\mathbf{B})$ (29), is symmetric.

With allowance for (24) and (25), one can obtain [5, 9] the reflection and transmission factors $P_B = I_B/I_i$ and $P_0 = I_0/I_i$, where I_i, I_B, and I_0 are the intensities of, respectively, the incident, the reflected, and the transmitted beam. Specifically, the results are

$$P_B(y) = \frac{\sin^2[(\pi t/\Delta_0)\sqrt{1+y^2}]}{1+y^2}, \quad (30)$$

$$P_0(y) = 1 - P_B(y). \quad (31)$$

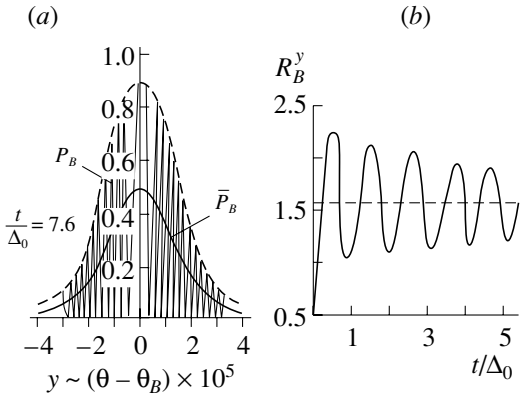

Fig. 5 [9]. (*a*) Calculated profile of the reflection curve (30) and (*b*) integrated reflecting power (35) for the case of Laue diffraction.

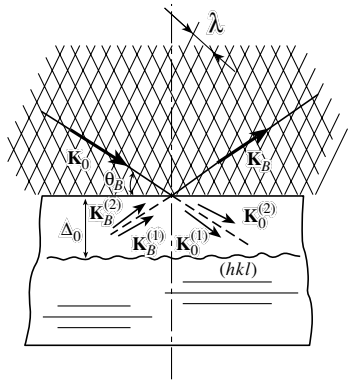

Fig. 6 [15]. Schematic representation of neutron waves under the conditions of reflection in symmetric Bragg geometry.

Relation (31) expresses the law of particle-number conservation in crystals that do not absorb neutrons. As follows from (30), the profile of reflected-radiation intensity (see Fig. 5*a*) has an oscillating form, the period of these oscillations being dependent on the crystal thickness t ($y = 0$) and on the extinction length Δ_0.

There are two extreme cases: that of thick crystals ($t/\Delta_0 \gg 1$) and that of thin crystals ($t/\Delta_0 \ll 1$); the first of these is of particular interest for dynamical diffraction, and it is the case that is illustrated in Fig. 5*a* ($t/\Delta_0 = 7.6$). At parameter values in expressions (30) that are admissible in an actual experiment [9] [$\lambda_n = 2.6$ Å; $t = 2$ mm; (220) Si at $\beta = 1$ and $t/\Delta_0 \sim 30$], the angular spacing between neighboring maxima is $0.05''$. So high an energy resolution has not yet been achieved under standard experimental conditions. Moreover, the spread of the values of λ_n and t smooths down the oscillations, which are averaged in an actual experiment; as a result, $P_B(y)$ takes the form

$$\bar{P}_B(y) = \frac{1}{2}\frac{1}{1+y^2}. \qquad (32)$$

This is a Lorentz curve (see Fig. 5*a*); at the above parameter values, it has the half-width of $(\Delta y)_H = 2''$, its maximum at $\beta = 1$ being exactly coincident with θ_B.

The integrated reflection intensities can be determined either in terms of the scale y or in terms of the angular scale θ:

$$R_B^y = \int P_B(y)dy, \quad R_B^\theta = \int P_B(\theta)d(\theta_B - \theta_B). \qquad (33)$$

They will differ by a factor of about 10^{-5}; more specifically, they are related by the equation

$$R_B^\theta = \frac{|V(\mathbf{B})|}{E\sqrt{|\beta|}\sin 2\theta_B}R_B^y. \qquad (34)$$

The form of the integrated neutron reflection R_B^y (see Fig. 5*b*), which is referred to as the Waller integral

$$R_B^y = \int_{-\infty}^{\infty} \frac{\sin^2[(\pi t/\Delta_0)\sqrt{1+y^2}]}{1+y^2}dy \qquad (35)$$
$$= \frac{\pi}{2}\int_0^{2\pi t/\Delta_0} J_0(x)dx,$$

also exhibits oscillations that are smoothed to such an extent that $R_B^y \to \pi/2$ with increasing t/Δ_0. While the profile of reflection from a crystal has not yet been observed in the case of Laue geometry, oscillations of the integrated-reflection curve were repeatedly observed in experiments where either the crystal thickness [18, 19] or the neutron energy [13] was changed. By changing the period of oscillations, which is determined by zeros of the Bessel function $J_0(2\pi t/\Delta_0)$, one can obtain precise information about the extinction length Δ_0 and, hence, about the interaction potential $V(\mathbf{B})$ and the coherent amplitude b_{coh}.

6. DYNAMICAL SCATTERING IN BRAGG GEOMETRY

Under the conditions of Bragg geometry, in which case the reflecting planes are approximately parallel to the crystal surface, the reflected beam ($\mathbf{K}_B$) escapes from the crystal through the front surface (see Fig. 6) and $\beta < 0$; at the back wall of the crystal—that is, at $(\mathbf{n}\cdot\mathbf{r}) = t$—the diffracted wave $\Psi_B = \Psi_B^{(1)} + \Psi_B^{(2)}$ is

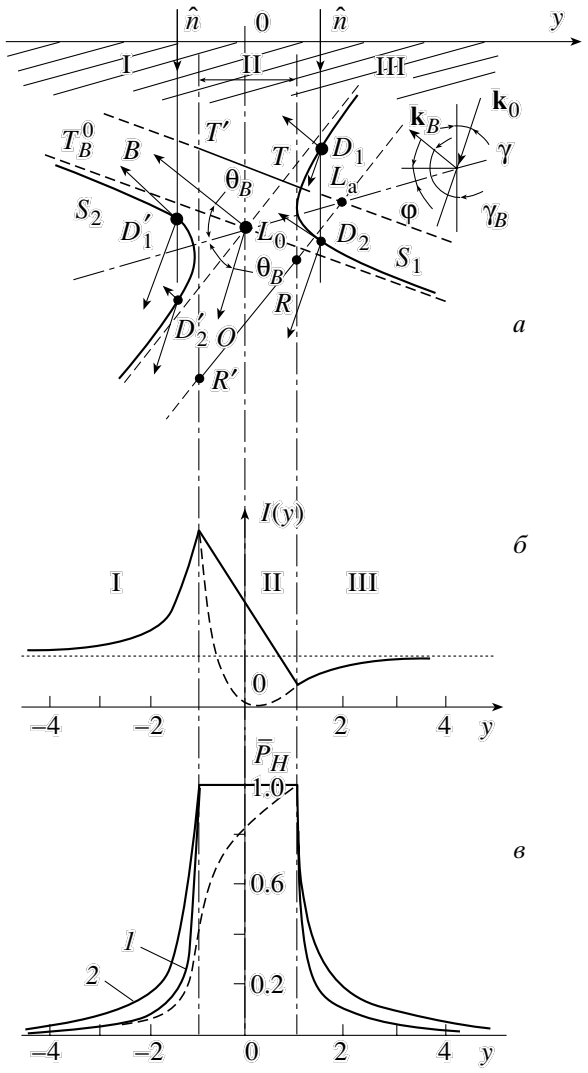

Fig. 7 [5]. Diffraction in Bragg geometry: (*a*) dispersion surfaces in asymmetric reflection; (*b*) intensities of the neutron wave field in a crystal as a function of $y \sim (\theta - \theta_B) \times 10^5$ in three regions of a maximum; and (*c*) profile of the Bragg reflection curve as calculated by the (*1*) Darwin and (*2*) Ewald formulas, as well as (dashed curve) with allowance for absorption.

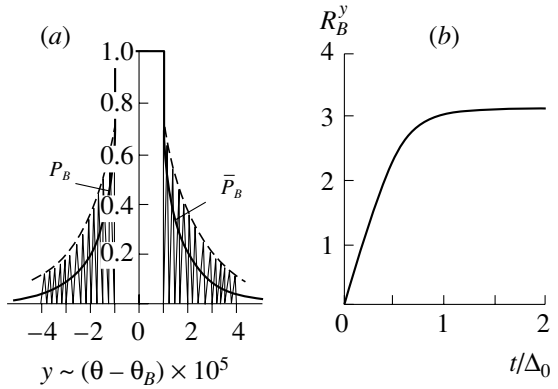

Fig. 8 [9]. (*a*) Calculated profile of the reflection curve and (*b*) integrated reflecting power for the case of Bragg diffraction.

then set to zero, which imposes the boundary condition on the amplitudes of the waves in the form

$$U_1(\mathbf{B})\exp(iA\sqrt{y^2-1}) + U_2(\mathbf{B})\exp(-iA\sqrt{y^2-1}) = 0, \quad (36)$$

where A is the reduced crystal thickness defined in Section 4. For $\beta < 0$, expressions (26) and (25) for $\varepsilon_{1,2}$ and $\mathbf{K}^{(1,2)}$, respectively, also become complex-valued (see [1]), which indicates that the amplitude of the wave in question decreases exponentially toward the crystal depth. In addition to true absorption, Bragg diffraction may lead to, in a specific region of the reflection maximum, an interference attenuation of the neutron wave field in a crystal (extinction), the effect of extinction being much more pronounced than the effect of absorption in the majority of cases. In the region where $|y| < 1$, the neutron wave penetrates into the crystal only at the depth equal to the extinction length Δ_0, the absorption factor $P_B(y)$ becoming equal to unity.

This phenomenon has a clear geometric interpretation in terms of constructions in the reciprocal space. For a general case, the scheme of Bragg reflection is given in Fig. 7*a*: the crystal surface forms an acute angle φ with reflecting planes; this presets a specific orientation of the dispersion surfaces S_1 and S_2. As in the Laue case, the procedure for tracing the reflection profile is equivalent, by virtue of the continuity of the tangential components, to the motion of the normal $\hat{n}$ along the crystal surface from left to right. But here, the entire region of reflection can be broken down into three parts (Figs. 7*a*, 7*c*): in regions I ($y < 1$) and III ($y > 1$), a continuation of the normal intersects one of the branches of the dispersion surface, S_2 or S_1, only one coupling point, D_1' or D_2—that which is closer to the Lorentz sphere T_0—yielding a strong wave. On this basis, we can conclude that the incident wave of wave vector $\mathbf{K}_0^{(1)}$ from the point D_1'' (first wave) is dominant in region I and that the $\mathbf{K}_0^{(2)}$ wave from D_2 (second wave) prevails in region III. As to region II, the total reflection of the incident wave occurs there—the continuation of the normal traverses the vertex part of the dispersion surface and begins to intersect the intermediate region.

Obviously, the effect of the total reflection of the incident wave in region II is associated with the exponential decay of the wave field in the crystal with depth. The question of which wave (the first or the

second one) determines the neutron field in region II is solved unambiguously in favor of the second wave (for details, see [5]); therefore, the general pattern of the neutron wave field in a crystal changes as soon as there arises a deviation from the exact value of the Bragg angle θ_B. In region I, the two waves are in phase, their maxima lying in atomic planes; in region III, the waves are in antiphase, so that there are their minima in the same plane. In region II, there is only one wave, whose maxima and minima move monotonically from one extreme position to the other. Figure 7*b* shows the graph that illustrates the total intensity of the wave field in a crystal, the dashed curve in region II representing the intensity value that takes into account some commonly adopted extinction. A sharp asymmetry of the maximum with respect to the medium point of this intensity distribution within the crystal is worthy of special note; at the same time, the reflection curve (see Fig. 7*c*, curve *1*), also referred to as Darwin's profile, is symmetric, an asymmetry in it arising only in the presence of a significant absorption of radiation in a crystal (dashed curve).

For Bragg geometry, in which case $\beta < 0$ (see Fig. 6), we will now consider in more detail the structure of the profile of reflection from an ideal crystal. At the front surface, we then have the boundary conditions

$$U_1(0) + U_2(0) = 0,\ U_1(\mathbf{B}) + U_2(\mathbf{B}) = U_0(\mathbf{B}). \tag{37}$$

The condition in (36) holds at the back surface. As in the Laue case, which is specified by Eqs. (30) and (31), one can then obtain expressions for the reflection and the transmission factor. The results are

$$P_B(y) = [y^2 + (y^2-1)\cot^2(A\sqrt{y^2-1})]^{-1}, \tag{38}$$
$$P_0 = 1 - P_B.$$

The reflection-curve profile as given by Eq. (38) is depicted in Fig. 8*a* under the condition $t/\Delta_0 = 3$. In the region $|y| < 1$, the intensity of the reflected beam is equal to unity; beyond this region—that is, for $|y| > 1$—there are quick oscillations decreasing in magnitude. Averaging over these oscillations determines the reflection-curve profile:

$$\bar{P}_B(y) = \begin{cases} 1 & \text{for } |y| < 1, \\ 1 - \sqrt{1-y^{-2}} & \text{for } |y| > 1. \end{cases} \tag{39}$$

The curve represented by (39) was obtained by Ewald for a not very thick, nonabsorbing crystal, in which case the radiation that has penetrated deep inside undergoes partial reflection from the back surface and then escapes from the crystal, propagating together with the radiation reflected by the surface layer owing to primary extinction. For a similar crystal that is, however, extremely thick, Darwin obtained a different solution:

$$\bar{P}_B(y) = \begin{cases} 1 & \text{for } |y| < 1, \\ y - \sqrt{y^2-1} & \text{for } |y| > 1. \end{cases} \tag{40}$$

In Fig. 7*c*, this profile is represented by curve *1*. The fundamental difference between the two approaches is that Ewald proceeded from the presence of interaction between the wave reflected from the back wall and the incident wave, while Darwin assumed, in his calculations, that the incident wave is completely attenuated in the crystal before reaching the back surface. Denoting by $\Delta\theta$ the total-reflection region ($-1 < y < +1$) and taking into account Eq. (24), we obtain

$$\Delta\theta = \frac{2|F_N(\mathbf{B})|\lambda_n^2}{\pi v_c \sin 2\theta_B}\sqrt{\left|\frac{\cos\gamma_B}{\cos\gamma}\right|}; \tag{41}$$

therefore, the total-absorption region can be enlarged or diminished by appropriately choosing the angles of the incident and the reflected neutron beam.

This Fankuchen effect [20] was used to obtain neutron beams of small angular spread; it can easily be illustrated by a graphical construction (see Fig. 7). The lengths of the straight-line segments RR' and TT' are dependent on the orientation of reflecting planes with respect to the crystal surface and are related to the angles of the incident and the reflected beam by the equation

$$\frac{\cos\gamma_B}{\cos\gamma} = \frac{TT'}{RR'}.$$

As can be seen from Fig. 7*a*, TT' and RR' are the segments belonging to the reflection spheres with the centers at O and B and lying between the normals that are tangent to the dispersion surfaces S_1 and S_2. If the incidence of a beam is strictly symmetric, in which case $\beta = 0$ ($TT' = RR'$), the FWHM of the Ewald and the Darwin curve (respectively, curve *2* and curve *1* in Fig. 7*c*) are

$$\Delta y_{\mathrm{E}} = 4\sqrt{3}/3 \cdot \Delta\theta, \quad \Delta y_{\mathrm{D}} = 3\sqrt{2}/2 \cdot \Delta\theta; \tag{42}$$

that is, they differ by less than 10%.

It should be emphasized that, as imperfections in the crystal lattice become more pronounced—that is, as there arise cluster formations, dislocations, small-angle boundaries, etc.—the quantity Δy increases; the reflection curve assumes the form of a Gaussian distribution, as it does in the case of a higher momentum spread of the beam; and the reflecting power of crystals grows [21]. The dynamical description of scattering becomes ever less acceptable, and there arises the need for taking into account the diffuse component of scattering. As the degree of disorder

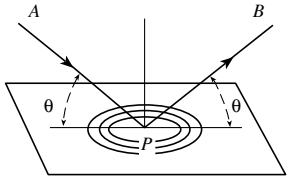

Fig. 9 [26]. Conditions of the reflection of the neutron beam traveling from the point A to the point B and undergoing reflection from an individual crystal plane according to the method of cophasal Fresnel zones.

in the atomic structure increases, the kinematical approach becomes ever more appropriate [10].

With the aid of Eqs. (38) and (39), one can obtain an expression for the reflecting power of a crystal in the case of Bragg scattering. The result is

$$R_B^y = \pi \tanh A, \tag{43}$$

where $A = \pi t/\Delta_0$. This dependence is depicted in Fig. 8*b*, whence we can see that, at large crystal thicknesses—specifically, for $t/\Delta_0 > 1$—we have $R_B^y \to \pi$, which is twice as great as the corresponding value in the Laue case [see Eq. (35)]. If $t/\Delta_0 \ll 1$, which corresponds to a thickness that is smaller than 10^{-4} cm, the integrated reflecting power is proportional to the effective crystal thickness $t/\cos\gamma$ and R_B^y takes the form

$$R_B^y = \frac{|F_N(\mathbf{B})|^2 \lambda_n^3}{v_c^2 \sin 2\theta} \frac{t}{\cos\gamma}. \tag{44}$$

The deviation from this proportionality is associated with the extinction phenomenon (see above). Since many actual crystals have a pronounced mosaic structure, with a size of mosaic grains being smaller than 10^{-5}–10^{-4} cm, expression (43) is applicable only to the reflecting power of one small block of a mosaic structure.

In the case of Bragg diffraction, the profile of reflection from a perfect crystal—it is also referred to as a Darwin table (or box)—was observed in a number of experiments [13, 22]. However, the most correct results were obtained by using the crystal-collimation technique [23], which ensures the convolution of the reflection profile with a curve that has a width of a few tenths of a second [24]. In principle, this problem can be solved by using an antiparallel spectrometric position of perfect crystals [25], as has already been done in the case of x-ray radiation.

7. REFLECTING POWER OF PERFECT CRYSTALS

Here, we will consider in more detail processes occurring in large perfect crystals during the formation of a diffractive neutron reflection (reflex) from the family of reflecting planes (hkl), bearing in mind the circumstance that a major part of our studies were performed with nearly perfect single crystals of germanium that have the dislocation density of $N_d \sim 10^1$–10^3 cm^{-2}.

We assume that a neutron beam travels from a point A and, after reflections at the point P of the reflecting plane, arrives at the point B. The plane APB is orthogonal to the reflecting plane, as is schematically shown in Fig. 9. With respect to the reflection plane, the ray AP is directed at an angle θ that satisfies Bragg's law $2d\sin\theta = \lambda_n$, where d is the interplane spacing and λ_n is the neutron wavelength. In order to deduce the intensity of the reflected wave at the point B, we will make use of the method of Fresnel zones.

The first Fresnel zone determines the set of points on a plane such that, for these points, the difference of the distances that the rays travel from this plane to the point B does not exceed $\lambda/2$—that is, this is a set of cophasal emitters. The second Fresnel zone is a set of cophasal emitters shifted in phase with respect to the first one by $\pi/2$, etc. For the method to be applicable, it is necessary that the plane be completely filled with emitters. For thermal neutrons, this requirement is satisfied. The area of the first Fresnel zone is $[(\pi r_1 r_2)/(r_1 + r_2)](\lambda/\sin\theta)$, where $r_1 = AP$ and $r_2 = PB$. At $\lambda \sim 1$ Å, a zone of area 3×10^{-8} cm^2 contains more than 10^7 atoms. If n is the density of atoms in the plane, the amplitude of the scattered wave is proportional to $n[(\pi r_1 r_2)/(r_1 + r_2)](\lambda/\sin\theta)$.

The contribution of each zone to the total amplitude of the scattered wave is known [21]. If a plane wave is incident on a reflecting plane, then $r_1 \to \infty$. As a result, the ratio of the amplitude of the reflected wave at the point B to the amplitude of the incident plane wave is $q = n\lambda A/\sin\theta$, where A is the amplitude of radiation coming from one atom. Going over from a plane that is uniformly filled with atoms to the (hkl) crystallographic plane, we must make the substitutions $n \to N_c d$ and $A \to F_N(hkl) \equiv F$, where N_c is the number of unit cells in a unit volume, d is the interplane spacing, and F_{hkl} is the structural amplitude. In this case, the amplitude of the scattered wave assumes the form

$$q_{hkl} = N_c d(\lambda/\sin\theta)F_{hkl} = 2N_c d^2 F_{hkl}. \tag{45}$$

As follows from Eq. (45), the differential reflecting power q_{hkl} of crystals is independent of the neutron wavelength. For the strongest neutron reflexes of some known crystals, the values of q_{hkl} are given in Table 2, whence it follows that, in a perfect crystal, each reflecting plane such that it can generate a diffractive reflection and that it is traversed by a

Table 2. Reflecting power of crystals

Crystal	Diamond		Ge		Si		NaCl		Cu	
Reflection plane (hkl)	(111)	(220)	(111)	(220)	(111)	(220)	(111)	(220)	(111)	(220)
q_{hkl}, 10^{-5}	6.8	3.6	8.4	4.4	4.3	2.3	3.0	4.8	5.6	4.2
Q_n, 10^{-2} cm^{-1} ($\lambda_n \sim 1.1$ Å)	1.64	2.14	2.03	2.61	1.04	1.36	0.08	0.3	1.06	0.98
S_n, angular seconds ($\lambda_n \sim 1.1$ Å)	1.2	1.1	1.1	0.98	0.6	0.53	0.33	0.6	1.0	0.9

neutron contributes, to the amplitude of reflection, a value that is smaller than 1/10 000 of the primary-beam amplitude.

By way of example, we indicate that, for reflection from a (111) germanium single crystal ($q_{111} = 8.4 \times 10^{-5}$), it follows that, upon traversing about 12 000 (111) atomic planes, a major part of the primary beam goes over via diffraction (in the case where Bragg's law $2d_{hkl}\sin\theta_B = m\lambda_n$ is exactly satisfied) into the reflected beam. The maximum depth at which thermal neutrons penetrate is $3.26\ \text{Å} \cdot 12\,000 \simeq 4\ \mu$m. Calculations for all substances presented in Table 2 yield values on the same order of magnitude (a few microns); obviously, the absorption of neutrons concurrently becomes immaterial.

However, the process of formation of a diffractive reflection actually proceeds in a somewhat different way. First, the overwhelming majority of crystals possess a perfect structure only within small blocks (crystallites) having characteristic linear dimensions in the range 10^{-5}–10^{-4} cm. The whole single crystal consists of a mosaic of such blocks, the spatial disorientation of the blocks determining the angular width of integrated diffractive reflection. It follows that, by analogy with the optics of visible light, the model of diffraction-reflex formation is valid only within one crystallite, where one disregards the attenuation of the primary neutron beam owing to the formation of a secondary one. Second, there exist crystals like those of diamond, SiO_2, NaCl, Si, Ge, GaAs, InSb, and CdS, where large regions are formed (of dimension about a few cm^3) where the arrangement of atoms is strictly regular, so that their nuclei scatter neutrons coherently. The description of the diffraction process on the basis of the method employing cophasal Fresnel zones is inapplicable to such highly perfect single crystals without modifications, since this description takes no account of the multiple rescattering of the reflected wave into the transmitted one, and vice versa, but this rescattering becomes decisive in the case being considered.

In order to describe diffractive reflection from mosaic single crystals, use is most often made of the quantity Q that is referred to as the integrated reflection [21] or the reflection power [27] of a crystal. It can be shown [4] that, if the rocking curve is changed when the crystal on which a monochromatic neutron beam is incident is rotated in both directions with respect to the Bragg angle (θ_B), the intensity of reflection is proportional to $Q\Delta V$, where ΔV is the crystal volume participating in reflection and

$$Q = \frac{\lambda_n^3 N_c^2}{\sin 2\theta_B} F_{hkl}^2. \qquad (46)$$

It can be seen that Q greatly depends on the neutron wavelength; therefore, values for the thermal point ($E_n \sim 0.025$ eV) are given in Table 2. The quantity ΔV may be quite significant, since the majority of crystallites that form a mosaic single crystal participate in the formation of a reflex. It follows that, by appropriately choosing the dimensions of the crystallites, the degree of their disorientation, and the crystal thickness, one can arrive at the situation where more than half of neutrons belonging to the primary beam and corresponding to Bragg's law are reflected [21].

If a highly perfect three-dimensional lattice of nuclei occupies the entire volume of the single crystal used, the interaction of the incident primary beam (wave) with the secondary one formed as the result of diffraction (of the reflected wave) becomes important, as was indicated above. A unified neutron wave field is then formed within such a crystal (see Sections 3–5), and diffraction effects—in particular, the intensity of reflection—are described by the dynamical theory of scattering [5, 9]. The phenomenon of primary extinction—that is, the process of energy transfer from the incident beam (transmitted wave within the crystal) to the reflected one (the wave traveling in the direction of diffraction in the crystal)—becomes crucial, under such conditions, in the formation of a neutron reflex (see Fig. 10).

Since the atomic planes are strictly parallel, the multiple rescattering of neutrons from the transmitted wave to the reflected one, and vice versa, occurs in this case, whereby a unified wave field is formed. The path traveled by radiation in the crystal volume increases considerably, and it becomes necessary to take into account neutron absorption (especially for

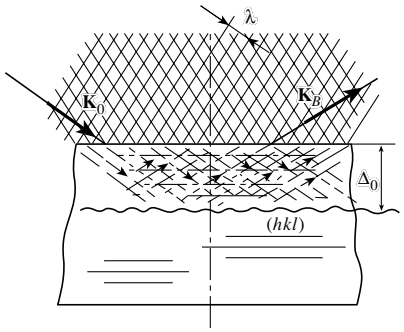

Fig. 10 [15]. Schematic representation of neutron-reflex formation in the multiple rescattering of radiation on strictly parallel atomic planes in the case of Bragg geometry.

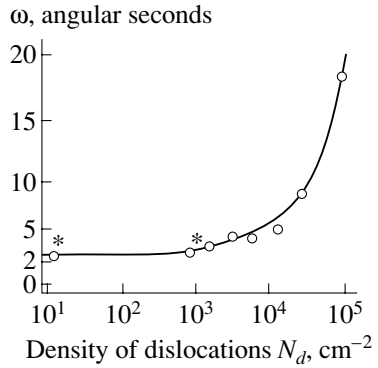

Fig. 11 [29]. Results obtained by Eichhorn *et al.* (in the early 1970s) [30], who measured the FWHM of the (111) reflex from a germanium single crystal at $\lambda_n \approx 1.5$ Å. Shown additionally in this figure are the results from [14] (asterisks), which are rescaled to the corresponding value of λ_n.

neutron-absorbing crystals like InSb and CdS), the penetration depth being defined in this case as the thickness at which the intensity of neutrons is fully converted from one wave to the other. This depth is the extinction length Δ_0, which was introduced previously [see formula (23) in Section 4] and which is about 80 μm for the above example [$\lambda_n \sim 1.7$ Å; Ge (111)]; this is a value that is much greater than the penetration depth of radiation calculated on the basis of the optical model of Fresnel zones (about 4 μm). At the same time, there occurs, as in the optical case, a complete transfer of energy from the incident to the reflected radiation; for crystals weakly absorbing neutrons (diamond, SiO_2, NaCl, Si, Ge, GaAs), the reflection factor P_B computed under the condition $\theta = \theta_B$ is equal to unity.

For the case of Bragg diffraction, which is illustrated in Fig. 10, this corresponds, according to Eqs. (38)–(40), to total neutron reflection in the rather narrow angular range $\Delta\theta = 2S = [2\lambda^2 N_c/(\pi \sin\theta_B)]F_{hkl}$ [see Eq. (41) and Fig. 8]. The values of the quantity S are also presented in Table 2; in the case of a germanium crystal used by way of illustration [$\lambda_n \sim 1.7$ Å; Ge (111)] and $\theta = \theta_B$, we have $\Delta\theta = 2.1''$. A nearly total reflection of neutrons means that the existence of radiation characterized by the above parameter values is forbidden in the crystal being considered. The presence of forbidden energy bands in semiconductor crystals—recall that electron states of specific energy values cannot exist there—is an excellent analog of this phenomenon.

In the case of Laue diffraction, the total reflection of neutrons is possible only at $\theta = \theta_B$, the entire theoretical profile of the reflected-beam intensity having an oscillating shape whose envelope has a FWHM value of about $2S$ (see Fig. 5*a*). The amplitude of the peak of this envelope is, however, one-half as great, on average, as that in the Bragg case and changes as a function of the crystal thickness or λ_n (see Fig. 5*b*). Concurrently, the extinction length Δ_0 is less than that in the Bragg case approximately by a factor of 2. This circumstance can easily be understood on the basis of relation (23), where the angle γ_0 for the Bragg and for the Laue case differs by $\pi/2$. However, only the case of a symmetric diffractive reflection or the case that differs from it only slightly—that is, the case of $\gamma_B \ll 1$ for Laue diffraction and the case of $(\pi/2 - \gamma_B) \ll 1$ for Bragg diffraction—is taken into account in (23). It is of considerable interest to construct a theoretical model that could describe the dynamical diffraction of neutrons at an arbitrary angle between reflecting planes and the crystal surface. Such a model would make it possible to understand how the transition from the Laue to the Bragg case occurs—that is, when the extinction process undergoes a qualitative change. At $\gamma_B = 0$, a strictly periodic structure of extinction waves (the period is Δ_0) is observed in the crystal volume, while, at $\gamma_B = \pi/2$, there is a fast exponential decay of the neutron field, with the relaxation length being about Δ_0. However, one has to admit that the above approach to dynamical theory on the basis of the formalism due to Ewald and Laue cannot lead to constructing such a model. This requires developing new theoretical approaches.

However, we should bear in mind the following: although $P_B = 1$ and although a perfect crystal totally reflects a neutron beam under certain conditions, this reflection occurs, in both cases, into an angular interval of a few seconds and only a moderately small volume of the substance participates in the formation of this reflex. It follows that, in relation to a mosaic crystal, a perfect one is characterized by a much lower integrated reflection intensity, which is proportional to $Q\Delta V$, its intensity at the peak remaining at approximately the same level.

The measurements performed in [28] with germanium single crystals subjected to considerable mechanical loads revealed that the intensity of reflection is in direct proportion to the degree of crystal mosaicism (the FWHM value for the rocking curve, ω). The number of neutrons removed from the beam by a mosaic single crystal ($\omega_m \sim 15'$) increases in relation to that for a perfect crystal ($\omega_c \sim 3''$) by a factor of $(15 \cdot 60''/3'') \sim 300$; concurrently, the particle-penetration depth increases from 0.1 to about 7 to 8 mm. Single crystals exhibit a similar behavior in response to an increase in the concentration N_d of dislocations distorting the crystal lattice: the reflecting power at the peak remains at the same level, while the width of the reflex grows sharply from $N_d \sim 10^3$ cm^{-2} (see Fig. 11), thereby increasing the integrating intensity of reflection.

As in the case of mosaic crystals, this is due to an increase in the volume participating in reflex formation; the latter in turn is caused by the fact that reflecting planes cease to be strictly parallel—the phenomenon of primary extinction begins to disappear, and the radiation penetrates into the interior of the crystal at an ever greater depth. The experiment reported in [31] revealed that, up to a concentration value of about 10^4 cm^{-2}, this increase is due to the fact that the reflected intensity of the diffuse component, which is present as a background, is added to the dynamical component, the intensity being gradually redistributed between them. From the experimental results presented in Fig. 11, it follows, however, that, over the rather large interval $N_d \sim 10^0$–10^3 cm^{-2}, the diffuse and the dynamical component can be separated only by using special procedures, such as those that employ a three-crystal spectrometer where the positions of the crystals used are parallel and a sectioned Bragg topography.

8. DIRECTIONS OF NEUTRON CURRENTS IN A PERFECT CRYSTAL

While the true reflection profile in the case of Laue geometry—it is described by expression (30) and is of an oscillating form—has so far defied all attempts at its experimental observation, the pattern of the neutron-field distribution over the crystal volume and, hence, the pattern of the neutron distribution at the exit of the crystal have received adequate study. But prior to describing relevant experiments and, what is more important, to explain their results, it is necessary to discuss the directions of neutron currents and to give an account of the theory of spherical-wave propagation in a perfect crystal, since this is the best approximation to an actual experiment (see Fig. 14 below).

The directions of neutron currents are of particular interest: with the aid of these, one can describe wave fields in a crystal as rays propagating along neutron currents. The neutron currents for the fields $\Psi^{(j)}$ are described by the well-known quantum-mechanical expression

$$\mathbf{j}_j = \frac{\hbar}{2im}(\Psi^{(j)*}\nabla\Psi^{(j)} - \Psi^{(j)}\nabla\Psi^{(j)*}). \qquad (47)$$

In the wave functions given by (20), the vectors $\mathbf{K}_0$ and $(\mathbf{K}_0 + \mathbf{B})$ can be replaced by $\mathbf{k}_0$ and $\mathbf{k}_B$ (see Fig. 3*a*), since, according to (25), the wave vectors $\mathbf{K}^{(1,2)}$ differ only slightly from $\mathbf{k}$. Using expressions (2) and (22) and discarding quickly oscillating terms upon averaging over the crystal volume, we arrive at [9]

$$\mathbf{j}_{1,2} = \frac{\hbar k}{m}\left[\frac{\mathbf{k}_0}{k}|U_{1,2}(0)|^2 + \frac{\mathbf{k}_B}{k}|U_{1,2}(\mathbf{B})|^2\right]. \qquad (48)$$

Multiplying expression (48) by unit vectors aligned with the vectors $\mathbf{k}_0$ and $\mathbf{k}_B$, we obtain the components of the neutron current in the general case of Laue geometry. If $\Omega_{1,2}$ are angles between atomic planes and the vectors $\mathbf{j}_{1,2}$, the neutron-current directions can be expressed in terms of the parameters $\Gamma_{1,2}$ by using Eqs. (21) and (26); that is,

$$\Gamma_{1,2} = \frac{\tan\Omega_{1,2}}{\tan\theta_B} = -\frac{1-|\chi_{1,2}|^2}{1+|\chi_{1,2}|^2} \qquad (49)$$
$$= -\frac{1-|\beta||y \mp \sqrt{y^2+\mathrm{sgn}\beta}|^2}{1+|\beta||y \mp \sqrt{y^2+\mathrm{sgn}\beta}|^2}.$$

From expression (49), it follows that, with increasing $\delta\theta = \theta - \theta_B$, which is the deviation of the angle of incidence from the exact Bragg value, the angles $\Omega_{1,2}$ increase very rapidly, with the result that, in the interior of the crystal, the fields $\Psi^{(1)}$ and $\Psi^{(2)}$ fast become spatially separated, which leads to the disappearance of their interaction. But in fact, this conclusion is valid only in the case of plane waves. The problem appears to be more involved upon taking into account the actual divergence of the beam and its momentum spread. A general theory of this kind has not yet been developed.

In the case of Laue diffraction ($\beta > 0$), which is discussed at the moment, the neutron-current directions lie within the so-called Bormann triangle or fan ($-\theta_B < \Omega_{1,2} < \theta_B$ or $-1 < \Gamma_{1,2} < 1$). Because of the spatial separation of the neutron beams, the usual conditions of interference between the two neutron fields $\Psi^{(1)}(y)$ and $\Psi^{(2)}(y)$ of the single incident wave must be replaced by the so-called conditions of spherical interference [23]. Only in this case does there exist the interference between the wave fields $\Psi^{(1)}(y)$ and

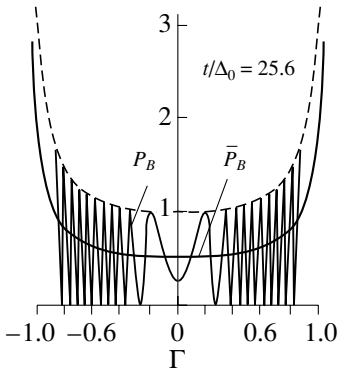

Fig. 12 [9]. Calculated intensity profile for the case of Laue diffraction (Bormann fan).

$\Psi^{(2)}(-y)$ of two different partial waves that propagate in each of the directions determined in terms of the parameters $\Gamma_1(y) = \Gamma_2(-y)$. These spherical interference conditions are of paramount importance for theoretically describing the intensity-distribution profile (Bormann fan) shown in Fig. 12.

The concepts of an incident plane wave, which were used in deriving expressions (48) and (49) for neutron currents, may be valid if the angular spread of the incident beam covers a small part of the region of total reflection from a perfect crystal, $\Delta\theta_B \sim (1{-}2)''$ (see Tables 1 and 2). In practice, it is next to impossible to collimate a neutron beam to such a great extent. In order to obtain an angular spread of about 10^{-6} rad, it is necessary to employ slits of width 0.1 mm, which, because of considerable intensity losses associated with a modest neutron-beam density, is close to the limit achievable in practice. Therefore, the dynamical theory of scattering must be extended in such a way as to include the description of divergent incident beams specified by a superposition of plane waves; that is,

$$\Phi_i(\mathbf{k},\mathbf{r}) = \int_{-\infty}^{\infty} \frac{d^3k'}{(2\pi)^3} F(\mathbf{k},\mathbf{k}')\exp(i\mathbf{k}'\cdot\mathbf{r}), \qquad (50)$$

where $F(\mathbf{k},\mathbf{k}')$ is the factor that describes the shape of the incident beam and which takes into account the character of an adopted assumption (that of a plane, a spherical, an ellipsoidal, or a hyperbolic wave or something else). The above arguments demonstrate that, unfortunately, the wave fields in a crystal become complicated for an exact consideration even in the approximation of spherical waves; therefore, it is necessary to introduce some simplifying assumptions.

First, we assume that, as in the case of an actual experiment, a diverging monochromatic beam of neutrons enters through a narrow slit, whereupon its intensity spreads over the entire Bormann fan.

Second, different partial waves are separated if the crystal is sufficiently thick; the phenomenon in question can then be described in a way similar to that adopted in the geometric optics of visible light—in this approach, each wave in a crystal is considered as a ray parallel to the neutron-current direction.

Third, we will restrict our analysis, for the sake of simplicity, to calculating the symmetric Laue case, where the directions of the neutron currents for the waves $\Psi^{(1)}(-y)$ from (49) are specified as

$$\Gamma = \frac{y}{\sqrt{1+y^2}} = \frac{\tan\Omega}{\tan\theta_B} = \frac{x}{t\tan\theta_B}, \qquad (51)$$

with x being the coordinate of the slit (as before, t is the crystal thickness).

If it assumed that the phases of different partial waves are independent, the intensities of the waves $\Psi^{(1)}$ and $\Psi^{(2)}$ must be summed. Considering that the intensity I_i propagates in space into a finite angular interval $\delta\Gamma$, we obtain

$$\bar{I}_{0,B}(\Gamma) = (|\Psi^{(1)}_{0,B}(-y)|^2 + |\Psi^{(2)}_{0,B}(y)|^2)\frac{dy}{d\Gamma}. \qquad (52)$$

Using expressions (30), (31), and (50), we can represent the intensity profiles for the transmitted and the reflected beam [$\bar{P}_0(\Gamma)$ and $\bar{P}_B(\Gamma)$, respectively] as

$$\bar{P}_0(\Gamma) = \frac{1-\Gamma}{2(1+\Gamma)\sqrt{1-\Gamma^2}}, \qquad (53)$$

$$\bar{P}_B(\Gamma) = \frac{1}{2\sqrt{1-\Gamma^2}}. \qquad (54)$$

The intensity profile $P_B(\Gamma)$ (54), which is represented by the smooth solid curve in Fig. 12, exhibits an increase in the intensity toward the edges of the Bormann fan. This effect was first observed in x-ray diffraction and then in neutron diffraction on InSb by Knowles [11] in 1956 and was explained by Kato [22, 32].

In order to obtain information about the fine structure of the intensity profile (oscillating line in Fig. 12), all incident plane waves [at this point, our consideration is performed at the level of a superposition of plane waves in the form (50)] are assumed to be coherent. Further, the dependence of $\mathbf{k}$ on y can be determined from Fig. 13*b* with the aid of relations (15), (23), and (24). The result is

$$\mathbf{k} = \mathbf{k}_B + \frac{\pi y}{\Delta_0}\left(\hat{n} + \frac{\hat{x}}{\tan\theta_B}\right), \qquad (55)$$

where $\hat{n}$ and $\hat{x}$ are unit vectors. Thus, the incident beam,

$$\Phi_i(\mathbf{r}) = \int_{-y_0}^{y_0} dy\Psi_i(\mathbf{r},y), \qquad (56)$$

for $y \to \infty$ describes a wave packet strongly localized near the immobile entrance point (slit); in the interior of the crystal, neutron waves are determined from the boundary conditions (27) as

$$\Phi_{0,B}(\mathbf{r}) = \exp(i\mathbf{K}_0 \cdot \mathbf{r}) \tag{57}$$
$$\times \int_{-\infty}^{\infty} dy[U_1(0,\mathbf{B})\exp(iT_1) + U_2(0,\mathbf{B})\exp(iT_2)],$$

where $\mathbf{K}_0$ is the wave vector of the incident wave and $T_{1,2}$ is obtained from expressions (26), (30), and (31) in the form $T_{1,2} = \pm A\sqrt{1+y^2} + Ay\Gamma$. For rather thick crystals, the amplitudes $U_{1,2}$ are functions that vary slowly in relation to $\exp(iT_{1,2})$, whence it follows that, in order to transform expression (57), one can make use of the stationary-phase method [25], where the stationary-phase point y_i must be determined from the equation $dT_j/dy = 0$. The relevant integral is then given by

$$\Phi_{0,B}^{(j)}(\mathbf{r}) = \left(\frac{2\pi}{d^2T_j/dy^2}\right)^{1/2} \Psi_{0,B}^{(j)} \tag{58}$$
$$\times \exp\left[\frac{i\pi}{4}\mathrm{sgn}\left(\frac{d^2T_j}{dy_j^2}\right)\right]_{y=y_i}.$$

The neutron waves $\Psi_{0,B}^{(j)}(|y_i|)$ propagate along the direction Γ (51), and these are the waves that are assumed to interfere in the approximation being considered. Normalizing the incident beam as $I_i = 2U_0^2\Delta_0\tan\theta_B$, we can find that, in the symmetric Laue case, the intensity profiles are given by

$$P_0(\Gamma) = \frac{(1-\Gamma)\cos^2(A\sqrt{1-\Gamma^2}+\pi/2)}{(1+\Gamma)\sqrt{1-\Gamma^2}}, \tag{59}$$

$$P_B(\Gamma) = \frac{\sin^2[A\sqrt{1-\Gamma^2}+\pi/2]}{\sqrt{1-\Gamma^2}}. \tag{60}$$

A comparison of these expressions with the corresponding expressions (53) and (54), which were obtained in the plane-wave approximation, reveals typical interference oscillations both for the transmitted-intensity profile $P_0(\Gamma)$ and for the reflected-intensity profile $P_B(\Gamma)$ (see oscillating line in Fig. 12).

A more rigorous pattern for the shapes of the incident (O) and the reflected (B) beam can be obtained with the aid of spherical waves, in which case the form factor (50) assumes the form

$$F(\mathbf{k},\mathbf{k}') = \frac{U_0}{k'^2 - k^2}. \tag{61}$$

In expression (61), one can perform integration with respect to k'_z. The result is

$$\Phi_i^{(s)}(\mathbf{k},\mathbf{r}) = \frac{U_0\exp(ikr')}{4\pi r'} \tag{62}$$

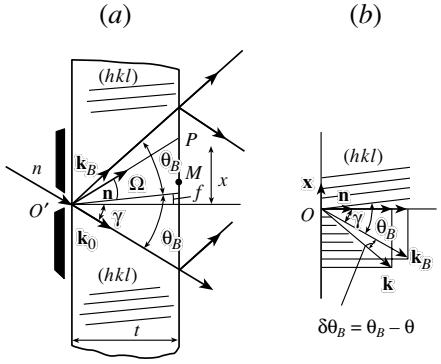

Fig. 13 [9]. (a) Illustration to the calculation of the intensities in the asymmetric Laue case; (b) relationships between the wave vectors involved.

$$= \frac{iU_0}{8\pi^2}\int dk'_x dk'_y \frac{\exp(i\mathbf{k}'\cdot\mathbf{r}')}{k'_z},$$

where $k'_z = \sqrt{k_0^2 - k_x'^2 - k_y'^2}$. Equation (62) is a spherical wave with the origin at the point O' (see Fig. 13), where $\mathbf{r} = \mathbf{r}_0 + \mathbf{r}$. As in the study of Kato [32], it is convenient to introduce the coordinate system where the vector $\mathbf{r}'_z$ is parallel to $\mathbf{k}_0$ and where the vector $\mathbf{r}'_y$ is orthogonal to a reflection plane. Integration with respect to k'_y can be performed by the stationary-phase method. The result is

$$\Phi_i^{(s)}(\mathbf{k},\mathbf{r}) = \frac{iU_0}{4\pi\sqrt{2\pi kr'}}\exp(i\mathbf{k}_0\cdot\mathbf{r}' - i\pi/4) \tag{63}$$
$$\times \int dk'_x \exp(ik'_x r'_x).$$

The approximation specified by Eq. (61) is equivalent to the approximation of a spherical wave front; therefore, the angular region of k'_x can be replaced by $k'_x = k(\theta_0 - \theta)$, with the result that, for symmetric Laue diffraction, one can write

$$\int dk'_x \exp(ik'_x r'_x) \tag{64}$$
$$= \frac{\pi}{\Delta_0\sin\theta_0}\int dy \exp\left[\frac{i\pi y}{\Delta_0} + \frac{x}{t\tan\theta_0}\right].$$

It can easily be seen that expressions (56) and (63) differ primarily by the normalization factors; since the incident wave and the neutron waves within the crystal, $\Phi_{0,B}$, are considered in the same approximation, the neutron-reflection and the neutron-transmission profile can be calculated with the aid of (57) and be represented in the final form

$$P_0(\Gamma) = \frac{\pi A(1-\Gamma)}{2(1+\Gamma)}J_1^2(A\sqrt{1-\Gamma}), \tag{65}$$

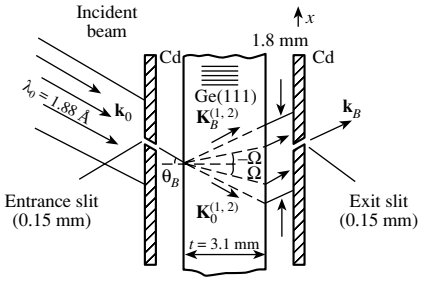

Fig. 14 [15]. Layout of an experiment aimed at observing the neutron-intensity distribution (Bormann fan) in the case of Laue diffraction.

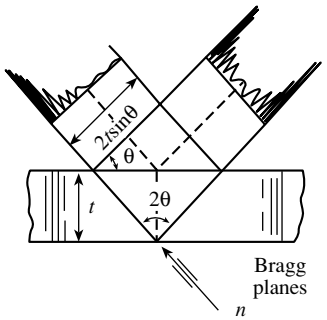

Fig. 15 [12]. Spatial intensity distribution for the Laue diffraction of a spherical neutron wave on a planar plate of perfect crystal structure.

$$P_B(\Gamma) = \frac{\pi \mathrm{A}}{2} J_0^2(A\sqrt{1-\Gamma^2}), \qquad (66)$$

where J_0 and J_1 are Bessel functions of the zeroth and the first order. The results that were obtained above in the approximation of rays and which are specified by Eqs. (59) and (60) are reproduced upon replacing these Bessel functions by their asymptotic expansions for $A \gg \pi$.

Let us now proceed to discuss experiments that make it possible to prove the validity of the model adopted here for neutron fields in a perfect crystal weakly absorbing neutrons.

9. PROFILES OF NEUTRON REFLECTION

Experiments that confirmed the correctness of theoretical considerations on wave radiation fields in the interior of a perfect crystal were performed in the late 1950s by Kato for x-ray radiation [33, 32, 22] and ten years later by Shull [13, 14] in the United States for the irradiation of silicon and germanium crystals with neutrons. A similar series of experiments was performed at the MEPI reactor [15, 31] by using an instrument specially adapted to these purposes. The layout of these experiments is given in Fig. 14. It has already been indicated in Section 5 that, if neutron radiation is incident on a perfect crystal oriented according to Laue geometry exactly at the angle θ_B, the energy of the radiation propagates exactly along the atomic planes.

But if the incident beam is slightly deflected from θ_B (that is, if the crystal is rotated through a small angle from the exact Bragg position), running neutron waves are also excited in it; however, their amplitudes $U_1(r)$ and $U_2(r)$ are not equal to each other. Therefore, neutrons will propagate at some angle to reflecting planes. As the deviation from θ_B increases, the directions of neutron-wave propagation in the crystal (and the positions of the points at which the neutron waves escape from the crystal) will be symmetric with respect to the direct-propagation direction through the crystal (accordingly, with respect to the point at which the nondeflected beam escapes from the crystal). The limiting positions of the points of escape will correspond to the directions of energy propagation at the angles $+\theta_B$ and $-\theta_B$ with respect to the planes. If the incident beam is diverging—this is always so in actual experiments—propagation will occur in all directions between these two values of θ.

In order to obtain the intensity distribution over the entire Bragg range of angles, it is necessary to introduce, in the crystal, a neutron beam over all angles corresponding to the aperture of its propagation under the diffraction condition—that is, to realize the conditions of spherical waves. The angular range into which there occurs a diffractive reflection from a perfect crystal, $\Delta\theta$, is rather narrow [see Table 1 and Eq. (41)], only a few angular seconds. In any realistic geometry of an experiment that employs reasonable dimensions of scanning slits (for example, 0.13 mm, as in the study of Shull [13], or 0.15 mm, as in the experiments performed at MEPI; see Fig. 14), the neutron beam will therefore have components that propagate over the entire angular range $[-\theta_B, +\theta_B]$, since its aperture considerably exceeds $\Delta\theta$. Within the crystal, the beam will excite running neutron waves in all directions within the above angular range, while, at the exit of the crystal, the radiation will be described by formulas (65) and (66) for, respectively, the transmitted and the reflected beam. This result is peculiar to the approximation of spherical waves. The corresponding profiles of the spatial intensity distributions are schematically shown in Fig. 15.

The experiment at MEPI was performed by scanning the back crystal surface (see Fig. 14) with a narrow (0.15 mm) slit, the entrance slit of the same width being fixed at the front surface. Use was made there of dislocation-free ($N_d \leq 10\ \mathrm{cm}^{-2}$) (111) germanium crystals of thickness 3.1 mm whose reflecting planes were orthogonal to the crystal surface to a precision of about 7′. The initial neutron wavelength was $\lambda_0 \sim 1.88$ Å, and the value of λ_n was then reduced with a

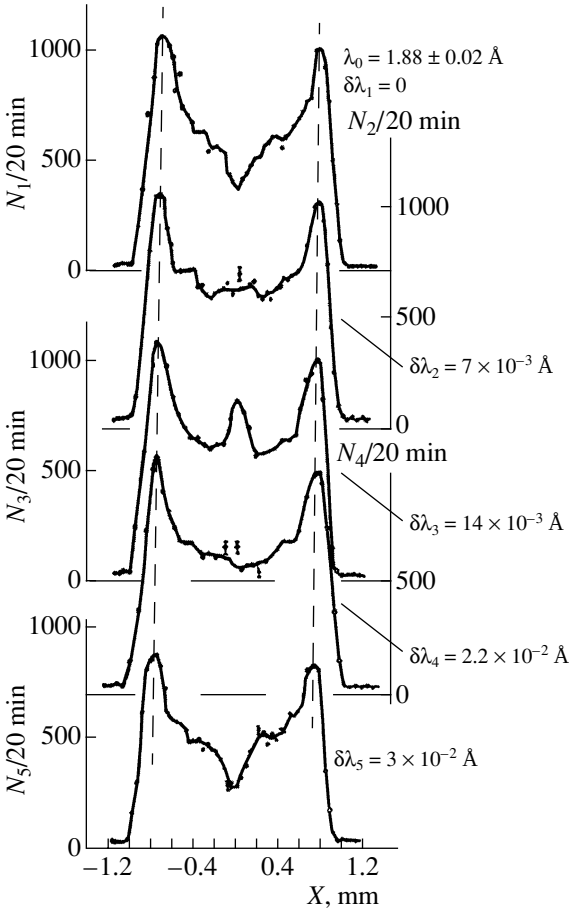

Fig. 16 [15]. Intensity distributions for reflection from (111) Ge that were obtained at various values of the neutron wavelength (Bormann fan).

step of $\delta \sim 7 \times 10^{-3}$ Å. For each value of the wavelength, scanning with a slit (a linear displacement of 0.1 mm) was performed, with the exposure at the measurement point being about 20 min. In all, seven spatial intensity distributions $P_B(\Gamma)$ (66), which were previously dubbed a Bormann fan, were taken, five of these being shown in Fig. 16.

As might have been expected, the feature that undergoes the most pronounced rearrangement in response to a change in λ_n is the profile at the center of the distribution—that is, in the segment that the radiation propagating strictly along crystal planes reaches. This rearrangement is clearly seen in Fig. 16—a minimum in the upper distribution $N_1(X)$ gives way to a maximum in the medium one $N_3(X)$, whereupon there appears a trend toward a minimum in the lower dependence $N_5(X)$. These features lead to a noticeable change in the reflecting power of a crystal. Comparing these pictures with the computed profile in Fig. 12, we can arrive at the conclusion that the calculated profile complies with the medium distributions $N_{2,4}(X)$, on which it

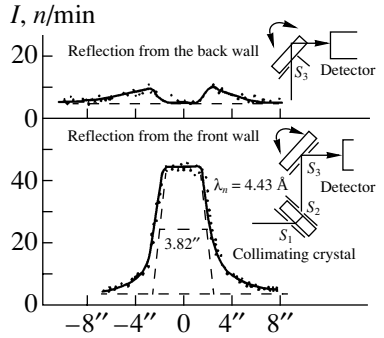

Fig. 17 [35]. Layout and results of Shull's experiment aimed at observing the profile of neutron reflection from a perfect silicon crystal in the case of Bragg geometry.

was impossible, because of insufficient resolution, to obtain oscillations at the center of the Bormann fan. In the following, we will discuss these results.

In the case of Bragg geometry, the true profile of neutron-beam reflection—that is, a Darwin table—from a perfect crystal was observed by many authors [13, 24, 25, 34], but the most representative results were obtained by Shull, who used silicon crystals [$(hkl) = (111)$]. Figure 17 displays the layout of his experiment and the results that he obtained with a perfect silicon crystal at $\lambda_n = 4.43$ Å. The success of the experiment was due to the use of a neutron beam that was incident on the crystal under study upon traversing a collimating crystal (see Fig. 17), which is shown in Fig. 14 on an enlarged scale (in the next section, we will describe this procedure in greater detail). By varying the neutron wavelength λ_n, a state was chosen that corresponds to the maximum of the intensity at the center of the Bormann fan [see $N_3(X)$ in Fig. 16]; this ensured a beam divergence at a level of $\delta\theta \sim 10^{-6}$ rad and $\delta\lambda_3 \sim 10^{-4}$ Å. Such a neutron beam was directed onto a crystal cut in Bragg geometry; owing the rotation of the crystal with a step of $\sim 0.1''$, it was possible to obtain the profiles of neutron reflection both from the front and from the back wall of the crystal (see Fig. 17).

To an acceptable degree of precision, the profile of reflection from the front crystal face is described by expressions (39) or (40); in all probability, some excess of the intensity with respect to the calculated one beyond the reflection plateau is due to the presence of weak diffuse scattering. In contrast to the experiment that was described above (Fig. 17) and which was devoted to studying the angular distribution of the intensities, an experiment under the same conditions [$\lambda_n = 4.43$ Å; Si; $(hkl) = (111)$] that was performed without Authier's collimator and which is based on scanning, with a slit, a plane orthogonal to the axis of the reflected neutron beam yields the pattern of the

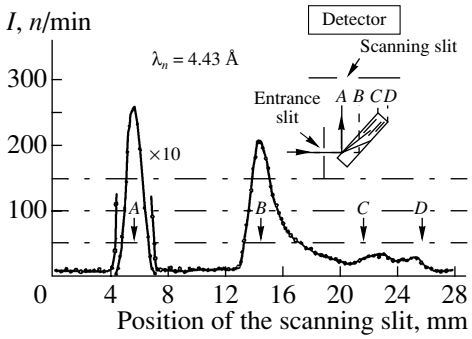

Fig. 18 [13]. Spatial distribution of the neutron intensity in scanning a beam reflected in the case of Bragg geometry.

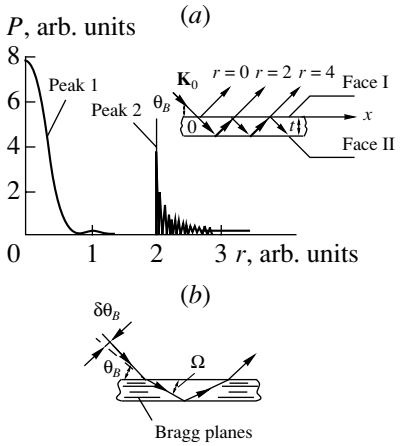

Fig. 19 [9]. (*a*) Calculated intensity profile for Bragg diffraction; (*b*) relationship between the wave vectors in a crystal for neutrons occurring beyond the total-reflection region.

spatial intensity distribution (see Fig. 18). But prior to interpreting the shape of a spatial distribution, it would be reasonable to provide an analytic description of processes occurring in a crystal and leading to the formation of the neutron field.

Let us consider schematically processes accompanying the interaction of the neutron ray $\mathbf{K}_0$ with a perfect plane-parallel crystal whose reflecting planes (hkl) are parallel to the crystal surface (Fig. 19*b*). The total reflection of a neutron wave (vector $\mathbf{K}_B$ in Fig. 6) occurs at the outer crystal face; this process is described by the Ewald solution (39), obtained for the case in which two strong waves are excited in a crystal (a transmitted and a reflected one—see Section 6) and which is realized most often in practice. The effect of total reflection in the range $|y| \leq 1$ is due to the fact that the wave field in a crystal undergoes an exponential decrease, which leads to a total conversion of the incident wave into a diffracted one. An effective attenuation of the wave field occurs at a depth of about the extinction length Δ_0 [see Eq. (23)]. In the region $|y| > 1$, the incident wave travels freely through the crystal, only undergoing a partial reflection at the crystal–vacuum interfaces because of the jump in the potential energy of neutrons (see Fig. 19*b*) [31].

If absorption does not occur, which is so, to a considerable extent, in dealing with silicon crystals, the result obtained by averaging, over oscillations, the distribution of the diffracted-beam intensity at the face I in the approximation of an incident spherical monochromatic wave having a narrow wave front (the crystal thickness t is much larger than the wave-front width specified by the slit) is given by [9]

$$P(r) = \frac{\pi A}{2}\left[\frac{2J_1(Ar)}{Ar}\right]^2\Theta(r) \qquad (67)$$
$$+\sum_{n=1}^{\infty} 8\left(\frac{2n}{r+2n}\right)^4\left(\frac{r-2n}{r+2n}\right)^{2n-2}\frac{\Theta(r-2n)}{\sqrt{r^2-(2n)^2}},$$

where $A = \pi t/\Delta_0$ is the reduced crystal thickness; r is a dimensionless parameter (see Fig. 19*a*) that is proportional to the coordinate x reckoned within the face I of the crystal from the point of incidence of the neutron beam in the plane of the figure; $\Theta(r) = 0$ for $x \leq 0$, and $\Theta(r) = 1$ for $x > 0$; and $J_1(x)$ is a Bessel function of the first order. In the case of symmetric Bragg diffraction considered at the moment (the reflecting planes are parallel to the crystal surface), the vector $\mathbf{B}$ of the reciprocal lattice is orthogonal to the crystal surface and $r = x/(t\tan\theta_B)$. Because of rather large dimensions of crystals used in experiments, one can consider only the region $0 \leq r < 4$ in calculating the spatial distribution of the diffracted intensity. According to (67), the distribution of the intensity will then have the form

$$P(r) = P_0(r)\Theta(r) + P_1(r)\Theta(r-2) \qquad (68)$$
$$= \frac{\pi A}{2}\left[\frac{2J_1(Ar)}{Ar}\right]^2\Theta(r) + \frac{128\Theta(r-2)}{(r+2)^4\sqrt{r^2-4}},$$

where $P_0(r)$ and $P_1(r)$ are the intensities of the reflected beams for $n = 0$ and $n = 1$, respectively. For the case of $A = 5$, the result of the theoretical calculation of the distribution in (68) is given in Fig. 19*a*. By making use of the asymptotic expansion of Bessel functions, it can be found that, for $r \to 0$, we have $P_0 \to \pi A/2$ and that, for $Ar \gg 1$, P_0 decreases approximately in proportion to $4/(A^4r^2)$. In the case of a thick crystal, $A \gg 1$, the term $P_0(r)$ is therefore different from zero in a close vicinity of $r \sim 0$, so that it is convenient to represent it in the following in form of a Dirac delta function. Requiring fulfillment of the normalization condition, we arrive at $P_0(r) = (16/3)\delta(r)$.

Formula (68) can be interpreted as follows: according to (38) (see Section 6), radiation incident to the region $|y| < 1$ undergoes total reflection at the crystal surface that is parallel to reflecting planes. Waves for which $|y| > 1$ split in amplitude at face I (see Fig. 19*a*)—upon undergoing mirror reflection from the surface, some neutrons of the incident beam propagate along with diffracted radiation (for which $|y| < 1$), giving rise to peak 1, while other neutrons propagate into the interior of the crystal. This means that the function $P_0(r)$ in (67) and (68) predominantly describes radiation incident on the crystal in the vicinity of the Bragg angle. Some part of the radiation that penetrated into the crystal is reflected from face II and then, upon undergoing a partial reflection at face I, leaves the crystal, giving rise to peak 2, which thereby entirely corresponds to rays for which $|y| > 1$. The angle between the direction of wave propagation within the crystal and reflecting planes (see Fig. 19*b*) is specified by relation (49), $\tan\Omega = [(y^2-1)/y^2]\tan\theta_B$, whence it follows that the deviation of a ray incident on a crystal from θ_B by a value of about an angular second causes its rotation in a crystal through a few angular degrees.

The theoretical consideration in [31] gives grounds to state that, in the case of diffraction in Bragg geometry, there is an effect that is analogous to the emergence of the Bormann fan in the case of Laue diffraction. Indeed, peak 1 in the spatial distribution in Fig. 18 is an extinction peak (position A)—it is formed by neutron reflection within the angular limits of the region of total diffractive reflection by a surface layer, $\sim(2\text{–}3)\Delta_0$ (about 200 μm). Further, the scanning slit fixes the absence of reflected neutrons up to the position where the parameter $r = x/(t\tan\theta_B)$ becomes equal to $r = 2$, and peak 2, which corresponds to reflection from face II (position B of the scanning slit), appears in the neutron distribution $P(r)$. According to (68) (see Fig. 19*a*), this is an asymmetric peak; it demonstrates a smooth decrease in the mean intensity of neutrons for $r > 2$ in the distribution $P(r)$, which is the result of averaging over characteristic interference oscillations. The actual distribution profile obtained experimentally by Shull is always smeared because of a finite collimation, the momentum spread of the beam, and wavefront distortions due to the use of finite-dimensional slits and the geometry of the sample. The general form of this distribution is shown in Fig. 18, which also indicates the special features of the experiment being discussed. Similar experiments were performed at MEPI [31] with (111) germanium crystals. This made it possible, first, to develop a method for determining the "differential" (layer-by-layer) reflecting power of crystals having various degrees of deviations from a perfect structure and to substantiate an optimum value of the monochromator-crystal thickness [28] and, second, to study interference effects in diffuse scattering on dislocations in nearly perfect crystals [36].

10. "PENDULUM BAND" EFFECT

The spherical-wave approximation, which was used in Section 8, describes most accurately the actual pattern of neutron-field formation in a perfect single crystal and makes it possible to understand completely the results shown in Fig. 16. Neutrons incident on a crystal strictly at the Bragg angle propagate along reflecting planes; radiation-energy transfer occurs in the form of two running waves $[(\Psi_0^{(1)} + \Psi_B^{(1)})$ and $(\Psi_0^{(2)} + \Psi_B^{(2)})]$ whose wave vectors differ by about 10^{-6} from the absolute value of the vector $|\mathbf{k}| = 2\pi/\lambda_n$ ($\lambda_n = 2\times10^{-8}$ cm, $|\mathbf{k}| \sim 3\times10^{-8}$ cm^{-1}). It follows that, at some regular intervals [Δ_0 is the period of the pendulum solution (23); it is about 10^{-3} cm], there occurs beating of these waves—that is, an interference enhancement or suppression that leads to radiation-energy transfer from one component to the other and to a nonuniform density for the experimentally observed reflected intensity $P_B(\Gamma)$ (60). In view of the analogy with the interaction occurring between two coupled pendula, Ewald called, many years ago, this, purely interference, effect of the intensity in the central part of the Bormann fan a "Pendullosung" [17]. The crystal thickness t or the neutron wavelength λ_n (or both) is a parameter whose variation converts a maximum into a minimum, and vice versa. For example, this was so in Shull's experiments [13] or in the experiment that was described in the preceding section and where, in scanning with a slit, the authors observed a change in the neutron intensity at the center of the Bormann fan versus λ_n and measured the intensity of the reflected neutron beam (see Fig. 16).

Oscillations of the neutron-reflection intensity $P_B(\Gamma)$ were also observed in changing the crystal thickness, various experimental procedures being possible in this case. Zippel was the first who performed such an experiment [18]. He diminished the thickness of a perfect silicon crystal by etching layers of thickness 2 to 3 μm off its surface and measured the reflecting power of a specific volume of a crystal cut in Laue geometry. By repeating such an experiments many times, he obtained a fragment of the integrated reflection curve (see Fig. 5*b*) in its initial segment.

The oscillating part of this curve can also be reproduced by the "slope method" [19]. Within this method, one measures the intensity of scattering from the effective optical crystal thickness t^*, which is

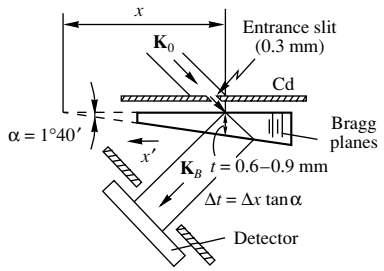

Fig. 20 [38]. Layout of an experiment aimed at observing oscillations of the neutron-reflection intensity on a wedge-shaped germanium crystal (111) in the case of Laue geometry.

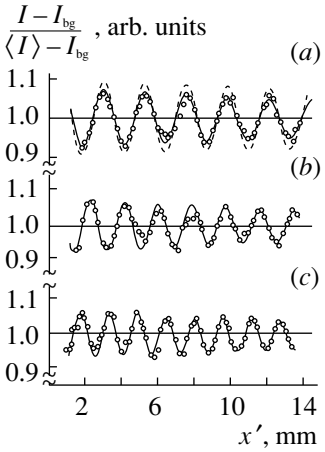

Fig. 21 [38]. Oscillations of the diffracted-beam intensity versus x', which is the position of the sample (wedge-shaped germanium crystal) with respect to the slit. The solid curves were computed with allowance for the geometry of the experiment and for the momentum spread of the beam; here, I is the experimental intensity value, I_{bg} is the background level, and $\langle I\rangle$ is the average value of the intensity. In Fig. 21*a*, $\lambda_n = 1.64$ Å, $\langle I\rangle = 14\,600$ pulses, and $I_{bg} = 650$ pulses; the dashed curve represents the theoretical dependence in the case of a monochromatic wave and an infinitely narrow slit. In Fig. 21*b*, $\lambda_n = 1.97$ Å, $\langle I\rangle = 8900$ pulses, and $I_{bg} = 650$ pulses, while, in Fig. 21*c*, $\lambda_n = 2.30$ Å, $\langle I\rangle = 16\,900$ pulses, and $I_{bg} = 1300$ pulses.

changed by rotating the sample used about the normal to the reflecting plane. This study was performed by Somenkov and his colleagues at the Kurchatov Institute of Atomic Energy (IAE). Experiments that are simpler from the methodological point of view were carried out by using crystals cut in the form of wedges: in [37], the scattering plane was orthogonal to the edge of the wedge, while, in [38], it was parallel to this edge. In the experiment that was reported in [38] and which was performed at the MEPI reactor, pendulum bands were observed in neutron diffraction on a wedge-shaped perfect germanium crystal (see Fig. 20) for which $t = x\tan\alpha$, where α is the wedge opening angle and x is the crystal position with respect to the collimating slit. In the case where the wave is monochromatic and where the slit is infinitely narrow, the dependence of the intensity on the slit position is determined by the Waller integral (35), which, with allowance for the relation $P_B(x) = R_B^y(x\tan\alpha)$, can be recast into the form

$$P_B(x) = \frac{\pi}{2}\int_0^{2\pi x\tan\alpha/\Delta_0} J_0(z)dz. \qquad (69)$$

For the (111) reflection used, the results calculated on the basis of (69) and normalized to the averaged intensity level are represented by the dashed curve in Fig. 21*a*. The measurements were performed at a facility that was adapted for dealing with perfect crystals [39]. A plate from germanium single crystal characterized by a dislocation density N_d less than 10 cm^{-2} and cut in the form of a wedge with opening angle $\alpha = 1°46'10'' \pm 10''$ served as a sample. One of the crystal surfaces was oriented to be orthogonal to reflecting planes. The sample was subjected successively to grinding, chemical polishing, and deep etching with the aim of removing the damaged surface layer. The slit width was about 0.3 mm, which ensured a sufficient contrast of pendulum bands and a high intensity level. The slit was placed immediately adjacent to the sample in such a way that its edges were parallel to (111) planes to within 10′.

The experimental profiles were taken by successively shifting the sample in the 111 direction with a step of 0.2 mm and by recording the diffracted beam. A monochromatic beam was obtained via the reflection of a "white" beam from a pyrolitic-graphite crystal, the collimation angular divergence being about 25′. A comparison of the curve calculated according to (69) with the experimental profiles demonstrates that the contrast of the observed pendulum bands is less than the theoretical contrast. This is due to a finite slit width and to the collimation angular divergence of the beam. The relevant corrections were computed with allowance for the specific geometry of the experiment. For the neutron-wavelength values used ($\lambda_n = 1.64$, 1.97, 2.30 Å), the results of these calculations are represented by solid curves in Fig. 21 and are in good agreement with experimental data.

The method for observing pendulum bands that was implemented at MEPI makes it possible to determine the extinction length (or coherent scattering amplitude) to a precision of about the relative momentum spread of the beam, the latter being not greater than a percent in actual experiments. By way of example, we indicate that, from the curve obtained

at $\lambda_n = 1.64$ Å (Fig. 21*a*), the value of $b_{coh} = (0.83 \pm 0.02) \times 10^{-12}$ cm was determined for the coherent scattering amplitude. If a precision measurement of the coherent-scattering amplitude b_{coh} is required, this method cannot compete with the interferometric method, which ensures accuracies of 10^{-4}. However, it has the advantage of simplicity in an implementation for experiments where external fields—for example, electromagnetic or supersonic ones—must be applied to the sample under study. In these cases, the external fields acting on the sample change the mechanism and parameters of neutron diffraction on perfect crystals, and this is determined from the form of oscillations of the intensity.

In all cases listed above (variations in the neutron wavelength λ_n or the sample thickness t; "slope" or "wedge" methods), the depth of the intensity modulation was significantly less than that in measurements of oscillations in the central part of the Bormann fan (see Fig. 22), which were constructed on the basis of an analysis of data in Fig. 16 [distributions $N_{1-7}(X)$], because the reflected beam was recorded there over nearly the entire Bormann fan.

One interesting point is worthy of note: the neutron distributions in the Bormann fan that feature oscillations of the intensity in the central part had been obtained experimentally before the theory of spherical waves in a perfect crystal was formulated, and it was these experiments that gave impetus to developing this theory, since the theory of plane waves yielded, for the distributions in question, formula (53), which does not reproduce the presence of a fine structure. Yet another circumstance that emphasizes the precision character of these experiments is that the fine structure at the fan center is smeared for some natural reasons, including a finite width of the slits, a specific momentum spread of neutrons in the beam, the fact that faces of the crystal are not parallel, and the presence of imperfections in its structure; therefore, only precision experiments could reproduce the correct physical pattern of the phenomenon in question.

The experimental procedure described above also made it possible to make advances in observing the true reflection profile in the case of Bragg diffraction. The neutron beam that escaped from the crystal strictly at the center of the Bormann fan was incident on a perfect crystal with $(hkl) = (220)$ reflecting planes parallel to its surface, and, in the case of its rotation within a few angular seconds, Shull [13] observed the neutron-reflection profile (see Fig. 17) that is predicted by the dynamical theory of diffraction [Section 6, formula (38)]. The point is that a perfect crystal that reflects neutrons according to Laue and which is surrounded by narrow slits in such a way that only a beam that is incident strictly at the Bragg angle and which propagates in the crystal in the direction parallel to (hkl) planes is a unique collimating system. It transmits neutrons reflected by the crystal into an angular range of a few tenths of an angular second within the first period of the oscillations of the reflection curve (Fig. 5*a*). It is hardly possible to create such a collimation in a natural way, since this requires transmitting a neutron beam through slits of width 1 mm that are separated by a distance of $(0.2'' \approx 10^{-6}$ rad) 1 km, but this would lead to a catastrophic decrease in the intensity. At the same time, it is precisely such an angular resolution of a probing beam that is required for observation in order that its convolution with the true reflection profile under study not lead to the smoothing of the latter.

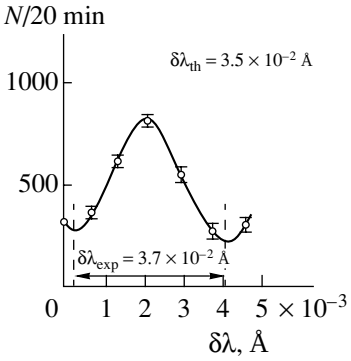

Fig. 22 [15]. Oscillations of the intensity in the central part of the Bormann fan shown in Fig. 16 for various values of the neutron wavelength λ_n.

Thus, we conclude that, if one were able to perform an "ideal" experiment that is free from the above experimental limitations, the Bormann distribution of the intensities would be such as that which is shown in Fig. 12. And if one were able to take a photograph of it and not forced to plot it point by point, a series of interference bands would be observed in the distribution. These bands would be widely spaced at the center and would be "infinitely" convergent toward the edges. In an actual experiment, it is impossible to see interference beating near the edges because of a finite resolution, and oscillations of the intensity are observed only in the internal region. It can be assumed that they are equivalent to Newton's rings in the optical case, with the exception of the fact that they are rectilinear, although this circumstance can be taken into account by applying a cylindrical lens tightly pressed to a planar glass plate. If we now view this optical system from the upward direction at normal angle of light incidence, we will see straight interference bands that approach each other toward the edges and which are the broadest in the central region. This is precisely the effect that mani-

fested itself in the case of neutrons as an equivalent of Newton's rings in the optical case and which demonstrates a deep analogy between the neutron optics of perfect crystals and the optics of visible light.

11. PHYSICAL PRINCIPLES OF NEUTRON INTERFEROMETRY

Any of the experiments studying neutron scattering can be described in terms of quantum mechanics as follows: an incident beam whose state is described by the wave function Ψ goes over, as the result of some interaction, into the state whose wave function is $\hat{W}\Psi$ [12]. The problem almost always consists in determining the operator $\hat{W}$, which in principle contains the entire body of information about the sample (object, target, ensemble of scatterers), neither Ψ nor $\hat{W}\Psi$ being physically observable. Of particular interest is the case where there is no absorption within the sample. In terms of quantum mechanics, zero absorption corresponds to the unitary operator $\hat{W} = \exp(i\hat{\Phi})$, where $\hat{\Phi}$ is a Hermitian operator; therefore, the total intensity summed over all scattering channels does not change:

$$I = \int (\hat{W}\Psi)^*(\hat{W}\Psi)d\tau = \int \Psi^*\Psi d\tau = 1. \quad (70)$$

The underlying idea of interferometry consists in attempts at extracting information about $\hat{W}$ from the observation of a coherent process of superposition (interference) of the states $\hat{W}\Psi$ and Ψ as a "reference" beam:

$$I_\pm \equiv \frac{1}{2}\int (\hat{W}\Psi \pm \Psi)^*(\hat{W}\Psi \pm \Psi)d\tau = 1 + \langle\cos\hat{\Phi}\rangle. \quad (71)$$

As examples of interaction involving no absorption, in which case $\hat{W}$ is a unitary operator, we can indicate the following: (i) the interaction of neutrons of wavelength λ_n with a plane-parallel plate of thickness t from a homogeneous substance having the neutron-refraction factor $n_\lambda \simeq 1 - \lambda_n^2 b_n N/\pi$ [for this interaction, we have $\hat{W} = \exp(i\varphi)$, where $\varphi = 2\pi t(n-1)/\lambda_n$] and (ii) the rotation of the spin of a neutron that traverses the region of a uniform magnetic field $\mathbf{B}$ over the time interval τ [the operator in question then has the form $\hat{W} = \exp(i\mathbf{S}\cdot\mathbf{a}/2)$, where $\mathbf{S}$ is the Pauli vector and $\mathbf{a} = \gamma\tau\mathbf{B}$, with γ being the gyromagnetic ratio].

With the advent of lasers, the interference of light waves (which is an optical phenomenon known since the times of Newton) led to holography (1960–1962), a method that has been well developed at present. The essence of this phenomenon consists in the interference of deflected and scattered waves with a coherent reference beam, which are all made to intersect at one spatial point. At the level of the phases of the waves, the entire body of information about the spatial structure of scattering substance is encoded in a hologram with a volume resolution of about the wavelength of light ($\lambda \sim 10^{-6}$ m). This technique makes it possible not only to measure the macroscopic properties of a homogeneous sample but also to assess the properties of individual elements of its structure.

It is an ardent desire of modern physicists to apply these methods to short-wavelength ($\lambda \sim 10^{-10}$ m) radiations, such as electrons, x-ray photons, and thermal neutrons. Difficulties in controlling a neutron beam (as well as a beam of x-ray photons)—that is, in coherently splitting it by means of refraction and in subsequently making the resulting components intersect at some point—arise because of the fact that the refraction factor for these radiations is close to unity for all substances. Problems associated with the creation of coherent sources and the impossibility of detection with a spatial resolution less than a few microns complicate the situation still further.

Nevertheless, Maier-Leibnitz and Springer [40] successfully used in 1962 a biprism to bring beams into line and to demonstrate that a neutron interferometer can in principle be created. A control of a beam is considerably simplified with the aid of Bragg diffraction on perfect crystals, which was first applied by Bonse and Hart [41] in 1965 in order to create an x-ray interferometer. The simplest version of the interferometer—a so-called interferometer of the LLL type (Laue diffraction on three successive crystal plates cut from the same single crystal) (see Fig. 23)—implements a diffractive splitting of a beam (S), refraction (M), and bringing into line (A). It is the version that was realized by Rauch *et al.* [42] in 1974 as a neutron interferometer and which later became an efficient instrument for fundamental studies in the realms of nuclear and solid-state physics.

Combined dynamical diffraction on several perfect crystals must be used to achieve a coherent splitting of beams and their subsequent superposition. A relevant theory was developed in the late 1960s and the early 1970s [16, 26] for directly interpreting results that had already been obtained experimentally. In the case of neutron (or x-ray) diffraction on a single plate of a crystal (see Sections 5, 6), the plate thickness t is the only parameter that affects the results. In the presence of several crystals, the results of dynamical diffraction may depend not only on the thicknesses of the crystals but also on their relative positions and orientations and, sometimes, on the distinctions between their interplane spacings.

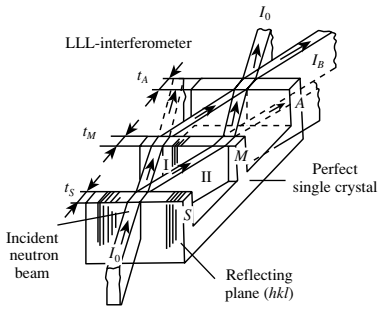

Fig. 23 [42]. First neutron interferometer of Rauch on the basis of silicon crystals: (S) crystal splitter, (M) crystal reflector, and (A) analyzing crystal.

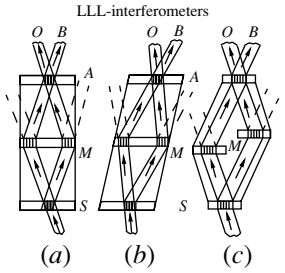

Fig. 24 [12]. Various types of LLL interferometers (trajectories of neutron fluxes are indicated without taking into account the expansion of rays by the Bormann fan): (a) symmetric, (b) asymmetric, and (c) skew-symmetric version.

An interferometer of the LLL type is an instrument that fully realizes the physical principles of combined dynamical diffraction on crystals weakly absorbing neutrons. The calculated profile of the curve of reflection from such crystal—for example, from silicon crystals—is displayed in Fig. 5, while the spatial distribution of the intensity is shown in Fig. 15. These curves represent intensities, which are the squares of wave-function amplitudes, while information about phases is lost. However, it is interferometers that make it possible to monitor the behavior of a neutron beam at the level of phases. Upon undergoing diffraction on the plate S (of thickness t_S), a neutron whose behavior is described by the split wave function $\Psi_{0,B}^{(1,2)}$ arrives at the plate M (t_M), which makes the beams intersect at one point (the problems of focusing are omitted here) on the plate A. Here, the beams interfere and, in the resulting pattern, the intensity is suppressed if the wave functions of the beams are in antiphase and is enhanced if they are in phase. As a result, an interferometer acquires the properties of a phase resonator. Let us now assume, in the gap between the plates S and M, some object of nonzero neutron-optical density ρ_n is inserted in such a way that it intersects the path of one neutron beam (or of both, but differently). In this case, the phase difference between the beams arriving at the plate A will change, which is manifested as a decrease or as an increase in the intensity in the detectors that record the neutron beams I_0 and I_B after the plate A (see Fig. 23).

Because of "zero" absorption in silicon (there is presently no information in the literature about the creation of interferometers from other substances), it is necessary to take into account both dynamical wave fields with antinodes ($\Psi^{(1)}$, $\mathbf{K}^{(1)}$) and nodes ($\Psi^{(2)}$, $\mathbf{K}^{(2)}$) in atomic planes. As a result, it is usually more difficult to attain conditions of a good contrast. In the 1970s and 1980s, researchers developed various schemes of neutron (and x-ray) interferometers of the LLL type that involve symmetric, asymmetric, and skew-symmetric Laue reflection (see Fig. 24); interferometers of the BBB and the BB type (use is made there of Bragg diffraction); and interferometers of the mixed LBBL type. A detailed discussion of these devices can be found in [12, 15].

With the aid of LLL interferometers, a number of fundamental experiments have been performed since 1974. Each experiment has its own special features, but, in all of them, it was necessary to create the phase difference between beams I and II (see Fig. 25)—in particular, this can be done by inserting a sample in the gap between the crystal plates of the interferometer. A precision measurement of the coherent scattering length b_{coh} for solid-state, liquid, and gaseous substances was one of the first applications of the LLL interferometer.

A sample in the form of a plane-parallel plate is positioned on the trajectory of the beam between the crystals S and M (Fig. 25), whereupon one rotates it about an axis that is orthogonal to the plane of ray propagation and measures the integrated intensity I_0 in the transmitted beam O or the integrated intensity I_B in the reflected beam B. The characteristic oscillations of the intensity as a function of the optical thickness of samples from various metals are shown in Fig. 26. The nature of these oscillations is quite obvious: any substance characterized by the reflection factor n_λ [see Eq. (11) in Section 3] causes phase shifts between the two waves because of the difference of the distances Δd traveled by neutrons in it:

$$\frac{\Psi_0^{\mathrm{I}}}{\Psi_0^{\mathrm{II}}} = \exp[iK(1-n_\lambda)\Delta d]. \qquad (72)$$

This leads to periodic modulations of the intensity upon traversing an interferometer; that is,

$$\frac{I_0(\Delta d)}{I_0(0)} = \frac{1}{2}\left[1+\cos\left(\frac{2\pi\Delta d}{D_\lambda}\right)\right], \qquad (73)$$

where $D_\lambda = 2\pi/(\lambda_n N b_{\mathrm{coh}})$ is the "single-wave" thickness. It is the expression in (73) that makes

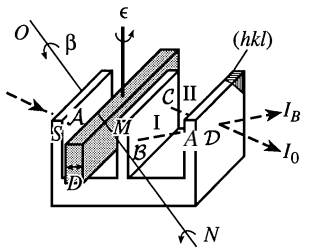

Fig. 25 [9]. Arrangement of solid-state samples in an LLL interferometer (ε is the axis of sample rotation) and scheme of the rotation of the entire instrument (about the ON axis) in a gravitational experiment: (S) crystal splitter, (M) crystal reflector, (A) crystal analyzer, and (D) sample.

it possible to use such measurements to determine precisely the coherent scattering amplitude b_{coh}. As can be seen from Fig. 26, the greater the amplitude b_{coh} in absolute value—that is, the higher the scattering ability (neutron-optic density) of a substance—the higher the frequency of the oscillations. The smallness of b_{coh} in vanadium, $b_{\mathrm{coh}}^{\mathrm{V}} = 0.048 \times 10^{-12}$ cm, is responsible for the distinctive features of oscillations for this metal (see Fig. 26). It is usually used to manufacture plane-parallel vessels for experiments with liquid samples. In order to perform measurements for gases, one usually employs plane-parallel vessels from aluminum that are of much larger dimensions than those for liquids, since it is more convenient to measure the pressure of a gas than to move vessels. The sample is then placed on one of the beam trajectories—for example, $\mathcal{AC}$ (see Fig. 25). At present, interference measurements have been performed for gaseous hydrogen, nitrogen, oxygen, helium-3, helium-4, argon, and xenon and for many solid-state samples. The accuracy of the measurements of b_{coh} was 10^{-3} for gases and 10^{-4} for solid-state samples; combined with the relative simplicity of the relevant experimental procedure and its universality with respect to different subjects of investigation, this creates unique possibilities. The above accuracy can still be improved by one order of magnitude by additionally stabilizing the interferometer; however, it is not the experimental procedure but the features of a sample (its composition, uniformity, geometry, etc.) that impose limitations on the accuracy. On the other hand, this opens a new field for the application of interferometry to solving problems in solid-state physics, since there arises the possibility of establishing the hydrogen and the deuterium concentration in metals to a precision of 0.02 to 0.06% by measuring the single-wave thickness as a function of their content in metals. An example of the results obtained from such measurements is given in Fig. 26*b*.

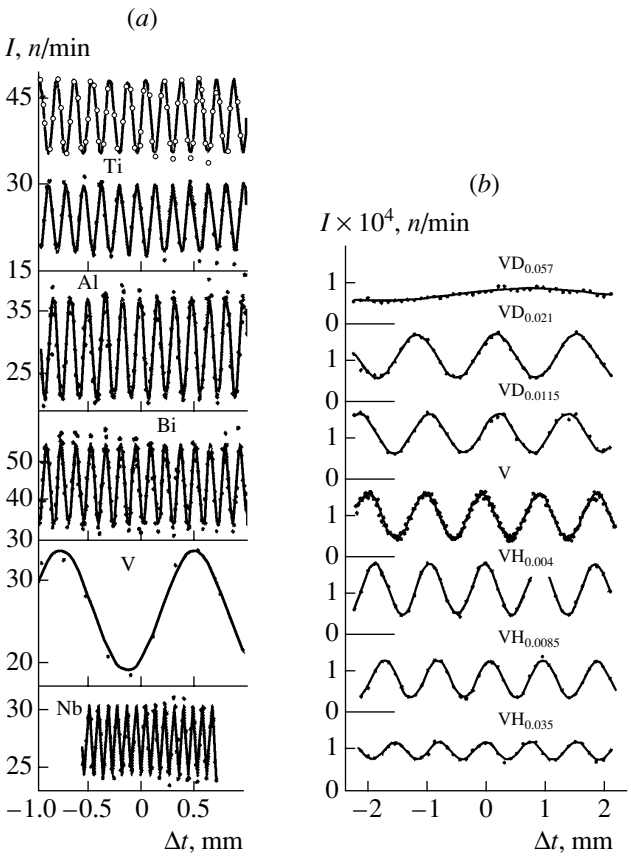

Fig. 26 [9]. (*a*) Characteristic oscillations of the intensity of the neutron beam that traversed an interferometer versus the sample thickness for various metals: open and closed circles represent, respectively, the intensity I_B of the beam B and the intensity I_0 of the beam O; (*b*) results obtained by measuring the oscillations of the intensity for VH or VD samples with the aim of determining the hydrogen or the deuterium concentration.

An observation of phase shifts caused by gravity [43] is yet another remarkable experiment that was performed with an interferometer. If the trajectories I and II of the motion of neutrons are at different altitudes—that is, the motion of the particles occurs in different gravitational potentials—there arises a phase shift $\Delta\varphi$ associated with gravity. For waves that traversed an interferometer, we can in general write the relation

$$\Delta\varphi = \frac{1}{\hbar}\int\limits_{\mathrm{I}} \mathbf{p}d\mathbf{r} - \frac{1}{\hbar}\int\limits_{\mathrm{II}} \mathbf{p}d\mathbf{r} = \frac{1}{\hbar}\oint \mathbf{p}d\mathbf{r}. \qquad (74)$$

Since the experiment in question was performed on the surface of the rotating Earth, this circumstance must be taken into account; that is, the Hamiltonian must be written in a rotating coordinate frame in the

presence of gravity. Specifically, we have

$$H = \frac{p^2}{2m_i} - G\frac{Mm_g}{r} - (\boldsymbol{\omega}\cdot\mathbf{L}), \qquad (75)$$

where $\mathbf{L} = [\mathbf{r}\times\mathbf{p}]$; $\boldsymbol{\omega}$ is the angular frequency of rotation of the system; and m_i and m_g are, respectively, the inertia and the gravitational mass. Calculating $\mathbf{p}$ and $\mathbf{r}$ from classical Hamilton's equations and using Eq. (74), one can obtain the semiclassical expression for the phase shift in the form

$$\Delta\varphi_0 = \frac{m_i}{\hbar}\oint \dot{\mathbf{r}}d\mathbf{r} - \frac{m_i}{\hbar}\oint(\boldsymbol{\omega}\cdot\mathbf{r})d\mathbf{r}, \qquad (76)$$

where the first term is responsible for the possible change in the particle momenta along the contour of integration (trajectories I + II), including the change that is associated with the effect of the force of gravity, while the other term takes into account the rotation of the coordinate frame. The existence of this effect for light was first demonstrated by Sagnac in 1913 in an experiment where an optical interferometer was placed, together with a source, on a rotating platform.

Such an experiment with a neutron interferometer was first performed in 1975 at Michigan State University (USA) [43]. Neutrons moving in the direction ON [see Fig. 25, but without the insertion of the sample (in the form of a plate) into the interferometer] are split at the point $\mathcal{A}$ into two coherent beams traveling along the trajectories I and II and converge at the point $\mathcal{D}$. If the $\mathcal{ABCD}$ plane is not horizontal, the coherent beams are in different gravitational fields, which induce different changes in the phases of neutron waves. If the interferometer is rotated about the axis ON, the phase difference varies according to the relation $\Delta\varphi = \Delta\varphi_0 + \sin\beta$, where $\Delta\varphi_0 = \Delta\varphi_g + \Delta\varphi_{\text{Sagnac}}$ and β is the angle of rotation of the plane of the trajectory with respect to the horizontal. The phase shift associated with gravity, $\Delta\varphi_g$, is

$$\Delta\varphi_g = -m_i m_g\left(\frac{g}{2\pi\hbar^2}\right)\lambda_n S, \qquad (77)$$

where S is the area of the parallelogram $\mathcal{ABDC}$ and g is the acceleration due to gravity. In measuring $\Delta\varphi$—that is, in rotating the interferometer about the horizontal axis ON—the gravitational phase shift changes and can be determined by studying the periodic modulation of the intensities I_0 and I_B. Prior to performing experiments with neutrons, the instrument was calibrated by using x-ray radiation; the absence of a change in the detector counting rates served as a test. The observed periodicity in the detector counts versus β was due to the effect of the changing gravitational potential. The phase shift associated with the Sagnac effect is $\Delta\varphi_{\text{Sagnac}} = 4\pi m_i\hbar^{-1}(\boldsymbol{\omega}\cdot\mathbf{S})$, where $|\mathbf{S}|$ is the area of the parallelogram $\mathcal{ABDC}$ and $\boldsymbol{\omega}$ is the frequency of Earth's rotation ($|\boldsymbol{\omega}| = 7.29\times10^{-5}$ s^{-1}). In the experiment with a neutron interferometer, both effects were discovered and were measured to a fairly high degree of precision. From the value of $\Delta\varphi_g$, one can extract the value of $\sqrt{m_i m_g}$ and compare it with the neutron mass as determined from the energy balance of a nuclear reaction [43]: $m_n = 1.6747\times10^{-24}$ g. The experimental value of the phase shift proved to be $\Delta\varphi_g = 57.35°$, whence one can easily see, with the aid of Eq. (77), that $\sqrt{m_i m_g} = (1.675\pm0.003)^{-24}$ g. Thus, the equivalence of the gravitational and the inertia mass at the microscopic level was established to a precision of 10^{-3}.

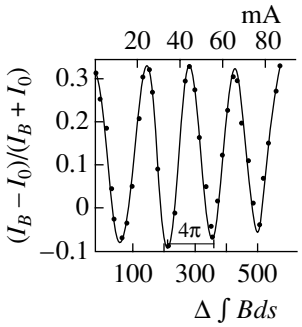

Fig. 27 [9]. Observation of the characteristic 4π periodicity of a spinor; the measurements were performed for an unpolarized incident beam of neutrons; $\Delta\int Bds$ is the difference of $\int Bds$ between the beam trajectories I and II.

A neutron LLL interferometer made it possible to demonstrate yet another fundamental property of the neutron, 4π symmetry of its wave function [9]. It was repeatedly mentioned above that, upon traversing an interferometer, the intensity of a neutron beam is determined by the coherent sum of two waves: $I = |\Psi^{\text{I}} + \Psi^{\text{II}}|^2$. If a region featuring a nuclear magnetic potential (sample) is now placed on one of the trajectories or if a gravitational ascent or fall of a neutron is implemented, the phase of the corresponding wave function changes, which cause a change in the intensity of counting in the detectors. Let us now create, on one of the trajectories—for example, on trajectory I—a local region of a uniform magnetic field $\mathbf{B}$. In this field, the neutron spin will undergo precession through the angle $\alpha = \pm\omega_{\text{L}}\tau = \pm\gamma BDm_n\lambda_n\hbar^{-1}$, where $\omega_{\text{L}} = \gamma B$ is the Larmor frequency of precession, D is the distance traveled by a neutron in the field over the time $\tau = D/v_n$, and γ is the gyromagnetic ratio. The spinor wave function for a neutron on trajectory I, which is subjected to the

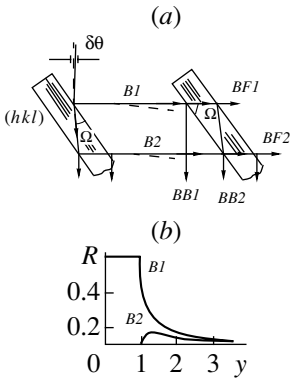

Fig. 28 [44]. (*a*) Fundamentals of the operation of a BB interferometer: optical path of neutron beams in the instrument; (*b*) reflecting power of the first crystal plate for two interfering beams *B1* and *B2*.

effect of the magnetic field, is then given by

$$\begin{pmatrix} \Psi^{\mathrm{I}}_{+}(\alpha) \\ \Psi^{\mathrm{I}}_{-}(\alpha) \end{pmatrix} = \begin{pmatrix} e^{i\frac{\alpha}{2}} & 0 \\ 0 & e^{-i\frac{\alpha}{2}} \end{pmatrix} \begin{pmatrix} \Psi^{\mathrm{I}}_{+}(0) \\ \Psi^{\mathrm{I}}_{-}(0) \end{pmatrix}.$$

It follows that the expression for the neutron counting rate upon traversing the interferometer has the form

$$I_0(\alpha) = |\Psi^{\mathrm{I}}_{+}(\alpha) + \Psi^{\mathrm{II}}_{+}(0)|^2 + |\Psi^{\mathrm{I}}_{-}(\alpha) + \Psi^{\mathrm{II}}_{-}(0)|^2$$
$$= \frac{1}{2} I_0(0) \left[1 + \cos\left(\frac{\alpha}{2}\right)\right].$$

The period of this function is 4π. A proof of the statement that the intensity-difference function $(I_B - I_O)/(I_B + I_O)$ is periodic is given in Fig. 27 for the dependence on $\Delta \int Bds$, which is the difference of the values of $\int Bds$ for the trajectories I and II. The period of oscillations of the intensity is $T = (716.8 \pm 3.8)°$, which confirms, to a fairly high degree of precision, the 4π symmetry of the neutron wave function.

12. SHULL'S INTERFEROMETER

In a classical form, a crystal interferometer—it involves splitting a primary wave into two coherent components, which, after acquiring a phase difference, are then made to intersect in some spatial region—was for the first time implemented in Bragg geometry as a two-crystal x-ray interferometer [42]. For thermal neutrons, this version of interferometer was developed by Shull and his colleagues [44], who showed that dynamical diffraction in Bragg geometry (see Section 6) can also be well used in interferometers of angstrom wavelength. Basic ideas of a two-crystal interferometer in Bragg geometry can easily be understood with the aid of Fig. 28*a*. Neutron radiation incident at a small deviation $\Delta\theta$ from the exact Bragg angle is partly reflected from the entrance surface of the crystal, forming the ray *B1*, and partly penetrates into its interior. From (49), it can easily be found that the angle Ω between the direction of propagation within the crystal and the planes of the crystal lattice satisfies the relation

$$\tan\Omega = \frac{y^2 - 1}{y^2} \tan\theta_B, \qquad (78)$$

where y is given by (24). In Section 6, it was shown that, for $|y| < 1$, radiation cannot propagate within the crystal—this is the total-reflection region, where a Darwin plateau is observed (see Fig. 7*c*). Neutron radiation that is incident beyond this region undergoes amplitude splitting at the entrance surface into the reflected and the transmitted component.

The reflected component, together with the radiation propagating into the angular range within the plateau region, forms the beam *B1*. The transmitted component propagates through the crystal; some part of it is reflected from the back surface of the crystal (see Fig. 28*a*) and, upon undergoing a partial reflection from the front (entrance) surface, escapes from the crystal in the form of a beam propagating in the direction strictly parallel to the partly reflected component *B1*. The theory of dynamical diffraction reveals that the reflection factor for these beams, which is defined as the ratios of their intensities to the intensity of the primary beam, depends only on y and that the component *B1* for the region $|y| > 1$ will be coherent with respect to the equivalent components of the beam *B2*. The second crystal (Fig. 28*a*) serves for recombining these coherent components by making them intersect in some spatial region and by forming phase-sensitive separate interference beams *BB2* and *BF2*.

Part of the beam *B1* is reflected from the back surface of the second crystal and, upon traversing the front surface, interferes with that part of the beam *B2* which undergoes reflection from the front surface, thereby forming the outgoing beam *BB2*. The second outgoing beam *BF2* can also serve as an interfering beam. From Fig. 28*a*, it can be seen that the length of the path has the same value for the two components of the beam *BB2*, but this cannot be said about the beam *BF2*. As a result, a stronger interference contrast proves to be achievable for the beam *BB2* if a phase difference is generated (by introducing an object of different neutron-optical difference in the beam *B2* or *B1*), which makes it possible to use a system of two perfect crystals as an interferometer.

The idea of this type of a BB interferometer was tested for the case where a neutron beam was used together with a single crystal of silicon, which is a standard substance for LLL interferometers. Plates of this crystal were cut along (220) crystallographic planes; they had a thickness of 9.186 mm and a

transverse dimension of 37.465 mm. In order to obtain a monochromatic neutron beam, a "white" neutron beam was reflected from graphite and was then filtered from higher orders by transmitting it through a filter of pyrolitic graphite. The wavelength of beam neutrons was $\lambda_n = 2.717$ Å, its spread being ± 0.015 Å, which corresponded to the mean Bragg angle of 45.04° in the interferometer; the fraction of higher order neutrons did not exceed 2%. The interferometer was protected from mechanical and thermal vibrations.

The interferometric scheme was first tested by studying the intensity profiles for two beams *BB1* and *BB2* (scanning with a slit H) reflected by the second crystal and for the beams *BF1* and *BF2* (scanning with a slit V) traversing the second crystal (see Fig. 29*a*). Figure 29*b* displays the measured distribution of the intensity of the beam BF; it complies well with the distribution computed on the basis of the dynamical theory of diffraction with allowance for a finite resolution of the measurements (the measured data and the calculated curve were normalized to the height of the first peak). As can be seen, both peaks have extended tails to the right of the maximum; this might have been expected because of an effect of the Bormann fan type that exists in a crystal and which is enhanced here by the propagation of neutrons through the second crystal. The background level between the peaks A and B proved to be higher than the expected one, and this was explained by the presence of diffuse thermal scattering of neutrons on the first crystal plate.

The distribution of the intensity reflected from the second crystal in the direction BB (scanning with the slit H) (see Fig. 29*c*) is also in good agreement with the prediction of the dynamical theory of diffraction. Here, the peak of the beam *BB2* again immediately follows the peak of the beam *BB1*, the width of the latter being determined by a finite resolution of the procedure. For the profile of the interference beam *BB2*, the dashed curve in Fig. 29*c* represents the result that is expected in the case of a coherent superposition of the amplitudes for the wave components in this beam; the dashed curve corresponds to the noncoherent sum of the intensities. That the observed profile is not reproduced by the calculated one can be tentatively explained by the influence of residual effects of thermal and vibrational instabilities on the interference. Once a constant temperature field around the facility had been ensured, the observation of interference phenomena in the beam *BB2* became possible.

Interference oscillations of the intensity were observed in the case of rotation of an aluminum plate 2.77 mm thick, which changed the phase of the beam *B1* in relation to the phase of the beam

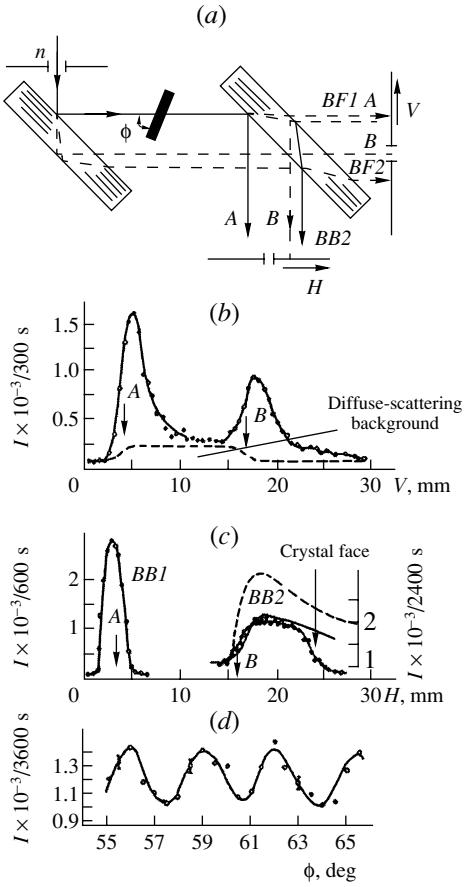

Fig. 29 [44]. Shull's experiments with a BB interferometer: (*a*) layout of the experiments; (*b*) experimental results and theoretical prediction for the intensity profile of the beams *BF1* and *BF2* that was obtained by moving the slit V; (*c*) as in Fig. 29*b*, but for the beam *BB2* [during the motion of the slit H]; and (*d*) modulation of the intensity of the beam *BB2* upon the rotation of an aluminum phase plate through the angle ϕ.

B2 (see Fig. 29*a*), with the result that there arose modulations of the intensity of the beam *BB2*. The period of these oscillations (see Fig. 29*d*) complies well with the value of the coherent scattering amplitude for Al: $b_{\mathrm{coh}} = 0.3449 \times 10^{-12}$ cm. It is of importance that a significant distinction of this type of neutron interferometer from other existing types is that, in it, there does not arise an expanding Bormann fan in one of the interfering beams (in the beam *B1*). This beam can be made as narrow as the collimation of the primary beam, its width being determined by the extinction length in the first crystal (about 0.1 mm in the case being discussed). This feature of the interferometric scheme may be of use if it is necessary to obtain the position phase information about the sample under study (in this case, the sample is arranged across a narrow beam) or if a strong and highly uniform electromagnetic field must be

used in interferometric experiments. In any case, this version of a BB crystal interferometer possesses the advantages of the simplicity of realization and of higher resolution in relation to the LLL scheme.

13. SPECTROMETRY OF HIGH ANGULAR AND ENERGY RESOLUTIONS

Thus, perfect crystal plates arranged in strictly parallel positions (especially in the case of Laue geometry) form a diffraction "resonator" system such that a change in the phase relations for the neutron wave in one of its beams leads to sharp periodic modulations of the intensity upon traversing the interferometer. However, this does not exhaust the properties of such a system. If we now rotate one of the crystal plates with a very small step about an axis that is orthogonal to the scattering plane, we will find that the intensity of the reflected beam decreases very fast and that the FWHM of the reflection curve is 2 to 3″, which is about 10^{-5} rad. If a sample, which plays the role of a scatterer, is inserted in between the crystals, the shape of this curve changes; any change may be discovered if it exceeds 10^{-5} rad. Therefore, such a system makes it possible to study, with a high angular resolution of about 3″, the spatial spectra of neutrons scattered by the sample. In other words, there arises the possibility of performing precision spectrometric investigations with an absolute resolution of $\Delta q \geq 10^{-5}$ Å^{-1} in the scattering vector. As a rule, crystal plates used to create an interferometer are oriented in Bragg geometry; this considerably improves the sensitivity of instruments that employ neutron radiation. In scientific periodicals and in well-known monographs, such crystal systems are referred to as two-crystal neutron spectrometers (TCNS), while the method for obtaining spatial spectra is referred to as the method of a two-crystal spectrometer.

Two-crystal spectrometer on the basis of perfect crystals. The property of perfect crystals to reflect diffractively thermal neutrons (or x-ray photons) into a narrow angular interval opens the possibility for creating spectrometers of high angular and energy resolution. In dealing with neutron beams in practice, use is made of two- or three-crystal schemes, where the first crystal always plays the role of a monochromator (M), while those that follow play the role of an analyzer (A) or a sample (D) (see Fig. 30). In order to ensure a high performance of such schemes, precision experimental equipment is required for achieving, in a neutron beam, desirable parameters in the angular resolution ($\delta\theta \sim 10^{-5}$ rad) and in the degree of monochromatization (to $\Delta\lambda/\lambda \sim 10^{-5}$).

Let us consider the trajectories of rays [5] in the case where a two-crystal spectrometer (TCS) is traversed by a thermal-neutron beam (see Fig. 30) whose horizontal and vertical angular divergences are, respectively, $\alpha_m \sim 10^{-2}$ rad (about 30′) and $\varphi_m \sim 5 \times 10^{-2}$ rad (about 3°), where the index m denotes the maximum value of the angles—that is, $\alpha_m = c/z$ and $\varphi_m = h/z$, with c, h, and z being, respectively, the width of the collimator slits, their height, and the distance between the slits. Neutrons of wavelength λ_0 are reflected at the angle θ_B from the monochromator (M) and are incident on the analyzer (A), diffraction occurring in the nth order of reflection. By successively rotating the crystal A, one measures the intensity $P(\beta)$ of radiation reflected from it. Upon reflection from the monochromator, the angular deflection of an arbitrary beam with the parameters λ, θ, α, φ, and n from the central beam $(\lambda_0, \theta_0, \alpha = 0, \varphi = 0, n)$ is

$$\tilde{\alpha} = \alpha - \frac{\varphi^2}{2}\tan\theta_0^M(\lambda_0, n^M) - \frac{\lambda - \lambda_0}{\lambda_0}\tan\theta_0^M(\lambda_0, n^M), \quad (79)$$

where the second term describes the deflection of the ray due to the vertical divergence φ_m, while the third term represents smearing caused by the wavelength spread. If the crystal playing the role of the analyzer is rotated through the angle β with respect to the exact Bragg position, the angle of reflection becomes $(\theta_0 - \beta)$ for the parallel (Fig. 30*b*) and $(\theta_0 + \beta)$ for the antiparallel (Fig. 30*a*) arrangement. For the reflection of an arbitrary ray with the parameters λ, α, and φ from the crystal A, the angle of reflection will have opposite signs for the parallel and the antiparallel arrangement and will differ from the angle of reflection for the central beam by the quantity

$$\tilde{\beta} = \pm\beta \pm \alpha - \frac{\varphi^2}{2}\tan\theta_0^A(\lambda_0, n^A) - \frac{\lambda - \lambda_0}{\lambda}\tan\theta_0^A(\lambda_0, n^A), \quad (80)$$

where the lower and the upper signs refer to, respectively, the antiparallel $(n, +n)$ (Fig. 30*a*) and the parallel $(n, -n)$ (Fig. 30*b*) arrangement, while n^A are the indices of the order of reflection from the crystal A.

It is now necessary to specify the intensity distributions of the neutron beam versus the divergence parameters α_m and φ_m and the wavelength λ_n. Let us introduce a geometric dimensionless parameter $G(\alpha, \varphi)$ and the function $I(\lambda - \lambda_0)d\lambda$ as the beam intensity in the interval $(\lambda, \lambda + d\lambda)$ and normalize them in such a way that the beam intensity within the elementary intervals $d\alpha$, $d\varphi$, and $d\lambda$ is determined by multiplying the functions G and I by the widths of these intervals. With the aid of this factorization, the

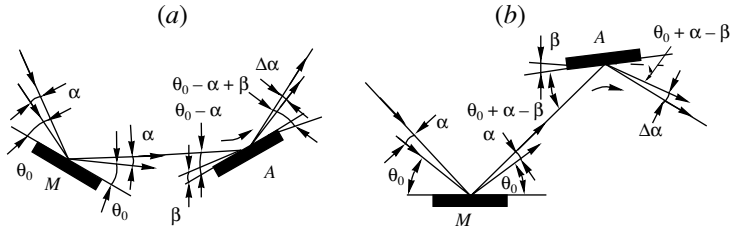

Fig. 30 [15]. Trajectories of rays in spectrometers for (a) an antiparallel ($n, +n$) and (b) a parallel ($n, -n$) arrangement of crystals (the notation for the angles is given in the main body of the text).

β dependence of the neutron flux reflected from the crystal A can be represented as

$$P(\beta) = \int_{-\varphi_m}^{\varphi_m} \int_{-\alpha_m}^{\alpha_m} \int_{\lambda_{\min}}^{\lambda_{\max}} G(\alpha, \varphi) \times I(\lambda - \lambda_0) R^M(\tilde{\alpha}) R^A(\tilde{\beta}) d\alpha d\varphi d\lambda, \quad (81)$$

where R^M and R^A are functions that characterize the reflecting power of the crystals and which correspond to the reflection indices n^M and n^A.

The general form (81) is simplified if one addresses the actual case of narrow maxima of the reflecting-power functions R^M and R^A, which corresponds to reflection from perfect crystals. In the limit where R^M and R^A are assumed to be different from zero only at the vanishing values of their arguments, it is straightforward to obtain the variance of the spectrometer—that is, the variance of the angular distribution of neutrons versus their energy:

$$D \equiv \frac{d\beta}{d\lambda} = \frac{n^M}{2d \cos \theta^M} \mp \frac{n^A}{2d \cos \theta^A}. \quad (82)$$

From (82), it follows that, if use is made of identical crystals, in which case $\theta_M = \theta_A = \theta_0$, and of the reflexes $n^M = n^A$ in the parallel arrangement [this corresponds to the minus sign in (82)], the variance of the spectrometer is equal to zero, and the entire spectral range of neutron wavelengths that is determined by α_m passes through the spectrometer. Under the same conditions, the variance is maximal for the antiparallel arrangement of the crystals [plus sign in (82)], and only those neutrons pass through the spectrometric system that were selectively chosen from the "white" spectrum by the crystal M and from the monochromatic line by the crystal A, which reflects into the range $\Delta\theta \sim 10^{-5}$ rad. Moreover, we have $R^A = R^M = R$, which simplifies expression (81).

Further, the function $G(\alpha, \varphi)$ describes in (81) the divergence of the primary beam and, by virtue of the independence of the vertical (φ_m) and the horizontal (α_m) divergence (as a rule, the collimator slits have a rectangular shape), can be represented in the form $G(\alpha, \varphi) = G_1(\alpha) G_2(\varphi)$. Although G_1 and G_2 differ from zero in the angular range $\sim 10^{-3}$–10^{-2} rad, the effective range of variation of the function $G_2(\varphi)$, which takes into account the vertical divergence in accordance with the value of the term $(\varphi^2 \tan \theta_0)/2$ in (79) and (80), is on the same order of magnitude as the width $R \sim 10^{-5}$ rad. Moreover, the shape of the resulting reflecting curve $P(\beta)$ ceases to be dependent on the vertical divergence if the reflecting planes of the crystals A and M are strictly parallel. All this makes it possible to simplify expression (81) and to analyze each case of the arrangement of crystals (see Fig. 30). We begin by considering the parallel (n, $-n$) arrangement.

Parallel arrangement of crystals (Fig. 30b). If the (n, $-n$) scheme of a spectrometer is used, the function $P(\beta)$ differs from zero in a narrow region of β values, the width of the rocking curve being commensurate with the width $\delta\theta_0$ of a dynamical maximum from one crystal. The effective region $\Delta\lambda$ of the wavelengths of neutrons participating in the formation of the rocking curve is determined by the horizontal divergence α_m; for conventional values of $\alpha_m \sim 10^{-2}$, $\lambda_0 \sim 2$ Å, and $\theta_0 \sim 20°$, it is $\Delta\lambda \sim \alpha_m \lambda_0 \cot \theta_0 \sim 2 \times 10^{-2}$ Å and, as can be shown by analyzing expression (81), is independent of β. Contrasting the narrow range (about 10^{-5} rad) of variation of R against the slow variations of the functions $G(\alpha)$ and $I(\lambda)$ within a few angular seconds and the wavelengths $\Delta\lambda$, we can factor these functions outside the integral sign and recast expression (81) into the form

$$P(\beta) = k \int_{-\infty}^{\infty} R(\alpha) R(\alpha - \beta) d\alpha, \quad (83)$$

where

$$k = \int_{\lambda_{\min}}^{\lambda_{\max}} \int_{-\frac{\varphi_m}{2}}^{\frac{\varphi_m}{2}} G\left[\frac{\lambda - \lambda_0}{\lambda} \tan \theta(\lambda_0, n)\right] \times G(\varphi) I(\lambda - \lambda_0) d\varphi d\lambda$$

is a constant. It can easily be seen that, for a parallel scheme of the two-crystal spectrometer, the reflection curve (which is also referred to as the rocking curve) $P(\beta)$ (83) is symmetric with respect to $\beta = 0$. This property is preserved even if the profiles of dynamical reflexes (Darwin tables) for each of the crystals (M and A) are not symmetric because of neutron reflection. A dedicated analysis of the problem concerning the relationship between the experimentally observed quantity $P(\beta)$ and the calculated profile of the dynamical maximum of reflection from the crystal playing the role of an analyzer revealed [5] that it is impossible to single out unambiguously the undistorted profile by simple analytic methods. However, this spurious symmetry is successfully used to perform precision investigations into neutron optics and small-angle neutron scattering.

Let us discuss processes occurring in an $(n, -n)$ spectrometer from a somewhat different point of view. The fact that the width of $P(\beta)$ is close to the width of the Darwin reflection profile is explained as follows: in contrast to what we have in a white beam, the scatter of the neutron wavelength λ_n and the scatter of the direction of propagation are not independent in the beam reflected from the monochromator, since they are related by Bragg's law. In this, "correlated," beam, a specific neutron-propagation direction determined to within a Darwin width corresponds to each value of λ_n. Therefore, the crystal analyzer simultaneously reflects neutrons of different energies, forming parallel beams only within the reflection width $\Delta\theta$.

Thus, a crystal analyzer in a strictly parallel arrangement reflects simultaneously the entire set of narrow Darwin profiles R_i that are contained within the angular limits determined by the horizontal divergence α_m. Each of these reflected parallel rays is characterized by a statistical weight inherent in it and is determined by the corresponding wavelength value within the interval $\Delta\lambda = \alpha_m\lambda_0 \cot\theta_0$. The simplest estimate reveals that, at the values used for the horizontal divergence ($\alpha_m \sim 10^{-2}$ rad) and for the width of the Darwin table plateau ($2S \sim 2 \times 10^{-5}$ rad), the number of such parallel channel beams realized in a two-crystal parallel spectrometer is about $\alpha_m/2S = 10^{-2}/2 \times 10^{-5} \sim 500$.

If the crystal A is rotated about an axis orthogonal to the plane of analysis (horizontal plane) with a step of about $0.1''$ (about 5×10^{-7} rad) and if it is not arranged, at the same time, in a strictly parallel position, there occurs "detuning" of all R_i ($i \approx 500$) simultaneously. Now, as soon as the angle β becomes larger than S, the intensity of the neutron flux decreases sharply, so that the FWHM of the curve $P(\beta)$ proves to be only slightly larger than $2S$. It was indicated above that this is a consequence of the narrowness of the rocking curve for a two-crystal spectrometer based on perfect crystals and that this makes it possible to use successfully the $(n, -n)$ scheme for performing experiments aimed at studying small-angle scattering with a high resolution in the scattering vector.

Let us indicate some properties of a spectrometer featuring perfect crystals arranged in a strictly parallel position.

First, instruments constructed on the basis of this principle have a rather low sensitivity; the reason for this is that crystals having a perfect lattice are characterized by a low integrated reflecting power (see Section 7 above). Although their reflecting power at the peak is equal to unity if Bragg geometry is used, the reflex is formed by a thin (about 10^2 μm) crystal layer and occurs in a very narrow (about 10^{-5} rad) angular range, and this cannot be compensated by the fact that a rather wide spectral range $\Delta\lambda \sim 10^{-2}$ Å is reflected simultaneously. In relation to the case of traditional mosaic crystals of parallel arrangement, the sensitivity is lower by a factor of 10^2 to 10^3.

Second, the shape of double-reflection curves $P(\beta)$ (instrumental line in experiments studying small-angle scattering) is poorly approximated by a Gaussian or a Lorentzian curve. The contour of the curve $P(\beta)$ is formed by superpositions of a few hundred profiles of the Darwin table type (see Fig. 8) beyond whose total-reflection region there are quick oscillations decreasing in amplitude, the averaging line of this beating varying in proportion to β^{-2}. A decrease in the intensity of the reflex as a function of the angle is of the $(\theta - \theta_B)^{-2}$ type and is weak, which means that particles that have traversed a two-crystal system can be recorded at angles that are two orders of magnitude larger than $2S \sim (2\text{–}3)''$.

Third, the question of the FWHM of the reflection curve $P(\beta)$ is of crucial importance. In the case where use is made of the two-crystal scheme, the narrowing of this curve to a width smaller than $2\sqrt{2}S$, which is the size of the total-reflection region, is possible with the aid of the Fankuchen effect [45]. In a neutron beam, such experiments [46] were performed with germanium crystals having a dislocation density of about 10^3 cm^{-2}, and it was shown that the use of asymmetric Bragg reflection leads to the narrowing or the broadening of the dynamical maximum and, hence, of the curve $P(\beta)$.

To complete the discussion of a parallel $(n, -n)$ arrangement, we note that, as a rule, the "broadening" of the rocking curve is associated with the presence of imperfections in the structure of the crystals used; therefore, a two-crystal spectrometer can be

employed to study the degree of their imperfection—it is the way in which the results reported in [29, 30] were obtained. As yet another reason, we can indicate a vertical mismatch $\Delta\varphi$ of the reflecting planes of the two crystals, which broadens the curve $P(\beta)$ as $\delta(\Delta\theta) = (1/2)(\Delta\varphi/\cos\theta)^2$ [5, 31]; this requires adjusting crystals to a precision higher than $3'$. For typical values in (111) germanium crystals and $\lambda_n \sim 1.5$ Å, we have

$$\frac{1}{2}\left(\frac{\Delta\varphi}{\cos\theta}\right)^2 \sim (9\times 10^{-4}) \sim 10^{-6}$$
$$\sim 0.2'' \ll \delta\theta = 10^{-5} \sim 2''.$$

Therefore, the properties of the two-crystal $(n, -n)$ scheme disclose themselves only if use is made of crystals where the density of imperfections (for example, dislocation loops, clusters of defects, or small-angle boundaries) is $N_d < 10$ cm^2 and if $\Delta\varphi \leq 10^{-3}$ rad, in which case the broadening does not exceed a few percent of the intrinsic width equal to $2S$.

Antiparallel arrangement of the two-crystal spectrometer (Fig. 30*a*). The analytic expression for $P(\beta)$ in the case of the $(n, +n)$ arrangement of crystals is similar to expression (81) for $(n, -n)$ with the only difference that the lower signs are employed in expression (80) for $\tilde{\beta}$. A qualitative analysis of expression (81) then leads to the following results. According to formula (82), the variance of such a system is maximal—it is twice as great as the variance of the one-crystal spectrometer—while the β range in which the function $P(\tilde{\beta})$ has a sizable value is much wider than the angular width of the dynamical maximum for one crystal and is commensurate with the angular divergence α_m. An analysis of the argument of the function $P(\tilde{\beta})$ for the antiparallel arrangement shows that expression (80) takes the form

$$\tilde{\beta} = \{\beta - 2\tan\theta_0^A(\lambda_0, n^A)\} \qquad (84)$$
$$-\{\alpha - \tan\theta_0^A(\lambda_0, n^A)\} - \frac{\varphi^2}{2}\tan\theta_0^A(\lambda_0, n^A).$$

Here, the second term in braces must be small for the function $R(\tilde{\beta})$ characterizing the second crystal to be noticeably different from zero. It follows that, if the crystal analyzer is rotated from the average position through an angle $\tilde{\beta}$, both crystals select, from the entire spectrum of waves, the narrow spectral band

$$\delta\lambda = \pm\frac{1}{2}\frac{\lambda - \lambda_0}{\lambda}\tan\theta_0^A \cdot \beta.$$

The width of this line is smaller than that in the case of the parallel arrangement by the factor β/α_m. As to the ray reflected from the crystal analyzer, it represents a highly monochromatic probing bundle of neutron trajectories parallel to within the Darwin width $2S$.

Physically, this can be explained in the following way: for each specific position $\tilde{\beta}'$ of the crystal analyzer, the spectrum developed by the analyzer in angles from $-\alpha_m$ to $+\alpha_m$ and, accordingly, in λ_n over the interval $\Delta\lambda \sim 2\alpha_m\lambda_0\cot\theta_0 \sim 0.01$ Å features such a beam that is selected by the analyzer from this spectrum to a precision of $2S$. Other neutrons are not reflected in this case. As a matter of fact, a rotation of the crystal analyzer in β therefore means a shift of the spectral interval $\delta\lambda \sim 2d\cos\theta_B \cdot 2S \sim 10^{-5}$ Å within the region $\Delta\lambda \sim 0.01$ Å and, accordingly, a shift of the angular window $2S$ within the interval $\pm\alpha_m$. The last circumstance leads to plotting the profile of primary collimation of the spectrometric scheme.

Finally, an important distinctive feature of the antiparallel two-crystal scheme is that the function $P(\tilde{\beta})$ has no symmetry, since a transformation similar to the transformation that is given by (81) and which was made for the parallel arrangement can be applied in this case only under some special conditions. The effect of vertical divergence cannot be eliminated here, nor can the function $I(\lambda - \lambda_0)$, since it undergoes noticeable changes over the entire reflection range that is specified by the function $P(\tilde{\beta})$ and which is commensurate with the vertical divergence. The effective range of variation of α is small in relation to α_m. This makes it possible to extend integration with respect to α over the entire interval from negative to positive infinity. It follows that, for the antiparallel scheme, the expression for $P(\tilde{\beta})$ can be represented in the form of a convolution only if it is assumed that the beam incident on the crystal monochromator is already monochromatic, its divergence being given by (α, φ), and that the dependence on φ can be disregarded [such assumptions are used to obtain a simple form of $P(\tilde{\beta})$], in which case we have

$$P'(\tilde{\beta}) \approx \int_{-\infty}^{\infty} R(\alpha)R(\beta - \alpha)d\alpha, \qquad (85)$$

where the proportionality factor has been omitted. A comparison of this formula with (83) shows that replacement of β by $-\beta$ in (85) does not yield an equivalent result; therefore, the reflection curve taken under the conditions of crystal-analyzer rotation in the antiparallel scheme does not possess an instrumental symmetry with respect to the point $\beta = 0$ or with respect to any other value of β. Unfortunately, this property cannot be tested experimentally in the two-crystal $(n, +n)$ scheme because of a strong dispersion effect.

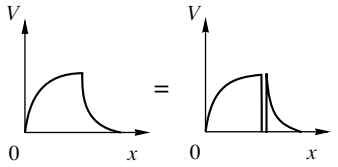

Fig. 31 [52]. Illustration of the fact that a potential featuring no slit (on the left) and a potential featuring a slit of infinitely small width (on the right) are absolutely equivalent from the point of view of quantum mechanics.

It is obvious, however, that a neutron beam ("probing ray") that traversed a two-crystal spectrometer in the parallel arrangement possesses genuinely unique properties—an angular divergence of about 2 to 3″ ($2S \sim 10^{-5}$ rad) and an energy resolution of $\delta\lambda \sim 10^{-5}$ Å—but this probe can be used only in experiments at a high-flux reactor of the HFR in Grenoble. The feasibility of this can be demonstrated by taking, for an analyzer, a third perfect crystal—that is, by constructing a three-crystal neutron spectrometer. This problem was also successfully solved in the past decades [47, 48]; as a result, it became possible to perform unique experiments aimed at studying diffuse scattering [49].

14. ALTERNATIVE THEORETICAL APPROACHES TO DESCRIBING DYNAMICAL NEUTRON DIFFRACTION

In recent years, interest in the dynamical theory due to Darwin has been rekindled to a considerable extent (see, for example, the monograph of Pinsker [5]). The original form of this theory has the advantage that its conclusions are quite transparent, but the theory further evolved along different lines—through the development of the formalism due to Laue and Ewald. But when there arose the problem of constructing the theory of x-ray scattering on weakly deformed crystals, difficulties of a fundamental character in modifying Laue–Zachariasen theory [50] became obvious. The point is that some of its concepts, including that of a conventional Bloch wave and that of a dispersion surface, are inapplicable under different conditions of scattering.

For the sake of completeness, it should be mentioned that, as far back as 1914, Darwin [2], who considered the problem of x-ray diffraction on crystals, used the method that involves breaking down media into layers, which is analogous to the invariance principle discussed below, but, later on, this approach was not developed. The invariance principle as formulated by Ambartsumyan [51] in a condensed form is as follows:

(i) The scattering properties of a semi-infinite medium do not change upon supplementing it with a layer of finite thickness Δt.

(ii) The scattering properties of a layer of finite thickness t do not change upon adding, to it, a layer of thickness Δt from one side and removing the identical layer from the other side.

Darwin imagined the crystal to be split into crystal planes and assumed that one atomic plane reflects radiation with an amplitude $-iq$ and transmits it with an amplitude $1 - iq - h$, where the quantity h characterizes absorption. He then considered the amplitude of the wave incident on the nth crystal plane from the surface, T_n, and the amplitude of the wave going away from it, S_n. He obtained recursion equations relating these amplitudes for the nth and the $(n+1)$th plane. Solving these equations, Darwin derived his famous formula for total reflection from a semi-infinite crystal [see formula (40) from Section 6]. This approach was developed by Ignatovich [52], who indicated that dynamical neutron diffraction can be described on the basis of two theoretical procedures—that of breaking down a medium into layers (invariance principle) and that of the theory of multiple wave scattering. The proposed method consists in the following.

In considering some potential (see Fig. 31), the results obtained by calculating the reflection and transmission factors do not change if the potential is split by a narrow gap within which it can be set to an arbitrary constant value. We set it to zero, in which case the reflection amplitude ρ and the transmission amplitude τ for the potential as a discrete unit can be expressed in terms of the corresponding amplitudes ρ_i and τ_i associated with its parts; that is,

$$\tau^l = \tau_2^l \sum_{n=0}^{\infty} [\rho_1^r \rho_2^l] \tau_1^l = \tau_2^l (1 - \rho_1^r \rho_2^l)^{-1} \tau_1^l \qquad (86)$$

and, by analogy,

$$\rho^l = \rho_1^l + \tau_1^r \rho_2^l (1 - \rho_1^r \rho_2^l)^{-1} \tau_1^l. \qquad (87)$$

In these expressions, we have introduced the superscripts l and r in order to distinguish reflection and transmission factors from the left and from the right. Relations (86) and (87) remain valid both for scalar quantities and for matrices and operators. Formula (87) makes it possible to obtain the amplitude of reflection from an arbitrary semi-infinite periodic potential.

Splitting one period from this potential and recalling that, by virtue of the invariance principle, the properties of a semi-infinite medium do not change if a finite layer is removed from it (or added to it), we can write relation (87), where ρ_2 is replaced by ρ, which is

the amplitude of reflection from the entire layer. As a result, we obtain the equation

$$\rho = \rho_1 + \tau_1\rho(1-\rho_1\rho)^{-1}\tau_1, \qquad (88)$$

where ρ_1 and τ_1 are the amplitudes of, respectively, reflection and transmission for one period. For the sake of simplicity, it is assumed that the period is symmetric; therefore, the indices l and r are omitted.

The wave function $\Psi(x)$ within a periodic potential has a Bloch form; that is, $\Psi(x) = \exp(iqx)\phi(x)$, where $\phi(x)$ is a periodic function and q is a Bloch wave number. For an arbitrary periodic potential, the phase factor $X_1 = \exp(iqa)$ that the wave function acquires upon a shift of one period obeys the equation

$$X_1 = (1-\rho_1\rho)^{-1}\tau_1. \qquad (89)$$

Substituting (89) into (88), we can obtain a set of equations determining ρ and X_1 in terms of the amplitude of reflection from one period:

$$\rho = \rho_1 + \tau_1\rho X_1, \quad X_1 = \tau_1 + \rho_1\rho X_1. \qquad (90)$$

For three-dimensional systems, reflection and transmission amplitudes are matrices. The idea of Ignatovich consists in the following. Let us consider an ideal semi-infinite medium filled with a monoatomic cubic lattice of side length a and split it into periods by planes parallel to the entrance surface. The incident wave undergoes diffraction on each such plane, thereby generating a set of waves. These waves are scattered on periods that follow, yielding the same set of diffracted waves. Having found the transmission and reflection matrices for one period by the method of multiple wave scattering, we apply the splitting method to determine the quantities of interest.

In the theory of multiple wave scattering, the wave function $\Psi(\mathbf{r})$ formed as the result of multiple rescattering on individual nuclei is given by

$$\Psi(\mathbf{r}) = \exp(i\mathbf{k}\cdot\mathbf{r}) - \sum_n \Psi(\mathbf{r}_n)\frac{b_n}{|\mathbf{r}-\mathbf{r}_n|}\exp(ik|\mathbf{r}-\mathbf{r}_n|), \qquad (91)$$

where $\Psi(\mathbf{r}_n)$ is an effective local illuminating the nucleus that is situated at the point $\mathbf{r}_n$.

The local field at the nucleus of number n is determined by the equation

$$\Psi(\mathbf{r}_n) = \exp(i\mathbf{k}\cdot\mathbf{r}_n) - \sum_{j\neq n} \Psi(\mathbf{r}_j)\frac{b_n}{|\mathbf{r}_n-\mathbf{r}_j|}\exp(ik|\mathbf{r}_n-\mathbf{r}_j|). \qquad (92)$$

Equations (91) and (92) form the basis of the theory of multiple wave scattering. Goldberger and Seitz [6] were the first to apply these equations to dynamical neutron scattering.

In the case of a crystal plane featuring a square lattice, Eqs. (91) and (92) are invariant under translations; therefore, it is natural to solve these equations by applying a Fourier transformation [52]; that is,

$$\Psi(\mathbf{r}_i) = C\exp(i\mathbf{k}_{||}\cdot\mathbf{r}_i), \qquad (93)$$

where C is a constant that has the same value for all nuclei. This means that the local field for all nuclei separated by a distance r from each other can differ only by the phase factor $\exp(i\mathbf{k}_{||}\cdot\mathbf{r})$, where $\mathbf{k}_{||}$ are the components of the wave vector $\mathbf{k}$ of the incident wave that are parallel to the plane being considered (let it be coincident with the yz coordinate plane).

Substituting (93) into (92), one can obtain

$$C = [1+bS]^{-1}, \qquad (94)$$

$$S = S' + iS'' = \sum_{j\neq 0}\exp(i\mathbf{k}\cdot\mathbf{r}_j)\frac{1}{|\mathbf{r}_j|}\exp(ik|\mathbf{r}_j|).$$

The substitution of (93) into (91) yields a set of waves scattered by the crystal plane; that is,

$$\Psi(\mathbf{r}) = \exp(i\mathbf{k}\cdot\mathbf{r}) - C\sum_n \frac{2\pi ib}{a^2k_{n\perp}}\exp(ik_{n\perp}|x| + i\mathbf{k}_{n\parallel}\cdot\mathbf{r}_{\parallel}). \qquad (95)$$

Here, $\mathbf{r}_{||} = (y,z)$ and $\mathbf{k}_n = (k_{n\perp}, \mathbf{k}_{n||})$ are the wave vectors of diffracted waves that are formed as the result of the transformation $\mathbf{k}_{||} \to \mathbf{k}_{n||} = \mathbf{k}_{||} + \boldsymbol{\tau}_n$ by adding the reciprocal-lattice vector $\boldsymbol{\tau}_n = (2\pi/a)(n_y, n_z)$, where n_y and n_z are integers. By virtue of the energy-conservation law, the normal components of the wave vectors of diffracted waves are $k_{n\perp} = \sqrt{k^2 - \mathbf{k}_{n||}^2}$.

By convention, we consider all waves traveling to right of the crystal as transmitted ones and all waves traveling to the left of it as reflected ones. With allowance for this assumption, it follows from (95) that, for one period, the expressions for the transmission and reflection matrices can be represented as

$$(\hat{\tau}_1)_{mn} = \left(\delta_{mn} - i\frac{2\pi N_2 b_{\mathrm{coh}}}{k_{n\perp}}\right)\exp(ik_{n\perp}a), \qquad (96)$$

$$(\hat{\rho}_1)_{mn} = -i\frac{2\pi N_2 b_{\mathrm{coh}}}{k_{n\perp}}\exp(ik_{n\perp}a),$$

where $N_2 = 1/a^2$ is the two-dimensional density of atoms in the plane and the factor $\exp(ik_{n\perp}a)$ describes the increment of the phase due to the propagation of the diffracted wave over an empty gap.

Using the splitting principle and taking into account multiple rereflections, one can write, by analogy with (90), equations for the matrices $\hat{\rho}_\infty$ of reflection

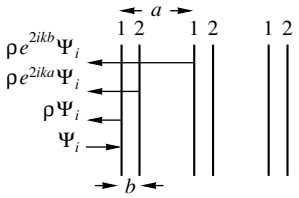

Fig. 32 [52]. Forbidden Bragg reflection.

from a semi-infinite crystal and for the Bloch phase $\hat{X} = \exp(i\hat{q}a)$:

$$\hat{\rho}_\infty = \hat{\rho}_1 + \hat{\tau}_1\hat{\rho}_\infty\hat{X}, \quad \hat{X} = \hat{\tau}_1 + \hat{\rho}_1\hat{\rho}_\infty\hat{X}. \qquad (97)$$

The set of Eqs. (97) can be solved to as a high degree of precision as is desirable. In this way, one can easily describe all diffraction phenomena.

In [52], it is stated that this method makes it possible to calculate the intensities of diffracted peaks to an arbitrarily high degree of precision and for any number of diffracted waves. In addition, this method enables one to predict and explain new effects; although such effects could also be predicted on the basis of the Ewald method, which is generally accepted in the theory of dynamical diffraction, it is the proposed theory of splitting that renders them especially transparent. For example, it is stated that forbidden reflexes—that is, reflexes for which the structural factor is equal to zero—are not strictly speaking forbidden. In them, reflections can be total, in just the same way as in allowed reflexes, the narrowness of the diffraction peak being the only distinctive feature of forbidden reflexes.

Suppose that the crystal being considered has a diatomic unit cell, so that it can be represented as that which consists of two systems of planes parallel to the entrance surface (see Fig. 32). Further, we assume that the width of one period is a and that the distance between the nearest planes is $b = a/4$. If the wavelength λ_n of a neutron incident orthogonally on the entrance surface is a, the phase difference between the waves reflected from two neighboring planes will be $2(2\pi b/\lambda) = \pi$; therefore, these waves will suppress each other, despite the fact that reflections from neighboring periods will differ in phase by 4π. However, waves reflected from two neighboring planes suppress each other completely only in the case where their amplitudes are identical. In fact, reflection from plane 1 in Fig. 32 leads to an attenuation of the wave incident on plane 2. Thus, the amplitude of the wave reflected from one period is proportional to $1 - \tau^2 \neq 0$, where τ characterizes transmission for one plane. If the crystal is sufficiently thick, reflection is total despite the smallness of $|1 - \tau^2|$.

The method based on splitting media made it possible to predict the emergence of two reflecting beams in the case where the Bragg and Laue conditions are satisfied simultaneously. In the case of Laue diffraction (see Section 5), two pairs of waves, Ψ_1 and Ψ_2, are formed simultaneously in the crystal. At the lattice nodes, the first pair of waves has a maximum, while the second has a zero. If the conditions of Bragg's law are satisfied, Ψ_1 is attenuated toward the interior of the crystal. As a result, only one group of waves, Ψ_2, reaches the exit surface, as is the case in the Bormann–Kagan–Afanas'ev effect. As to the group of waves Ψ_1, it is reflected, with the result that there arise two reflected waves, that which underwent mirror reflection and that which underwent diffraction. In principle, such an effect is possible if diffraction occurs on (100) planes of a perfect α-quartz crystal; this makes it possible to plan similar experiments with neutron beams, rendering the above theoretical considerations more valuable.

At the same time, there exists an alternative method for constructing the dynamical theory of diffraction.

In 1962, Takagi [53] proposed using a different approach to the problem of dynamical x-ray diffraction and presented fundamental equations for describing waves in a crystal. These equations are nothing but Darwin's recursion relations written in a differential form [5]. This approach made it possible to consider both scattering on slightly deformed crystals and scattering of wave packets. These strategies can be extended to the case of neutron diffraction as well, and this was done by Bushuev and Tyulyusov [54]. For this purpose, one can represent, instead of going over to the Bloch solution (2) in the Schrödinger Eq. (1), the neutron wave function in the form of an expansion in terms of reciprocal-lattice vectors; that is,

$$\Psi(\mathbf{r}) = \sum_B \Psi_B(\mathbf{r})\exp(i\mathbf{k}_B\cdot\mathbf{r}), \qquad (98)$$

where $\mathbf{k}_B = \mathbf{k}_0 + \mathbf{B}$, $\mathbf{B}$ being a reciprocal-lattice vector (see Section 3). As before, the potential is taken in the form (3). The functions $\Psi_B(\mathbf{r})$ are assumed to be slowly varying, since the fast part is entirely absorbed in the term $\exp(i\mathbf{k}_B\cdot\mathbf{r})$. Estimates show [54] that

$$\frac{\partial}{\partial r}\Psi_B(\mathbf{r}) \sim \left(\frac{V}{E}\right)\Psi_B\cdot(\mathbf{r})k. \qquad (99)$$

From Table 1, it can be seen that this ratio is about 10^{-6}, which is much less than unity. Further, substituting (98) and the potential (3) into Eq. (1), one can easily obtain an infinite set of equations for diffraction:

$$\left(\frac{2mE}{\hbar^2} - k_B^2\right)\Psi_B + 2i\mathbf{k}_B\nabla\Psi_B = \frac{2m}{\hbar^2}\sum_{B'} V_{B-B'}\Psi_{B'}. \qquad (100)$$

In view of (99), we have disregarded here the second derivative of the wave function $\Psi_B(\mathbf{r})$ with respect to spatial coordinates. In order to determine the leading terms in the sum, the set of Eqs. (100) is written in the approximation where the first derivative of $\Psi_B(\mathbf{r})$ is also disregarded (it is considered that the relation $E = \hbar^2 k^2/2m$ then holds):

$$\Psi_B(\mathbf{r}) = \left(\frac{k^2}{k^2 - k_B^2}\right) \sum_{B'} \left(\frac{V_{B-B'}}{E}\right) \Psi_{B'}(\mathbf{r}). \quad (101)$$

It is obvious that, since $(V/E) \sim 10^{-6}$, the existence of a nontrivial solution requires fulfillment of the relation $(k^2 - k_B^2)/k^2 \ll 1$, whereby strong reflection is selected. This condition is equivalent to (8) and implies that the nodes **B** are close to the Ewald sphere (see Fig. 1). We note that this situation is identical to that which arises in perturbation theory for a degenerate level of a quantum-mechanical system [55], in which case states associated with this level are mixed.

From the set of Eqs. (100), one can obtain equations for any number of waves corresponding to reciprocal-lattice nodes that are close to the Ewald sphere or, what is the same, reflections of any order. Here, we will consider the two-ray approximation described in Section 4. We have

$$\begin{cases} 2i\dfrac{\mathbf{k}_0}{k^2}\nabla\Psi_0 = \dfrac{V_0}{E}\Psi_0 + \dfrac{V_{-B}}{E}\Psi_B, \\ 2i\dfrac{\mathbf{k}_0}{k^2}\nabla\Psi_B = \dfrac{V_B}{E}\Psi_0 + \left(\dfrac{V_0}{E} - \alpha\right)\Psi_B, \end{cases} \quad (102)$$

where $\alpha = (k^2 - k_B^2)/k^2 = 2(\theta - \theta_B)\sin 2\theta_B$, which coincides with the definition (15) of the angular-tuning parameter α.

The spatial shape of the incident beam is taken into account in formulating boundary conditions. Suppose that the beam incident on the crystal surface has the form

$$\Psi(\mathbf{r} \,:\, \mathbf{r} \in \sigma_{\text{in}}) = A_0(\boldsymbol{\rho})\exp(i\mathbf{k}\cdot\boldsymbol{\rho}), \quad (103)$$

where σ_{in} is the entrance surface of the crystal and $\boldsymbol{\rho}$ is the radius vector in this plane. At the entrance surface, one can then impose the boundary condition

$$\Psi_0(\boldsymbol{\rho}) = A_0(\boldsymbol{\rho}). \quad (104)$$

The characteristic scale of variation of the function $A_0(\boldsymbol{\rho})$ must be much greater than the wavelength, and this is usually so under the conditions of actual experiments. The other boundary condition is written in the usual form

$$\Psi_B(\mathbf{r} \,:\, \mathbf{r} \in \sigma_{\text{out}}) = 0, \quad (105)$$

which means the absence of incoming radiation at the lower crystal surface σ_{out}.

If we now assume that a plane wave is incident on a crystal, the boundary condition (104) will take the form

$$\Psi_0(\boldsymbol{\rho}) = 1. \quad (106)$$

Let us choose the z axis to be directed into the interior of the crystal and to be orthogonal to its surface, so that

$$\sigma_{\text{in}} = \{\mathbf{r} \,:\, z = 0\}, \quad \sigma_{\text{out}} = \{\mathbf{r} \,:\, z = t\}, \quad (107)$$

where t is the crystal thickness. On the basis of the symmetry conditions (105) and (106), it seems possible to treat the slowly varying amplitudes of the wave functions as functions of only the coordinate z. In this case, the set of Eqs. (102) assumes the form

$$\begin{cases} 2i\dfrac{k_{0z}}{k^2}\dfrac{\partial\Psi_0(z)}{\partial z} = \dfrac{V_0}{E}\Psi_0(z) + \dfrac{V_{-B}}{E}\Psi_B(z), \\ 2i\dfrac{k_{Bz}}{k^2}\dfrac{\partial\Psi_B(z)}{\partial z} = \dfrac{V_B}{E}\Psi_0(z) + \left(\dfrac{V_0}{E} - \alpha\right)\Psi_B(z), \end{cases} \quad (108)$$

where k_{gz} is the projection of the vector $\mathbf{k}_g$ onto the z axis ($\mathbf{g} = 0, \mathbf{B}$). Solving the set of Eqs. (108), we obtain the wave functions in the form

$$\begin{cases} \Psi_0 = \dfrac{1}{2}\dfrac{(y - \sqrt{y^2-1})\exp[i\xi\sqrt{y^2-1}(t-z)] - (y + \sqrt{y^2-1})\exp[i\xi\sqrt{y^2-1}(z-t)]}{iy\sin(\xi\sqrt{y^2-1}t) - \sqrt{y^2-1}\cos(\xi\sqrt{y^2-1}t)}, \\ \Psi_B = \dfrac{1}{2}\dfrac{\exp[i\xi\sqrt{y^2-1}(z-t)] - \exp[i\xi\sqrt{y^2-1}(t-z)]}{iy\sin(\xi\sqrt{y^2-1}t) - \sqrt{y^2-1}\cos(\xi\sqrt{y^2-1}t)}, \end{cases} \quad (109)$$

where we have introduced the following notation:

$$\delta = \frac{k^2}{2k_z}\alpha, \quad \xi = \frac{k^2}{k_z}\frac{\sqrt{V_B V_{-B}}}{E},$$
$$y = \frac{E}{\sqrt{V_h V_{-h}}}\left(\frac{V_0}{E} - \alpha\right).$$

For $|y| < 1$, this will be a solution that decays toward the interior of the crystal and which is known to describe the extinction phenomenon. For $|y| > 1$, the behavior of slowly varying amplitudes $\Psi_{0,B}(z)$ in the crystal becomes periodic, the wavelength being

$\sqrt{y^2-1}/\xi$. From the definition of ξ, it can be seen that, at $|\sqrt{y^2-1}| \sim 1$, this length is on the same order of magnitude as the extinction length introduced in Section 4 (apart from the Debye–Waller factor, whose absence is explained by the disregard of thermal vibrations of the crystal in this model). It follows that the two pairs of waves in a crystal can be considered not as two pairs of waves with the wave vectors (20), which differ only slightly within each pair, but as two waves that are characterized by the vacuum wave vectors, but which are modulated by long waves whose wavelength is about the extinction length. Under the Darwin table, these waves transform into exponentially decreasing functions. Such a consideration substantially extends the concept of the extinction length and gives reasons to introduce the term "extinction waves," by which we mean the behavior of the slow component of the wave function (98).

This approach is advantageous in that one can solve, within this approach, the dynamical theory of diffraction without the use of the plane-wave approximation—that is, under the conditions of the dynamical diffraction of an arbitrary wave packet. This provides, for example, the possibility of adequately describing experiments with neutron beams of arbitrary aperture and, in addition, of complicated spatial structure.

15. SOME FEASIBLE EXPERIMENTS WITH PERFECT CRYSTALS

Completing the description of the dynamical diffraction of thermal neutrons on perfect crystals weakly absorbing neutrons, we deem it reasonable to make some comments and give some explanations. As was indicated in the Introduction, the creation of the dynamical theory of diffraction is due to Darwin, Laue, and Ewald, who published their results immediately after the discovery of x-ray diffraction on crystals in 1912. An experimental corroboration of this theory for x-ray photons was obtained only in the late 1940s, the discovery of the following effects serving the proof of the formation of a unified wave field in the volume of a perfect crystal:

(i) the phenomenon of primary extinction in diffraction and the presence of the total-reflection region (Darwin table) in the case of Bragg diffraction;

(ii) the effect of "pendulum bands," which consists in oscillations of the intensity at the center of the Bormann fan and in oscillations of the intensity in integrated reflection in the case of Laue diffraction;

(iii) the anomalous transmission (absorption) of x-ray photons in the region of a diffraction reflex from a perfect crystal (Bormann effect);

(iv) An anomalous narrowness (of about an angular second) and a rather slow decrease of the reflection-radiation profiles.

With the advent of research reactors in the 1950s, all these effects were rediscovered for neutron radiation. From the early 1970s, the attention of researchers studying these realms has been focused primarily on the utilization of these phenomena with the aim of developing precision methods for investigations into nuclear, neutron, and solid-state physics. As excellent examples of this, we can indicate (see also above) neutron topography and interferometry, as well as precision two- and three-crystal spectrometry on the basis of perfect crystals. In addition, much effort of researchers has gone into exploring dynamical neutron diffraction on a distorted crystal lattice. These local distortions are defects of different origins in nearly perfect crystals or deformations accompanying the excitation of ultrasound in a crystal. Effects of a resonance character, including neutron- and x-ray-acoustic resonances (see [56] and [57], respectively) and oscillations of the diffraction intensity versus a variation in the amplitude of an ultrasound [58, 59], were discovered in the latter case.

Having the magnetic moment of $\mu = -1.91315\mu_{\text{nucl}}$, neutrons interacting with atoms that involve noncompensated electron shells undergo not only nuclear but also magnetic dipole–dipole scattering. This makes it possible to obtain intense beams of polarized neutrons [60]. There are a great number of studies (see [61–64]) that were devoted to developing the dynamical theory of neutron scattering on perfect magnetic crystals of the Fe and Ni type. However, experiments did not yield positive results, primarily because of the absence of large magnetically ordered perfect crystals. At the same time, a series of experiments performed by Somenkov and Kvardakov with weakly ferromagnetic crystals ($FeBO_3$, α-Fe_2O_3, Fe_3BO_6), whose thin layers possess nearly perfect crystal lattices [65, 66], proved to be quite successful. Dynamical effects, such as pendulum bands in the scattering intensity, which are observed if the thickness, temperature, or the orientation of the magnetic field is changed, and anomalous neutron transmission, were observed and studied. It was found that imperfections of the crystal and the magnetic structure, a constant and a variable magnetic field, magnetic domains, and phase transitions exert influence on dynamical effects and on the intensity of neutron scattering on the above crystals. In addition, nonlinear magnetoelastic resonance effects associated with the excitation of modes of magnetoelastic vibrations were discovered and explored. In those experiments, the modulation of the intensity was as great as a few tens of percent. This was associated with special features of the scattering of radiation

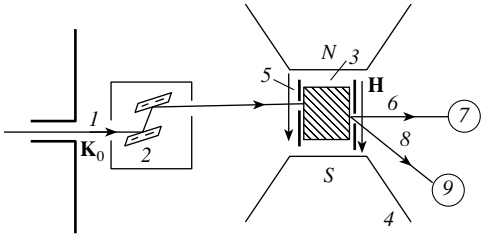

Fig. 33 [72]. Proposed scheme of experiments aimed at observing a multifrequency precession of the neutron spin. A beam of unpolarized neutrons (*1*) that has undergone reflection from crystal monochromators (*2*) is directed to a perfect crystal (*3*) cut asymmetrically and placed in a field **H** generated by a magnet (*4*). Reflection occurs from a family of planes (for example, (220) or (111)); slits (*5*) manufactured from a neutron-absorbing substance serve as collimators. The intensities I_d (beam *8*) and I_t (beam *6*) are measured by neutron detectors (*9* and *7*).

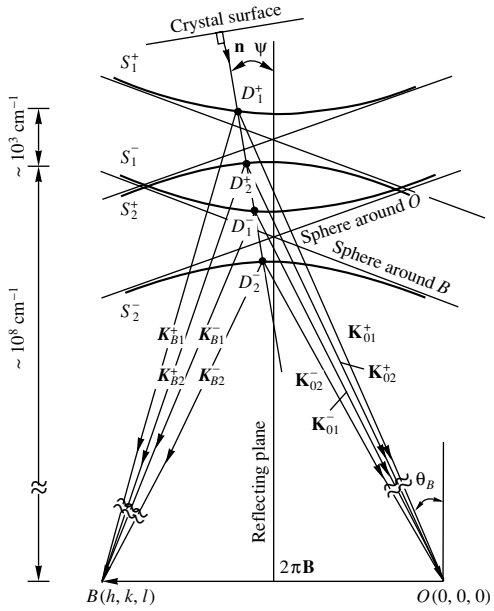

Fig. 34 [72]. Dispersion surface in the reciprocal space for the case of Laue neutron diffraction on a nonmagnetic crystal and asymmetric reflection; the application of a magnetic field leads to the splitting of the dispersion surface and to the generation of four Bloch waves in the crystal that propagate in the directions O and B and which form a unified wave field.

in nearly perfect crystals—specifically with a high sensitivity of neutron-diffraction intensity to weak deformations of a crystal lattice.

However, there exists a line of investigations that has yet to be realized experimentally, although it has been well developed theoretically. The point is that, as far back as 1964, Baryshevsky and Podgoretsky showed [67] that the propagation of slow polarized neutrons through a target containing polarized nuclei is accompanied by neutron-spin precession about the direction of the target-polarization vector, this precession being caused by the difference of nuclear-scattering amplitudes for different states of the neutron–nucleus system. This phenomenon was experimentally discovered by the groups of Forte [68] and Abraham [69]. Later on, Baryshevsky showed [70] that, under the conditions of dynamical diffraction on polarized nuclei, there can occur a multifrequency precession of the neutron spin.

In the presence of a constant uniform magnetic field of strength from a few tens of to a few thousand oersteds that is generated by a conventional electromagnet, a similar phenomenon may also occur in the case of neutron diffraction on a nonmagnetic crystal where nuclei are unpolarized [71]. A major part of the flux of **H** is then within the bounded region of space between the poles of this electromagnet, the strength of the magnetic field decreasing sharply as one moves away from this region in the lateral direction. When neutrons traverse the spatial region where **H** changes, the particle spins tend to align adiabatically with the field direction; therefore, special methods for introducing neutron beams in the magnetic-field region—for example, methods that employ superconducting screens or some other devices controlling the neutron-spin direction—should be applied in implementing the experiments being discussed.

Let us place a crystal in the central part between the poles of the magnet and direct a beam of neutrons of wave vector $\mathbf{K}_0$ onto it (see Fig. 33). In this case, the field in which our nonmagnetic perfect crystal occurs can be considered to be constant and uniform. We choose the quantization axis to be aligned with the direction of the magnetic-field strength **H**. The incident neutron beam can be represented as a superposition of two neutron beams of the same wave vector $\mathbf{K}_0$ that are totally polarized, their polarization directions being parallel and antiparallel to the quantization axis. At the boundary of the magnetic-field region, the neutron beam undergoes refraction, the refraction factors for the two beam components differing by spin orientations being different because of the different energy of interaction with the magnetic field (Zeeman splitting effect), $\pm\mu\mathbf{H}$. Upon undergoing refraction at the boundary of **H**, the incident neutron beam will have two different wave vectors; that is,

$$\mathbf{K}_\sigma = \mathbf{K}_0 + K_0 q_\sigma \boldsymbol{\rho}, \quad q_\sigma = \frac{\pm m\mu H}{\hbar^2 K_0(\mathbf{K}_0 \cdot \boldsymbol{\rho})}. \quad (110)$$

Here, the plus (minus) sign corresponds to neutrons whose spins are parallel (antiparallel) to the vector **H**; $\boldsymbol{\rho}$ is a unit vector directed along the normal to the

boundary of the magnetic-field region; and m and μ are the neutron mass and the neutron magnetic moment, respectively. The incident-neutron wave function immediately at the crystal surface can be represented in the form

$$\Psi = \begin{pmatrix} C_+ e^{i(\mathbf{K}_+ \cdot \mathbf{r})} \\ C_- e^{i(\mathbf{K}_- \cdot \mathbf{r})} \end{pmatrix},$$

where $\begin{pmatrix} C_+ \\ C_- \end{pmatrix}$ is the spin wave function for incident neutrons immediately at the crystal surface, the coefficients $C_\pm$ already including the additional phase increment that arises owing to the propagation of the neutron beam through the magnetic-field region in front of the entrance crystal surface. In the Schrödinger Eq. (1), the effective periodic potential of neutron–nucleus interaction develops the spinor component $\hat{V}(\mathbf{r}, \hat{\boldsymbol{\sigma}})$. The operator set of Eqs. (13), which is written in the two-ray approximation, then decouples into two independent sets of equations [71] for the spin wave-function components parallel and antiparallel to the quantization axis aligned with the vector **H**. This set of equations has a form that is standard for the dynamical theory of diffraction (see Section 4); in the two-ray approximation, it reduces to a set of algebraic equations, which eventually leads to a solution to a dispersion equation that is similar to Eq. (18). But in contrast to what we had in the case of $\mathbf{H} = 0$ (see Fig. 3), the two-sheet surface of rotation for $\mathbf{H} \neq 0$ now splits, which results in the doubling of the branches (sheets), the excitation points D_1^+, D_2^+, D_1^-, and D_2^- (see Fig. 34) generating four Bloch waves that describe the propagation of neutrons in a crystal under the conditions of dynamical diffraction. The points D_1^+ and D_2^+ (D_1^- and D_2^-) are the centers of excitation of two Bloch waves corresponding to the polarized incident-neutron state of spin parallel (antiparallel) to the direction of the magnetic field in the crystal. Four wave vectors $\mathbf{K}_1^+$, $\mathbf{K}_2^+$, $\mathbf{K}_1^-$, and $\mathbf{K}_2^-$ corresponding to these Bloch waves propagating in the directions O and B are not equal to one another in general. In all, there now exists a superposition of eight waves ($\mathbf{K}_{01,B1}^\pm$; $\Psi_{01,B1}^\pm$ and $\mathbf{K}_{02,B2}^\pm$; $\Psi_{02,B2}^\pm$) in a nonmagnetic crystal placed in the field **H** (in contrast to four waves at $\mathbf{H} = 0$—see Section 5), which form a unified wave field (see Fig. 34). In accordance with this, all of the aforementioned dynamical effects, including those that are the most easily observed—specifically, the effect of pendulum bands and oscillations of the intensity at the center of the Bormann fan (see Sections 9, 10)—acquire different features. Therefore, the series of experiments aimed at observing these effects in perfect germanium crystals (so far, such experiments have been performed only by Shull and only with silicon crystals) that is discussed in the present article may be considered as a sound basis for observing the phenomenon of multifrequency neutron-spin precession.

The proposed experimental scheme (see Fig. 33) is somewhat modified: a wedgelike crystal is installed instead of a plane-parallel one (see Fig. 20), and the collimating slit at the exit surface is removed. Aperiodic oscillations of the intensity (instead of strictly periodic ones, as in Fig. 21) are then expected to be observed either versus the crystal position or versus the magnetic-field strength **H**. If it is necessary to make the effect more contrastive, a narrow slit at the exit crystal surface is arranged exactly at the center of the Bormann fan (see Fig. 14); in addition, one can vary both the magnetic-field strength and the neutron energy. Calculations at $H \leq 6$ kOe for (111) and (220) reflexes from perfect germanium crystals cut asymmetrically according to Laue ($\psi \sim 15°$; see Fig. 34) demonstrate that, even at low-flux reactors, it is feasible to observe multifrequency precession.

A positive answer to the question of whether it is possible in principle to observe such effects upon the application of a magnetic field of a few kilooersted if use is made of perfect nonmagnetic crystals was given in the study of Rauch *et al.* [73], who employed the ISIS pulsed source at the Rutherford Appleton laboratory. The statement that the interaction of the magnetic field **B** with the magnetic moment μ of a neutron reflected from a perfect crystal causes a Zeeman splitting of a reflex and the corresponding shift of the neutron scattering vector **q**, $\Delta q = \pm(\mu B m)/(\hbar^2 q)$, was tested experimentally by Shull [74] as far back as 1979. With a pulsed source, this phenomenon was used to create a device for storing cold neutrons. This device, whose schematic representation is given in Fig. 35*a*, consists of a silicon crystal of length 1.07 m with reflecting plates cut on each side along the (111) plane. In the strictly inverse-scattering case realized here, the neutron-wavelength was $\lambda_n \sim 6.27$ Å, while the resolution in the scattering vector was $\Delta q/q = 4 \times 10^{-5}$. The plates were placed within electromagnets to which current pulses ensuring control of locking crystals were supplied. The direction of the neutron momentum was shifted in space by a magnetic field, and this led to an angular shift of the Darwin reflection curve (see Fig. 35*b*), thereby causing the opening or the locking of the system. The system is filled with neutrons upon the application of a magnetic pulse generated by coils, the pulse amplitude being 1.3 T, since a pulse of amplitude 1.26 T causes a reflection-curve shift of value exactly equal to the

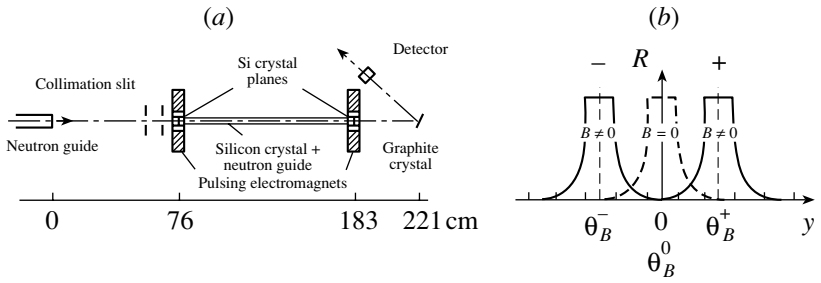

Fig. 35 [73]. (*a*) Layout of a device that is intended for storing cold neutrons and which is based on the use of perfect crystals; (*b*) relative shift of the Darwin table upon the application of a magnetic field.

width of the reflection plateau. Neutrons are released from the system by applying a magnetic pulse to the second crystal. A successful implementation of this storage device opens prospects for observing the phenomenon of multifrequency neutron-spin precession. An account of the methodological basis for performing such experiments is given in the present article.

As was mentioned in Sections 3 and 4, the two-ray case of the dynamical theory of scattering occurs most often in practice, but it is at the same time a particular case. If λ_n is small and if several nodes of the reciprocal lattice occur near the surface of the Ewald sphere, we have to deal with the multiwave approximation, since there arises the possibility of simultaneous neutron reflection from several crystal planes occurring under conditions close to those of Bragg's law. The effect of such multiwave scattering can be taken into account in the kinamatical approximation, where there are two strong and many weak waves in a crystal. This is done by introducing, in the set of dynamical equations, a correction for transitions of neutrons from strong into weak waves and by neglecting inverse processes.

In the dynamical approximation, where it is necessary to take into account the effect of all waves in a crystal, a theoretical analysis of multiwave scattering is more involved than that in the two-wave case even in the presence of a magnetic field. The dispersion surface does not split into two independent surfaces of lower order (see Fig. 34), but it represents a single surface of sixth or higher order. A specific analysis of the dispersion surface and of known dynamical effects is impossible without recourse to numerical methods.

The anomalous-transmission effect, which is an analog of the Bormann effect in x-ray crystal optics, is one of the most interesting phenomena in neutron scattering on absorbing perfect crystals. It is convenient to illustrate the physical meaning of the effect by following Ewald [17]. It was indicated in Section 5 that, in the case of symmetric Laue geometry (see Fig. 4), four waves of different wave vectors and amplitudes propagate in two directions symmetric with respect to reflecting planes, provided that the conditions of Bragg's law are strictly satisfied ($\theta = \theta_B$). Let us decompose each of these vectors into two components, that along crystal planes and that orthogonal to them, as is shown in Fig. 36*a*. The normal components are then directed along (against) the reciprocal-lattice vector. The components directed along reflecting planes are summed in pairs, forming two running waves of frequency determined by λ_n. These waves transfer energy through the crystal to its back face. Their normal components, which are directed oppositely and which are equal in magnitude, form standing waves (see Fig. 36*b*). To a high precision ($|n_\lambda - 1| \sim 10^{-5}$–$10^{-6}$), the spacing between the nodes (antinodes) is equal to the spacing between neighboring reflecting planes. The nodes of one standing wave occur within atomic planes, while its antinodes are in between them. In the second standing wave, the arrangement of nodes and antinodes is reversed (see Fig. 36*c*). If nuclei strongly absorbing neutrons are situated in these crystallographic planes, the second component will be strongly absorbed with increasing distance from the entrance crystal surface; on the contrary, the propagation of the first component is accompanied by a reduced absorption, so that the anomalous transmission of neutrons will be observed.

In the case of neutrons, this phenomenon, which is an analog of the Bormann effect (anomalous trans-

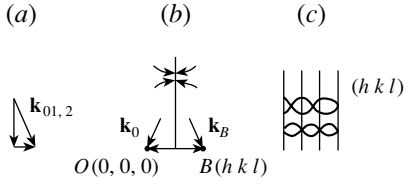

Fig. 36 [75]. (*a*) Formation of standing waves under the conditions of dynamical Laue diffraction: decomposition of the wave vector into two components, that along reflecting planes and that orthogonal to them; (*b*) formation of standing waves; and (*c*) positions of the antinodes and nodes of standing waves.

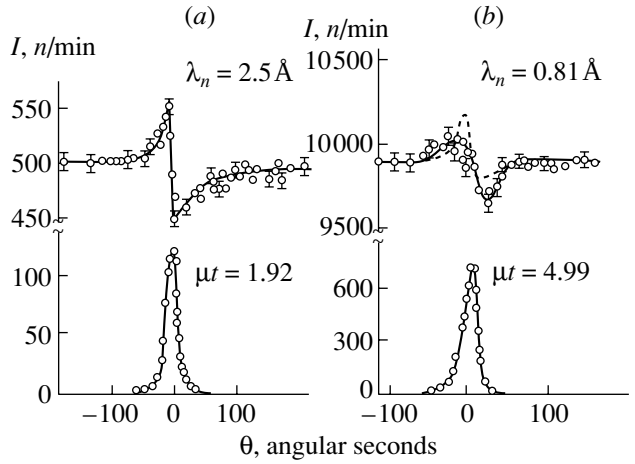

Fig. 37 [76]. Transmission and reflection curves for a perfect neutron-absorbing crystal of CdS that were obtained with the aid of the weak-dispersion scheme of a two-crystal spectrometer (*a*) for predominantly potential scattering and (*b*) near the absorption resonance. The dashed curve represents the calculated dependence.

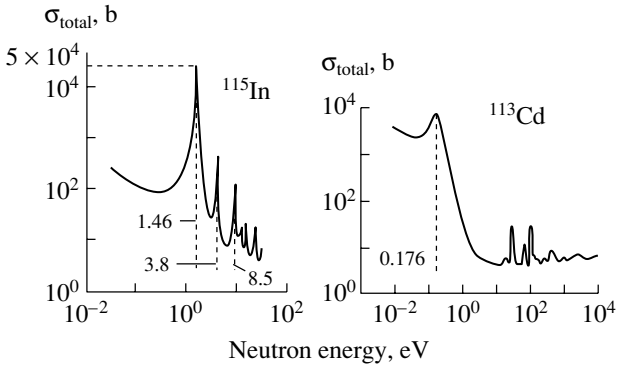

Fig. 38 [77]. Cross sections for the total absorption of slow neutrons in the isotopes ^{115}In and ^{113}Cd. The dependence of the (n, γ) cross section is superimposed on the region where the total-absorption cross section in question varies in proportion to $1/v$; for ^{115}In, three sharp resonances are clearly seen at energies of 1.46, 3.8, and 8.5 eV. The isotope ^{113}Cd has a resonance level at 0.176 eV, and a smeared resonance curve is superimposed on the $1/v$ law.

mission of x rays), was studied theoretically by Kagan and Afanas'ev [7] and is referred to as the neutron-optical Kagan–Afanas'ev effect. It is obvious that, in weakly absorbing crystals like those of silicon, this effect is unobservable in practice, but it was observed in InSb and CdS crystals, whose nuclei have a low-lying resonance level. The dispersion transmission curve $P_0(y)$ for neutrons was first obtained for an InSb crystal by Knowles, who reported his results in 1956 in the article "Anomalous Absorption of Slow Neutrons and X-Rays in Nearly Perfect Single Crystals" [11]. This was the first experimental evidence of anomalous transmission (absorption), although quantitative agreement with the theory was not achieved. The calculated value $\mu_0^{\text{theor}}t$ proved to be less than its experimental counterpart ($\mu_0^{\text{expt}}t \sim 1.8$–$2$ in the thermal part of the spectrum) by a few tens of percent. This was attributed to the presence of imperfections in the crystal used. More reliable results were obtained by Shil'shtein and Somenkov [76] for a perfect CdS crystal. The effect was observed for scattering in Laue geometry both (Fig. 37*a*) for predominantly potential neutron scattering and (Fig. 37*b*) near the region of the resonance ($E_{\text{res}} = 0.176$ eV) in the ^{113}Cd nucleus (see right panel in Fig. 38). This point calls for a dedicated consideration.

It was repeatedly stated that, under the conditions of dynamical diffraction, the behavior of a neutron in the interior of a perfect crystal is described by a superposition of four waves having different wave vectors. According to quantum-mechanical postulates, a neutron is as if smeared within the crystal, simultaneously interacting with the entire ensemble of nuclei (there are about 10^{23} of them). The time over which this interaction occurs is $\sim 10^{-7}$ s. Near the resonance, we can assume that the scattering process proceeds through the channel of compound-nucleus formation. But under the conditions of diffraction, not only is it impossible to indicate a specific nucleus on which scattering occurs, but also nuclear levels responsible for scattering undergo collectivization—that is, the entire ensemble of nuclei in the crystal becomes a macroscopic resonator [75]. The complicated mechanism of neutron–nucleus interaction brings about the question of whether dynamical effects survive in the presence of noncoherent and resonance scattering and the question of what features of scattering appear in this case.

Experiments along these lines were performed by measuring the transmission intensity of Laue neutron scattering on a perfect CdS crystal [76] at a neutron energy of 0.14 eV ($\lambda_n \sim 0.81$ Å), which is close to the resonance region for the ^{113}Cd nucleus ($E_{\text{res}} = 0.176$ eV; $\lambda_n^{\text{res}} = 0.67$ Å). It was shown that, near the resonance region, there is an effect consisting in the suppression of the inelastic nuclear-reaction channel and manifesting itself in the dispersion character of transmission curves (see Fig. 37*b*). That the theoretical curve (dashed one) differs significantly from the experimental curve was attributed by the authors of the experiment to imperfections of the CdS crystal, to the effect of the multiwave scattering process, and to higher orders of reflection. In relation to the experiment of Knowles [11], the study being presently discussed was able, however, to come closer to the

resonance energy and, despite the aforementioned difficulties, to obtain a contrast far beyond the statistical error (five to six standard deviations). At the same time, the advantages of experiments with InSb crystals, which possess a crystal structure (similar to that of silicon and germanium) whose deviations from a perfect structure are nearly nonexistent and which exhibits a distinct resonance peak associated with the isotope ^{115}In ($E_{\rm res} = 1.46$ eV; $\lambda_n^{\rm res} = 0.24$ Å) (see Fig. 38), are evident.

Such conditions make it possible to use rather thin crystals and to observe not only the anomalous absorption of neutrons but also the behavior of the intensity of gamma radiation originating from the (n, γ) reaction on ^{115}In. Difficulties encountered in dealing with CdS [76] can be overcome by using the crystal-collimator procedure, which was implemented in [15] for the case of a germanium crystal (see Section 9 and Fig. 14). In doing this, slits must be manufactured from borated polyethylene, while the InSb crystal must have a thickness in the range $t = 0.3$–0.5 mm. The use of (111) reflection makes it possible to get rid of the (222) and (333) higher orders, which are not involved in this reflection. For a crystal monochromator, one can employ the same InSb cut in Bragg geometry. This will permit applying the dispersion-free scheme and going away from a direct beam at an angle of $2\theta_B \sim 4°$; in this case, the energy resolution and, hence, the order of the wave approximation can be varied by changing the width of the exit slit. A step-by-step variation of λ_n can be performed in just the same way as in the experiment described in Section 9.

A low intensity of 1.46-eV neutrons ($\lambda_n \sim 0.24$ Å) in the spectrum of a stationary reactor, the reduction of the efficiency of ^{3}He detectors in recording such neutrons, and a decrease in the reflecting power of crystals, as well as deteriorating background conditions, may become insuperable problems for such an experiment. However, the spectrum of the IBR-2 pulsed reactor, of a source of the ISIS type, or of the hot source of the reactor at the Laue–Langevin Institute (Grenoble) contains a sufficient number of such neutrons; therefore, it is possible in principle to study the effect of anomalous neutron transmission in the immediate vicinity of the resonance by using procedures, estimates, and results for germanium that are presented in this article.

Completing the discussion of the problems of dynamical neutron diffraction on perfect crystals, we would like to indicate that the series of investigations for germanium crystals that is described here was performed at the MEPI reactor in the early 1980s. At that time, all of the effects listed above had already been discovered, which seems to reduce the value of those efforts. By that time, however, such experiments had been performed only by Shull, who used silicon crystals and who did not indicate his experimental procedures and the absolute intensity values, although it was obvious that the implementation of the collimating-crystal procedure (that of Authier's collimator in the x-ray technique) requires overcoming serious difficulties. Therefore, the success of neutron-optics experiments with germanium crystals at low-flux reactors gives sufficient grounds to discuss problems considered in this section.

Furthermore, the Bragg scattering of neutrons on perfect crystals seems the only possibility for creating intense coherently coupled neutron beams with the aim of employing them to solve interferometric problems. A neutron interferometer, which was first created in 1974, proved to be an efficient tool for fundamental investigations in nuclear and solid-state physics. However, the development of these studies is hindered by the small volume of space between the crystal plates S, M, and A (about 30 cm^2) (see Fig. 23); a considerable enhancement of this volume is possible upon the creation of a polycrystal interferometer, where plates reflecting neutrons are not connected by a unified single-crystal base and are separated by a distance of a few tens of centimeters. An implementation of such a device—and there are no fundamental physical principles that would prohibit this [12, 16]—will immediately open wide prospects for operating with cryostats, strong magnetic fields, heaters, etc., whereby the range of solid-state- and nuclear-physics problems to be addressed on the basis of the aforementioned methods will be considerably extended. It is clear that the requirement for the instrument to ensure a high contrast will become stringent since the Doppler and static phase shifts of neutron waves can only increase [15]. The degree of contrast may in principle be improved by going over to crystals absorbing thermal neutrons, such as InSb, in which case the anomalous-absorption effect is inevitably present (see Fig. 36 and explanations to it). Owing to this, one pair of waves in a crystal (for example, $\mathbf{K}_0^{(1)}$, Ψ_0; $\mathbf{K}_B^{(1)}$, Ψ_B) is efficiently suppressed in the S and M plates successively, so that the neutron field in the A crystal is a simpler combination than in the case of nonabsorbing silicon; concurrently, the modulation in the O and B beams (see Fig. 24) proves to be significantly greater. This effect may appear to be quite pronounced if InSb crystals are exposed to slow neutrons of $E_n \sim 0.5$ eV (the interferometer used is extended along the beam direction since $2\theta_B \sim 12°$), but this, however, again requires solving some technological problems.

In any case, a polycrystal interferometer that employs the effect of anomalous neutron absorption may become a universal and precise instrument that would

open the possibility of studying a wide range of physical phenomena by performing a direct measurement of the phase shift of a neutron wave instead of measurements of various cross sections.

Finally, a small half-width of the reflection curve for perfect crystals of silicon and germanium can be used to create spectrometers that possess simultaneously a high angular and a high energy resolution and which make it possible to record a deflection of neutrons from a straight-line trajectory between the crystals at angles of $\sim 10^{-5}$–10^{-6} rad and changes of $\Delta q \sim 10^{-5}$–10^{-4} Å^{-1} in the scattering vector. This property of dynamical diffraction opens remarkable prospects for performing precision investigations of small-angle and diffuse neutron scattering on inhomogeneities in condensed media.

16. CONCLUSION

Summarizing the aforesaid, we would like to note that effects associated with dynamical diffraction were discovered more than 80 years ago. This was due to the presence of perfect crystals in nature, like rock crystal (α-SiO_2), diamond (C), and rock salt (NaCl). On obtaining x rays as a tool at their disposal, many physicists whose activities covered the beginning of the 20th century embarked on studying the phenomenon of diffraction on an ensemble of scatterers perfectly ordered in space—that is, atoms forming the lattice of a perfect crystal. Concurrently, the dynamical theory of x-ray diffraction on perfect crystals was developed, and this theory made it possible to explain successfully all the effects listed at the beginning of the preceding section.

As was compellingly demonstrated in the monograph of Cowley [78], the theory and the effects discovered experimentally proved to be universal for all kinds of radiation, including x rays, thermal neutrons, slow neutrons, and protons. Any consideration of the diffraction process at the microscopic level starts from a description of particle interaction with a perfect lattice of scatterers, atoms or nuclei, and only after that does one go over to real structures. Naturally, each kind of radiation has specific features inherent in it—in this article, we have considered the case of neutrons, which makes it possible to explore the effects in question by using various crystals of large dimension. The magnetic moment of neutrons renders them appropriate for studying effects of dynamical scattering on perfect magnetoactive crystals, thereby considerably extending the range of their application in these realms of diffraction physics.

The aforementioned phenomenon of multifrequency neutron-spin precession in a diamagnetic perfect crystal placed in a uniform magnetic field is quite accessible to studying at a reactor yielding neutron fluxes of intermediate values. Recall that the beating of the intensity of diffracting waves arise owing to the splitting of neutron wave functions into components characterized by different phase shifts that are dependent on the crystal thickness, the magnetic-field strength, and the neutron wavelength. Investigation of this phenomenon in the vicinity of neutron resonances would be especially tempting. In the region of neutron resonances, it is desirable to continue studying nuclear reactions under the conditions of dynamical neutron diffraction [11, 76] with the aim of exploring in greater detail the collectivization of nuclear levels in neutron diffraction [7].

The neutron-beam studies that spanned the period from the 1940s to the 1960s and which employed perfect crystals made it possible to create, in later years, unique equipment for performing investigations in the realms of nuclear and condensed-matter physics. For example, the technique of a high-angular-resolution two-crystal spectrometer operating under the conditions of Bragg diffraction was developed [79]. At present, such spectrometric schemes are successfully used to study ultrasmall-angle neutron scattering on inhomogeneities in solid-state samples [79]. In the future, it seems feasible to construct an instrument that would make it possible to implement a four-crystal scheme for perfect crystals. In this scheme, the second and the third crystal along the beam direction are arranged in the antiparallel dispersion position, while the third and the fourth one form a two-crystal $(1, -1)$ spectrometer. Estimates reveal that, if such a device is mounted after the neutron guide for thermal neutrons from a high-flux reactor, this would enable one to obtain a flux of $\Phi_{\text{out}} \sim 2 \times 10^4$ n/cm^2 s at the output, with the wavelength spread being $\Delta\lambda/\lambda \sim 10^{-5}$. This would provide the possibility of studying small-angle scattering with an angular resolution of about 5×10^{-6} rad. It seems that such an instrument can sharply extend the regions of investigation of quasielastic coherent neutron scattering, as well as of diffuse and small-angle scattering on inhomogeneous samples and crystals containing defects.

The fact that, in the case of Laue diffraction, coherent beams are obtained at the exit of the crystal used made it possible to create neutron interferometers. It was shown above that, with the aid of such instruments, the accuracy in measuring the amplitude for coherent scattering of nuclei was improved by two orders of magnitude for many elements, the identity of the inertia and the gravitational mass in microscopic physics was established experimentally to a precision of 10^{-4}, and the 4π symmetry of the neutron wave function was proven experimentally. However, a relatively small volume of space between crystal plates forming such interferometers is a serious obstacle to attempts at extending the range of their application.

For future advancements along these lines, it is therefore desirable to construct a neutron interferometer whose operating plates are not connected by a unified single-crystal base. This would make it possible to place experimental equipment in the space between the plates and to solve many physics problems at the level of neutron-wave phases.

If the lattice of nuclei is not strictly perfect—that is, there is a small number of defects in the crystal used—then diffuse scattering, known in x-ray optics as Huang scattering, appears near the Bragg peak. Being tightly linked with the Bragg reflex (scattered neutrons are deflected from the exact Bragg direction at a very small angle of about 10″—20″; therefore, $|\Delta\mathbf{k}| \ll |\mathbf{k}|$), it generates a diffuse halo around it in the form of a low-intensity peak. As a result, the diffuse and the Bragg component of the neutron field interact, giving rise to dynamical effects that were first discovered by the authors of [36, 49]. There is presently no theory of this phenomenon, and it seems that, in order to describe it adequately, it is necessary to develop one of the alternative theoretical approaches to the dynamical theory of diffraction that have been described in the present article.

Thus, we have seen that, despite more than fifty years of its history, dynamical neutron diffraction is still a flourishing realm of modern science. On one hand, it presents some as-yet-unresolved problems of fundamental interest; on the other hand, remarkable techniques and procedures for studying matter that are being extensively used at present and which undoubtedly show great promise for future were developed in this field.

ACKNOWLEDGMENTS

We are grateful to F.S. Dzheparov, V.K. Ignatovich, and D.V. L'vov for stimulating discussions and to A.O. Eidlin, S.K. Matveev, and D.S. Denisov for participation in experiments with a neutron beam from the MEPI reactor.

This work was supported by the Russian Foundation for Basic Research (project nos. 00-02-17837 and 00-15-96656) and by the Ministry for Higher Education of the Russian Federation (grant no. TOO-7.5-2769).

REFERENCES

1. P. P. Ewald, Phys. Z. **14**, 465 (1913); **14**, 1038 (1913); Z. Kristallogr. **56**, 129 (1921).
2. C. G. Darwin, Philos. Mag. **27**, 315 (1914); **27**, 675 (1914); **43**, 800 (1922).
3. M. von Laue, Sitzungsber. – Bayer. Akad. Wiss., Math.-Phys. Kl., 303 (1912).
4. R. W. James, *The Optical Principles of the Diffraction of X-rays* (Bell, London, 1950; Inostrannaya Literatura, Moscow, 1950).
5. Z. G. Pinsker, *X-ray Crystal Optics* (Nauka, Moscow, 1982).
6. M. L. Goldberger and F. Seitz, Phys. Rev. **71**, 294 (1947).
7. Yu. M. Kagan and A. M. Afanas'ev, Zh. Éksp. Teor. Fiz. **49**, 1504 (1965) [Sov. Phys. JETP **22**, 1032 (1966)]; Zh. Éksp. Teor. Fiz. **50**, 271 (1966) [Sov. Phys. JETP **23**, 178 (1966)].
8. V. F. Sears, Can. J. Phys. **56**, 1261 (1978); Phys. Rep. **82**, 1 (1982).
9. H. Rauch and D. Petrascheck, in *Topics in Current Physics* (Springer-Verlag, Berlin, 1979), p. 303.
10. M. A. Krivoglaz, *Diffraction of X-rays and Neutrons in Nonideal Crystals* (Naukova Dumka, Kiev, 1983).
11. J. W. Knowles, Acta Crystallogr. **9**, 61 (1956).
12. *Neutron Interferometry,* Ed. by U. Bonse and H. Rauch (Clarendon, Oxford, 1979).
13. C. G. Shull, Phys. Rev. Lett. **21**, 1585 (1968); *Proceedings of the Summer School of Joint Institute for Nuclear Researches, Alushta, 1969* (Ob'edin. Inst. Yad. Issled., Dubna, 1970), p. 345.
14. C. G. Shull and W. M. Shaw, Z. Naturforsch. A **28**, 657 (1973).
15. Yu. G. Abov and N. O. Elyutin, *Coherent Scattering of Neutrons: Textbook* (Mosk. Inzh.-Fiz. Inst., Moscow, 1988).
16. U. Bonse, in *Proceedings of the 5th International Congress on X-ray Optics and Microanalysis* (Springer-Verlag, Berlin, 1969), p. 1.
17. P. Ewald, Usp. Fiz. Nauk **89**, 287 (1966).
18. D. Zippel, K. Kleinstück, and G. E. R. Schulze, Phys. Lett. **14**, 174 (1965).
19. N. E. Belova, F. A. Eichhorn, V. A. Somenkov, *et al.*, Preprint No. 3346 (9), IAÉ im. I.V. Kurchatova (Kurchatov Institute of Atomic Energy, Moscow, 1980); V. A. Somenkov, S. Sh. Shilstein, N. E. Belova, and K. M. Utemisov, Solid State Commun. **25**, 593 (1978).
20. I. A. Fankuchen, Nature **138**, 193 (1937).
21. G. E. Bacon, *Neutron Diffraction* (Clarendon, Oxford, 1975; Inostrannaya Literatura, Moscow, 1958).
22. N. Kato, Acta Crystallogr. A **25**, 119 (1969).
23. A. Authier, Bull. Soc. Fr. Mineral. **84**, 51 (1961).
24. K. Kohra and S. Kikuta, Acta Crystallogr. A **24**, 200 (1968); S. Kikuta, I. Ishikawa, and K. Kohra, J. Phys. Soc. Jpn. **39**, 471 (1975).
25. Yu. G. Abov, F. G. Kulidzhanov, N. O. Elyutin, and A. O. Éĭdlin, in *Neutron Physics: Proceedings of the 6th All-Union Conference on Neutron Physics, Kiev, 1983* (TsNIIatominform, Moscow, 1984), Vol. 3, p. 299.
26. U. Bonse, in *Proceedings of the International Summer School on X-ray Dynamical Theory and Topography, Limoger, 1975,* Ed. by F. Balibar (Laboratoiry de Mineralogie et Cristallographie, Paris, 1975).

27. A. Z. Men'shikov, S. G. Bogdanov, *et al.*, in *Neutronography of Metals and Alloys* (Inst. Fiz. Met., Sverdlovsk, 1977), Tr. Inst. Fiz. Met., Vol. 35, p. 89.
28. V. G. Vologin, S. G. Teploukhov, A. O. Éĭdlin, *et al.*, Prib. Tekh. Éksp., No. 2, 12 (1994).
29. F. Eichhorn, M. Kosmowski, H. G. Schöpf, and G. E. R. Schulze, Phys. Status Solidi A **30**, 155 (1975).
30. F. Eichhorn, M. Kosmowski, H. G. Schöpf, and G. E. R. Schulze, Phys. Status Solidi A **4**, 445 (1971).
31. A. O. Éĭdlin, S. K. Matveev, and N. O. Elyutin, Preprint No. 22-88, MIFI (Moscow Engineering Physics Institute, Moscow, 1988).
32. N. Kato, Acta Crystallogr. A **25**, 119 (1969).
33. N. Kato and A. R. Lang, Acta Crystallogr. **12**, 787 (1959).
34. A. O. Éĭdlin, N. O. Elyutin, and F. G. Kulidzhanov, *Experimental Methods in Nuclear Physics of Medium and Low Energies* (Énergoatomizdat, Moscow, 1986), p. 36.
35. C. G. Shull, J. Appl. Crystallogr. **6**, 257 (1973).
36. Yu. G. Abov, A. O. Éĭdlin, D. S. Denisov, *et al.*, Zh. Éksp. Teor. Fiz. **104**, 4072 (1993) [JETP **77**, 966 (1993)].
37. S. Kikuta, K. Kohra, N. Minakawa, and K. Doi, J. Phys. Soc. Jpn. **31**, 954 (1971).
38. S. K. Matveev, A. O. Éĭdlin, and N. O. Elyutin, Kristallografiya **36**, 759 (1991) [Sov. Phys. Crystallogr. **36**, 424 (1991)].
39. Yu. G. Abov, F. G. Kulidzhanov, N. O. Elyutin, and S. N. Nizovoĭ, Prib. Tekh. Éksp., No. 4, 52 (1984).
40. H. Maier-Leibnitz and T. Springer, Z. Phys. **167**, 386 (1962).
41. U. Bonse and M. Hart, Appl. Phys. Lett. **6**, 155 (1965); **7**, 99 (1965); **7**, 238 (1965).
42. H. Rauch, W. Treimer, and U. Bonse, Phys. Lett. A **47A**, 369 (1974).
43. A. W. Overhauser and R. Collela, Phys. Rev. Lett. **33**, 1237 (1974).
44. A. Leilinder, C. G. Shull, J. Arthur, and M. A. Horn, Phys. Rev. A **28**, 487 (1983).
45. I. A. Fankuchen, Phys. Rev. **53**, 910 (1938).
46. A. O. Éĭdlin, N. O. Elyutin, F. G. Kulidzhanov, and S. N. Nizovoĭ, *Experimental Methods and Equipment in Nuclear-Physics Research* (Énergoatomizdat, Moscow, 1984), p. 93.
47. F. G. Kulidzhanov, A. O. Éĭdlin, and N. O. Elyutin, Pis'ma Zh. Tekh. Fiz. **12**, 1003 (1986) [Sov. Tech. Phys. Lett. **12**, 414 (1986)]; Yu. G. Abov, N. O. Elyutin, and A. O. Éĭdlin, in *Proceedings of Neutron Conference, Kiev, 1987* (Kiev, 1988), Vol. 4, p. 47.
48. A. P. Besedin, N. O. Elyutin, A. O. Éĭdlin, and F. G. Kulidzhanov, Kristallografiya **30**, 575 (1985) [Sov. Phys. Crystallogr. **30**, 334 (1985)].
49. Yu. G. Abov, A. O. Éĭdlin, D. S. Denisov, *et al.*, Pis'ma Zh. Éksp. Teor. Fiz. **63**, 237 (1996) [JETP Lett. **63**, 252 (1996)].
50. W. H. Zachariasen, *Theory of X-ray Diffraction in Crystals* (Dover, New York, 1967).
51. V. A. Ambartsumyan, in *Proceedings of the All-Union Symposium Confined 40th Anniversary of Leading of Invariance Principle in Radiative Transport Theory, Byurokan, 1981* (Akad. Nauk Arm. SSR, Yerevan, 1981), p. 9.
52. V. K. Ignatovich, Yad. Fiz. **62**, 792 (1999) [Phys. At. Nucl. **62**, 738 (1999)].
53. S. Takagi, Acta Crystallogr. **15**, 1311 (1962).
54. V. A. Bushuev and A. N. Tyulyusov, in *Proceedings of the 4th National Conference on Application of X-ray, Synchroton Radiations, Neutrons and Electrons for Material Research, Moscow, 1999,* p. 255.
55. L. D. Landau and E. M. Lifshitz, *Course of Theoretical Physics,* Vol. 3: *Quantum Mechanics: Non-Relativistic Theory* (Nauka, Moscow, 1974; Pergamon, Oxford, 1977).
56. B. Chalupa, R. Michalec, L. Horalic, and P. Vikula, Phys. Status Solidi A **97**, 503 (1986).
57. I. R. Éntin, Pis'ma Zh. Éksp. Teor. Fiz. **26**, 392 (1977) [JETP Lett. **26**, 269 (1977)].
58. I. R. Entin and I. A. Smirnova, Phys. Status Solidi A **106**, 339 (1988).
59. E. M. Iolin, É. V. Zolotoyabko, É. A. Raĭtman, *et al.*, Zh. Éksp. Teor. Fiz. **91**, 2132 (1986) [Sov. Phys. JETP **64**, 1267 (1986)].
60. Yu. G. Abov, A. D. Gul'ko, and P. A. Krupchitsky, *Polarized Slow Neutrons* (Atomizdat, Moscow, 1966).
61. V. A. Belyakov, *Diffraction Optics of Periodic Media of Complex Structure* (Nauka, Moscow, 1988).
62. V. A. Belyakov and R. Ch. Bokun, Fiz. Tverd. Tela (Leningrad) **18**, 2399 (1976) [Sov. Phys. Solid State **18**, 1399 (1976)].
63. H. H. Schmidt and P. Deimel, Solid State Phys. **8**, 1991 (1975).
64. H. H. Schmidt and P. Deimel, Phys. Status Solidi B **73**, 87 (1976).
65. V. V. Kvardakov, V. A. Somenkov, and S. Sh. Shilstein, *Observation of Dynamical Effects in Neutron Scattering by Perfect Magnetic Crystals,* Mater. Sci. Forum **27/28**, 220 (1988).
66. M. V. Zalepukhin, V. V. Kvardakov, V. A. Somenkov, and S. Sh. Shil'shteĭn, Zh. Éksp. Teor. Fiz. **95**, 1530 (1989) [Sov. Phys. JETP **68**, 883 (1989)].
67. V. G. Baryshevskiĭ and M. I. Podgoretskiĭ, Zh. Éksp. Teor. Fiz. **47**, 1050 (1964) [Sov. Phys. JETP **20**, 704 (1964)].
68. M. Fopte, Nuovo Cimento A **18**, 727 (1973).
69. A. Abragam, G. L. Beccella, *et al.*, Phys. Rev. Lett. **31**, 776 (1973).
70. V. G. Baryshevskiĭ, Pis'ma Zh. Éksp. Teor. Fiz. **33**, 78 (1981) [JETP Lett. **33**, 74 (1981)]; V. G. Baryshevskii and S. V. Cherepitsa, Phys. Lett. A **90A**, 267 (1982); Phys. Status Solidi B **123**, 379 (1985).
71. V. G. Baryshevsky, *Nuclear Optics of Polarized Media* (Énergoatomizdat, Moscow, 1995).
72. S. V. Cherepitsa, Candidate's Dissertation in Physics and Mathematics (Minsk, 1987).

73. M. Schuster, H. Rauch, *et al.*, Phys. Lett. A **144**, 297 (1990).
74. A. Zeilinger and C. G. Shull, Phys. Rev. B **19**, 3957 (1979).
75. Yu. G. Abov, Usp. Fiz. Nauk **166**, 949 (1996) [Phys. Usp. **39**, 891 (1996)].
76. S. Sh. Shil'shteĭn, V. A. Somenkov, and V. N. Dokashenko, Pis'ma Zh. Éksp. Teor. Fiz. **13**, 301 (1971) [JETP Lett. **13**, 214 (1971)]; Pis'ma Zh. Éksp. Teor. Fiz. **12**, 80 (1970) [JETP Lett. **12**, 56 (1970)]; S. Sh. Shil'shteĭn and V. A. Somenkov, Kristallografiya **20**, 1096 (1975) [Sov. Phys. Crystallogr. **20**, 670 (1975)].
77. K. N. Mukhin, *Experimental Nuclear Physics,* Vol. 1: *Physics of Atomic Nuclei* (Énergoatomizdat, Moscow, 1983).
78. J. M. Cowley, *Diffraction Physics* (American Elsevier, New York, 1975; Mir, Moscow, 1979).
79. Yu. G. Abov and N. O. Elyutin, in *Proceedings of the 4th Moscow International ITEP School of Physics, Zvenigorod, 2001,* Ed. by A. L. Suvorov, Yu. G. Abov, and V. G. Firsov (Akademprint, Moscow, 2001).

Translated by A. Isaakyan

Physics of Atomic Nuclei, Vol. 65, No. 11, 2002, pp. 1980–1984. Translated from Yadernaya Fizika, Vol. 65, No. 11, 2002, pp. 2036–2041.

REVIEWS

Parity Nonconservation in Nuclear Physics

G. A. Lobov

Institute of Theoretical and Experimental Physics,
Bol'shaya Cheremushkinskaya ul. 25, Moscow, 117259 Russia

Received October 17, 2001

Abstract—We present an overview of the parity-nonconservation effects in nuclear physics. In the processes of polarized neutron scattering by nuclei, apart from the ordinary dynamical enhancement, we also consider the additional resonant enhancement in the entrance channel due to the proximity of the compound-nucleus p-wave resonance. We discuss the problem of extracting information on the electroweak interaction of nucleons from nuclear data. © *2002 MAIK "Nauka/Interperiodica".*

To search for the old is to find the new.
Confucius

1. INTRODUCTION

Almost 40 years have elapsed since the discovery of parity nonconservation in nuclear physics [1]. Wigner [2] was the first to introduce the concept of wave-function parity. He also discovered a mirror symmetry (the conservation of spatial parity) by formulating the parity conservation law. Over the elapsed time, the study of parity nonconservation in nucleon–nucleon and nuclear interactions has become a separate field of fundamental research in nuclear and particle physics.

The parity-nonconservation effects in nuclear physics are difficult to study theoretically and experimentally. An experimental study involves precision measurements of the subtle electroweak-interaction effects against the background of electromagnetic and strong interactions whose intensity is many orders of magnitude higher. A theoretical study uses quark models for the hadrons and gauge theories for the electroweak and strong interactions as a unified dynamical approach in a consistent quantitative analysis of the parity-nonconservation effects in nuclear physics. At the same time, it became much more difficult to theoretically study the parity-nonconservation effects in nuclear physics, because it is necessary to simultaneously use the formalism of unified gauge theories and the low-energy phenomenology of strong interactions when passing from the quark description of the phenomenon to its hadron description and to construct adequate wave functions of the nuclear systems. Thus, a proper description of the parity-nonconservation effects at all three structural levels—the quark, hadron, and nuclear levels—and the ability to pass from one level to another are required [3–10].

In the standard model, the structure of the electroweak interaction for nucleons is determined by quark currents, mainly by u and d quarks [11]. The electroweak interaction of nucleons in nuclei, just as in the one-boson exchange model in the strong interaction, is described by the potentials of light-meson (π, ρ, ω) exchange between nucleons. However, in contrast to the strong interaction, the diagrams for one-boson exchange in the electroweak interaction contain not two but only one strong-interaction vertex. The other vertex is determined by the electroweak interaction [6–10]. These potentials determine the radial dependence of the electroweak interaction for nucleons and the isospin selection rules:

$$\Delta T = 1 \tag{1}$$

for π- and ω-meson exchange and

$$\Delta T = 0, 2 \tag{2}$$

for ρ-meson exchange.

The Fermi weak interaction constant

$$G_{\mathrm{F}} = 10^{-5}/m^2$$

(where m is the nucleon mass) in nuclei is made "dimensionless" by the effective mean distance between the nucleons, $r_0 \approx 1/\mu$, where μ is the π-meson mass. Therefore, the fundamental electroweak interaction constant for nucleons in nuclei is the dimensionless constant

$$G = G_{\mathrm{F}}\mu^2 \approx 2 \times 10^{-7}. \tag{3}$$

By definition, the constant (3) is equal to the ratio of the characteristic matrix element between the single-particle nuclear states from the parity-nonconserving Hamiltonian of the electroweak nucleon interaction in the nucleus to the characteristic

1063-7788/02/6511-1980$22.00

energy scale of the residual internucleon interaction (see Section 2).

Note that in the CP-invariant theory of electroweak interaction for nucleons, the exchange of any neutral pseudoscalar meson, in particular, a π^0-meson, between nucleons is forbidden. In this theory, the P-odd and C-odd vertex cannot be constructed, because the neutral pseudoscalar meson has a positive C parity. Thus, in the CP-invariant theory of electroweak interaction, the exchanges of only charged $\pi^{\pm}$ mesons are permitted between nucleons.

2. THE ENHANCEMENT OF PARITY NONCONSERVATION IN NUCLEI

Parity nonconservation in nuclear physics was first observed in the reaction $^{113}\mathrm{Cd}(\vec{n},\gamma)\,^{114}\mathrm{Cd}$ [1] with polarized neutrons. The detected P-odd asymmetry of the photon emission relative to neutron polarization was $-(4.1 \pm 0.8) \times 10^{-4}$ [12]. This value is much larger than the fundamental electroweak interaction constant (3) for nucleons in nuclei. This enhancement can be explained by the high level density of the compound nucleus [4, 5]. Let us briefly consider the mechanism of this enhancement. The wave function of the compound-nucleus state can be expanded in the products of single-particle functions:

$$\psi = \sum_{i=1}^{N} a_i \varphi_i, \tag{4}$$

where φ_i are the products of the wave functions for excited particles and holes (the superpositions of one, three, five, etc., quasiparticle configurations). The characteristic number of terms in the sum (4) is determined by the intensity of the residual internucleon interaction. If ω is the energy scale of this interaction and D is the distance between the energy levels of the compound nucleus, then

$$N \sim \omega/D. \tag{5}$$

This estimate can be obtained, for example, in the model of an absolutely black nucleus. The distance D between the compound-nucleus levels exponentially decreases with increasing number of excited particles, i.e., nuclear mass number A. Thus, in intermediate-mass nuclei ($A \sim 100$),

$$D \sim 1\text{–}10\ \mathrm{eV},$$

and in heavy fissionable nuclei ($A \sim 240$),

$$D \sim 1\ \mathrm{eV}.$$

Thus, for the characteristic distance between single-particle energy levels $\omega \sim 1$ MeV, the following estimate for N in expression (5) is valid:

$$N \sim 10^5\text{–}10^6. \tag{6}$$

For such strong mixing of states, the coefficients a_i in (4) have the same order of magnitudes because of the normalization condition

$$|a_i| \sim 1/\sqrt{N}. \tag{7}$$

The matrix element from the single-particle Hamiltonian W that describes the parity-nonconserving electroweak interaction of the nucleon in the nucleus between two compound-nucleus states of the type (4) clearly has the form

$$M = \left\langle \sum_i a_i \varphi_i | W | \sum_k b_k \varphi_k \right\rangle = \sum_{i,k} a_i^{+} b_k \langle i|W|k\rangle. \tag{8}$$

The matrix element in (8) at each fixed i is nonzero only for several values of k, when φ_i and φ_k differ by the state of only one particle. It is quite natural to assume that the signs of the individual terms in the sum (8) are random. For this reason, Eq. (8) contains the incoherent sum of N terms; each of them is equal to $\langle W\rangle/N$ in order of magnitude. As a result, we obtain

$$|M| \sim \langle W\rangle/\sqrt{N}, \tag{9}$$

where $\langle W\rangle$ is the characteristic matrix element between single-particle states. Since the matrix elements of the mixing between different levels of the compound nucleus have the same order of magnitudes, the maximum mixing takes place between the nearest levels. The mixing coefficient is

$$R = \frac{|M|}{D} \sim \frac{|\langle W\rangle|}{\omega}\sqrt{N} = G\sqrt{N}, \tag{10}$$

where G is given by expression (3) and specifies the characteristic mixing scale for single-particle levels. Thus, the mixing coefficient (10) in nuclei contains the dynamical enhancement factor $\sqrt{N}$. This factor is of the order of 10^3 in fissionable nuclei and 10^2 in intermediate-mass nuclei, such as Cd, Sn, and others.

It should be emphasized that N is the number of "principal" components in the wave function (4) that mainly contribute to the wave-function normalization. It thus immediately follows that the statistical formation mechanism for the compound–compound mixing intensity dominates over the so-called valence mechanism [13].

For the existence of a dynamical enhancement, it is important that the intensity of the residual internucleon interaction that mixes single-particle levels be comparable to the distance between the single-particle levels of opposite parity. As an example, let us consider a gas of particles that move in a common potential without interacting with one another. In this

case, the distance between the mixing levels remains a single-particle one and there is no enhancement even at a high system level density.

Apart from the P-odd asymmetry of the photon emission during the capture of polarized neutrons by ^{113}Cd and other nuclei [14], yet another P-odd effect was investigated in experiments on nuclei, circular polarization of the photons emitted by excited nuclei after the capture of unpolarized neutrons [12].

3. PARITY NONCONSERVATION IN NEUTRON SCATTERING BY NUCLEI

There are two parity-nonconservation effects in polarized-neutron scattering by nuclei: the cross-section asymmetry A_n in the scattering of longitudinally polarized neutrons and the spin rotation φ of neutrons polarized transversely to their momentum. The first and second effects are proportional, respectively, to the pseudoscalar quantity $(\mathbf{s}_i \cdot \mathbf{p}_n)$ and to $\mathbf{p}_n[\mathbf{s}_i \cdot \mathbf{s}_f]$, where $\mathbf{p}_n$ is the momentum of the incident neutron and $\mathbf{s}_i$ and $\mathbf{s}_f$ are the spins of the incident and scattered neutrons, respectively.

The parity-nonconservation effects in polarized-neutron scattering by nuclei are a rare example of physical phenomena whose theory was constructed [15] well before their experimental detection [16, 17]. References to more recent studies, their chronology, and the history of discoveries can be found in [14, 18]. In the theory [15], the P-odd effects in complex nuclei are significantly enhanced due to the dynamical enhancement (see Section 2) of compound-nucleus state mixing and structural peculiarities of the neutron scattering. This theory [15] predicts an enhancement of the scattering-cross-section symmetry for longitudinally polarized neutrons A_n with energy E close to the energy E_p of the compound-nucleus p-wave resonance. When the energy distance to the p resonance is much smaller than that to the nearest s resonance, the following expression for the cross-section asymmetry is valid:

$$A_n = 2\sqrt{\Gamma_s(E)/\Gamma_p(E)}\langle s|W|p\rangle/(E_p - E_s), \quad (11)$$

where Γ_s and Γ_p are the energy-dependent neutron widths of the s and p resonances, respectively; E_s is the energy of s resonance; and $\langle s|W|p\rangle$ is the matrix element of the weak interaction operator between single-particle states of the compound nucleus.

The asymmetry (11) is determined by the interference of two Breit–Wigner scattering amplitudes, the P-even and P-odd amplitudes. The P-even amplitude describes the scattering of neutrons in the initial p state with their transition to the final p state through the resonance p state of the compound nucleus. The P-odd amplitude describes the scattering of neutrons in the initial s state with their transition to the final p state. In this case, the transition from the s state to the p state is attributable to the weak interaction between the nucleons in the compound nucleus. Thus, the ratio of the amplitudes interfering in the entrance channel of the reaction for elastic neutron scattering by nuclei determines the magnitude of the P-odd effect (11). The last two terms in Eq. (11) are, by definition, the mixing coefficient (10) containing the dynamical enhancement factor $\sqrt{N}$. The first term in (11) (the square root of the width ratio) for low-lying resonances with $E_p \sim 10$ eV has the following order of magnitude:

$$(k_p R)^{-1} \sim 10^2 - 10^3, \quad (12)$$

where k_p is the neutron momentum and R is the nucleus radius.

Thus, during elastic neutron scattering, the P-odd effect (11) contains the additional (with respect to the dynamical factor) resonant enhancement factor (12) in the entrance channel attributable to the proximity of the compound-nucleus p-wave resonance. As a result, the parity-nonconservation effect (11) in intermediate-mass nuclei can be of the order of 10^{-1}–10^{-2}. Among the nuclei in which the P-odd asymmetry (11) was found, it is at a maximum for the ^{139}La nucleus, 0.15 [16, 18]. This result closely corresponds to the above estimate. Such a large effect in the ^{139}La nucleus can be explained by the presence of a weak p-wave resonance with energy $E_p = 0.75$ eV and an anomalously strong (i.e., with a large neutron width) s resonance.

The spatial-parity nonconservation in the fundamental electroweak interaction in compound-nucleus states leads to yet another surprising effect in unpolarized neutron scattering by unpolarized nuclei. In this case, the unpolarized neutrons are a superposition (with equal weights) of two longitudinal polarization states, along and against to the momentum direction. However, because of parity nonconservation, these two longitudinal polarization states are scattered differently by nuclei, which leads to an asymmetry in the scattering cross section (11); i.e., it gives rise to neutron longitudinal polarization proportional to A_n. If a target of unpolarized ^{139}La nuclei is used as the scatterer, then for $E \sim 1$ eV we can obtain 15% longitudinal polarization of neutrons [19]. Thus, the violation of the fundamental symmetry, the spatial parity, leads to quite a pragmatic consequence.

Here, we do not discuss in detail another parity-nonconservation effect in polarized neutron scattering by nuclei, the spin rotation φ of neutrons polarized transversely to their momentum. This effect is discussed in detail in [20]. Note only that an anomalously large angle of neutron spin rotation in the ^{204}Pb

isotope was detected experimentally [21]. However, the available experimental data contain no suitable p resonance in this isotope to explain the large P-odd effect of the compound-nucleus s- and p-state mixing by the electroweak interaction of nucleons. For this reason, it was hypothesized that there is an as yet experimentally undiscovered subthreshold neutron p resonance. Presently, the implications of this hypothesis are being studied experimentally and this resonance is being sought.

4. PARITY VIOLATION IN NUCLEAR FISSION BY POLARIZED NEUTRONS

This is one of the most interesting phenomena in nuclear physics. Its essence is that the escape probabilities of a fission fragment along and opposite to the initial neutron spin direction are different. The asymmetry is $\sim 10^{-4}$ [22]. The parity violation in fission is unusual in that this effect manifests itself in the motion of an almost macroscopic object, a fission fragment containing about 100 nucleons. To elucidate the mechanism of parity violation in fission, it is first necessary to understand how a two-particle electroweak interaction affects the essentially collective, virtually macroscopic motion of a system of heavy fragments. Yet another problem that casts doubt upon the correctness of the first experimental result is related to the large number of fragment final states (more than 10^{10}). If the sign of the effect randomly depended on the system final state, as in the case of (n,γ) reactions, then the asymmetry in the escape of fission fragments would be strongly suppressed in an experiment where all final states are recorded almost simultaneously. Therefore, it was necessary to elucidate why this effect does not disappear when averaged over the fragment final states. An attempt to phenomenologically describe the formulated problems was made in [23]. Thus, the essence of the parity-violation effects in nuclear fission by polarized neutrons is as follows. Fission is quite a peculiar process. Although many degrees of freedom were excited at the beginning and at the end of the process, the fission proceeds through a small number of intermediate collective states, fission channels. This result has long been known in nuclear physics [24]. In contrast to the (n,γ) process, fission is a process with a small number of channels, because the fission widths obey the Porter–Thomas distribution and this distribution is broad. For a large number of degrees of freedom, this distribution would be narrow, as in the case of the radiative-width distribution. The P-odd effect of fragment asymmetry in fission (just as the ordinary P-even effects) is formed precisely at the intermediate ("cold") fission stage. At this stage, the nucleus is a pear-shaped top. In other words, a strongly deformed nucleus consists of two clusters with different masses close in magnitude to the masses of nuclei with filled shells. Asymmetry in the fragment escape direction arises from the mixing of rotational levels of opposite parity, which exist in such a system. In this case, the rotational states are mixed by the universal mechanism [15] of electroweak interaction at the compound-nucleus stage. The transfer of P-odd mixing from one stage to another is related to a small uncertainty in the energy of the excited nucleus. This makes it possible to separate out the time dependence in the total wave function and, thereby, to prevent the forgetting of the initial stage. Based on this universal mechanism, which takes into account the dynamical enhancement in the compound nucleus, we obtained an estimate that is in agreement with experiment.

Unfortunately, the uncertainty in the population of spin states for the compound ^{234}U, ^{236}U, and ^{240}Pu nuclei and the lack of information on the fission channels prevent an unambiguous comparison of experimental data with model predictions. However, under certain assumptions, the model correctly describes the sign of the effect and its relative magnitude, despite the complex dynamics of the fission process and its distinct collective nature.

5. CONCLUSION

The P-odd effects in the electroweak interaction of neutrons with nuclei considered here are of considerable interest in nuclear physics. Their study provides a deeper insight into the complex structure of the nucleus and its excited states. In investigating such an essentially many-particle system as the nucleus with its "many-sided" structure, the main problem is probably to establish which concepts and degrees of freedom correspond to the phenomena being observed. Success in this direction can be achieved by using experimental data, a theoretical analysis of model systems, and general relations based on the fundamental symmetries.

At present, the possibilities for extracting information on the fundamental electroweak nucleon–nucleon interaction from data on the P-odd effects in nuclear physics are somewhat limited. The reason is that the effects under discussion can be observed with relative ease only in intermediate-mass and heavy nuclei. In these nuclei, the dynamical enhancement of the compound-nucleus state mixing and the additional resonant enhancement (12) in the entrance channel due to the proximity of the compound-nucleus p-wave resonance are large. Thus, the enhancement effects, on one hand, facilitate the experimental observation of P-odd effects by making them large, and, on the other hand, they make

it difficult to extract information on the fundamental electroweak interaction of nucleons.

Nevertheless, such studies yielded the matrix elements from the effective Hamiltonian for the electroweak interaction of nucleons. The model for the compound-nucleus state mixing by electroweak interaction is undoubtedly appealing in that, in this model, one can trace the magnitude of the P-odd effects from the value determined by the fundamental constant (3) to the experimentally expected value of the effect defined by Eqs. (10)–(12).

Despite the complex structure of compound-nucleus states, one might expect certain statistical information on the details of the electroweak interaction of nucleons in nuclei to be obtained with the accumulation of experimental data.

The splendid beauty of nature did not fade after the discovery of strong mirror-symmetry violation in nuclear physics. This violation is not a flaw of nature but more likely evidence of its puzzling perfection and astounding beauty!

ACKNOWLEDGMENTS

I am grateful to Yu.G. Abov for the long-term fruitful collaboration in the studies of parity nonconservation in nuclear physics. V.V. Vasiliev, A.D. Gul'ko, O.N. Ermakov, I.L. Karpikhin, P.A. Krupchitsky, A.L. Suvorov, and other coworkers join in this gratitude in connection with Abov's birthday.

This work was supported by the Russian Foundation for Basic Research, project no. 01-02-16024.

REFERENCES

1. Yu. G. Abov, P. A. Krupchitsky, and Yu. A. Oratovsky, Phys. Lett. **12**, 25 (1964).
2. E. Wigner, Z. Phys. **43**, 624 (1927).
3. E. M. Henley, Annu. Rev. Nucl. Sci. **19**, 367 (1969).
4. I. S. Shapiro, Usp. Fiz. Nauk **95**, 361 (1968).
5. R. J. Blin-Stoyle, *Fundamental Interactions and the Nucleus* (North-Holland, Amsterdam, 1973).
6. G. A. Lobov, At. Energy Rev. **12**, 505 (1974).
7. G. A. Lobov, Yad. Fiz. **30**, 1353 (1979) [Sov. J. Nucl. Phys. **30**, 703 (1979)].
8. B. Desplanque, J. F. Donoghue, and B. R. Holstein, Ann. Phys. (N.Y.) **124**, 449 (1980).
9. G. A. Lobov, Nucl. Phys. A **577**, 449 (1994).
10. B. Desplanque, Phys. Rep. **297**, 1 (1998).
11. L. B. Okun, *Leptons and Quarks* (Nauka, Moscow, 1990; North-Holland, Amsterdam, 1984).
12. Yu. G. Abov and P. A. Krupchitskiĭ, Usp. Fiz. Nauk **118**, 141 (1976) [Sov. Phys. Usp. **19**, 75 (1976)].
13. V. A. Rodin and M. G. Urin, Fiz. Élem. Chastits At. Yadra **31**, 976 (2000).
14. P. A. Krupchitsky, *Fundamental Investigations with Polarized Slow Neutrons* (Énergoatomizdat, Moscow, 1985).
15. V. A. Karmanov and G. A. Lobov, Pis'ma Zh. Éksp. Teor. Fiz. **10**, 332 (1969) [JETP Lett. **10**, 212 (1969)]; G. A. Lobov, Izv. Akad. Nauk SSSR, Ser. Fiz. **34**, 1141 (1970).
16. V. P. Alfimenkov, S. B. Borzakov, Vo Van Tkhuan, *et al.*, Pis'ma Zh. Éksp. Teor. Fiz. **34**, 308 (1981) [JETP Lett. **34**, 295 (1981)]; **35**, 42 (1982) [**35**, 51 (1982)].
17. E. A. Kolomensky, V. M. Lobashev, A. V. Pirozhkov, *et al.*, Phys. Lett. B **107B**, 272 (1981).
18. V. P. Alfimenkov, Usp. Fiz. Nauk **144**, 361 (1984) [Sov. Phys. Usp. **27**, 797 (1984)]; S. J. Seestrom, in *Time Reversal Invariance and Parity Violation in Neutron Reactions,* Ed. by C. R. Gould (World Sci., Singapore, 1993), p. 220; V. A. Karmanov and G. A. Lobov, Nauka SSSR **6**, 1 (1988); Yu. G. Abov, in *Proceedings of the First Moscow International School in Physics at the Institute of Theoretical and Experimental Physics, Zvenigorod, 1998* (Usp. Fiz. Nauk, Moscow, 1999), p. 9; Usp. Fiz. Nauk **166**, 949 (1996) [Phys. Usp. **39**, 891 (1996)].
19. S. A. Biryukov, Yad. Fiz. **45**, 1511 (1987) [Sov. J. Nucl. Phys. **45**, 937 (1987)].
20. G. A. Lobov, Yad. Fiz. **63**, 1465 (2000) [Phys. At. Nucl. **63**, 1387 (2000)].
21. V. P. Bolotsky, O. N. Ermakov, R. Golub, *et al.*, Yad. Fiz. **59**, 1873 (1996) [Phys. At. Nucl. **59**, 1808 (1996)].
22. G. V. Danilyan, B. D. Vodennikov, V. P. Dronyaev, *et al.*, Pis'ma Zh. Éksp. Teor. Fiz. **26**, 197 (1977) [JETP Lett. **26**, 186 (1977)]; G. V. Danilyan, Usp. Fiz. Nauk **131**, 329 (1980) [Sov. Phys. Usp. **23**, 323 (1980)].
23. O. P. Sushkov and V. V. Flambaum, Usp. Fiz. Nauk **136**, 3 (1982) [Sov. Phys. Usp. **25**, 1 (1982)].
24. A. Bohr and B. R. Mottelson, *Nuclear Structure*, Vol. 1: *Single Particle Motion* (Benjamin, New York, 1969; Mir, Moscow, 1971).

Translated by S. Slabositsky

Physics of Atomic Nuclei, Vol. 65, No. 11, 2002, pp. 1985–1994. Translated from Yadernaya Fizika, Vol. 65, No. 11, 2002, pp. 2042–2051.

REVIEWS

Methods for Investigating Nuclear Matter under the Conditions Characteristic of Its Transition to Quark–Gluon Plasma

G. A. Leksin

Institute of Theoretical and Experimental Physics,
Bol'shaya Cheremushkinskaya ul. 25, Moscow, 117259 Russia

Received February 7, 2002

Abstract—We briefly consider the properties of deep inelastic nuclear reactions on dense fluctuations of nuclear matter (fluctons). We discuss the properties of the fluctons, which can be many-quark bags or "drops" of quark–gluon plasma: the characteristic parameters of nuclear matter in a flucton—temperature and density close to the critical values for a phase transition. These values can be reached or exceeded if the flucton–flucton collision events are separated out. The separation method is discussed.

1. INTRODUCTION

Recently, it has been announced that quark–gluon plasma (QGP) was discovered at CERN in collisions between beams of high-energy accelerated ions. The idea of colliding-beam experiments is to produce a high pion density in the volume of colliding nuclei, which can (and even must, according to current views) give rise to QGP. Figure 1 shows the state diagram for nuclear matter with the normalized density ρ/ρ_0 plotted against temperature T_0, where ρ_0 is the nuclear density of the order of 0.17 of the nucleon density; the curve is the expected boundary of transition to QGP.

Here, we will not discuss the question of whether QGP was discovered in CERN experiments or not. Undoubtedly, there are some features (a decrease in the cross section for the production of J/ψ mesons, an enhanced production probability of strange particles) that may suggest a transition to QGP. Let us discuss other possibilities for the formation of QGP and consider the features that accompany this formation.

The idea is to analyze in detail the so-called deep inelastic nuclear reactions (DINRs), which have been studied for 35 years [1]. The well-known properties of the DINRs led the authors of [2, 3] to hypothesize some ten years ago that these reactions take place when incident particles interact with dense fluctuations of nuclear matter (fluctons). Fluctons can be excited to a temperature sufficient for their transition to QGP. In other words, the fluctons are "drops" of QGP [3].

In this paper, we consider the place of DINRs among other nuclear reactions and their properties that allowed them to be represented as the interaction of particles with fluctuations of nuclear matter (fluctons) as well as the properties of the fluctons as drops of QGP. The last section of this paper is devoted to separating out the flucton–flucton interaction events in collisions of accelerated nuclei with target nuclei. Here, one might expect the density of the nuclear matter to double in the interaction region and a more confident phase transition to QGP.

2. DEEP INELASTIC NUCLEAR REACTIONS

There is elastic diffraction scattering of an incident particle by a nucleus with low momentum transfers known as forward scattering. Occasionally, it is accompanied by the excitation of the nucleus followed by its deexcitation or even breakup, which is generally described in terms of evaporation. At energies $\geq$100 MeV, there is quasi-elastic or, better to say, quasi-free scattering of incident particles by isolated, almost free nucleons; their interaction reduces to their motion in the mean field of the nucleus with the corresponding Fermi momenta. There

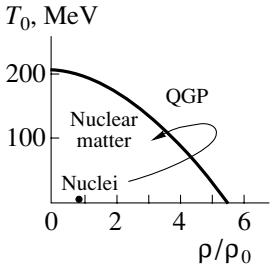

Fig. 1. The state diagram for nuclear matter: the density ρ/ρ_0 normalized to the nuclear density versus temperature T_0. The curve is the expected boundary of a phase transition to QGP.

1063-7788/02/6511-1985$22.00

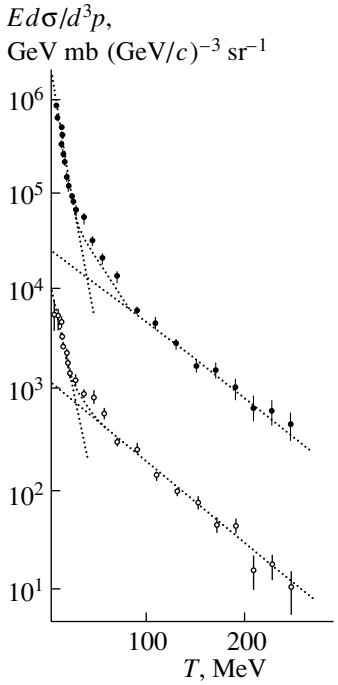

Fig. 2. The energy dependence of the invariant function for the neutrons escaping from lead (closed circles) and carbon (open circles) at an angle of 119° in the laboratory frame under the action of protons with energy of 7.5 GeV.

is a more delicate process: backward elastic scattering of the proton by the nucleus as a whole, for example, $pd \to dp$, when the proton flies backward in the laboratory frame, while the deuteron flies forward with a high momentum and energy, which is hundreds of times higher than the deuteron binding energy. Quasi-elastic knockout of fast deuterons from nuclei is also known. The concept of fluctons was introduced precisely when describing this phenomenon. Of course, inelastic scattering by fluctons, which leads to excitation and fragmentation, is also possible. It is precisely these processes, which, as we will see below, proceed at the quark level, that are called DINRs.

All of the above processes have distinctive features: for example, the diffraction nature of the elastic scattering by nuclei noted above; distinct maxima in the momentum spectra of the particles from quasi-elastic scattering and a weak (as $A^{1/3}$) dependence of the cross sections for these processes on the atomic number of the nucleus; rapidly decaying backward elastic scattering with increasing initial energy; isotropy in the rest frame of the nucleus of soft (up to 40–50 MeV) nucleons in evaporation; etc. The DINRs also have a number of characteristic remarkable features, which are dealt with below. Let us consider a simple example of DINRs.

Figure 2 shows a typical inclusive energy spectrum of the nucleons (to be more precise, the invariant function $f = Ed\sigma/d^3p$, where $Ed\sigma/d^3p$ is the cross section per unit phase volume and E is the total energy of the outgoing particle) emitted at a fixed angle $\theta \geq 90°$ in the laboratory frame. More specifically, Fig. 2 shows the spectrum of the neutrons (these were easier to record at low kinetic energies T than protons) escaping from Pb and C nuclei at an angle of 119° under the action of protons with an energy of 7.5 GeV. We see that the data are satisfactorily fitted by two decreasing exponential functions (the scale along the vertical axis is logarithmic). The left exponential function is parametrized by $f = Ce^{-T/T_0}$, where $T_0 \sim 5$–8 MeV, i.e., of the order of the binding energy of the nuclei. This function commonly represents the evaporation spectrum. The right exponential function has an order of magnitude smaller slope and, hence, cannot refer to evaporation (or some preequilibrium process that is probably responsible for an excess of events at 50–60 MeV) and describes the DINRs. No scattering by an object at rest (or with Fermi momentum) can generate such nucleons. They can be generated in collisions with objects of mass d, t, etc. Each nucleon kinetic energy T can be associated with a minimum mass with which an incident particle must collide in order that the secondary particle could have the recorded energy at a given escape angle. The required minimum mass, in units of the nucleon mass m_N, is called a cumulative number, and the escaping particles are called cumulative particles. By kinematically separating the cumulative particles, we can study the DINRs and their properties under "pure" conditions without interference from other processes.

Of course, in the kinematic domain under consideration, which is forbidden for the production of particles on individual nucleons, there could be particles from backward elastic scattering by structures with cumulative integer numbers $2, 3, \ldots$. However, their traces are generally unseen in the studied spectra at high energies. We actually deal with inelastic nuclear reactions, and the cumulative numbers apparently change continuously.

Clearly, the cumulative-particle spectrum must be bounded by the incident-particle energy (or, more precisely, by the energy left by the incident particle in the nucleus). Hence, it cannot extend beyond the cumulative numbers larger than A for the target nucleus. Naturally, these boundary effects "spoil" the exponential dependence, and they should be taken into account in studying the DINR properties. In practice, the "vanishing" of the phase space on the right has little effect for heavy targets and secondary-particle momenta up to 1–2 GeV/c.

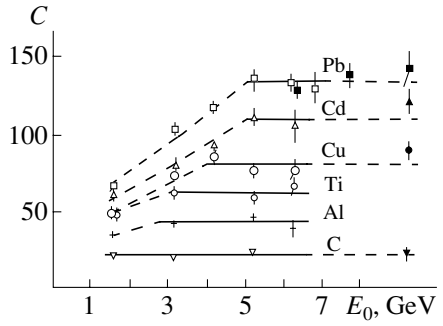

Fig. 3. The coefficient $C(T_0 = 125$ MeV) in the parametrization of the invariant function $f = C\exp(-T/T_0)$ in the reaction pA(C, Al, Ti, Cu, Cd, Pb) $\to pX$ for a proton escape angle of 120° in the laboratory frame versus the incident-proton energy. The filled circles refer to the initial energy of 400 GeV.

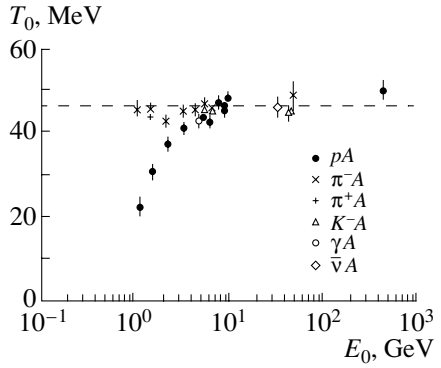

Fig. 5. Dependence of the slope parameter T_0 for the invariant function of the protons escaping under the action of $p, \pi^{\pm}, K^-, \gamma, \bar{\nu}$ with various energies E_0; the escape angle is 120° in the laboratory frame.

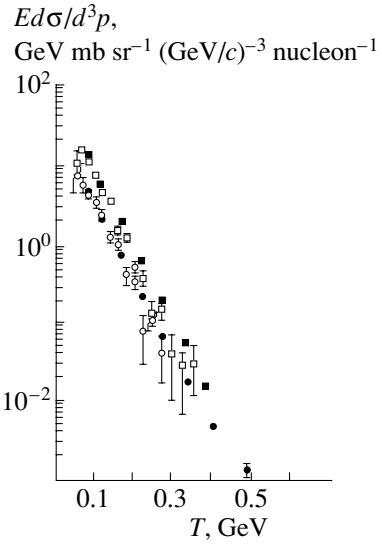

Fig. 4. The invariant functions for protons per nucleon that escape from the C (○, ●) and Cu (□, ■) targets under the action of protons with energies of 400 (●, ■) and 7.5 GeV (○, □); the escape angles are 160° and 162°, respectively.

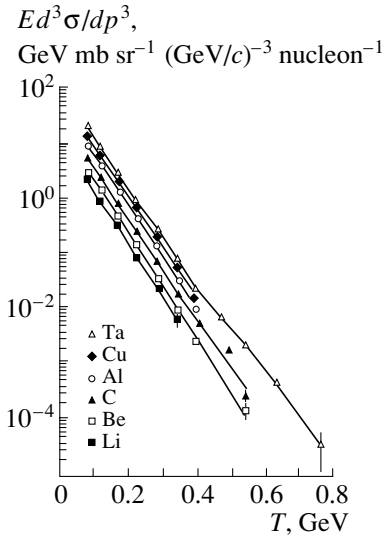

Fig. 6. The proton invariant functions normalized to the number of nucleons in the target nucleus for various nuclei (Li, Be, C, Al, Cu, Ta); the proton escape angle is 160°. The energy of the incident protons is 400 GeV.

The spectrum shown in Fig. 2 extends to 250 MeV. In what follows, we present the spectra of the particles escaping with energies up to 3 GeV; i.e., the DINRs take place at large momentum transfers, suggesting that the reactions proceed at the quark level. The flucton is a quark structure rather than a nucleon one. Indeed, the nucleon momentum in the nucleus can be ~ 1 GeV/c if two nucleons come within a distance of $\sim 1/7$ fm between their centers. The nucleons are compressed or, better to say, pressed into one another. For this reason, it seems illegitimate to talk, as is occasionally done, about the interaction of an incident particle with an isolated nucleon moving with a large momentum (~ 1 GeV/c) in the flucton.

3. DINR PROPERTIES: NUCLEAR SCALING AND SUPERSCALING

Thus, we can separate the DINRs purely kinematically and study their properties in detail. These properties are unexpected and peculiar. Here, we mention and comment only on those properties that are related to superdense states.

First, we deal with the properties called "nuclear scaling." If the inclusive spectrum of the cumulative particles from the reaction $a + A \to b + X$ at a fixed angle is fitted by the function $f = Ed\sigma/d^3p =$

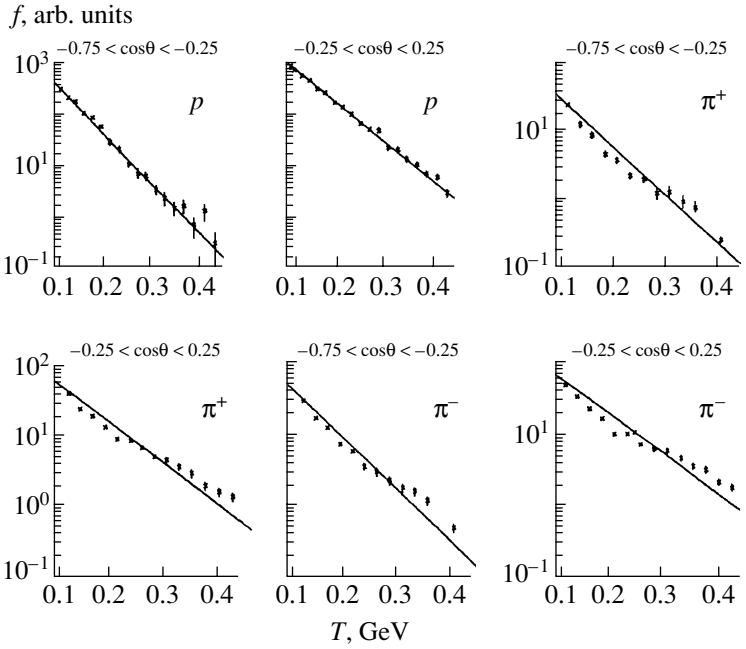

Fig. 7. Comparison of the invariant functions for the protons and $\pi^{\pm}$ mesons produced in the reactions $e^{16}\mathrm{O} \to p(\pi^{\pm})X$ (points) and $p\mathrm{C} \to p(\pi^{\pm})X$ (solid lines); the initial electron energy is 5 GeV.

Ce^{-T/T_0}, as was done above (see Fig. 2), then the nuclear scaling can be written as $C \neq C(E_0, a)$ and $T_0 \neq T_0(E_0, a, A)$, where E_0 is the incident-particle energy, a is the type of incident particle ($p, \pi^{\pm}, \nu, \gamma$, etc.), and A is the type of target nucleus; i.e., the parameters C and T_0 do not depend on these arguments. The figures that follow, whose number could be increased, show the properties of nuclear scaling.

In Fig. 3, the coefficient C is plotted against the initial proton energy in the reaction $p + A \to p + X$. The filled circles on the right indicate C for an initial energy of 400 GeV. We see that the coefficient C is not only constant with energy but also that the scaling is asymptotic, starting from a certain energy of the incident particles. A direct comparison of the proton yields from C and Cu nuclei at energies 7.5 and 400 GeV can be seen in Fig. 4.

Figure 5 shows that T_0 is independent of E_0, a, and A. Here, we also see, starting from some energy, the scaling behavior for the protons escaping at a fixed angle of 120° in the laboratory frame under the effect of various primary particles and various nuclei. Of course, the equality of the slopes for the proton

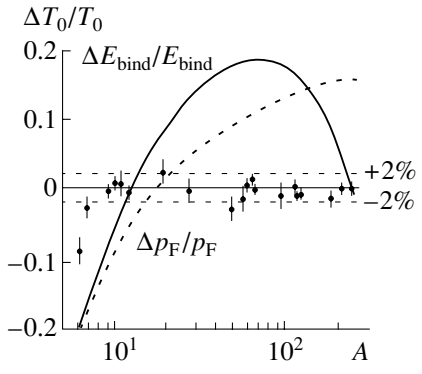

Fig. 8. Slope of the proton invariant function normalized to the mean slope versus atomic number A of the target nucleus: binding energy versus A (solid curve) and Fermi momentum normalized to the mean Fermi momentum versus A (dashed curve).

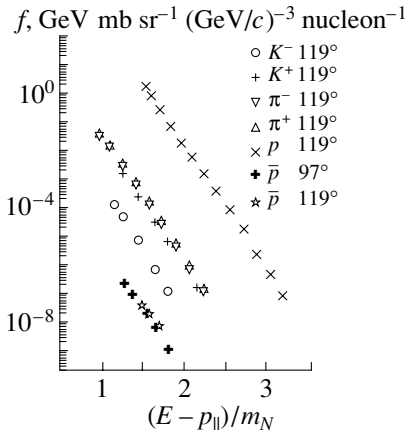

Fig. 9. Invariant functions of the protons, $\pi^{\pm}$ mesons, $K^{\pm}$ mesons, and antiprotons escaping from Cu at an angle of 119° in the laboratory frame for initial energy of 10 GeV versus light-cone variable $(E - p_{\|})/m_N$.

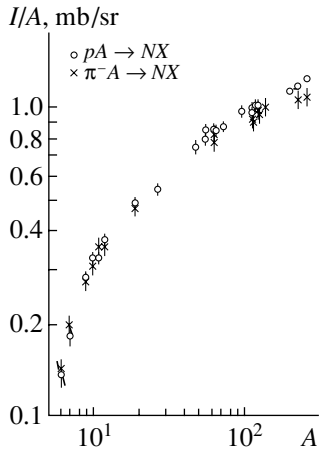

Fig. 10. A dependence of the nucleon yields normalized to the number of nucleons in the target nucleus escaping at an angle of 120° in the reactions $p(\pi^-)A \to NX$. The energies of the incident protons and π^- mesons are 7.5 and 5 GeV, respectively.

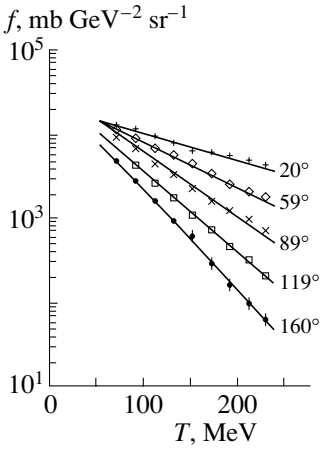

Fig. 11. Invariant functions of the protons escaping from Pb at an initial energy of 7.5 GeV; the escape angles are 20°–160°.

spectra from C and Cu nuclei is also seen in Fig. 4, where the incident particles are protons with energies of 7.5 and 400 GeV. Figure 6 also shows that, at 400 GeV, the slopes of the proton spectra are constant for different nuclei. (Some discrepancy between the curves at high secondary energies of the protons escaping from light nuclei and, hence, at large cumulative numbers has already been discussed above as resulting from the effect of the kinematic boundary.) The proton invariant functions and angular distributions of charged $\pi^\pm$ mesons in the reactions $pA \to p(\pi^\pm)X$ and $eA \to p(\pi^\pm)X$ are compared in Fig. 7. Finally, a careful numerical comparison of the parameters T_0 for different nuclei using data obtained in one experiment under identical conditions for the central part of the spectrum underlies Fig. 8. This figure shows a plot of $\Delta T_0/T_0$ against A, where T_0 is the value averaged over A. We see that T_0 is constant with an accuracy higher than 2%. For comparison, the figure also shows the A dependence of the relative binding energy E_{bind} of the nucleus and the relative mean Fermi momentum p_{F}. Apart from the invariance of T_0, the sharp difference between the behavior of the spectral slopes and the behavior of the binding energy and the Fermi momentum allows them to be attributed to different objects: E_{bind} and p_{F} to the properties of nuclear matter and T_0 to the properties of nuclear-matter fluctuations (fluctons). This means that we study not specific nuclei but fluctons in different nuclei whose distribution in cumulative number proves to be similar.

We demonstrated the scaling properties using secondary protons as an example, although they are also valid for other secondary particles. Thus, in Fig. 7, they were shown not only for protons but also for $\pi^\pm$ mesons escaping in the reactions $hA \to h(\pi^\pm)X$ and $eA \to p(\pi^\pm)X$ [4]. We see from comparison of the neighboring figures that the proton and pion spectra have identical slopes. The slope of the spectrum for cumulative Λ particles is known [5] to be the same as that of the neutron spectrum. Figure 9 [6] was particularly impressive. It shows the behavior of the invariant functions for protons and antiprotons as well as positively and negatively charged pions and kaons as a function of the light-cone variable $(E - p_\parallel)/m_N$. (The spectral slope in light-cone variable asymptotically coincides with the slope T_0 in kinetic energy of the secondary particles and with the spectral slope in cumulative number). The properties being demonstrated were even called "superscaling." These include the following properties:

(1) $T_0 \neq T_0(b)$—the spectral slope T_0 does not depend on the type of escaping particle.

(2) The yields of π^+ and π^- are equal.

(3) The yields of K^+ and π^+ are equal.

(4) There is an hierarchy of yields that fits well into the dependence of the yields of sea quarks (including strange quarks) in the secondary particle. The hierarchy of yields is a clear indication that the DINRs proceed at the quark level.

Thus, the DINRs are characterized by an invariant quantity T_0 or, in other words, by a shift symmetry in variables E_0, A, a, b—independence of the initial particle energy and of the types of target nucleus, incident and escaping particles. The manifestations of the above symmetries in interactions of a hadron with chaotic structures (fluctons) can also be surprising.

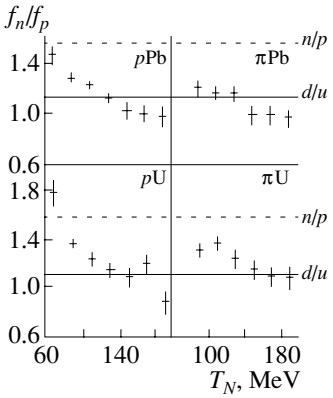

Fig. 12. The ratio of the neutron and proton yields from isononsymmetric Pb and U nuclei versus the kinetic energy of the escaping nucleons; the escape angle is 120° and the initial energy is 7.5 GeV for protons and 5 GeV for pions. The $\pi^{\pm}$ data are averaged. The dashed lines represent the neutron-to-proton ratio in the target nuclei, and the solid lines represent the d/u-quark ratio in the Pb and U nuclei.

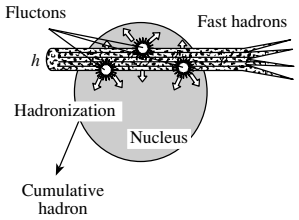

Fig. 13. A scenario for the successive interaction of an incident particle with fluctons along its trajectory in the nucleus (see text).

4. OTHER DINR PROPERTIES

The invariant functions of DINRs have a strong A dependence (Fig. 10), which, strictly speaking, cannot be parameterized in the form A^{α} (a linear dependence on a logarithmic scale along both axes). However, if this parameterization is, nevertheless, made (as is commonly done), then it turns out that $\alpha > 1$. This behavior should be compared with the dependence $A^{1/3}$ characteristic of quasi-free processes at low momentum transfers on the periphery of the nucleus. In other words, the contribution of particles from fluctons dominates for heavy nuclei when the particles escape from nuclei forward at cumulative numbers < 1. This makes it possible to compare, for example, the spectra of the protons from Pb over a wide range of angles (see Fig. 11). To a first approximation, all spectra can be described by the same expression $f = \exp\{-T(1 - \beta_{fl}\cos\theta)/T_0\}$ with the parameter T_0, which conserves the symmetry properties. This dependence can be interpreted as the escape of a massless or almost massless particle (a quark) from a system moving at velocity β_{fl}, from which particles escape isotropically with the same characteristic value of $T_0 \cong 100$ MeV. Thus, T_0 characterizes the fluctons rather than the spectrum at a certain escape angle.

Isosymmetrization is yet another property of the DINRs. The ratio of the neutron and proton yields from isononsymmetric heavy Pb and U nuclei is shown in Fig. 12. It is much smaller than the neutron-to-proton ratio in the target nuclei ($\sim$1) and close to the ratio of the numbers of d to u quarks in the nuclei. The question arises as to whether this is an indication of fluctons isosymmetrization or further evidence that the reaction proceeds at the quark level. The Coulomb interaction may be, however, operative. A detailed discussion of this problem can be found in [7].

Above, we discussed the properties of the DINRs established in inclusive experiments. In DINRs with a large multiplicity of secondary particles, the exclusive approach is difficult to use and unpromising. However, a comprehensive study can be carried out by measuring the correlation functions of the particles

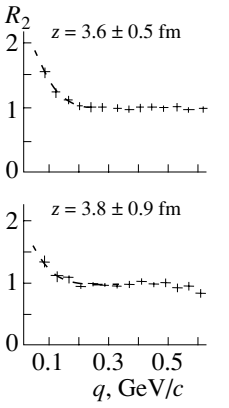

Fig. 14. The correlation function R_2 (see text) versus the relative momentum of a pair of $\pi^{\pm}\pi^{\pm}$ mesons from the reaction $e^{16}\mathrm{O} \to \pi^{\pm}\pi^{\pm}X$. The electron energy is 5 GeV.

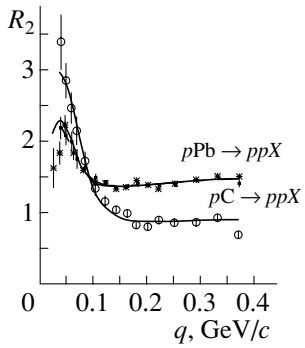

Fig. 15. The correlation functions of two protons from the reactions $p\mathrm{C} \to ppX$ (○) and $\mathrm{pPb} \to ppX$ (∗, ■) versus their relative momentum; the initial energy is 7.5 GeV.

escaping in DINRs. Here, we do not touch upon the results of studies of pair particle correlations in detail, in particular, the dependence of the correlation function

$$R_2 = \sigma_{\text{tot}} E_1 E_2 \times [d^2\sigma/(d^3p_1 d^3p_2)]/[(d\sigma/d^3p_1)(d\sigma/d^3p_2)] = \sigma_{\text{tot}} f_{1,2}(p_1p_2)/f_1 f_2$$

on the angle of separation of particles 1 and 2 with momenta p_1 and p_2, although the data obtained suggest that the DINRs arise from the excitation of fluctons along the trajectory of the incident particle in the nucleus [8]. The scenario for the DINRs is illustrated in Fig. 13. However, it should be said that the so-called narrow correlations between particles with low relative velocities or between identical particles with small relative momenta $q = p_1 - p_2$ were studied. These studies allow us to determine the space-time region of particle escape, i.e., to judge the flucton size.

Figure 14 shows a plot of the correlation function for pairs of pions from the reactions $e^{16}\text{O} \to \pi^\pm\pi^\pm X$ [4] against the relative momentum of pairs of identical pions. We clearly see a manifestation of Bose symmetrization for $q \to 0$. The Fourier transform of the q dependence is known to determine the spatial characteristic of the pion emission region r. In this specific case, we obtain the characteristic size of the ^{16}O nucleus or, more precisely, the mean distance between fluctons in the nucleus. The derived values of r are determined by this distance rather than by the flucton size (according to Fig. 13).

Figure 14 is one of many examples that illustrate the standard method of determining the spatial size of the interaction region proposed by Kopylov and Podgoretsky [9]. It is important that this method could be applied to the individual components $r_\parallel$ and $r_\perp$ if we measure $R(q_\parallel)$ at small $q_\perp$ and $R(q_\perp)$ at small $q_\parallel$.

The correlation functions for proton and neutron pairs can also be used to determine the sizes. In this case, however, we have to consider a more complex dependence of the correlation function on q. First, according to the Pauli exclusion principle, it decreases the value of the correlation function from 1 to 1/2 for unpolarized identical nucleons for $q \to 0$. The strong interaction causes an increase in the correlation function at small q. The electromagnetic interaction causes the correlation function for slow charged particles to become zero. The contributions are different for different pairs of particles. For example, for nn pairs, there is no electromagnetic interaction but the Pauli exclusion principle works, whereas, for np pairs, there is neither an electromagnetic interaction nor any effect of the Pauli exclusion principle. The correlation function for two protons from the reactions $p\text{C} \to ppX$ and $p\text{Pb} \to ppX$ at an initial incident-particle energy of 7.5 GeV is shown in Fig. 15 [10]. The total sizes $r = \sqrt{(r_\parallel^2 + r_\perp^2)}$ derived in describing these data (curves in Fig. 15) are 3.02 ± 0.4 and 5.42 ± 0.4 fm for C and Pb, respectively, and seem quite reasonable. However, of the above factors, only the Pauli exclusion principle gives an effect that depends separately on $r_\parallel$ and $r_\perp$ or the corresponding components of the relative momentum. For different $r_\parallel$ and $r_\perp$, the correlation functions must differ as in Fig. 16 [10], where the corresponding experimental data are presented. Two distributions are shown for the reaction $p\text{Pb} \to ppX$: one is plotted against $q_\perp$ at small $q_\parallel$ and the other is plotted against $q_\parallel$ at small $q_\perp$. We see that they differ. This implies that the region sizes in $r_\parallel$ and $r_\perp$ are different; the region is nonspherical in shape, and it has the shape of a tube along the trajectory of the incident particle (see Fig. 13). The processing of the data shown in Fig. 16 yielded the values for Pb: $r_\parallel \cong 5$ fm (on the order of the distance between the the emission centers for Pb) and $r_\perp \approx (1/3{-}1/4)r_\parallel$. The value of $r_\perp$ limits the flucton size from above.

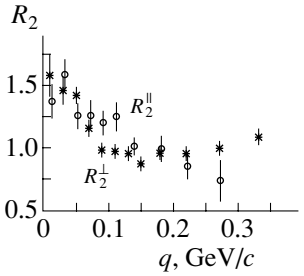

Fig. 16. The correlation functions of two protons from Pb at an initial energy of 7.5 GeV versus the longitudinal relative momentum at small transverse momentum (○) and versus the transverse relative momentum at small longitudinal momentum (∗).

5. THE FLUCTON PROPERTY: THE FLUCTON IS A DROP OF QGP

Thus the above (and other independent) facts suggest that, in DINRs, the incident particle can interact with a fluctuation of nuclear matter, a flucton, which shows up as a small dense structure of several nucleons that lost their individuality. This is most likely a many-quark bag with blurred boundaries and with a density increasing with cumulative number.

For the flucton density to be estimated, we must know the flucton content and size. The content, the flucton mass in nucleon masses, is limited from below by the cumulative number. The flucton distribution in cumulative number is specified by the distribution of

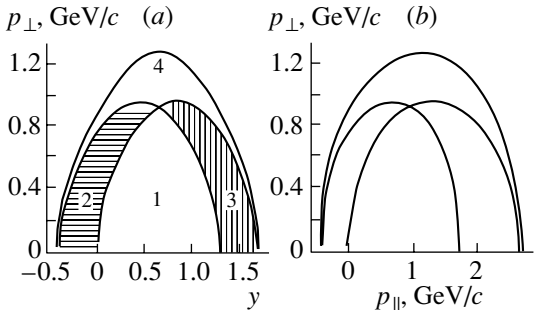

Fig. 17. Kinematic boundaries for the reactions $N + 2N \to N + X$, $2N + N \to N + X$, and $2N + 2N \to N + X$ in the coordinates y (speed) and $p_\perp$ (transverse momentum) for an initial energy of 1 GeV/nucleon (a); the same in the coordinates $p_\perp$ and $p_\parallel$ (b). Region 1 is filled with nucleons from the reactions $N + N \to N + X$, $N + 2N \to N + X$; region 2 is filled with nucleons from the reaction $N + 2N \to N + X$; region 3 is filled with nucleons from the reaction $2N + N \to N + X$; and region 4 is filled with nucleons from the reaction $2N + 2N \to N + X$.

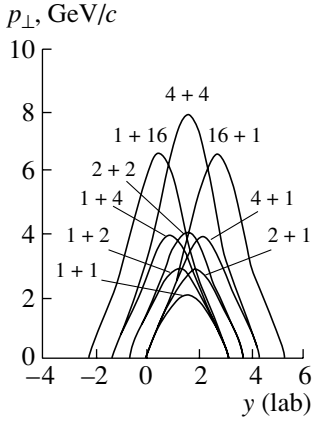

Fig. 18. Kinematic boundaries similar to those in Fig. 17*a* for the *flucton* + *flucton* $\to pX$ reaction at an initial energy of 10 GeV/nucleon. The numbers near the curves are the masses of the colliding fluctons, in nucleon masses.

the invariant function in this number, which is unambiguously related to the distribution of the invariant function in kinetic energy.

The flucton size has already been discussed above. The flucton was devised as an object with a size on the order of the nucleon size. Experimental data yield an estimate of $r_\perp = 1.2$–1.7 fm. One should take into account the fact that $r_\perp > r_\parallel$, because the incident particle touches and excites the fluctons near its trajectory. If $r_\parallel = r_N$, then the density of a fluctuation with the cumulative number 2 or 3 is a factor of 2 or 3 higher than the nucleon density and almost an order of magnitude higher than the nuclear density. It would be of great importance to know this density with a higher accuracy.

The flucton is a quark structure. This is probably confirmed by the ratio of the neutron and proton yields from isononsymmetric nuclei, and the hierarchy of the yields of $p, \pi^\pm$, $K^\pm$, and $\bar{p}$ particles from nuclei becomes clear. Indeed, no sea quarks are needed for the production of protons; one sea quark is needed for the production of pions and a K^+ meson; two sea quarks are needed for the production of a K^- meson; and three sea quarks are needed for the production of an antiproton. Figure 9 shows a surprising phenomenon: the yields of cumulative pions and K^+ mesons are equal, which corresponds to an effective enhancement of strangeness. Occasionally, this phenomenon is considered as evidence of quark–gluon plasma.

Can we speak about the flucton as a drop of QGP? As was said in Section 4, there is a reference frame in which the slope of the cumulative-particle spectrum does not depend on the particle escape angle; i.e., the spectra can be interpreted as evaporation ones with a temperature $T_0 \approx 100$ MeV. At such a temperature and at the density estimated above, the flucton phase positions are beyond or near the phase-transition boundary.

As has been noted above, the temperature does not depend on the incident energy—there is an analogy with a first-order phase transition. The other shift symmetries noted above should also be recalled. All secondary particles have equal slopes and, hence, equal temperatures. They are thermalized, which is the most surprising thing for fluctuations. In general, temperature characterizes equilibrium systems. However, the equality between the temperatures of different components is commonly considered to be an indicator of equilibrium. The width of the energy range occupied by the phase transition is surprising. It is possible that these are the properties of nonequilibrium nonlinear multiparticle systems.

It appears that the plasma to be observed (or that has been observed) at CERN in collisions of energetic ions differs from that in the fluctuations that play a role in the DINRs. Here, the plasma is most likely a baryon-saturated one. Other plasma characteristics can also differ, but the regions on the phase diagram in Fig. 1 occupied by them are close.

6. DOUBLY CUMULATIVE PRODUCTION

Although the DINRs have been studied for many years, they undoubtedly deserve a further analysis from different perspectives, which were partially touched upon here. Let us consider the possibility of studying the doubly cumulative processes that can take place in flucton–flucton collisions, which must give rise to clusters of matter of an even higher density than the density of an individual flucton.

Characteristics of the recorded proton for the reaction $dd \to pt$ and an initial deuteron energy of 1 GeV/nucleon (θ, p, and T_p and E_p are given in angular degrees, GeV/c, and GeV, respectively)

θ_{CM}	$p_\parallel$(lab)	y	$p_\perp$	T_p(lab)	$p_\parallel$(CM)	E_p(CM)	θ_{lab}
0.0000	2.6956	1.5424	0.0000	2.8548	1.2543	1.5674	0.0000
15.0000	2.6427	1.4802	0.3246	2.8236	1.2115	1.5674	7.0032
30.0000	2.4876	1.3292	0.6271	2.7322	1.0862	1.5674	14.1497
45.0000	2.2409	1.1447	0.8869		0.8869	1.5674	21.5928
60.0000	1.9194	0.9557	1.0862	2.3974	0.6271	1.5674	29.5069
75.0000	1.5450	0.7702	1.2115	2.1768	0.3246	1.5674	38.1031
90.0000	1.1432	0.5876	1.2543	1.9400	0.0000	1.5674	47.6536
105.0000	0.7414	0.4051	1.2115	1.7032	−0.3246	1.5674	58.5366
120.0000	0.3669	0.2195	1.0862	1.4826	−0.6271	1.5674	71.3341
135.0000	0.0454	0.0305	0.8869	1.2932	−0.8869	1.5674	87.0675
150.0000	−0.2013	−0.1539	0.6271	1.1478	−1.0862	1.5674	107.7937
165.0000	−0.3564	−0.3049	0.3246	1.0564	−1.2115	1.5674	137.6678
180.0000	−0.4093	−0.3671	0.0000	1.0252	−1.2543	1.5674	179.9995

How can the doubly cumulative production be distinguished? Is there a kinematic region for the reaction $A + A \to h + X$ to which only flucton–flucton collisions that do not reduce to nucleon–flucton collisions can contribute? It turns out that this kinematic region exists.

The kinematic regions for the inelastic reactions

$$N + 2N \to N + \mathrm{X}, \quad (1)$$

$$2N + N \to N + X, \quad (2)$$

$$2N + 2N \to N + X, \quad (3)$$

where N is the nucleon, are shown in Fig. 17a; here, y is the speed and $p_\perp$ is the transverse momentum of the escaping particle (proton in the case being considered). The curves in the figure were calculated for the reactions $pd \to pd$, $dp \to pd$, and $dd \to pt$, respectively. Region 1 is filled with nucleons from the reaction (1) and with nucleons from the inelastic reaction $N + N \to N + X$; region 2 is filled with particles from the reaction (1); region 3 is filled with particles from the reaction (2); regions 2 and 3 are the zones of cumulative particle production. Region 4 corresponds mainly to large transverse nucleon momenta. Only doubly cumulative nucleons from the reaction $2N + 2N \to N + X$ can fall into this region. If the incident particle (deuteron and target) is also a deuteron, then the detection of events in region 4 is evidence of a doubly cumulative process.

Figure 17a was constructed for the proton escape from the reaction of a collision between two fluctons composed of two nucleons each at an initial energy of 1 GeV/nucleon. Similar curves were drawn for the escape of pions, nucleon pairs, and so on at various initial energies. For example, Fig. 18 shows the results of our calculations at an initial energy of 10 GeV/nucleon. We see that, in this case, one must record large transverse momenta of the escaping nucleon to fall into the region of doubly cumulative nucleon production. We also see that the region of $(2N + 2N)$ scattering can overlap with the region of the inelastic reaction $N + 4N$, let alone $N + 16N$ or $16N + N$. However, the production of pure, virtually backgroundless, double cumulative particles from $(4N + 4N)$ interactions in $(A + A)$ collisions is also possible in this case. The $(N + 16N)$ and $(N + 4N)$ events are both unlikely. However, to get rid of the background, we can always choose light incident and target nuclei.

The presentation of the reaction kinematical boundaries in the $y, p_\perp$ coordinates is traditional, because these are invariant quantities. However, in designing experiments, it is more convenient to use a presentation in the $p_\perp$, $p_\parallel$ coordinates, because, in this case, the range of angles for measuring the hadron spectra from the cumulative and doubly cumulative regions is clearly seen. In our case, this angle is $\sim 40°$. The spectrum should be measured precisely at this angle, crossing the boundary of single cumulative production. As an example, the table gives a summary of all characteristics for the recorded particle in the

case considered in Fig. 17. The region convenient for measurements is highlighted.

Of course, the doubly cumulative effect must exist. We already know from comparison of the antiproton escapes from nuclei bombarded by protons and deuterons [11] that the doubly subthreshold phenomenon exists. The following questions arise: What are the specific properties of the flucton–flucton interaction? Do the slopes of the inclusive spectra change when crossing the kinematic boundaries? How is the concept of nuclear scaling modified? What is the A dependence of the reaction? etc. Finally, it is of interest to know how the attainment of a high density affects the QGP properties and how the QGP properties are related in doubly cumulative production and in the attainment of the same density through an increase in the cumulative-particle momenta at fixed angles in hA, i.e., at large cumulative numbers.

REFERENCES

1. Yu. D. Bayukov *et al.*, Izv. Akad. Nauk SSSR, Ser. Fiz. **30**, 521 (1966).
2. V. S. Stavinskiĭ, Fiz. Élem. Chastits At. Yadra **10**, 949 (1979) [Sov. J. Part. Nucl. **10**, 373 (1979)].
3. V. B. Gavrilov, G. A. Leksin, S. M. Shuvalov, and K. Sh. Egian, Nucl. Phys. A **532**, 321 (1991).
4. P. V. Degtyarenko *et al.*, Z. Phys. A **350**, 263 (1994).
5. L. S. Vorob'ev *et al.*, Yad. Fiz. **53**, 732 (1991) [Sov. J. Nucl. Phys. **53**, 458 (1991)].
6. S. V. Boyarinov *et al.*, Yad. Fiz. **57**, 1452 (1994) [Phys. At. Nucl. **57**, 1379 (1994)].
7. L. S. Vorobyev, G. A. Leksin, and A. V. Stavinsky, Yad. Fiz. **59**, 694 (1996) [Phys. At. Nucl. **59**, 662 (1996)].
8. A. V. Vlasov *et al.*, Yad. Fiz. **58**, 669 (1995) [Phys. At. Nucl. **58**, 613 (1995)].
9. G. I. Kopylov and M. I. Podgoretskiĭ, Yad. Fiz. **15**, 392 (1972) [Sov. J. Nucl. Phys. **15**, 219 (1972)].
10. Yu. D. Bayukov *et al.*, Yad. Fiz. **50**, 1023 (1989) [Sov. J. Nucl. Phys. **50**, 638 (1989)].
11. Y. Sugaya *et al.*, Nucl. Phys. A **634**, 115 (1998).

Translated by R. Rogalyov

Physics of Atomic Nuclei, Vol. 65, No. 11, 2002, pp. 1995–1998. Translated from Yadernaya Fizika, Vol. 65, No. 11, 2002, pp. 2052–2055.

NUCLEI

Mechanism of Small Variations in Energy of Ultracold Neutrons Interacting with a Surface

E. V. Lychagin[1)], D. G. Kartashov[2)], A. Yu. Muzychka[1)], V. V. Nesvizhevsky[3)*], G. V. Nekhaev[1)], and A. V. Strelkov[1)]

Received May 28, 2002

Abstract—The cause of the small heating of ultracold neutrons (UCNs) by $\sim 10^{-7}$ eV with a probability of 10^{-8}–10^{-5} per collision with a surface was investigated. Neutrons heated in this way will be called vaporized UCNs (VUCNs). It was established that a preliminary heating of a sample in vacuum up to a temperature of 500–600 K can increase small-heating probability P_{VUCN} by a factor of at least ~ 100 and 10 on a stainless steel and a copper surface, respectively. For the first time, an extremely vigorous small heating of UCNs was observed on a powder of diamond nanoparticles. In this case, both the VUCN spectrum and the temperature dependence of probability P_{VUCN} were similar to those previously obtained for stainless steel, beryllium, and copper samples. On the surface of single crystal sapphire, neither the small heating of UCNs nor nanoparticles were found. All these facts indicate that VUCNs are likely produced by inelastic scattering of UCNs on weakly bound surface nanoparticles being in permanent thermal motion.

In 1997, we found an additional channel of losses of ultracold neutrons (UCNs) from traps [1]. These losses occur because UCNs increase their energy by $\sim 10^{-7}$ eV with a probability of 10^{-8}–10^{-5} per collision with a surface. If the energy of a neutron after this inelastic scattering exceeds a certain critical value, it leaves a trap. This process is similar to the "vaporization" of UCNs from the trap (see Fig. 1). For this reason, such neutrons are named "vaporized" UCNs (VUCNs).

For investigating the nature and characteristics of this phenomenon, a big gravitational spectrometer (BGS) was constructed. This spectrometer can simultaneously detect stored UCNs and formed VUCNs (see Fig. 2). Contrary to previous setups, the BGS provides the detection of VUCNs in a wider energy range (50–150 neV) and with higher efficiency ($\sim 50\%$). This efficiency is measured rather than estimated over the entire energy range in order to ensure the accuracy and reliability of results. The spectrometer was designed so that samples can be rapidly and conveniently replaced, and the setup can be adapted for various experimental problems. The spectrometer volume hermetically separated from the vacuum enclosure can be heated up to 600 K or cooled down to 80 K.

The layout of the BGS is shown in Fig. 3. A sample (*1*) is mounted at the spectrometer bottom inside cylinder *2*, which forms a storage volume for UCNs and presents a gravitational barrier for neutrons. Ultracold neutrons fill the spectrometer through the inlet neutron guide and are locked by valve *3*. A calibrated orifice in the spectrometer bottom allows measurements of neutron flux by monitoring detector *4*. Absorber *5* in the lower position removes UCNs of energies above the gravitational barrier. When the absorber is in the upper position, VUCNs formed in collisions of UCNs with the sample surface or walls can jump over the gravitational barrier and enter detector *6* through outlet valve *7*, which is opened throughout the measurements.

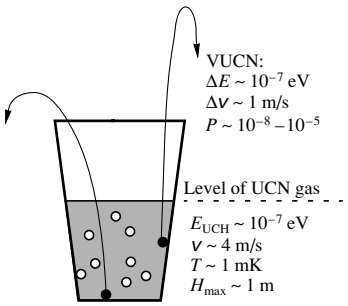

Fig. 1. Illustration of losses of UCNs via the formation of VUCNs.

[1)]Joint Institute for Nuclear Research, Dubna, Moscow oblast, 141980 Russia.
[2)]National Institute of Nuclear Physics, Pisa, Italy.
[3)]Institut Laue–Langevin, F-38042 Grenoble, France.
[*]e-mail: nesvizhevsky@ill.fr

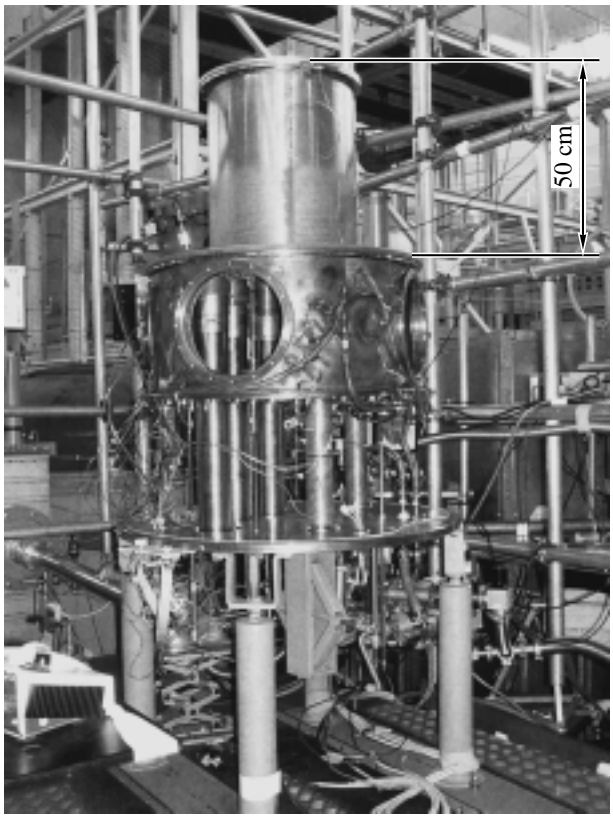

Fig. 2. Lower section of the big gravitational spectrometer. The height of the inner UCN-storage volume (gravitational barrier) is shown.

Figure 4 shows the typical time dependences of the detector count rate with various samples. During filling the spectrometer (0–100 s), the absorber is in the lower position. Neutrons of energies higher than the gravitational barrier penetrate in the detector through the gap between the absorber and walls of the storage volume; therefore, the detector count rate is high. After closing the inlet valve (the 100th second), these neutrons are rapidly absorbed in the absorber, and the

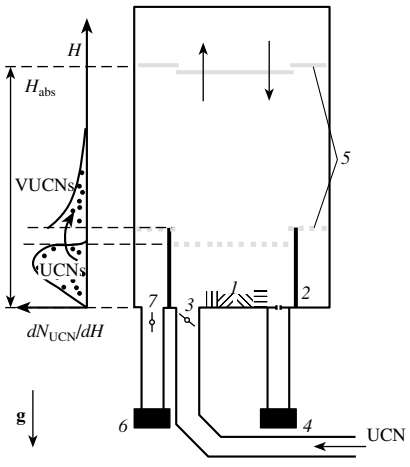

Fig. 3. Layout of the setup: (*1*) sample, (*2*) gravitational barrier, (*3*) inlet valve, (*4*) monitor, (*5*) absorber, (*6*) detector, and (*7*) outlet valve.

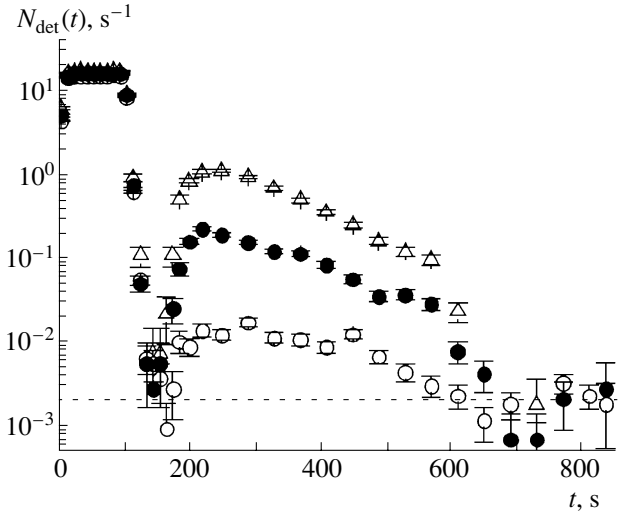

Fig. 4. Count rate as a function of time: measurements (○) on the surface of the empty copper spectrometer, (●) with stainless steel samples (SS2-2), and (△) with the diamond-nanoparticle powder. The dashed line shows the background level.

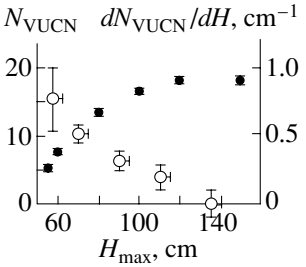

Fig. 5. (Left-hand ordinate axis, solid circles) Integral and (right-hand ordinate axis, open circles) differential spectra of neutrons heated on the stainless steel surface (SS1-3 sample) vs. the height of the upper position of the absorber. The integral spectrum is the number of VUCNs detected per cycle. The differential spectrum is obtained by the numerical differentiation of the integral spectrum corrected to the efficiency of VUCN detection.

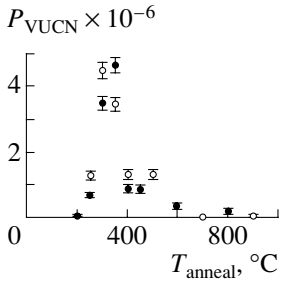

Fig. 6. Probability of the small heating of UCNs as a function of the annealing temperature for the stainless steel samples (solid circles) SS4-1 and (open circles) SS4-2.

detector count rate falls abruptly. If the absorber is lifted to the upper position after a certain time interval (the 170th second) in which all the UCNs of energies higher than the gravitational barrier are removed from the spectrometer, the detector count rate rises and, after a certain time, becomes proportional to the flux density of UCNs closed by the gravitational barrier in the spectrometer. This behavior is explained by the permanent production of VUCNs with energies higher than the gravitational barrier in the storage volume. At the 590th second, the absorber is sunk to the lower position, and the detector count falls down to the background value.

The probability of the small heating of UCNs interacting with a metal (stainless steel or copper) surface is measured with a higher accuracy by a more reliable method than in previous experiments [1–3]. In this case, the new measurement corroborates our previous results obtained with similar samples for both the probability of this process and the shape of the integral spectrum of heated neutrons.

For the first times, the integral spectrum of heated neutrons (see Fig. 5) was measured with an accuracy sufficient for calculating the differential spectrum.

We have established that the probability of small heating of UCNs depends on the procedure of preparing a stainless steel sample. Indeed, a preliminary heating of the sample at a temperature of 500–600 K for four hours abruptly increases the probability of small heating of UCNs by a factor of about 100. The independent measurements with identical samples indicate that this result is well reproducible (see Fig. 6). The similar abrupt increase in the probability of small heating (by a factor of 10) after heat treatment was also observed for the interaction of UCNs with a copper surface. It should be noted that the preliminary heating of surfaces of traps and samples up to these temperatures is the routine preparatory procedure in UCN-storage experiments. Therefore, the interpretation of experiments where UCN losses caused by small heating are not explicitly measured is unreliable.

We considered the acceleration of UCNs by the thermal motion of solid nanoparticles weakly bound to a surface as the most probable cause of the small heating of UCNs [4]. In order to verify this hypothesis, we deposited a powder ($\sim$1 cm^3) of diamond nanoparticles with a mean size of $\sim$5 nm (Ultradiamond-90) on an area of $\sim$150 cm^2 on the copper bottom surface of the spectrometer. In this case, the VUCN flux increased strongly (see Fig. 4), and the probability of VUCN formation reduced to this area was equal to $\sim 10^{-3}$ per collision. The VUCN spectra measured in this study and in [1–3] on the stainless steel surface coincide with the spectrum measured on the nanoparticle-powder surface (see Fig. 7). The temperature dependence of small-heating probability measured in the range of 100–300 K for the diamond-nanoparticle powder coincides with the dependences measured in [2] for the beryllium and copper surfaces. Furthermore, the VUCN spectrum is virtually independent of temperature in the temperature range 100–300 K.

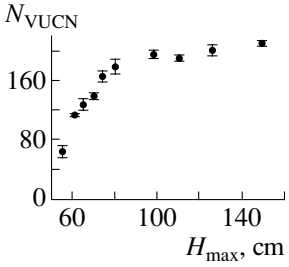

Fig. 7. Number (integral spectrum) of VUCNs detected per cycle, which were heated on the diamond-nanoparticle powder, as a function of the upper-position height of the absorber.

Whereas we observed a high VUCN flux from the nanoparticle powder, small heating of UCNs on the surface of a sapphire single crystal was not detected. The probability of this heating was measured to be $(0.0 \pm 1.2) \times 10^{-8}$ per collision. In this case, the scanning atomic force microscope observed no nanoparticle on this surface.

The results of this study indicate that the small heating of UCNs interacting with a surface is caused by their acceleration in collisions with very small solid particles that are weakly bound to the surface and are in permanent thermal motion.

ACKNOWLEDGMENTS

This work was supported by the Russian Foundation for Basic Research, project no. 00-02-17772, and by the INTAS, project no. 99-00508.

REFERENCES

1. V. V. Nesvizhevsky, A. V. Strelkov, P. Geltenbort, and P. S. Yaidjiev, ILL Annual Report (Grenoble, 1997), p. 62; Eur. J. Appl. Phys. **6**, 151 (1999); Yad. Fiz. **62**, 832 (1999) [Phys. At. Nucl. **62**, 776 (1999)]; A. V. Strelkov, V. V. Nesvizhevsky, P. Geltenbort, *et al.*, Nucl. Instrum. Methods Phys. Res. A **440**, 695 (2000).
2. E. V. Lychagin, A. Yu. Muzychka, V. V. Nesvizhevsky, *et al.*, Yad. Fiz. **63**, 609 (2000) [Phys. At. Nucl. **63**, 548 (2000)].
3. E. V. Lychagin, A. Yu. Muzychka, V. V. Nesvizhevsky, *et al.*, Preprint No. R3-2001-49, OIYaI (Dubna, 2001); Poverkhnost' (in press).
4. V. V. Nesvizhevsky, Yad. Fiz. **65**, 426 (2002) [Phys. At. Nucl. **65**, 400 (2002)].

Translated by V. Bukhanov

Physics of Atomic Nuclei, Vol. 65, No. 11, 2002, pp. 1999–2008. Translated from Yadernaya Fizika, Vol. 65, No. 11, 2002, pp. 2056–2065.

NUCLEI

Magnetic Resonance in Beta-Active Nuclei ^{8}Li at the Doubled Larmor Frequency in LiF Polycrystals Containing Dislocations

Yu. G. Abov, A. D. Gul'ko, F. S. Dzheparov, S. V. Stepanov*, and S. S. Trostin

Institute of Theoretical and Experimental Physics,
Bol'shaya Cheremushkinskaya ul. 25, Moscow, 117218 Russia

Received March 6, 2002

Abstract—The nuclear magnetic resonance in beta-active nuclei ^{8}Li at the doubled Larmor frequency in LiF polycrystals is studied before and after treating these polycrystals with an external pressure. A quantitative approach is proposed that makes it possible to calculate the parameters of the resonance line-shape function versus the dislocation structure of crystallites. Data suggesting that the samples under investigation that were subjected to a treatment with an external pressure develop dislocations whose Burgers vectors are parallel are obtained. © *2002 MAIK "Nauka/Interperiodica".*

1. INTRODUCTION

The method relying on the nuclear magnetic resonance of polarized beta-active nuclei (β-NMR) and employing the existence of correlations between the polarization of the nuclei involved and the asymmetry of their beta radiation was proposed by Shapiro [1] after the discovery of parity nonconservation in weak interactions. In the case of allowed transitions, the anisotropy of beta radiation from polarized nuclei has the form

$$W(\theta) = 1 + \frac{v}{c} P A \cos\theta, \qquad (1)$$

where θ is the angle between the direction of the nuclear-spin polarization P and the direction of beta-particle emission; v is the velocity of beta electrons; and A is the asymmetry factor, which is determined by the nature of a given beta transition. Creating polarized beta-active nuclei (β-nuclei) in matter and studying the dependence of $W(\theta)$ on time, external constant and radio-frequency magnetic fields, temperature, and pressure, one can explore phenomena caused by hyperfine and dipole–dipole interactions. Over the past decades, the development of β-NMR has rendered it a powerful tool for investigations in nuclear and solid-state physics [2–5].

In the experiment that is discussed below, β-nuclei ^{8}Li are formed directly in the LiF sample being investigated. This occurs upon the capture of a polarized thermal neutron by an unpolarized nucleus ^{7}Li. The compound nucleus $^8\vec{\mathrm{Li}}^*$ formed in this way then undergoes deexcitation via photon emission and occurs in the ground state. This is followed by its beta decay, the respective beta particles being emitted in accordance with the distribution in (1). The entire set of transformations is as follows:

$$\vec{n} + {}^7\mathrm{Li} \longrightarrow {}^8\vec{\mathrm{Li}}^* \,\gamma \longrightarrow {}^8\vec{\mathrm{Li}}\,{}^{\beta^-} \longrightarrow {}^8\mathrm{Be}^* \longrightarrow 2\alpha. \qquad (2)$$

Theoretical estimates show that, by the instant at which the ground state of the β-nucleus is formed, the degree of its polarization is close to 50%, which is five to six orders of magnitude greater than the equilibrium degree of polarization of crystal nuclei according to the Boltzmann factor (at room temperature and in magnetic fields of about a kilogauss).

By recording beta particles emitted along ($N_\uparrow$) and against ($N_\downarrow$) the direction of neutron-beam polarization, one can therefore measure the β-asymmetry

$$\varepsilon = \frac{N_\uparrow - N_\downarrow}{N_\uparrow + N_\downarrow} \propto P, \qquad (3)$$

which is proportional to the polarization P of the ensemble of β-nuclei in the sample. A detailed account of the nuclear-physics fundamentals of the β-NMR method and of its special features is given in [6], along with a comprehensive description of the equipment used in the β-NMR spectrometer and of the procedure of measurements.

The present article reports on a continuation of the β-NMR investigation of dislocations in crystals that was begun in [7]. This investigation is based on theoretical estimates presented in [8], which indicate that the magnetic resonance in β-nuclei at the doubled Larmor frequency $\omega = 2\omega_8$ (ω_8 is the Larmor frequency in a β-nucleus) is highly sensitive to the quadrupole interactions of β-nuclei with a surrounding medium.

*e-mail: sergey.stepanov@itep.ru

1063-7788/02/6511-1999$22.00

For the first time, a resonance in β-nuclei at the doubled Larmor frequency was experimentally discovered in [9, 10]. In [9], such a resonance was observed along with depolarization phenomena caused by the interactions of β-nuclei ^{110}Ag with radiation defects accompanying the reaction $^{109}\mathrm{Ag}(n,\gamma)^{110}\mathrm{Ag}$ in an AgCl crystal; therefore, this resonance was interpreted as a quadrupole one. In [10], a resonance at $\omega = 2\omega_8$ in a LiF polycrystal was recorded along with other multispin resonances caused by magnetic dipole–dipole interactions of a ^{8}Li nucleus ($T_{1/2} = 0.84$ s, $I = 2$) with the spins of ^{19}F and ^{7}Li nuclei (for the ensuing analysis, it is of importance that the polycrystalline sample studied there was obtained by grinding moderately small LiF crystals). In LiF, no influence of defects on the Larmor resonance at $\omega = \omega_8$ was found at room temperature; however, radiation defects identified with lithium vacancies in the coordination sphere closest to the β-nucleus were previously observed in [11] at lower (nitrogen) temperatures, and the constant of the corresponding electric quadrupole interaction was measured ($\omega_Q = 2\pi \cdot 11.7(4)$ kHz for the case where the external magnetic field is directed along the [111] axis).

A resonance at the doubled Larmor frequency in radioactive nuclei used as probes in cubic crystals becomes allowed under the effect of nonsecular terms in the dipole–dipole Hamiltonian (in higher orders of perturbation theory) or in the presence of quadrupole interaction with structural defects (in the first order of perturbation theory). In the first case, the rate of the resonance depolarization of β-nuclei in the presence of a radio-frequency magnetic field rotating with the frequency $2\omega_8$ and having the amplitude $H_1 = \hbar\omega_1/(g_8\beta_n)$ (here, β_n is the nuclear magneton, while g_8 is the g factor for the ^{8}Li nucleus—it is equal to 0.8267 [12]) proves to be proportional to $\dfrac{\omega_1^2}{\omega_{\mathrm{loc}}}\left(\dfrac{\omega_{\mathrm{loc}}}{\omega_8}\right)^4$, where $\omega_{\mathrm{loc}} = \sqrt{M_2}$ is the square root of the second moment of the Larmor resonance line (the characteristic strength of the local magnetic field in frequency units). However, the depolarization rate observed in the experiment reported in [10] exceeded the theoretical estimate by a factor of 300 [8]. In view of this, it was assumed in [8] that the resonance in question is of a quadrupole origin that is associated with the presence of radiation defects whose influence on the Larmor resonance is nevertheless unobservable, since the theoretical estimate of the line width of the Larmor resonance was matched with its experimental value.

A more detailed calculation revealed [13] that a point defect (vacancy) having an electric charge e causes depolarization of rate $R_Q(r)$ [see formula (27) below], where r is the distance between this point defect and the probe nucleus being considered. In order to explain experimental results reported in [10], it was necessary to assume that the local concentration of point defects near the ^{8}Li nucleus is about 0.01. So large a value cannot be an equilibrium one, but it is admissible for vacancies of radiation origin that are generated by the ^{8}Li nucleus during its formation in the relevant reaction (n,γ).

In subsequent experiments reported in [14], which were performed with defect-free LiF powder samples obtained by means of a chemical precipitation, a resonance at the doubled frequency was not observed, which disproved the hypothesis that radiation defects exert influence at room temperature. These defects either recombine fast through a vacancy-interstice process or recede from the β-nucleus within a rather short time at a distance so large that they do not cause the depolarization of the nucleus.

However, a distinct peak at the frequency $2\omega_8$ appeared after a treatment of the samples under study with an external pressure of 190 MPa [14]. It is natural to assume that, upon pressing (or upon the grinding of crystals as in [10]), there arise dislocations in the crystals of the powders. Causing the displacement of crystal ions, these dislocations generate, on the nuclear probes in question, an electric-field gradient that decreases slowly (in proportion to $1/r$) with increasing distance from a given dislocation. It is precisely this effect that leads to the emergence of a resonance.

In the present study, we perform a detailed analysis of the effect of dislocations on the depolarization of β-nuclei ^{8}Li in LiF. The ensuing exposition is organized as follows. In Section 2, we present a relationship between the strain tensor and the electric-field-gradient tensor in cubic crystals within the model of pointlike charges. Further, in Section 3, we consider a strain tensor for an arbitrarily oriented edge dislocation. The effective Hamiltonian for a magnetic resonance at a doubled Larmor frequency is obtained in Section 4. The next section is devoted to calculating the resonance-depolarization kinetics of nuclear probes in polycrystalline LiF samples containing dislocations. In Section 6, we discuss the results obtained by processing data from β-NMR experiments that studied the depolarization of ^{8}Li nuclei in LiF powders before and after treating them with an external pressure.

2. RELATIONSHIP BETWEEN THE STRAIN TENSOR AND THE ELECTRIC-FIELD-GRADIENT TENSOR IN CUBIC CRYSTALS

In the presence of the strain field $\mathbf{u}(\mathbf{x})$, the electrostatic potential generated by crystal ions in the

vicinity of a β-nucleus that occurs at the point $\mathbf{u}(0)$ near the coordinate origin can be represented as

$$\varphi(\mathbf{r})|_{r\to 0} = \sum_{\mathbf{x}\neq 0} \frac{e_{\mathbf{x}}}{|\mathbf{x}+\mathbf{u}(\mathbf{x})-\mathbf{r}-\mathbf{u}(0)|}\bigg|_{r\to 0}, \quad (4)$$

where $e_{\mathbf{x}}$ is the charge of the ion at the site $\mathbf{x}$. Retaining only the first term in the expansion of $\varphi(\mathbf{r})$ in a power series in the difference $\mathbf{u}(\mathbf{x})-\mathbf{u}(0)$, we obtain the the electric-field-gradient tensor at the β-nucleus position in the form

$$G_{\alpha\beta} \equiv G_{\alpha\beta}(\mathbf{r})|_{r\to 0} = (1-\gamma_\infty)\frac{\partial^2\varphi(r=0)}{\partial u_\alpha(0)\partial u_\beta(0)} \quad (5)$$

$$= (1-\gamma_\infty)\left.\frac{\partial^2\varphi(\mathbf{r})}{\partial r_\alpha \partial r_\beta}\right|_{r\to 0} = (1-\gamma_\infty)$$

$$\times \sum_{\mathbf{x}\neq 0}\left(\frac{\partial}{\partial x_\alpha}\frac{\partial}{\partial x_\beta}\frac{\partial}{\partial x_\mu}\frac{1}{x}\right)(u_\mu(\mathbf{x})-u_\mu(0))e_{\mathbf{x}}.$$

Hereafter, we imply summation over dummy indices. The above expressions for the tensor $G_{\alpha\beta}$ were multiplied by the Sternheimer factor, $1-\gamma_\infty$, which takes into account the perturbation of the electron shell of an ion including the nuclear probe and which changes the value of the electric-field gradient at the position of the nucleus. For the Li^+ ion, the value of $\gamma_\infty(Li^+)$ is small (0.255 [15]), since the electron shell of Li^+ involves only two electrons.

In the leading order in d/l, where d is the lattice constant and l is a characteristic distance at which $u_\mu(\mathbf{x})$ changes, we have

$$G_{\alpha\beta} = (1-\gamma_\infty) \quad (6)$$

$$\times \left.\frac{\partial u_\mu(\mathbf{x})}{\partial x_\nu}\right|_{x\to 0}\sum_{\mathbf{x}\neq 0} e_{\mathbf{x}}x_\nu \frac{\partial}{\partial x_\alpha}\frac{\partial}{\partial x_\beta}\frac{\partial}{\partial x_\mu}\frac{1}{x}.$$

Evaluating the derivatives involved and considering that, in cubic crystals, we have the relation

$$3\sum_{\mathbf{x}}(x_\alpha x_\beta/x^2)f(x) = \sum_{\mathbf{x}}\delta_{\alpha\beta}f(x), \quad (7)$$

where $\delta_{\alpha\beta}$ is a Kronecker delta symbol and $f(x) \equiv f(|\mathbf{x}|)$ is an arbitrary function that only serves to ensure convergence of lattice sums, we obtain

$$G_{\alpha\beta} = -(1-\gamma_\infty)\,\Phi_{\alpha\beta\mu\nu}\left.\frac{\partial u_\mu(\mathbf{x})}{\partial x_\nu}\right|_{x\to 0} \quad (8)$$

$$= -(1-\gamma_\infty)\Phi_{\alpha\beta\mu\nu}u_{\mu\nu}(0),$$

$$\Phi_{\alpha\beta\mu\nu} = \sum_{\mathbf{x}\neq 0}\frac{e_{\mathbf{x}}}{x^3}\left(15\frac{x_\alpha x_\beta x_\mu x_\nu}{x^4} - \delta_{\alpha\mu}\delta_{\beta\nu}\right. \quad (9)$$

$$\left. - \delta_{\alpha\nu}\delta_{\beta\mu} - \delta_{\alpha\beta}\delta_{\mu\nu}\right).$$

Here, we have considered that the tensor $\Phi_{\alpha\beta\mu\nu}$ is symmetric with respect to any permutation of the indices α, β, μ, and ν. Therefore, the derivative $\dfrac{\partial u_\mu(\mathbf{r})}{\partial r_\nu}$ has been replaced by the strain tensor $u_{\mu\nu} = \dfrac{1}{2}\left(\dfrac{\partial u_\mu}{\partial r_\nu} + \dfrac{\partial u_\nu}{\partial r_\mu}\right)$.

Preserving all the symmetry properties, we can recast the tensor $\Phi_{\alpha\beta\mu\nu}$ into the form

$$\Phi_{\alpha\beta\mu\nu} = \phi_0(\delta_{\alpha\mu}\delta_{\beta\nu} + \delta_{\alpha\nu}\delta_{\beta\mu} + \delta_{\alpha\beta}\delta_{\mu\nu}) \quad (10)$$

$$+ \phi_1\delta_{\alpha\beta}\delta_{\mu\nu}\delta_{\alpha\mu}.$$

The constants ϕ_0 and ϕ_1 in (10) are related by the condition requiring the vanishing of the trace of the electric-field-gradient tensor, $G_{\alpha\alpha} = 0$; as a matter of fact, this condition is equivalent to Laplace's equation $\dfrac{\partial^2}{\partial r_\alpha^2}\varphi(\mathbf{r}) = 0$ for the electrostatic potential. From here, we obtain $\phi_1 = -5\phi_0$. Considering that $e(Li^+) = -e(F^-) = e$, we can find for the face-centered cubic (FCC) lattice of a LiF crystal that

$$\phi_0 = -\frac{1}{2}\Phi_{1111} = \frac{3}{2}\sum_{\mathbf{x}\neq 0}\frac{e_{\mathbf{x}}}{x^3}\left(1-\frac{5x_1^4}{x^4}\right) \quad (11)$$

$$= 5.95\frac{e}{a^3} = 16.83\frac{e}{r_0^3},$$

where $a = 2.01$ Å is the minimum distance between the Li^+ and F^- ions in LiF and $r_0 = \sqrt{2}a = 2.84$ Å is the distance between the closest lithium ions. Convergence of the sum in (11) is ensured by the alternation of the signs of neighboring charges and by a rather fast decrease (in proportion to x^{-3}) of individual terms with distance. We note that, for spherical samples, the contribution of each ion sublattice to ϕ_0 is also finite:

$$\frac{3}{2}\sum_{\mathrm{Li}}\frac{1}{x^3}\left(1-\frac{5x_1^4}{x^4}\right) = \frac{0.64}{a^3}, \quad (12)$$

$$\frac{3}{2}\sum_{\mathrm{F}}\frac{1}{x^3}\left(1-\frac{5x_1^4}{x^4}\right) = -\frac{5.31}{a^3}.$$

Taking into account relations (8), (10), and (11), we obtain

$$G_{\alpha\beta} = 5.95(1-\gamma_\infty)\frac{e}{a^3}(\delta_{\alpha\beta}(5u_{\alpha\alpha} - \mathrm{tr}u) - 2u_{\alpha\beta}), \quad (13)$$

where no summation over α is implied.

The effect of elastic deformation of NaCl crystals on the quadrupole broadening of the NMR line of ^{23}Na nuclei was studied in [16]. The components of the tensor that relates the elastic deformation of the lattice to the electric-field gradient at the

position of the nucleus were determined there. The results proved to be (in the notation adopted in [16]) $S_{11} = \pm 2(0.3) \times 10^{15}$ and $S_{44} = \mp 0.5(1) \times 10^{15}$ in CGSE units. It is obvious that, within the measurement errors, these values are consistent with the relations $\Phi_{1111} = -2(1 - \gamma_\infty(\mathrm{Na}^+))\dfrac{5.95e}{a^3} = -1.7 \times 10^{15}$ CGSE and $\Phi_{1212} = -\Phi_{1111}/2$, which follow from our present calculation (in a NaCl crystal, the distance between the neighboring ions Na^+ and Cl^+ is $a = 2.8$ Å and $\gamma_\infty(\mathrm{Na}^+) = -5.45$ [15]).

3. STRAIN TENSOR FOR AN EDGE DISLOCATION

Since elastic strains decrease slowly with distance, the electric-field gradient at the position of the beta-active nuclear probe receives contributions from a large number of dislocations situated at distances from it that are large in relation to the lattice constant. In view of this, we will perform our analysis in the approximation of continual theory. Moreover, we consider only linear edge dislocations, because the inclusion of screw dislocations does not change the results significantly and because strain fields from dislocation loops decrease faster and, in all probability, do not contribute to the resonance at $2\omega_8$.

Let us assume that the powder in question consists of spherical crystallites and choose the coordinate origin at the position of the β-nucleus. We consider a linear edge dislocation having the Burgers vector $\mathbf{b} = b(\cos\varphi_{bx}, \sin\varphi_{bx}, 0)$ and the direction vector $\mathbf{n} = (0, 0, 1)$ and intersecting the xy plane at the point $\mathbf{r} = r(\cos\varphi, \sin\varphi, 0)$. At the origin of coordinates (that is, at the position of the β-nucleus), such a dislocation generates the strain field characterized by the tensor

$$U_z(\varphi_{bx}) u^0_{\alpha\beta}(r, \varphi - \varphi_{bx} - \pi) U_z(-\varphi_{bx}), \qquad (14)$$

where $U_z(\varphi_{bx})$ is the operator of rotation through the angle φ_{bx} about the z axis and, in Cartesian coordinates, the tensor $u^0_{\alpha\beta}(r, \varphi)$ has the form [17, 18]

$$u^0_{\alpha\beta}(r, \varphi) \qquad (15)$$
$$= \frac{b}{4\pi r} \begin{pmatrix} -\sin\varphi \cdot (2 + \cos 2\varphi) & \cos\varphi\cos 2\varphi & 0 \\ \cos\varphi\cos 2\varphi & \sin\varphi\cos 2\varphi & 0 \\ 0 & 0 & 0 \end{pmatrix}.$$

Here, we have also set the Poisson coefficient to zero (for LiF, it is small, 0.187 [17]). The length of the vector $\mathbf{b}$ is taken to be equal to the minimum distance (2.84 Å) between lithium ions in LiF. This corresponds to the case where a plastic deformation develops in a $\{110\}$ plane along the $\langle 110\rangle$ axis. This version is the most probable in FCC ion crystals [19].

The deformation from a dislocation arbitrarily oriented with respect to the β-nucleus is obtained upon applying, to the tensor in (15), the general transformation of a three-dimensional rotation through the Euler angles $\gamma + \varphi_{bx}$, β, and α. It is convenient to perform actual calculations for spherical tensors with the aid of the standard rotation matrices $D^2_{nm}(\gamma + \varphi_{bx}, \beta, \alpha)$ [20]. For this, we rewrite $u^0_{\alpha\beta}$ (15) in terms of the spherical components u^2_m as

$$u^0_{00} = \frac{b\cos\varphi}{2\sqrt{3}\pi r}, \quad u^0_{20} = \frac{3u^0_{zz} - \mathrm{tr}u}{\sqrt{6}} = \frac{b\sin\varphi}{2\sqrt{6}\pi r}, \quad (16)$$
$$u^0_{2\pm 2} = \pm\frac{ib\cos 2\varphi}{4\pi r} e^{\pm i\varphi}.$$

With the aid of relations (13)–(15), we can represent the spherical components of the electric-field gradient in the form

$$\frac{G^0_{20}(r, \varphi - \varphi_{bx} - \pi)}{1 - \gamma_\infty} = -\phi_0 \sqrt{\frac{3}{8}} \frac{b}{\pi r} \sin(\varphi - \varphi_{bx}), \quad (17)$$

$$\frac{G^0_{2\pm 2}(r, \varphi - \varphi_{bx} - \pi)}{1 - \gamma_\infty} = \frac{\phi_0 b}{4\pi r}[3\sin(\varphi - \varphi_{bx}) \times (1 + \cos(\varphi - \varphi_{bx})) \pm 2i\cos(\varphi - \varphi_{bx})\cos(2(\varphi - \varphi_{bx}))].$$

The components $G^0_{2\pm 1}$ vanish identically.

4. EFFECTIVE HAMILTONIAN CAUSING NUCLEAR DEPOLARIZATION AT THE DOUBLED LARMOR FREQUENCY

The Hamiltonian describing the quadrupole interaction (in frequency units) of the β-nucleus with all dislocations present in a crystallite that generate the total electric-field gradient $G_{\alpha\beta}$ at the position of the nuclear probe has the form

$$\mathcal{H}_Q = \frac{G_{\alpha\beta} Q_{\alpha\beta}}{6}, \qquad (18)$$
$$Q_{\alpha\beta} = \frac{3Qe}{2I(2I+1)\hbar}\left(I_\alpha I_\beta + I_\beta I_\alpha - \frac{2}{3} I(I+1)\delta_{\alpha\beta}\right),$$

where Q is the quadrupole moment of the β-nucleus (the ^{8}Li nucleus has $Q = 0.032(5) \times 10^{-24}$ cm^2 [2]). In accordance with (17), it will be convenient, in the following, to use the spin–tensor representation for $\mathcal{H}_Q$. The relevant formulas for going over to the spherical components of the tensors are given in [20].

The total spin Hamiltonian of a crystal can be represented in the form

$$\mathcal{H} = \mathcal{H}^I_z + \mathcal{H}^F_z + \mathcal{H}^{IF}_d + \mathcal{H}^F_d + \mathcal{H}^I_Q + \mathcal{H}^F_Q + \mathcal{H}_{\mathrm{rf}}(t)$$

$$= \mathcal{H}_{\rm st} + \mathcal{H}_{\rm rf}(t),$$

where superscripts correspond to the spins of the β-nucleus (I) and of the host nucleus of the crystal (F), while the subscripts z, d, and Q label Zeeman, dipole–dipole, and quadrupole interactions, respectively. The Hamiltonian $\mathcal{H}_{\rm rf}(t) = \mathcal{H}^I_{\rm rf}(t) + \mathcal{H}^F_{\rm rf}(t)$ describes the interaction with a variable (resonance) external field. A detailed discussion of various terms in $\mathcal{H}$ can be found in standard handbooks (see, for example, [20]). As usual, we assume that the constant magnetic field is directed along the z axis.

In calculating nuclear resonances at frequencies different from the Larmor frequency, it is necessary to take into account the presence of nonsecular terms (that is, terms that do not commute with the Zeeman component $\mathcal{H}_z = \mathcal{H}^I_z + \mathcal{H}^F_z$) in the Hamiltonian $\mathcal{H}$. Hereafter, we consider the case where the characteristic frequencies of quadrupole interaction are low in relation to Zeeman frequencies; that is, $\omega_Q \ll \omega_z$. The procedure for constructing an effective Hamiltonian $\mathcal{H}_{\rm eff}$ that corresponds to the nuclear-depolarization process at a frequency that is an integral multiple of the Larmor frequency consists in the following [8] (see also [21, chapter 6]). The total Hamiltonian $\mathcal{H}$ is broken down into a number of terms $\mathcal{H}_m$ satisfying the relations

$$\mathcal{H} = \sum_m \mathcal{H}_m, \qquad [\mathcal{H}_z, \mathcal{H}_m] = \omega_m \mathcal{H}_m, \qquad (19)$$
$$\mathcal{H}^+_m = \mathcal{H}_{-m}, \qquad \omega_{-m} = -\omega_m,$$

the last two of these expressing the fact that the original Hamiltonian is Hermitian.

By definition, the Hamiltonian $\mathcal{H}_0$, which commutes with $\mathcal{H}_z$, is referred to as the secular part of interaction. It is hardly possible to take directly into account nonsecular terms on the basis of time-dependent perturbation theory, because these terms are not small in relation to the term $\mathcal{H}_0$, which determines the resonance lineshape and its quadrupole splitting and which is not small in relation to $\mathcal{H}_z$. In order to sidestep this difficulty, we transform the original Hamiltonian in such a way that the terms $\mathcal{H}_{m\neq 0}$ acquire smallness sufficient for taking them into account according to time-dependent perturbation theory. Upon these transformations, there arise slowly oscillating terms that describe the resonance transitions being studied.

Restricting our consideration to describing one-photon transitions (for a more general case, the interested reader is referred to [8]), we consider the unitary transformation

$$\mathcal{H}^{(1)} = U_0 \mathcal{H}^{(0)} U_0^+, \qquad (20)$$
$$\mathcal{H}^{(0)} \equiv \mathcal{H}_{\rm st} = \mathcal{H}_z + \mathcal{H}^{(0)}_0 + \sum_{m\neq 0} \mathcal{H}^{(0)}_m,$$

$$U_0 = e^{iS_0}, \qquad S_0 = \sum_{m\neq 0} \frac{\mathcal{H}^{(0)}_m}{i\omega_m}.$$

Identical transformations [8] make it possible to recast $\mathcal{H}^{(1)}$ into the form

$$\mathcal{H}^{(1)} = \mathcal{H}_z + e^{iS_0^\times}\mathcal{H}^{(0)}_0 \qquad (21)$$
$$+ \left(e^{iS_0^\times} - \frac{e^{iS_0^\times} - 1}{iS_0^\times}\right) \sum_{m\neq 0} \mathcal{H}^{(0)}_m.$$

where $S_0^\times$ is often referred to as a superoperator. Its action is specified by the relation $S_0^\times \mathcal{H} = [S_0, \mathcal{H}]$. In deriving Eq. (21), we have considered that

$$(\exp(iS_0^\times) - 1)\mathcal{H}_z = (\exp(iS_0^\times) - 1)/(iS_0^\times)(iS_0^\times \mathcal{H}_z)$$
$$= -(\exp(iS_0^\times) - 1)/(S_0^\times) \sum_{m\neq 0} \mathcal{H}_m.$$

Since the operator S_0 features a smallness of order $\tilde{\omega}/\omega_z \ll 1$, where $\tilde{\omega} = \max\{\omega_Q, \omega_{\rm loc}\}$, with $\omega_{\rm loc}$ and $\omega_z = H_0/\hbar$ being, respectively, the local field from dipole–dipole interactions and an external field, it can be concluded from (21) that, in the transformed Hamiltonian $\mathcal{H}^{(1)}$, the nonsecular terms are reduced by the factor $\tilde{\omega}/\omega_z$. Indeed, the greatest of them are given by

$$iS_0^\times \mathcal{H}^{(0)}_0 \text{and} \frac{i}{2} S_0^\times \sum_{m\neq 0} \mathcal{H}^{(0)}_m.$$

One can again expand the resulting Hamiltonian $\mathcal{H}^{(1)}$ according to the rule specified by Eq. (19) and, on this basis, reduce its nonsecular terms still further, by applying a transformation of the type in (20).

By iteratively continuing the process of applying similar transformations, one can obtain ever smaller nonsecular terms and eventually reach the stage at which they can be disregarded, the secular terms contributing to the line-shape function for the resonances under study. For example, the secular terms can lead to the splitting of the line at the scale ω_Q.

The effective Hamiltonian of one-photon resonance transitions is contained among the terms of the time-dependent component $\mathcal{H}^{\rm new}_{\rm rf} = U\mathcal{H}_{\rm rf}U^+$ appearing in the new total Hamiltonian $\mathcal{H}^{\rm new} = U\mathcal{H}U^+$ and emerging from $\mathcal{H}_{\rm rf}$ upon the above transformations. Of these terms, those that become slowly oscillating upon a conventional transition to the interaction representations via the transformation $\mathcal{H}^{\rm new}_{\rm rf}(t) = U\mathcal{H}_{\rm rf}U^+ \to \exp(i\mathcal{H}^{\rm new}_0 t)\mathcal{H}^{\rm new}_{\rm rf}(t) \times \exp(-i\mathcal{H}^{\rm new}_0 t)$ are of importance for the resonance in question.

The effective Hamiltonian for the resonance at the double Larmor frequency $\omega = 2\omega_8$ is obtained upon

one unitary transformation (20) applied to the Hamiltonian $\mathcal{H}_z + \mathcal{H}_Q + \mathcal{H}_{\rm rf}(t)$; in doing this, it is sufficient to retain, in $\mathcal{H}_{\rm rf}(t)$, only the interaction of the β-nucleus with the radio-frequency magnetic field H_1 rotating with a frequency ω:

$$\mathcal{H}_{\rm rf}(t) = \mathcal{H}_{\rm rf}^{(+)}(t) + \text{h.c.}, \qquad (22)$$
$$\mathcal{H}_{\rm rf}^{(+)}(t) = \frac{\omega_1}{2} I_+ e^{-i\omega t}, \qquad \omega_1 = \beta_N g_8 H_1/\hbar.$$

As a result, the effective Hamiltonian for the resonance at $\omega = 2\omega_8$ can be represented in the form

$$\mathcal{H}_{\rm eff}(t) = \frac{1}{\omega_8}[\mathcal{H}'_Q, \mathcal{H}_{\rm rf}^{(+)}(t)] + \text{h.c.} \qquad (23)$$
$$= \mathcal{H}_{\rm eff}^{(+)}(t) + \mathcal{H}_{\rm eff}^{(-)}(t),$$

where

$$\mathcal{H}'_Q = \frac{1}{6}\frac{3Qe}{2I(2I-1)\hbar}(I_z I_+ + I_+ I_z)\sum_k G_{2-1}(k) \qquad (24)$$

is only that part of the total Hamiltonian $\mathcal{H}_Q$ which is proportional to the product $I_z I_\pm$ of the spin operators for the β-nucleus and $G_{2-1}(k)$ is the spherical component of the tensor of the electric-field gradient that is associated with the kth dislocation [in contrast to G^0_{2-1} from (17), it does not vanish since dislocations are arbitrarily oriented with respect to a constant magnetic field]. In (24), summation is performed over all dislocations present in the crystallite being considered.

From (23), it follows that, in scanning with a radio-frequency field in the vicinity of the frequency $2\omega_8$, each of the β-nuclei becomes exponentially depolarized with time at a rate W that is determined by a specific arrangement of dislocations around the nucleus and which is given by

$$W = \int_{-\infty}^{+\infty} \langle [I_z, \mathcal{H}_{\rm eff}^{(-)}][e^{-i\mathcal{H}_{z0}t}\mathcal{H}_{\rm eff}^{(+)}(t)e^{i\mathcal{H}_{z0}t}, I_z]\rangle_0 \frac{dt}{\langle I_z^2\rangle_0}, \qquad (25)$$

where the angular brackets $\langle \dots \rangle_0 = \text{tr}(\dots)/\text{tr}1$ denote that the trace is taken of the operator. The time evolution of the effective Hamiltonian in (23) is determined by the sum $\mathcal{H}_{z0} = \mathcal{H}_z + \mathcal{H}_0$ of the Zeeman Hamiltonian $\mathcal{H}_z$ and the secular part $\mathcal{H}_0$ of dipole–dipole interactions. It will be shown below that the main contribution to W comes from remote dislocations; therefore, one can disregard quadrupole splitting in (25). Transforming expression (25), we arrive at

$$W = \varkappa |F|^2, \quad \varkappa = \frac{16\pi}{5}(2I-1)(2I+3) \qquad (26)$$
$$\times \left[\frac{5.95}{6}\frac{\omega_1}{\omega_8}\omega_Q(1-\gamma_\infty)\right]^2 g_{2\omega_8}(\omega - 2\omega_8),$$

$$F = \sum_k \frac{G_{2-1}(k)}{1-\gamma_\infty}\frac{a^3}{e},$$

$$g_{2\omega_8}(\omega) = \int_{-\infty}^{+\infty} \frac{\langle I_-^2 I_+^2(t)\rangle_0}{\langle I_-^2 I_+^2\rangle_0} e^{-i\omega t}\frac{dt}{2\pi}.$$

As in (25), the evolution of the operator I_+ is determined by the Hamiltonian $\mathcal{H}_0$. From the results presented in [22], it follows that, to a fairly high precision, the line-shape function $g_{2\omega_8}(\omega)$ for the double resonance can be approximated by the doubly broadened line-shape function $g_{\omega_8}(\omega)$ (that is, a function that has a quadrupled second moment) for the Larmor resonance in β-nuclei.

The rate of resonance depolarization caused by the quadrupole interaction with a diamagnetic point defect that has an effective charge e_d is calculated in a similar way; that is,

$$R_Q(r) = \frac{32\pi^2}{75} \qquad (27)$$
$$\times (4I^2+4I-3)\frac{\omega_1^2}{\omega_8^2}\omega_Q^2 |Y_{21}|^2 \frac{a^6}{r^6} f^2(r) g(\omega - 2\omega_8),$$

where $f(r) \sim 1$ is a function that takes into account the effect of medium polarization on the electric-field gradient ($f = 1$ in a vacuum, and $f = \dfrac{2\epsilon+3}{5\epsilon}$ for a continuous medium [23], ϵ being its dielectric permettivity) and $\omega_Q = \dfrac{3Qee_d}{2I(2I-1)a^3\hbar}(1-\gamma_\infty)$ is a characteristic frequency of the quadrupole interaction between a vacancy and a β-nucleus that are separated by the minimum distance a between lattice sites.

5. RESONANCE-DEPOLARIZATION KINETICS OF β-NUCLEI AT THE DOUBLED LARMOR FREQUENCY

In order to describe the depolarization kinetics of the ensemble of β-nuclei in the sample being considered, it is necessary to sum the contributions to the polarization that come from all nuclei, each of which relaxes exponentially at its own depolarization rate (26). In other words, it is necessary to calculate the configuration expectation value

$$P(t) = \langle \exp(-Wt)\rangle, \qquad (28)$$

where averaging is performed over the arrangement of dislocations around a given β-nucleus (that is, over r, over the angle $\varphi - \varphi_{bx}$, and over the Euler angles), over the position of this β-nucleus in the crystallite (separation from the boundary), and over the orientation and the size of the crystallite itself.

From (26) and (27), it can be seen that W is a quadratic (bilinear) function of random variables. For the standard procedure of averaging [23] to be valid, it is necessary to reduce this function to a linear form. The following transformation is useful for this:

$$\langle \exp(-Wt)\rangle = \int_{-\infty}^{+\infty}\int_{-\infty}^{+\infty} \frac{d\mu_1 d\mu_2}{2\pi} \times \langle \exp[i\sqrt{2\varkappa t}(\mu_1 \mathrm{Re}F + \mu_2 \mathrm{Im}F)]\rangle. \quad (29)$$

According to (26), F involves summation over dislocations, but it is possible to go over from this summation to that over representative points of the dislocations (that is, each dislocation is represented by a lattice node that is the closest to the β-nucleus being considered and which belongs to this dislocation). Formally, one can extend summation over all nodes of the host-crystal lattice by introducing, under the summation sign, the occupation numbers $n_{\mathbf{r}}$ ($n_{\mathbf{r}} = 1$ if the vector $\mathbf{r}$ corresponds to a representative point of a dislocation; otherwise, $n_{\mathbf{r}} = 0$). An exponential whose argument involves a linear combination of occupation numbers is averaged by using the well-known procedure described in [23, 25]; that is,

$$\left\langle \exp\left[i\sqrt{2\varkappa t}(\mu_1 \mathrm{Re}\sum_{\mathbf{r}} n_{\mathbf{r}}\tilde{F} + \mu_2 \mathrm{Im}\sum_{\mathbf{r}} n_{\mathbf{r}}\tilde{F})\right]\right\rangle \quad (30)$$

$$= \exp\left(-\sum_{\mathbf{r}} c(\mathbf{r})\left[1 - e^{i\sqrt{2\varkappa t}(\mu_1 \mathrm{Re}\tilde{F}(\mathbf{r}) + \mu_2 \mathrm{Im}\tilde{F}(\mathbf{r}))}\right]\right),$$

where $c(\mathbf{r})$ is the concentration of representative points of dislocations with respect to the β-nucleus. Because of a slow decrease in the elastic fields of a dislocation ($\tilde{F}(r) \propto 1/r$, long-range behavior), an expression that is divergent at large r appears in the argument of the exponential on the right-hand side of (30). Therefore, the main contribution to the electric-field gradient comes from large distances, and we can restrict ourselves to an analysis of divergent terms:

$$P(t) = \left\langle \exp\left(-\varkappa t\left|\sum_{\mathbf{r}} c(\mathbf{r})\tilde{F}(\mathbf{r})\right|^2\right)\right\rangle. \quad (31)$$

In this formula, there still remains averaging over the Burgers angle φ_{bx}, over the Euler angles β and γ, and over the coordinates of the β-nucleus in the crystallite. The function $c(\mathbf{r})$ has the meaning of a dimensionless concentration of representative points of dislocations around the β-nucleus.

In order to demonstrate the effect of correlations in the distribution of dislocations over crystallites on the character of nuclear depolarization, we consider two possible limiting cases. In the first case, which, in the following, will be referred to, for the sake of brevity, as a two-dimensional case, all dislocations are directed identically and are characterized by identical Burgers vectors, and the vectors $\mathbf{r}_k$ connecting the β-nucleus with representative points of the dislocations are distributed at random in the Π plane orthogonal to $\mathbf{n}_k$, the concentration of these dislocations being independent of $\mathbf{r}$ and being trivially related to their total number n_d in the crystallite. This case simulates the situation where all dislocations in the crystallite were formed upon the strongest single compression of the crystallite.

In the second case, all the vectors $\mathbf{r}_k$, $\mathbf{n}_k$, and $\mathbf{b}_k$ are distributed at random, the condition $\mathbf{r}_k \perp \mathbf{n}_k \perp \mathbf{b}_k$ being of course satisfied. In the following, this case will be referred to as a three-dimensional one. It corresponds to the pattern of a gradual accumulation of dislocations in a crystallite as the result of multiple successive compressions of it.

In either case, depolarization kinetics proves to be nonexponential, but, in the region where the polarization of β-nuclei does not undergo sharp changes ($P(t) \gtrsim 0.1$), it is possible to linearize $\ln P(t)$ and to introduce the concept of an effective rate of the depolarization process:

$$P(t) = \exp(-W_{\mathrm{eff}}t).$$

It then turns out that, in the case where the distribution of dislocations is correlated in two dimensions, the effective depolarization rate $W_{\mathrm{eff}}^{(2)}$ depends on the characteristic size R of crystallites and on the mean spacing L between the dislocations as

$$W_{\mathrm{eff}}^{(2)} \propto \varkappa(Ra/L^2)^2. \quad (32)$$

In the case, of a random distribution of dislocations in three dimensions, the effective rate of the process is characterized by a different parametric dependence:

$$W_{\mathrm{eff}}^{(3)} \propto \varkappa(a/L)^2 \ln(R/a). \quad (33)$$

It follows that the ratio $W_{\mathrm{eff}}^{(2)}/W_{\mathrm{eff}}^{(3)}$ of the effective depolarization rates is proportional to $\dfrac{R^2}{L^2\ln(R/a)}$. Thus, we can see that, at sufficiently large values of the ratio R/L, the presence of correlations in the distribution of dislocations must have a drastic effect on the nuclear-depolarization process.

6. RESULTS OF EXPERIMENTAL-DATA PROCESSING AND THEIR DISCUSSION

We have investigated the angular asymmetry of beta radiation from ^{8}Li nuclei in LiF polycrystals at room temperature. The measurements have been

performed both in the mode that is differential with respect to time and in the integral mode. In the differential measurements, the asymmetry is proportional to the quantity that is obtained by averaging the polarization of β-nuclei over the time of sample irradiation with neutrons and over the duration $\Delta t = t_{n+1} - t_n$ of counting beta electrons in the nth channel of the time analyzer:

$$\frac{\varepsilon(t_n + \Delta t/2)}{\varepsilon_0} = \int\limits_{-\tau_{\rm irr}}^{0} d\tau \int\limits_{t_n}^{t_{n+1}} P(t-\tau) e^{-\lambda(t-\tau)} dt \Bigg/ \int\limits_{-\tau_{\rm irr}}^{0} d\tau \int\limits_{t_n}^{t_{n+1}} e^{-\lambda(t-\tau)} dt. \quad (34)$$

Here, $\lambda = \ln 2/T_{1/2} = 0.825\ \text{s}^{-1}$ is the rate of ^{8}Li beta decay and ε_0 is the limiting asymmetry value (that is, the value in the absence of a radio-frequency field). In each run of the measurements, the duration of sample irradiation with polarized neutrons was $\tau_{\rm irr} = 2.4$ s, while the channel width Δt was 0.2 s. The time spectrum was taken after treating the LiF powder with an external pressure. The data obtained in this way are presented in Fig. 1. Before pressing the sample, β-nuclei suffered virtually no depolarization. This indicates that the original lithium fluoride powder, which was obtained by the method of chemical precipitation was nearly free from defects. An analysis of the powder crystallites with an optical microscope revealed that they have a regular cubic shape and that the characteristic size of a crystallite is $R \approx 0.01$ mm.

In the absence of a radio-frequency field, a weak decrease in the asymmetry $\varepsilon(t)$ (it is shown by the dashed curve in Fig. 1) is due to the cross relaxation between ^{8}Li and ^{6}Li nuclei [5]. In all samples investigated in our experiments, the concentration of the ^{6}Li isotope was about 0.15%.

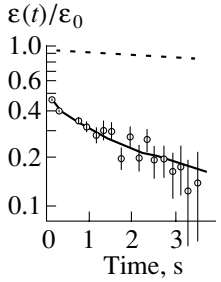

Fig. 1. Asymmetry of beta radiation from ^{8}Li nuclei as a function of time in a powder LiF sample treated with an external pressure of 190 MPa in a field of strength 216.3 G ($\tau_{\rm irr} = 2.4$ s, $\Delta t = 0.2$ s, $\varepsilon_0 = 5.68(4)\%$). The sample was irradiated with a radio-frequency field of amplitude $2H_1 = 35$ G at the frequency of $\nu = 2\omega_8/2\pi = 272.5$ kHz. The dashed curve represents the contribution to the depolarization of ^{8}Li nuclei from the cross-relaxation process involving ^{6}Li isotopes whose concentration in the sample is about 0.15%. The solid curve was calculated by formulas (31)–(34).

The experiments were performed at two values of the external-magnetic-field strength: 153.4 (at this value, the doubled Larmor frequency in ^{8}Li was $2\omega_8/2\pi = 193.2$ kHz) and 216.3 G ($2\omega_8/2\pi = 272.5$ kHz). The amplitude of the scanning radio-frequency field was $2H_1 = 15$ G and $2H_1 = 35$ G, respectively.

In the time-inegral mode of measurements (Figs. 2, 3), the asymmetry $\tilde{\varepsilon}(\nu = \omega/2\pi) = \varepsilon(t_0 + \Delta t/2)$ is accumulated in one time-analyzer channel that is open for a sufficiently wide (in relation to the beta-decay period) time interval $\Delta t \equiv \tau_{\rm obs}$.

The entire body of our experimental data concerning the resonance at the doubled Larmor frequency was subjected to a global treatment. In doing this, we took into account both the effect of the two-spin resonance [10] at the difference $\omega = \omega_7 - \omega_8$ of the Larmor frequencies in ^{7}Li and ^{8}Li and the weak contribution of the cross-relaxation process [5] involving the ^{6}Li isotope. The wing of the two-spin resonance was approximated by an exponential [22]. The line-shape function for the resonance at $\omega = 2\omega_8$ was taken to be a Gaussian function whose second moment is $4M_2$, where M_2 is the second moment of the Larmor resonance in ^{8}Li nuclei residing in LiF. Our experimental value of $M_2(2\omega_8)$, 27(3) kHz^2, is in good agreement with its theoretical estimate of 22 kHz^2. This is an important argument in favor of the quadrupole nature of the resonance at the doubled frequency.

In order to match the observed effective rate of the depolarization process with theoretical estimates, it was necessary to assume that the density of dislocations is $N_2 = 5(1) \times 10^7$ cm^{-2} and $N_3 = 9(2) \times 10^8$ cm^{-2} in the two cases considered in our investigation. From the literature, it is well known that the maximum accessible density of dislocations in LiF at the plasticity threshold (which is actually the fracture threshold) is 5×10^8 cm^{-2} [19]. Based on a comparison of our results with this last value, we arrive at the conclusion that, upon treatment of a powder sample with an external pressure, there arises a correlated two-dimensional distribution of dislocations in these crystallites.

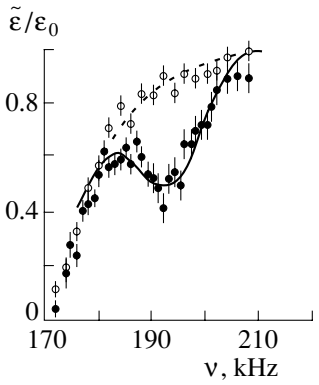

Fig. 2. β-NMR spectra of ^{8}Li nuclei according to measurements in the integral mode for LiF powder samples with respect to the frequency ν of an oscillating radio-frequency field of amplitude $2H_1 = 15$ G. Points represent (○) the β-NMR spectrum in the powder prior to treating it with an external pressure [these data were used in approximating (dashed curve) the wing of the shape function for the two-spin resonance at the difference of the Larmor frequencies in ^{7}Li and ^{8}Li] and (●) the β-NMR spectrum in the powder treated with an external pressure of 190 MPa. The solid curve was computed by formulas (31)–(34) with allowance for the parameter values of $H_0 = 153.4$ G, $\tau_{\rm irr} = 2.4$ s, $\tau_{\rm obs} = 4$ s, and $\varepsilon_0 = 5.86(16)\%$.

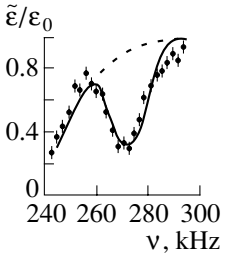

Fig. 3. (●) Integrated β-NMR spectrum of ^{8}Li nuclei in a LiF powder sample treated with an external pressure with respect to the frequency ν of an oscillating radio-frequency field of amplitude $2H_1 = 35$ G. The solid curve was computed by Eqs. (31)–(34) with allowance for the parameter values of $H_0 = 216.3$ G, $\tau_{\rm irr} = 2.4$ s, $\tau_{\rm obs} = 3$ s, and $\varepsilon_0 = 5.70(13)\%$. The dashed curve represents an exponential approximation of the wing of the shape function for the two-spin resonance at the difference of the ^{7}Li and ^{8}Li Larmor frequencies.

7. CONCLUSION

The present investigation has made it possible to establish unambiguously the nature of the nuclear resonance at the doubled Larmor frequency in nuclear probes of ^{8}Li in LiF crystallites. The resonance appeared upon treating, with an external pressure of 190 MPa, the powder sample under study, which consists of small crystallites. The only reasonable way to explain the emergence of the resonance is to assume that there arise dislocations in the powder crystallites. Our theoretical analysis has revealed that the resonance at the doubled frequency is characterized by a high sensitivity to quadrupole interactions; to state it otherwise, it is highly sensitive, in the case of cubic crystals, to the presence of structural defects generating an electric-field gradient at the positions of nuclear probes. Our calculations have demonstrated that the electric-field gradient depends on the distribution of dislocations in crystallites. Since the elastic fields of dislocations decrease rather slowly (in proportion to $1/r$), the presence of correlations in the orientation of dislocations may significantly increase the electric-field gradient at the positions of β-nuclei; on the contrary, chaoticity in the distribution of dislocations leads to the averaging of the electric-field gradient at the positions of resonating nuclei, thereby reducing it. This feature gives us sufficient grounds to believe that, upon a treatment of LiF powder samples, there arise, in crystallites, dislocations with a common direction of Burgers vectors. Owing to this, their deformation fields are added, causing some kind of a macroscopic crystallite deformation. The density of dislocations that has been found here for this case is $5(1) \times 10^7$ cm^{-2}, which is one-tenth as great as the maximum possible density of dislocations in LiF at the plasticity threshold. The competing hypothesis of a chaotic distribution of dislocations around a β-nucleus leads to the conclusion that the concentration of dislocations in LiF is much a higher—namely, $9(2) \times 10^8$ cm^{-2}, which is nearly twice as great as the admissible limit at the fracture threshold [19]. We deem that this proves the formation of a correlated structure of dislocations upon pressing lithium fluoride powders. In all probability, nascent fluctuations are directed along the ⟨110⟩ axis because, in LiF, a plastic deformation is most easily realized in planes of precisely the {110} type [19].

8. ACKNOWLEDGMENTS

This work was supported by the Russian Foundation of Basic Research (project nos. 00-02-17397 and 00-15-96656).

REFERENCES

1. F. L. Shapiro, Usp. Fiz. Nauk **65**, 133 (1958).
2. H. Ackermann, D. Dubbers, and H.-J. Stoeckmann, Adv. Nucl. Quadrupole Reson. **3**, 1 (1978).
3. H. Ackermann, P. Heitjans, and H.-J. Stoeckmann, Top. Curr. Phys. **31**, 291 (1983).
4. Yu. G. Abov, A. D. Gul'ko, F. S. Dzheparov, and S. S. Trostin, *Some Problems in Modern Nuclear Physics* (Nauka, Moscow, 1989), p. 193.
5. Yu. G. Abov, M. I. Bulgakov, S. P. Borovlev, *et al.*, Zh. Éksp. Teor. Fiz. **99**, 962 (1991) [Sov. Phys. JETP **72**, 534 (1991)].

6. Yu. G. Abov, A. D. Gul'ko, F. S. Dzheparov, *et al.*, *Modern Problems of Nuclear Physics and of the Physics and Chemistry of Condensed Media,* Ed. by Yu. G. Abov, A. L. Suvorov, and V. G. Firsov (Usp. Fiz. Nauk, Moscow, 1999), p. 155.
7. M. I. Bulgakov, F. S. Dzheparov, A. D. Gul'ko, *et al.*, Hyperfine Interact. **60**, 937 (1990).
8. F. S. Dzheparov and S. V. Stepanov, Preprint No. 139, ITÉF (Institute of Theoretical and Experimental Physics, Moscow, 1982).
9. K. Dorr, H.-J. Shoeckmann, *et al.*, J. Phys. C **15**, 4437 (1982).
10. Yu. G. Abov, M. I. Bulgakov, S. P. Borovlev, *et al.*, Pis'ma Zh. Éksp. Teor. Fiz. **35**, 424 (1982) [JETP Lett. **35**, 424 (1982)].
11. M. I. Bulgakov, A. D. Gul'ko, *et al.*, Pis'ma Zh. Éksp. Teor. Fiz. **27**, 481 (1978) [JETP Lett. **27**, 453 (1978)]; Preprint No. 138, ITÉF (Institute of Theoretical and Experimental Physics, Moscow, 1978).
12. A. Winnacker, D. Dubbers, F. Fujara, *et al.*, Phys. Lett. A **67A**, 423 (1978).
13. F. S. Dzheparov and S. V. Stepanov, *Modern Methods of NMR and EPR in Chemistry of Solid State* (Chernogolovka, 1985), p. 5.
14. Yu. G. Abov, M. I. Bulgakov, S. P. Borovlev, *et al.*, Izv. Akad. Nauk SSSR, Ser. Fiz. **50**, 2354 (1986).
15. P. C. Schmidt, K. D. Sen, T. P. Das, and A. Weiss, Phys. Rev. B **22**, 4167 (1980).
16. V. V. Lemanov, Zh. Éksp. Teor. Fiz. **40**, 775 (1961) [Sov. Phys. JETP **13**, 543 (1961)].
17. J. P. Hirth and J. Lothe, *Theory of Dislocations* (McGraw-Hill, New York, 1969; Atomizdat, Moscow, 1972).
18. L. D. Landau and E. M. Lifshitz, *Course of Theoretical Physics,* Vol. 7: *Theory of Elasticity* (Nauka, Moscow, 1987; Pergamon, Oxford, 1986).
19. B. I. Smirnov, *Dislocation Structure and Hardening of Crystals* (Nauka, Leningrad, 1981).
20. U. Haeberlen, *High Resolution NMR in Solids* (Academic, New York, 1976; Mir, Moscow, 1980); M. Mehring, *High Resolution NMR Spectroscopy in Solids* (Springer-Verlag, New York, 1976; Mir, Moscow, 1980).
21. M. Goldmant, *Spin Temperature and Nuclear Magnetic Resonance in Solids* (Clarendon, Oxford, 1970; Mir, Moscow, 1972).
22. Yu. G. Abov, A. D. Gul'ko, F. S. Dzheparov, *et al.*, Fiz. Élem. Chastits At. Yadra **26**, 1654 (1995) [Phys. Part. Nucl. **26**, 692 (1995)].
23. M. H. Cohen and F. Reif, Solid State Phys. **5**, 321 (1957).
24. F. S. Dzheparov and A. A. Lundin, Zh. Éksp. Teor. Fiz. **75**, 1017 (1978) [Sov. Phys. JETP **48**, 514 (1978)].
25. F. S. Dzheparov, V. S. Smelov, and V. E. Shestopal, Pis'ma Zh. Éksp. Teor. Fiz. **32**, 51 (1980) [JETP Lett. **32**, 47 (1980)].

Translated by A. Isaakyan

Physics of Atomic Nuclei, Vol. 65, No. 11, 2002, pp. 2009–2020. Translated from Yadernaya Fizika, Vol. 65, No. 11, 2002, pp. 2066–2078.

NUCLEI

Larmor Spin Precession and Neutron Optics

A. I. Frank, I. Anderson[1)], I. V. Bondarenko, A. V. Kozlov, P. Høghøj[1)], and G. Ehlers[1)]

Joint Institute of Nuclear Research, Dubna, Moscow oblast, 141980 Russia

Received March 11, 2002

Abstract—We consider the neutron-optical phenomena that emerge during the coherent interaction of a neutron with a sample when the neutron spin precesses in a magnetic field. As follows from general considerations, such an interaction gives rise to an extra precession phase, which is added to the Larmor precession phase. This phenomenon can be interpreted as a manifestation of the time delay due to a finite time of the neutron–sample interaction. The Larmor neutron spin precession with a constant frequency serves as a clock for measuring this time delay. We used such a clock to directly measure the difference between the neutron velocity in matter and its vacuum value. We also present the results of the first experiments in which Larmor clocks were used to measure the neutron tunneling time in the resonance of a quasi-bound state and the Bragg diffraction time. Prospects for further applications of the method are discussed. © *2002 MAIK "Nauka/Interperiodica".*

1. INTRODUCTION

It is well known that the neutron spin precession can be interpreted as the result of interference between the two spin components of the neutron wave function [1]. The validity of this approach was excellently demonstrated in experiments with neutron interferometers [2]. In general, the two plane waves

$$\psi_\pm = \exp[i(k_\pm x - \omega_\pm t)] \tag{1}$$

that correspond to the two spin components can differ both in wave numbers and in frequencies. The frequency difference arises if nonstationary devices are used to prepare the state with a precessing spin. If, however, only devices with a constant magnetic field are used for this purpose, then the two components of the wave function can differ only in the coordinate part. In that case,

$$k_\pm = k_0(1 \mp \mu B/E)^{1/2}, \quad E = \hbar^2 k_0^2/2m, \tag{2}$$

where k_0 is the wave number in the absence of a magnetic field; B is the magnetic induction; and m and μ are the neutron mass and magnetic moment, respectively. If the neutron moves in a constant magnetic field, then the phase difference Φ between the two waves identified with the precession angle depends only on the coordinate:

$$\Phi = \Delta k x \cong k_0 \frac{\mu B}{E} x = \omega_\mathrm{L} \frac{x}{v}, \tag{3}$$
$$\omega_\mathrm{L} = 2\mu B/\hbar, \quad \mu B \ll E.$$

Here, $\hbar$ is the Planck constant, v is the neutron velocity, and ω_L is the Larmor frequency.

[1)]Institute Laue–Langevin, Grenoble, France.

Let us now consider the case where a precessing neutron interacts with an object. The final state resulting from the coherent interaction can be described by introducing several two-component functions with complex amplitudes

$$f_\pm^{(i)} = \left|f_\pm^{(i)}\right| \exp(i\varphi_\pm^{(i)}), \tag{4}$$

where i is the channel number. The channels correspond to the transmission, reflection, or coherent scattering (diffraction by the object). Leaving aside the magnitude of each of the amplitudes, we focus on their phases. Because of the difference in the initial wave numbers k_+ and k_-, the values of φ_+ and φ_- in each channel will also differ. The coordinate part of the wave function in any channel is then

$$\Psi_\pm^{(i)}(x) = \left|f_\pm^{(i)}\right| \exp[i(k_\pm x + \varphi_\pm^{(i)})]. \tag{5}$$

This implies that the interaction gives rise to an extra precession phase,

$$\Delta\Phi^{(i)} = \varphi_+^{(i)} - \varphi_-^{(i)}, \tag{6}$$

which is added to the Larmor phase (3).

The extra precession phase attributable to the interaction with a nonmagnetic sample has long been known in neutron optics. Baryshevskii and Cherepitsa [3, 4] predicted the appearance of this phase during neutron diffraction by a nonmagnetic crystal. Frank [5, 6] found a similar effect during neutron refraction in matter and proposed to use it as the basis for the phase contrast method in neutron optics. The possibilities for using this phenomenon were also discussed in [7]. The first attempt to experimentally

observe the extra phase appearing during refraction was made in 1995 [8]. Subsequently, we performed such an experiment with a significantly higher accuracy [9, 10]. Below, we discuss the close relationship of these phenomena to the neutron interaction time.

2. OPTICAL SPIN ROTATION OF SPIN

2.1. Elementary Theory

Let us consider a simple example of the manifestation of the extra precession angle attributable to the interaction with a sample. Let the neutron traverse the distance L between points x_1 and x_2; there is a magnetic field B directed along the X axis in this entire region. Assume that the neutron spin at point x_1 is directed along the Z axis and that a d-thick slab of refracting material is placed on the beam path. According to aforesaid, the total precession phase must be expressed as

$$\Phi = \omega_{\mathrm{L}}\frac{L}{v} + \Delta\Phi. \tag{7}$$

Let us calculate the extra phase $\Delta\Phi$. In the absence of a field, the refraction in the sample causes the wave phase shift

$$\varphi = k[n(k) - 1]d, \tag{8}$$

where k is the wave number in a vacuum and n is the refractive index:

$$n = \sqrt{1 - \frac{4\pi\rho b}{k^2}} = \sqrt{1 - \frac{U}{E}}, \quad U = \frac{2\pi\hbar}{m}\rho b. \tag{9}$$

Here, ρ is the number density of nuclei in the material and b is the coherent scattering length. Assuming the Zeeman splitting $\Delta E = 2\mu B$ to be much smaller than the neutron energy E, we represent the phase difference between the two components as

$$\Delta\Phi = \frac{d\varphi}{dE}\Delta E = 2\mu B\frac{d\varphi}{dE}. \tag{10}$$

Simple calculations give

$$\Delta\Phi = \frac{2\mu B}{\hbar}\left(\frac{1-n}{n}\right)\frac{d}{v} \tag{11}$$
$$= \omega_{\mathrm{L}}\left(\frac{1-n}{n}\right)\frac{d}{v} \cong \omega_{\mathrm{L}}(1-n)\frac{d}{v}.$$

In most cases, $(1-n) \ll 1$ and the approximate equality in (11) holds with a high accuracy. Expression (11) was derived in [5, 6] from wave considerations similar to those given above, and the phenomenon itself was called optical spin rotation. Note one important circumstance. The factor $(1-n)$ in (11) is inversely proportional to the energy. Therefore, the effect itself $\Delta\Phi \propto v^{-3} \propto \lambda^3$, where λ is the neutron wavelength. Being barely measurable for thermal neutrons, the effect of optical spin rotation becomes significant for very cold and ultracold neutrons.

This result for $\Delta\Phi$ can also be easily obtained from the classical view of the time it takes for a neutron to traverse a sample of length d if its velocity in matter is assumed to be nv:

$$\Delta\Phi = \omega_{\mathrm{L}}\Delta t, \quad \Delta t = d\left(\frac{1}{nv} - \frac{1}{v}\right). \tag{12}$$

The equivalence of these two approaches is, of course, not accidental. The extra precession angle (optical precession) may well be interpreted as a manifestation of the neutron time delay that appears as the neutron flies through a refracting sample. Below, we return to this problem in connection with the interaction time in quantum mechanics.

2.2. The Experimental Setup and the Measuring Technique

Experimental observation of the phase shift due to the interaction with a sample involves significant difficulties. To explain one of them, let us write, so far arbitrarily, expression (7) as

$$\Phi = \omega_{\mathrm{L}}(t + \tau), \quad t = L/v, \tag{13}$$

where L is the length of the region with a magnetic field and τ is the neutron–object interaction time. For a reasonable length L, the time τ is several orders of magnitude shorter than the time of flight t. The relative smallness of τ, together with the requirement that the factor $\omega_{\mathrm{L}}\tau$ be practically measurable, imposes a lower limit on the Larmor frequency ω_{L}. Therefore, the factor $\omega_{\mathrm{L}}t$ becomes fairly large. This means that the measuring scheme being discussed requires a low beam-momentum spread $\Delta v/v$ for the Larmor phase variance to be moderately small: $|\Delta\Phi_{\mathrm{L}}| = |\omega_{\mathrm{L}}t\Delta v/v| \ll 1$. Otherwise, the beam will be depolarized and the measurement will not be possible. In practice, this condition is difficult to satisfy, because the required degree of monochromatization results in prohibitively large intensity losses.

The monochromatization problem can be circumvented by using a method called "neutron spin echo" (NSE) [11]. In this case, the neutrons successively traverse two rather than one flight base $L_{1,2}$ with the opposite precession direction. If the neutron velocity is constant along the entire path and if the condition

$$\int_{L_1} Bdl = \int_{L_2} Bdl \tag{14}$$

is satisfied, then the total Larmor phase on the path $L_1 + L_2$ is zero for all neutron velocities. Only the extent to which the echo condition (14) is satisfied imposes a practical constraint on the degree of

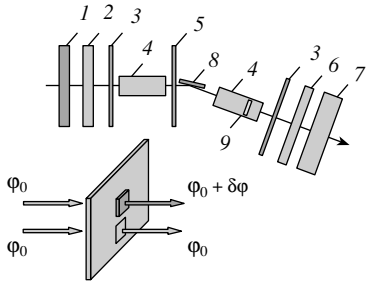

Fig. 1. The experimental setup with the IN15 spectrometer: (*1*) velocity selector, (*2*) polarizer, (*3*) $\pi/2$-flippers, (*4*) precession solenoids, (*5*) π-flipper, (*6*) polarization analyzer, (*7*) position-sensitive detector, (*8*) multilayer monochromator mirror, (*9*) sample position. The sample position is schematically shown below in one of the two beams formed by the diaphragm.

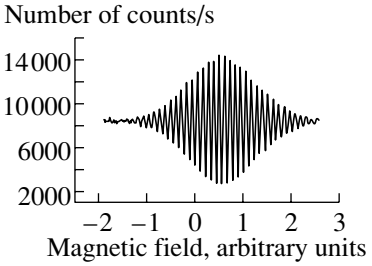

Fig. 2. Count rate against the additional magnetic-field strength in one of the solenoids (the echo pattern).

monochromatization. Placing the sample in one of the precession bases causes the phase to change by $\omega_L\tau$.

The first attempt to experimentally observe the neutron precession phase attributable to refraction in the sample was made in [8]. As was suggested in [5], the experiment was carried out with an NSE spectrometer. By measuring the extra precession angle when neutrons with the wavelength $\lambda = 5.7$ Å are passed through a long (up to 80 cm) silicon sample, the authors of [8] obtained $1 - n = (1.85 \pm 1.16) \times 10^{-5}$, where n is the refractive index. The calculated value was $1 - n = 1.07 \times 10^{-5}$.

We carried out a similar experiment using the IN15 spectrometer [12] at the Institut Laue–Langevin. Figure 1 shows the experimental setup. It is distinguished by an additional monochromator (*8*) (see Fig. 1) at the place where the sample is located in standard spin echo measurements. In our case, the sample was placed inside the precession solenoid.

As in most NSE spectrometers, the field in one of the solenoids can be changed in the IN15 instrument. This causes a change in the total precession phase and, accordingly, in the orientation of the polarization vector at the exit from the second solenoid. Since the neutrons then pass through the $\pi/2$ flipper and the analyzer, this change in the angle of the polarization vectors transforms into a change in the count rate, as shown in Fig. 2. The maximum oscillation amplitude of the count rate corresponds to the best approximation to the focusing condition (14), and the envelope shape depends on the velocity spectrum. By analyzing this kind of curve, we can obtain comprehensive information on the spectrum. In order to measure the precession phase Φ (for a given field B_0), it is by no means necessary to measure the entire curve each time. Near B_0, it can be assumed to be a sine wave $N(B) = a + b\sin[\Phi(B)]$ with a good accuracy. The oscillation period P can be determined from a single calibration measurement of the count-rate echo curve. In turn, to determine the phase, it will suffice to measure the count rate at three points, $B_0, B_0 \pm P/4$, corresponding to the phases Φ, $\Phi \pm \pi/2$. Solving the system of three equations with three unknowns a, b, and Φ yields the sought-for phase Φ. We made four measurements at the points Φ, $\Phi \pm \pi/2$, and $\Phi + \pi$, thereby overdetermining the system of equations. This made it possible to verify the consistency of the measurement results.

Stringent requirements are placed on the temporal stability of all setup parameters. The time variation in the magnetic field or in the effective precession base length due to thermal expansion of the construction results in a phase drift. Therefore, we simultaneously measured the precession phases in the two beams formed by the diaphragm. At each instant of time, only one beam passed through the sample, while the other beam was a reference beam. The sample was periodically moved from one beam to the other, which made it possible to separate the phase shift due to the presence of the sample from the instrumental phase difference between the beams. This method greatly increased the measurement stability, because the main sources of instability produced a simultaneous phase drift in both beams, while the remaining differential effect was averaged. A position-sensitive detector made such a synchronous measurement possible.

2.3. Experimental Results

We measured the precession phases introduced by samples for a number of materials [9, 10]. The measurements were carried out in a 0.13-T field with samples of various thicknesses. Figure 3 shows the results that we obtained.

Quite an unexpected result was obtained for pyrolytic graphite. In this case, the magnitude and even the sign of the extra phase depended on the sample orientation. It was by no means immediately clear

The results obtained for the density of the coherent scattering length ρb and the diamagnetic susceptibility χ (only statistical errors are given)

Material	ρb, 10^{-8} Å^{-2}		χ, 10^{-6} cm^3/g	
	experiment	tabular value	experiment	tabular value
Si	2.09 ± 0.03	2.15	-0.28 ± 0.03	-0.13
Be	9.65 ± 0.02	9.63	-1.77 ± 0.09	$\chi_{\|\|} = -2.38, \chi_\perp = -0.8$
Graphite	7.21 ± 0.13	7.5	-20.6 ± 0.17	$\chi_{\|\|} = -22.8, \chi_\perp = -0.4$

that this paradoxical effect was related to the anomalously large and anisotropic diamagnetic susceptibility of graphite. Since the magnetic induction B inside a diamagnetic is weaker than the external field H, the Larmor precession frequency decreases when a neutron penetrates the sample. For graphite, this effect exceeds the refraction effect. Therefore, instead of the extra phase attributable to the increase in the time of flight by refraction, we observe an effect of the opposite sign. However, it is caused not by the neutron "acceleration" in the material but by the slowdown of the specific Larmor clock used for the measurement. Thus, expression (11) for this effect should be rewritten to allow for diamagnetism as

$$\Delta\Phi \cong \omega_{\mathrm{L}}(1-n)\frac{d}{v} + \omega_{\mathrm{L}}\frac{B-H}{H}\frac{d}{v}. \qquad (15)$$

In contrast to the first refraction term proportional to the cube of the wavelength, the diamagnetic effect is proportional to the wavelength. Detection of this linear term would suggest the presence of a diamagnetic effect.

Therefore, we measured the wavelength dependence of the phase shift. At a fixed wavelength, we measured the extra phase shift for several thicknesses of samples of each material. Linear least-squares fitting of the experimental results yielded the specific phase shift per unit sample length at a given wavelength. The result of our analysis is represented by points with error bars in Fig. 4. The curves in Fig. 4 are the fits to the experimental data by the function $F(\lambda) = A\lambda + B\lambda^3$. Using the parameters A and B obtained from our analysis, we were able to obtain the diamagnetic susceptibility χ and the density of the coherent scattering length ρb for each of the materials. The table presents the results.

We see from the table that the experiemtal values of ρb are in satisfactory agreement with the tabular values and that the anomalous effect for graphite can be well explained by its diamagnetic properties. We also managed to reliably record the diamagnetic effect for beryllium. Crystal beryllium also possesses magnetic anisotropy. Unfortunately, however, the crystal orientation was not measured in the experiment, so no particular significance should be attached to the slight difference between the measured and tabular values of χ. The result for silicon is not completely clear. The experimentally obtained absolute value of the diamagnetic susceptibility χ is twice its tabular value. It should be noted, however, that we did not set the goal of carrying out a precision measurement of the extremely small effects caused by the diamagnetism of ordinary materials and did not analyze the possible methodological effects.

To conclude this section, we list our results. The

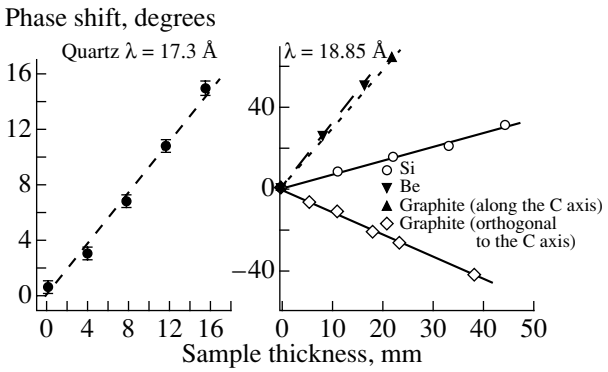

Fig. 3. The precession phase shift due to the presence of a sample in the beam.

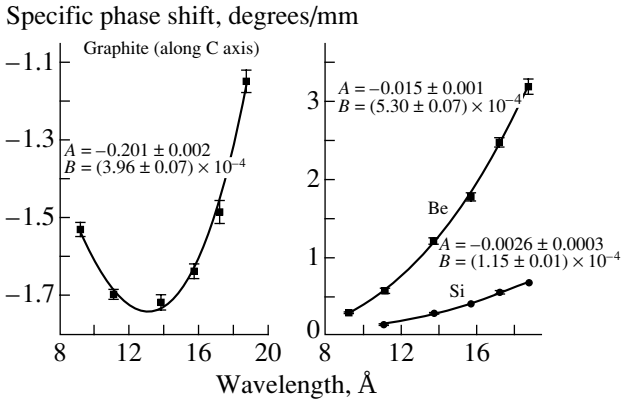

Fig. 4. Specific phase shift per unit sample length versus wavelength for pyrolytic graphite (left) oriented along the C axis and for beryllium and silicon (right).

extra precession phase attributable to refraction in the matter was recorded reliably. This effect can be described with a good accuracy by expression (11) corrected for the material diamagnetism (15). The method of measurement actually consisted in recording the change in the neutron time of flight, with the Larmor neutron spin precession frequency being used as a clock. The experimental results can be interpreted as a manifestation of the difference between the classical neutron velocities in a medium and in a vacuum, which was first measured in a direct experiment. Measurements over a wide wavelength range are a direct test of the dispersion law $k_1^2 = k^2 - 4\pi\rho b$, equivalent to expression (9) with an accuracy of several percent (k_1 is the wave number in the matter).

The high spectrometer stability and the two-beam technique made it possible to measure the change in precession phase by only a few degrees, while the measurement error of the time was 3.7×10^{-10} s. The total neutron time of flight of two solenoids with a total length of about 4 m is 0.017 s; i.e., it is eight orders of magnitude larger than the experimental sensitivity. Over this time, the precessing spin made 65 000 turns.

3. MEASURING THE TIME OF NEUTRON INTERACTION WITH QUANTUM OBJECTS

3.1. The Interaction and Tunneling Times in Quantum Mechanics

The interaction time in quantum mechanics has been the subject of intense debate for many decades. The question of how much time a particle spends in the interaction region appears to have been first formulated in [13]. In the 1950s, the concept of interaction time was formulated mathematically owing to the works by Bohm [14] and Wigner [15]. (The latter author also alluded to the unpublished paper by Eisenbud [16].) By now, the number of publications on this problem has reached several dozen. Here, we allude only to the reviews [17, 18] and to two recent papers [19, 20]. The wide variety of viewpoints expressed during this debate is largely attributable to differences in the definitions of physical clocks or the time measurement procedure.

The historically first definition of the interaction time going back to [14–16, 21] is the so-called phase time

$$\Delta t_\varphi = \hbar \frac{\partial \varphi}{\partial E}, \tag{16}$$

where φ is the phase shift of the plane wave that traverses the distance between points x_1 and x_2 enclosing the interaction (potential) region. Expression (16) corresponds to the total time spent by the particle on the path x_1–x_2, including the delay due to the interaction proper. Clearly, the time of free propagation in the absence of a potential should be subtracted from this time to determine the interaction time proper.

An important step in the study of the problem was taken in 1966 by Baz' [22]. Having turned to the problem of particle scattering by a spherical potential with the range of forces r_0, he defined the quantum clocks as follows: "Let us assume that there is an infinitesimal uniform field B directed along the z axis inside a sphere $R = r > r_0$; the field B is zero at $r > R$. We also assume that the scattered particles have spin $s = 1/2$ and magnetic moment $\mu = 2\mu s$. The spin (and the magnetic moment) of the incident particles is polarized along the x axis. If the particle falls into the sphere $r = R$, where the field B acts, then the magnetic moment begins to precess with the Larmor frequency $\omega = 2\mu B/\hbar$. Therefore, the spin of the particles that scattered and escaped from the sphere $r = R$ will be rotated through some angle θ relative to their initial direction. We can calculate this angle and, thus, determine the mean time of particle stay inside the sphere $r = R$: $T(E) = \theta/\omega$." [2)]

The "Larmor time" measured by such clocks is closely related to the Bohm–Wigner phase time. Indeed, the Larmor precession angle θ can be identified with the phase difference $\Delta\varphi$ between the two components of the wave function that correspond to the two spin components along the z axis and that differ in wave numbers (2). Defining, according to [22], the time delay due to the interaction as

$$\Delta t_\mathrm{L} = \frac{\Delta\varphi}{\omega_\mathrm{L}} \tag{17}$$

and taking into account the fact that

$$\omega_\mathrm{L} = \frac{2\mu B}{\hbar}, \quad 2\mu B = \frac{\hbar^2}{2m}(k_+^2 - k_-^2) = \Delta E, \tag{18}$$

we obtain the relation

$$\Delta t_\mathrm{L} = \hbar \frac{\Delta\varphi}{\Delta E}, \tag{19}$$

which is identical to (16) in the limit $B \to 0$.[3)]

Rybachenko [23] used the Baz' method to calculate the time it takes for a particle to pass through the barrier. In this one-dimensional problem, the region with a magnetic field occupies the interval (x_1, x_2), which encloses the potential region (a, b). The papers [22, 23] are currently the most cited papers on

[2)] In his paper, Baz' used the magnetic-field strength H rather than the magnetic induction B.

[3)] Actually, we have already used this relation between the interaction time and the derivative of the phase with respect to energy when calculating the optical spin rotation.

the quantum interaction time, and the term "Larmor clock" is widely used in scientific literature.

At the same time, the very idea of Larmor clocks has been repeatedly criticized (see, e.g., [17]). The point is that to properly solve the steady-state Baz'–Rybachenko problem with a plane wave, one has to take into account the wave reflection from the sharp boundaries of the region with a magnetic field. In this case, both the primary incident wave and the transmitted and reflected waves that appeared through the interaction with the potential are reflected. Allowance for the interference of all waves gives rise to an oscillating term in the final expression for the time; this term depends on the potential properties and on the geometry of the experiment. This circumstance led to the opinion that the method is improper. However, the method of solving this problem is well known [24]. It will suffice, first, to pass from a plane wave to an ensemble of quasi-monochromatic particles (a narrow wave packet) with width σ in k space and, second, to increase the extent of the region with a magnetic field in order for the conditions $|a - x_1|\sigma$ and $|b - x_2|\sigma \gg 1$ to be satisfied. Averaging over the ensemble then causes the oscillations to disappear in all final expressions. The averaged value should now also be taken as the interaction time. Using optical terminology, we can say that, in this case, the size of the region with a magnetic field significantly exceeds the coherence length, which makes the manifestation of interference phenomena impossible.

Recently, the interaction time has ceased to be a purely theoretical problem. The authors of [25] reported on experiments with electron tunneling in heterostructures in the presence of a magnetic field. Light-beam experiments on measuring the tunneling time were carried out in the mid-1990s [26, 27]. The rotation of the polarization plane in a birefringent medium [26] or the shift of an optical beam in total reflection [27] was used as the clock in these experiments. The first experiments with neutrons have also been carried out recently.

The authors of [28–30] came very close to the solution of the problem of measuring the interaction time. They used an NSE spectrometer to measure the extra precession angle that appears when the sample under study is placed on the path of neutrons precessing in a magnetic field. The geometry of the experiment corresponded to tunneling through the effective sample potential. However, the samples themselves were ferromagnetic and the dominating magnetic potential significantly differed for the two spin components. This difference between the conditions of the above experiment and those of the Baz'–Rybachenko setup, where the magnetic interaction was assumed to be small compared to the main scattering potential, makes doubtful the possibility of interpreting the results in terms of the interaction time.

3.2. Measuring the Tunneling Time in the Resonance of a Quasi-Steady State

We used the same instrument and mainly the same technique for the experiments on measuring the interaction time as those in the measurements of the time delay due to refraction. A significant difference was that, for the experiments on the time interaction, we had to pass to the geometry of grazing angles, which caused certain experimental difficulties.

An experiment on the resonance tunneling time was carried out with the so-called neutron interference filter [31–33]. This filter is a structure of three thin films deposited on a substrate (see Fig. 5). The outer films have a higher density of the scattering length ρb than the inner film. Since the interaction of long-wavelength neutrons with matter is well described by the effective potential $U = (2\pi\hbar^2/m)\rho b$, the potential structure of the filter is a double-humped barrier with a well in the middle. For appropriately chosen parameters, a quasi-bound state can appear in this potential. In this case, the filter transmission function has a distinctly resonant pattern.

We used a filter composed of two Ni layers (with a small amount of dissolved nitrogen) and a Ti/Zr film between them. The nitrogen admixture to nickel reduced the Curie temperature to a value much lower than the room temperature. The filter was prepared by magnetron sputtering on a silicon substrate. The layers were 300, 195, and 300 Å thick. The outer Ni(N) layers had a relatively high effective potential ($\sim$230 neV), while the effective potential of the Ti/Zr layer was nearly zero. In this structure, there was one level of a quasi-bound state with energy $E_0 \cong$ 127 neV and a half-width on the order of 4 neV.

We determined the spectrum of the incident neutrons from the Fourier transform of the count-rate echo curve. The spectral maximum corresponded to the wavelength $\lambda = 20.1$ Å with a half-width $\Delta\lambda/\lambda \cong 4.8\%$. Since the neutron energy was much higher than the filter resonance energy, the experiment was carried out in the geometry of grazing angles. The sample was a pile of 32 individual filters 20×26 mm in size cut out from the same 0.6-mm-thick plate after sputtering. The neutrons fell on the multilayer filter structure from the silicon substrate, as shown in Fig. 6. The angular distribution of the beam was formed by several slit apertures. Its calculated width was 3.2 mrad. The sample was fixed in a special device, a simple nonmagnetic goniometer, which was, in turn, placed inside the precession solenoid (see

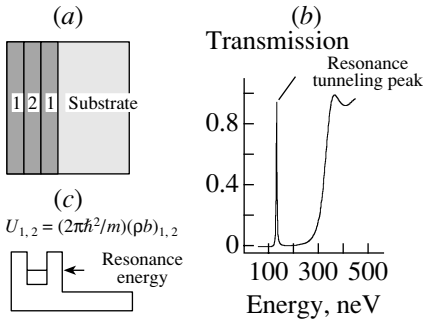

Fig. 5. The interference filter: (*a*) structure of three thin films 1–2–1, (*b*) transmission function, and (*c*) effective potential.

Fig. 1). The angle of neutron incidence on the sample was varied manually by turning the screw. The object was moved between the beams automatically with a pneumatic drive.

At a zero angle of incidence, the neutrons can freely pass through the silicon substrate without touching the multilayer filter structure. As the grazing angle increases, the probability of this direct passage decreases and becomes zero when the condition $\tan\alpha \approx \alpha = d/L$ is satisfied (see Fig. 6). In this case, the neutrons for which the resonance tunneling condition is not satisfied are reflected from the nickel films. Since detection is made by a position-sensitive detector, the reflected neutrons emerging from the sample at an angle different from the initial angle can be easily separated from the neutrons that directly passed through the sample. As the angle of incidence increases further, a secondary reflection from the nickel layer of the neighboring plate in the pile becomes possible. The doubly reflected neutrons emerge from the sample at the same angle as those passed without any reflection. They are indistinguishable from the latter and are the background source.

Figure 7 shows the measured dependence of the count rate on the grazing angle. The minimum count rate at an angle of 23 mrad corresponds to the overlap angle of the direct beam. The increase in count rate at large angles corresponds to the region of double reflection. Our results are in reasonable agreement with predictions, but it proved to be impossible to distinguish the resonant transmission peak in such measurements. According to calculations, the resonant tunneling should have taken place at $\alpha_r = 24.8$ mrad, i.e., slightly to the right of the minimum. Since the angular width of the tunneling peak, $\Delta\alpha \approx 0.4$ mrad, is an order of magnitude smaller than our angular resolution, its intensity is low.

This peak appears to be masked by background in the entire range of angles. At large angles, the background due to double reflection dominates. The background of direct transmission dominates to the left of the peak (and the count-rate minimum). Although the tunneling peak was not clearly distinguished, we measured the neutron precession phase in a relatively broad range of angles. The magnetic field on the sample was $B = 190$ G. Figure 8 shows the results of this measurement. As we see from the figure, the extra precession phase significantly increases near the expected position of the resonant tunneling peak (marked by an arrow). The delay corresponding to the maximum precession phase reaches $(2.17 \pm 0.2) \times 10^{-7}$ s. At small angles corresponding to direct transmission, the delay is close to 1.9×10^{-8} s caused by refraction in silicon (the dashed curve in the figure).

It would be reasonable to compare the measured delay in the neutron time of flight with the theoretical tunneling time. We determined the complex amplitude of the transmitted wave from the solution of the Schrödinger equation for the potential structure corresponding to the sample parameters. Near the resonance, the wave phase changes sharply, and, according to (19), the significant phase gradient corresponds to a large time delay. Exactly at the resonance, the calculated tunneling time is 4.26×10^{-7} s, while the time averaged over the entire transmission line is 2.27×10^{-7} s. Thus, the experimental delay agrees with the calculation, within the error limits.

We can probably assert with a high degree of confidence that the experimentally recorded significant time delay in neutron propagation is attributable to

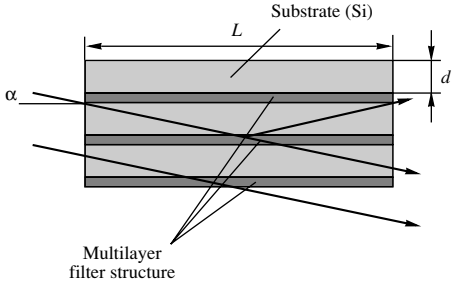

Fig. 6. Sample geometry in the experiment on the tunneling time.

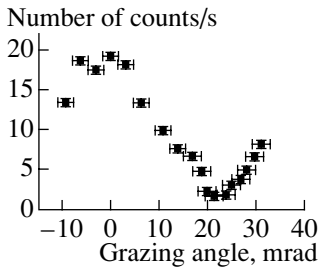

Fig. 7. Count rate versus grazing angle.

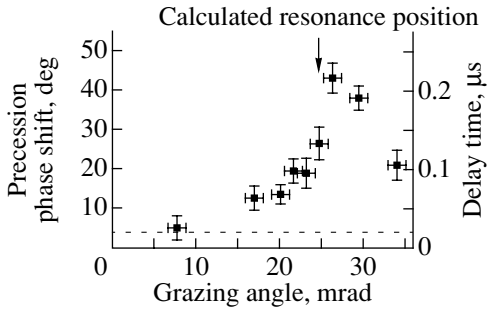

Fig. 8. The precession phase shift and the sample passage time versus grazing angle. The dashed line represents the phase shift due to refraction in the substrate (Si).

the passage time of the resonance of a quasibound state.

However, there is one fact that cannot yet be explained satisfactorily. The point is that the peak in the curve of the delay time (Fig. 8) has a width on the order of 15 mrad, while the calculated width of the angular distribution is several times smaller. Thus, the assumption of a physical broadening of the angular neutron distribution seems to be in conflict with the large time delay. We hope to continue these measurements in the nearest future with improved experimental conditions.

3.3. Measuring the Bragg Diffraction Time

In 1981, Baryshevskii [34] considered the problem of the diffraction of a neutron with a precessing spin by a nonmagnetic crystal. He showed that, in this case, the pattern of spin evolution does not reduce to the simple pattern of Larmor precession but significantly depends on the diffraction conditions. The physics of such multifrequency precession is quite simple. Close to the Bragg conditions, the phase of the wave produced by diffraction sharply depends on the wave number of the initial incident wave. In the presence of a magnetic field, the two spin components of the wave function have different wave numbers (2). The difference in the wave numbers of the initial wave leads to an extra phase difference between the final waves, which implies the appearance of an extra precession angle. According to the above results, we can, following the idea of A.I. Baz', associate this angle with the interaction time, in this case, with the diffraction time. Physically, the picture is quite similar to the case of resonant tunneling considered above.

Since the corresponding experiment is difficult to carry out, the multifrequency precession during neutron diffraction by a single crystal has not yet been observed. However, we attempted to carry out such an experiment with an artificial one-dimensional crystal, a Bragg mirror.

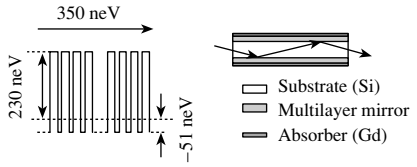

Fig. 9. The effective potential of a Bragg mirror and the sample structure.

In this experiment, we again used a pile of samples, each being a silicon plate 0.7 mm in thickness and 20×35 mm in size. A periodic thin-film structure composed of 30 pairs of Ni(V) and titanium layers was deposited on both sides of the plate. The films in each pair were 130 and 70 Å thick, respectively. A 7% admixture of vanadium to nickel reduced the Curie temperature. The densities of the scattering length for Ni(V) and Ti differ greatly (see Fig. 9), so the described structure is an interference mirror for neutrons with wavelengths of 430–530 Å. These wavelengths correspond to an energy on the order of 350 neV. The multilayer reflecting structure was coated with a 1000-Å-thick gadolinium film to absorb the neutrons that were not reflected from the mirror. The plate length was chosen in such a way that the neutrons underwent two reflections before emerging from the sample when the Bragg condition is satisfied.

We carried out our measurements with neutrons with the wavelength $\lambda = 19.8$ Å at $\Delta\lambda/\lambda = 7.6\%$. Figure 10 shows our main experimental results. In Fig. 10*a*, the counting rate is plotted against sample rotation angle. The right peak in this curve corresponds to double Bragg reflection. Its position and width are in reasonable agreement with the calculated values ($\theta_B = 43$ mrad at a half-width of 8 mrad). At the same time, the theoretical coefficient of reflection from an ideal structure at the Bragg peak is close to unity. In the experiment, it is appreciably smaller. The measured neutron delay time in the position of direct transmission was $(2.41 \pm 0.03) \times 10^{-8}$ s, which is close to the calculated value of 2.37×10^{-8} s related to refraction in the silicon substrate. However, in the geometry of double Bragg reflection, the delay increased by an order of magnitude and reached $(3.12 \pm 0.03) \times 10^{-7}$ s.

3.4. A Brief Discussion of the Results of the Experiments on the Interaction Time

The directly measured quantity in our experiments was the extra precession phase that appears when the object under study is placed in a beam of precessing neutrons. Based on the concept of a Larmor clock, we compare the recorded phase shift with the time delay

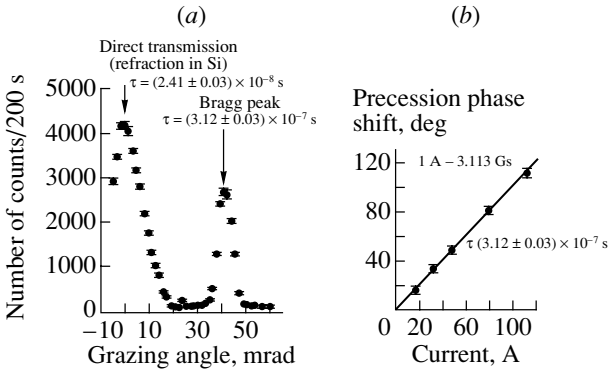

Fig. 10. (*a*) Count rate versus angle in the experiment on the diffraction time. The delay times measured at two points are shown. (*b*) Precession phase at the Bragg reflection peak versus current in the precession solenoid. The current–field relation and the delay time τ determined from the slope of the fitting straight line are shown.

due to the duration of the neutron-wave interaction with the object, according to (19).

Experimental conditions. The neutron reflection from the magnetic-field boundary may be ignored, because the characteristic size of the region with a magnetic field exceeds the coherence length by many orders of magnitude. The perturbing effect of the magnetic filed is also small. In a grazing-incidence geometry, the experimental conditions are determined by the wave vector component normal to the sample surface, $k_\perp = k\theta$, where θ is the grazing angle. Let us estimate the energy difference between the two spin components by considering only such normal motion:[4)]

$$\Delta E_{\mathrm{B}} = \frac{\hbar^2}{2m}(k_{\perp+}^2 - k_{\perp-}^2) = 2\mu B\theta^2 \approx 4 \times 10^{-12}\ \mathrm{eV}.$$

This value should be compared with the effective potential for neutrons $U \approx 10^{-7}$ eV. Thus, the experiment physically provides the condition for the passage to the limit $B \to 0$ in expression (19) for the Larmor time. Therefore, we can assume that both conditions for the validity of comparing the extra precession phase with the interaction time, i.e., the validity condition for Larmor clocks, are satisfied in the experiment.

Main results. In both cases, we recorded a relatively large (of the order of 0.2 μs) interaction time. This is the time during which a neutron with a "normal" velocity of several m/s remains localized in a region with sizes on the order of 10^{-5} cm. In the case of scattering through a quasi-bound state, the interaction time is of the same order of magnitude as the state lifetime $\tau_r = \hbar/\Gamma$, where $\Gamma \approx 4 \times 10^{-9}$ eV is the resonance width. In the case of Bragg reflection, however, the resonance width is $\Gamma \approx 10^{-7}$ eV. This corresponds to the resonance time $\tau_r \approx 7 \times 10^{-9}$ s, which is a factor of 20 lower than the recorded value. However, there is no contradiction here. The comparison of the scattering time with the resonance time obtained from the uncertainty relation is physically unjustified. The point is that the quantity Δt appearing in the uncertainty relation $\Delta E \Delta t \geq \hbar$ is the uncertainty in the exact knowledge of the collision time rather than in its duration (see, e.g., [35]).

4. NEUTRON SPIN PRECESSION AND PHASE CONTRAST IN THE OPTICS OF VERY SLOW NEUTRONS

We have already noted above that the experiment on observing the extra precession phase due to refraction is quite similar to the experiment with a neutron interferometer [1, 7]. In the latter case, only one of the two coherent waves passes through the sample and refraction in the sample results in the phase difference $\varphi = k(1-n)d$. This difference leads to a cosine-wave dependence of the intensity of the beam produced by the interference of two waves. In the experiment described in Section 2, two coherent waves with different wave numbers pass through a refracting sample. In this case, the waves coincide in space, but, because of the difference between the wave vectors, a differential effect appears; this effects that manifests itself in the precession phase. Expression (8) for the extra phase contains the same factor $(1-n)d$ that expresses the difference between the geometric and the optical paths in the sample. When the beam passes through the $\pi/2$ flipper and the analyzer, its intensity also exhibits a cosine-wave dependence on the precession phase (see Fig. 11).

This analogy gives grounds to hope that neutron spin interferometry (NSI) can be very useful in developing the phase contrast method in applied neutron optics [6, 7]. An important, if not crucial, factor here is the cubic wavelength dependence of the extra precession angle. In the experiment described in Section 2, the extra precession angle due to neutron refraction in quartz was about 20 degrees/cm for $\lambda =$ 20 Å and $B = 1300$ G. If a similar experiment were carried out with ultracold neutrons ($\lambda \approx 500$ Å), then refraction in quartz would produce an effect on the order of 2 degrees/μm in a relatively weak magnetic field (20 G).

To implement this idea requires creating a compact device, an NSE spectrometer for ultracold or very cold neutrons. Recall that we need to prepare a

[4)] In our experiment, the magnetic-field gradient near the edges of the precession solenoids is parallel to the neutron velocity vector, along the solenoid axis.

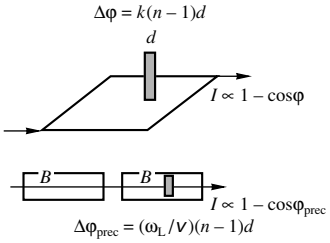

Fig. 11. The interferometer with coherent wave splitting and the spin-optical experiment.

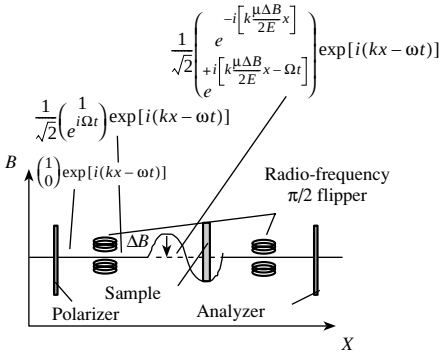

Fig. 12. A possible arrangement of the NSE spectrometer for very slow neutrons.

state in which the spin would be directed across the field and the spin components of the wave function would differ in the wave numbers. In the classical spin echo scheme, both these goals are accomplished using the same device, a spin flipper. Its operation is based on the nonadiabatic entrance of an initially polarized neutron into a region where the magnetic field is oriented differently than the initial one (see, e.g., [36]). Upon precession in this new field by an angle of $\pi/2$, the neutron nonadiabatically returns to the initial field.

This method works well for thermal and cold neutrons, but it is difficult to use for very cold or, in particular, ultracold neutrons. The point is that, because of the low neutron velocity, the nonadiabatic conditions can be satisfied only by placing the construction elements (the solenoid winding, the superconductive screen, etc.) directly in the neutron beam. The obstacle here is the rapid increase in the sensitivity of the NSI method with wavelength. The extra precession angle can arise even from refraction in the material of the construction elements, which imposes severe and difficult-to-fulfill requirements on the accuracy and homogeneity of their production.

A possible solution is to separate the spin flipper that prepares a state with a precessing spin from the spin echo device proper, where the two spin components of the wave acquire different wave numbers. Figure 12 shows a possible scheme of this device. This scheme uses a radio-frequency resonance flipper. This nonstationary device prepares a state with a precessing spin, but the spin components of the wave function differ in frequency rather than in wave number. The difference in the wave numbers appears if the neutrons enter a region of space where the magnetic-field strength $B + \Delta B$ differs from the field B in which the resonance spin rotation was made. Similar to expression (2), the wave numbers in the field $B + \Delta B$ are now given by the relation

$$k_\pm = k_0(1 \mp \mu\Delta B/E)^{1/2}, \qquad (20)$$

while the echo condition is given by expression (13), where ΔB should be substituted for B. Note that the field direction in the entire device is constant and that the change in the field strength can satisfy the adiabatic conditions.

Another possible method is based on the principle of neutron resonant spin echo in a zero field [37–39]. In this method, the magnetic field exists only in the radio-frequency flipper; passing through it, the neutrons appear in a zero field. In this case, the two spin components of the wave function for the resulting state differ both in frequency and in wave number.

The difficulty in using this method for very slow neutrons is that the spin of a precessing neutron makes a complete turn on a short path $\Lambda = \lambda E/(\mu B)$, which imposes stringent requirements on the positioning accuracy of the flipper and its geometry. The problem can be solved if we use a flipper made of a thin magnetic film whose induction direction is controlled by a relatively weak external field [40]. After passing through such a device, the component of the wave function with unchanged spin differs from the initial component only in amplitude,

$$\Psi_+(x,t) = t_+ \exp[i(k_0 x - \omega t)], \qquad (21)$$

while the other spin component is

$$\Psi_-(x,t) = t_- \exp[i(k_0(1-\gamma)^{1/2}x - \omega t + \Omega t)], \qquad (22)$$

$$\gamma = \Omega/\omega,$$

where Ω is the field rotation frequency. The spin rotation through $\pi/2$ corresponds to the equality of the amplitudes t_+ and t_-.

As we see, the spin components again differs in wave number. Therefore, according to the above general considerations, refraction in the sample will again give rise to the extra precession angle. As above, its value is described by expression (11), where the rotation frequency Ω should be substituted for the Larmor frequency ω_L. The sequence of $\pi/2$, π, $\pi/2$ flippers typical of NSE can be used for the purposes of phase contrast. In this case, the sample should be

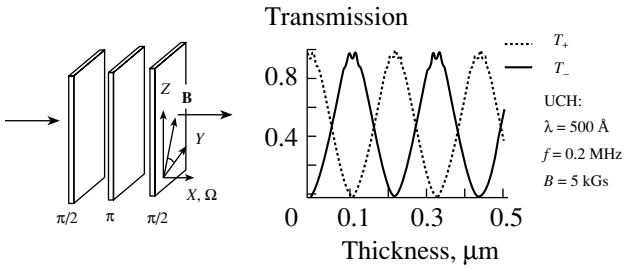

Fig. 13. A micro-NSE spectrometer with film spin flippers based on the rotation of magnetic induction. The intensities $T_\pm = |t_\pm|^2$ of the transmitted waves with the initial and reversed spin projections are plotted against film thickness.

placed in the gap between any of the flipper pairs. The magnetic induction inside all three magnetic films can be rotated synchronously. The $\pi/2$ and π flippers differ only in thickness, because both amplitudes t_+ and t_- exhibit a periodic dependence on the magnetic thickness (see Fig. 13).

5. CONCLUSION

We have considered some coherent phenomena that appear when a neutron wave with a spin precessing in a magnetic field interacts with matter. We call this division of neutron optics neutron spin optics (NSO) for short. NSO is now transforming from the object of purely theoretical investigation into a division of experimental physics. The discovery and subsequent wide use of the neutron spin echo method associated with the works by F. Mezei played a crucial role in this transformation. It is currently becoming clear that the NSO method, or, as it was called in [7], the NSI method, can be used to measure subtle neutron-optical effects. The relationship of this method to the concept of a quantum Larmor clock, which was initially put into scientific use by Baz' as an elegant theoretical technique, has now been realized. A further development of the method may allow a comprehensive program of experimental research on the interaction time in quantum mechanics to be implemented. The demonstration of the existence of optical spin rotation results in more optimistic prospects for a practical use of this phenomenon as a phase-contrast method. The idea of a phase-contrast neutron microscope now does not appear too utopian.

ACKNOWLEDGMENTS

We are grateful to V.V. Vasil'ev for help in the experiment and to V.E. Bunakov, G. Kali, V.G. Nosov, and B. Farago for stimulating discussions.

This work was supported by the Russian Foundation for Basic Research (project no. 01-02-17005) and the INTAS (grant no. 00-00043).

REFERENCES

1. F. Mezei, Physica B (Amsterdam) **151**, 74 (1988).
2. G. Badurek, H. Rauch, and J. Summhammer, Physica B (Amsterdam) **151**, 82 (1988).
3. V. G. Baryshevskiĭ, Pis'ma Zh. Éksp. Teor. Fiz. **33**, 78 (1981) [JETP Lett. **33**, 74 (1981)].
4. V. G. Baryshevskii and S. V. Cherepitsa, Phys. Lett. A **90A**, 267 (1982).
5. A. I. Frank, in *Proceedings of the 5th International School on Neutron Physics, Alushta, 1986,* D3,4,17-86-747 (Ob'edin. Inst. Yad. Issled., Dubna, 1986), p. 192.
6. A. I. Frank, Nucl. Instrum. Methods Phys. Res. A **284**, 161 (1989).
7. V. G. Baryshevskii, S. V. Cherepitsa, and A. I. Frank, Phys. Lett. A **153**, 299 (1991).
8. M. Hino, N. Achiwa, S. Tasaki, *et al.*, Physica B (Amsterdam) **213–214**, 842 (1995).
9. A. I Frank, I. V. Bondarenko, A. V. Kozlov, *et al.*, in *Proceedings of the VIII International Seminar on Interaction of Neutrons with Nuclei (ISINN-8), JINR, Dubna, 2000,* E3-2000-192, p. 215.
10. A. I. Frank, I. V. Bondarenko, A. V. Kozlov, *et al.*, Physica B (Amsterdam) **297**, 307 (2001).
11. *Neutron Spin Echo,* Ed. by F. Mezei (Springer-Verlag, Heidelberg, 1980).
12. P. Schleger, B. Alefeld, J. F. Barthelemey, *et al.,* Physica B (Amsterdam) **241–243**, 164 (1998).
13. L. A. MacColl, Phys. Rev. **40**, 621 (1932).
14. D. Bohm, in *Quantum Theory,* (Prentice-Hall, New York, 1951), p. 260.
15. E. P. Wigner, Phys. Rev. **98**, 145 (1955).
16. L. Eisenbud, PhD Dissertation (Princeton, 1948).
17. E. H. Hauge and J. A. Støvneng, Rev. Mod. Phys. **61**, 917 (1989).
18. R. Landauer and Th. Martin, Rev. Mod. Phys. **66**, 217 (1994).
19. C. R. Leavens and G. C. Aers, Phys. Rev. B **40**, 5387 (1989).
20. C. Bracher and M. Kleber, Ann. Phys. (Leipzig) **4**, 696 (1995).
21. T. Smith, Phys. Rev. **118**, 349 (1960).
22. A. I. Baz', Yad. Fiz. **4**, 252 (1966) [Sov. J. Nucl. Phys. **4**, 182 (1966)].
23. V. F. Rybachenko, Yad. Fiz. **5**, 895 (1967) [Sov. J. Nucl. Phys. **5**, 635 (1967)].
24. J. P. Falck and E. H. Hauge, Phys. Rev. B **38**, 3287 (1988).
25. P. Gueret, A. Baratoff, and E. Marclay, Europhys. Lett. **3**, 367 (1987).
26. M. Deutsch and J. E. Golub, Phys. Rev. A **53**, 434 (1996).
27. Ph. Balcou and L. Dutriaux, Phys. Rev. Lett. **78**, 851 (1997).
28. M. Hino, N. Achiwa, S. Tasaki, *et al.*, Physica B (Amsterdam) **241–243**, 1083 (1998).
29. M. Hino, N. Achiwa, S. Tasaki, *et al.*, Phys. Rev. A **59**, 2261 (1999).
30. M. Hino, N. Achiwa, S. Tasaki, *et al.,* Phys. Rev. A **61**, 013607 (2000).

31. A. Steyerl, W. Drexel, S. S. Malik, and E. Gutsmiedle, Physica B (Amsterdam) **151**, 36 (1988).
32. I. V. Bondarenko, V. I. Bodnarchuk, S. N. Balashov, *et al.*, Yad. Fiz. **62**, 775 (1999) [Phys. At. Nucl. **62**, 721 (1999)].
33. I. V. Bondarenko, A. I. Frank, S. N. Balashov, *et al.,* Nucl. Instrum. Methods Phys. Res. A **440**, 591 (2000).
34. V. G. Baryshevskiĭ, Pis'ma Zh. Éksp. Teor. Fiz. **33**, 78 (1981) [JETP Lett. **33**, 74 (1981)].
35. A. I. Baz', Ya. B. Zel'dovich, and A. M. Perelomov, *Scattering, Reactions and Decays in Nonrelativistic Quantum Mechanics* (Nauka, Moscow, 1966; Israel Program for Scientific Translations, Jerusalem, 1966).
36. Yu. G. Abov, A. D. Gul'ko, and P. A. Krupchitsky, *Polarized Slow Neutrons* (Atomizdat, Moscow, 1966).
37. R. Golub and R. Gähler, Phys. Lett. A **123**, 43 (1987).
38. R. Gähler and R. Golub, J. Phys. (Paris) **49**, 1195 (1988).
39. T. Keller, P. Zimmermann, R. Golub, and R. Gähler, Physica B (Amsterdam) **162**, 327 (1990).
40. A. I. Frank and A. V. Kozlov, in *Proceedings of the V International Seminar on Interaction of Neutrons with Nuclei (ISINN-5), Dubna, 1997,* E3-97-213 (JINR, Dunba, 1997), p. 411.

Translated by M. Kobrinsky

Physics of Atomic Nuclei, Vol. 65, No. 11, 2002, pp. 2021–2028. Translated from Yadernaya Fizika, Vol. 65, No. 11, 2002, pp. 2079–2088.

NUCLEI

Precise Atomic Scale Studies of Material Sputtering by Light-Ion Gases in the Prethreshold Energy Region

A. L. Suvorov*

Institute of Theoretical and Experimental Physics, Bol'shaya Cheremushkinskaya ul. 25, Moscow, 117259 Russia

Received October 17, 2001

Abstract—The basis and prospects of a new original technique of determining the yields of the sputtering of conductive materials and subatomic films on their surface by light ion gases in the prethreshold energy region (from 10 to 500 eV) are discussed. This information is of great importance both for science and applications. The technique is based on special modes of field ion microscopy and includes the cleaning of specimens by field-induced desorption and evaporation, and subsequent operations with the atomically clean and atomically smooth surface in a wide temperature range from cryogenic temperatures. The technique enables one to identify single surface vacancies, that is, to directly count single sputtered atoms. The original results obtained with the developed technique are briefly reviewed. The energy thresholds of sputtering and the energy dependences of the sputtering yields in the prethreshold energy region are presented and analyzed for beryllium, tungsten, tungsten oxide, mixed tungsten–carbon layers, three carbon materials, and subatomic carbon films on the surface of certain metals bombarded by hydrogen, deuterium, and/or helium ions. © *2002 MAIK "Nauka/Interperiodica"*.

1. INTRODUCTION

I present the concepts of a highly sensitive technique developed at the Institute of Theoretical and Experimental Physics for measuring the yields Y of sputtering of conductive materials by light ion gases (hydrogen, deuterium, and helium) in the prethreshold region (from a few to a few hundred eV) and some unique results obtained with this technique. It is well known that this information is of great importance both for science and applications.

A vast body of data on sputtering yields and their energy, angular, and temperature dependences has been obtained by various experimental methods for a wide variety of particles bombarding the surface of solids [1]. These data are strongly inconsistent, and inconsistency increases with decreasing energies of bombarding particles [2]. This is not surprising because the available methods, due to their features, are highly inaccurate in the prethreshold energy range. Determination of the energy threshold E_{th} of sputtering is particularly difficult, because it requires particularly sensitive, high-resolution methods identifying each vacancy produced on the sputtered surface by a bombarding ion (that is, we should count each atom removed from the surface). Among current experimental methods of surface diagnostics, field ion microscopy best meets these requirements. It is extensively used to study the structure of surface atomic layers; to investigate the formation, behavior, and evolution of crystal structure defects; and to analyze various radiation effects on the surface and in the volume of conductive materials [3–5].

This paper presents the basis of the novel highly sensitive experimental technique, as well as the results of its application for determining the thresholds of the sputtering of tungsten, tungsten oxide, mixed tungsten–carbon layers, beryllium, three carbon materials, and subatomic carbon films on several metallic substrates by light ion gases (H^+, D^+, and He^+). To a great extent, this paper reviews the results obtained by our group [6–9].

2. BASIS AND CAPABILITIES OF THE TECHNIQUE

In studies [6–9], we used tips with average radii $\bar{R}_{\mathrm{o}} \leq 100$ nm, which are typical for field ion microscopy. Some details of tip preparation for each of the studied materials are presented below.

The investigations were carried out with an original all metal field ion microscope [10]. A grid of the metal-ceramic cathode assembly was used to produce a set of pulses between the needle-shaped specimen (cathode) and microchannel plate (anode). The assembly was placed between the specimen and phosphor screen only during single irradiation pulses, which were produced by means of a two-step pulse change in high-voltage polarity. In this case, gas,

*e-mail: suvorov@itep.ru

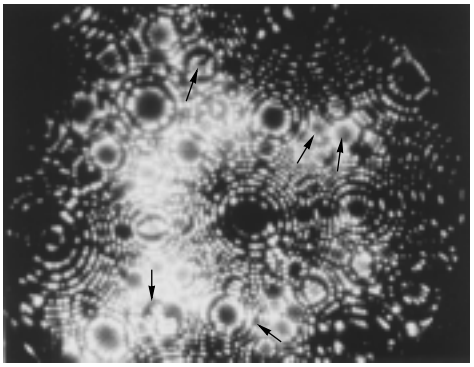

Fig. 1. Field ion image of the surface of the pure-tungsten specimen; the arrows indicate individual vacancies produced by a single pulse of D^+ ions [6].

which could simultaneously serve as an imaging gas, was ionized via the electron-impact mechanism at the instant of applying a short high-voltage pulse with opposite (negative) polarity and electron field emission by the specimen. The duration of these ion-producing high-voltage pulses was $\Delta\tau_1 \leq 0.1$ μs, and their amplitude was equal to $\Delta V_1 = 5.0$ kV. Simultaneously with a high-voltage pulse, a low-voltage negative pulse was applied to the specimen. Its duration was $\Delta\tau_2 \geq 10$ μs, and its amplitude ΔV_2 corresponded to the preset energy of bombarding ions and was varied from 10 to 500 V with a step of no less than 10 V. Diverse control analyses with various sequences of pulses of different parameters (in the diode and triode configurations) were carried out in parallel. In the triode configuration, the above mentioned grid of the cathode assembly was used.

Substantially different procedures were applied to measure sputtering yields Y for specimens (such as tungsten; see Fig. 1) for which good field ion images can be obtained and specimens (beryllium, carbon, etc.) for which good stable images cannot be obtained. In the first case, the procedure comprises the following basic stages: (a) a tip-shaped specimen is produced and placed into the field ion microscope, which can operate in three modes: as a field ion microscope, as a desorption ion microscope, and as a field emission microscope [5]; (b) the microscope is evacuated and gas (hydrogen, deuterium, or helium) is introduced, preliminary vacuum is 3×10^{-9} torr, and pressure after filling with gas is 10^{-6}–10^{-5} torr; (c) the specimen surface is preliminarily cleaned via desorption, and the specimen material is evaporated by the field in order to smooth the surface as well as possible; (d) the specimen surface is irradiated by pulses of chosen ions; (e) the specimen is again analyzed by the microscope to identify and count vacancies formed on their surface; (f) sputtering yields Y are calculated for a given energy of bombarding ions. Stages (c)–(f) are repeated many times for the same specimen. The number of irradiating pulses is varied from ten to a few hundred for low sputtering yields.

For materials for which good field ion images cannot be obtained, the above described procedure changes significantly. In this case, either field ion images whose resolution is worse than atomic or desorption ion images are analyzed, and local variations of ion currents and/or brightness are directly measured. The corresponding procedure involves above stages (a)–(c) and, then, implies the following stages: (d) the ion current to the microchannel plate (or to the chosen region of the plate if the rest of its area is shielded) is measured; (e) the total light flux from the phosphor screen or its part corresponding to the chosen area of the microchannel plate is measured; (f) the specimen surface is irradiated by pulses of the chosen ion gas; (g) the ion current and light flux are measured again; (h) sputtering yields Y for a given energy of bombarding ions are calculated from the differences of the ion currents and/or the light fluxes before and after the irradiation pulse. Stages (d)–(h) are repeated many times for the same specimen. This technique was developed for tungsten. In this case, the sputtering yields estimated by counting the number of surface vacancies on atomic-resolution tungsten images were used to correct the values obtained by the above technique.

An important stage of the determination of sputtering yields Y is calculation of irradiation fluences, which is a nontrivial problem. This problem, together with the estimation of the energy of bombarding ions and the counting of the number of single vacancies produced by irradiation, is responsible for some uncertainty in the resulting Y values. In the reviewed studies, the radiation fluence was calculated on the basis of the measured irradiation parameters [11], and the necessary average work function $\bar{\varphi}$ for the materials at hand was taken from [12]. With the given irradiation parameters, the tip surface with the average radius $\bar{R}_0 \approx 100$ nm was hit by $\sim 2.5 \times 10^7$ ions per second (this estimation was obtained for specimen irradiation by D^+ ions), which corresponded to deposition of 250 ions on the specimen surface during one pulse or to a flux density of 2.5×10^{17} ion $\mathrm{cm}^{-2}\mathrm{s}^{-1}$. In turn, $Y \approx 10^{-1}$ corresponds to the detection of $\sim$25 single vacancies observed by the microscope over the whole specimen surface after one irradiation pulse (the field ion image of the apex surface of the tip specimen with $\bar{R}_i \sim 100$ nm contains $\geq 10^5$ atoms); $Y \approx 10^{-2}$ corresponds to five vacancies per two irradiation pulses; $Y \approx 10^{-3}$ corresponds to one vacancy per four pulses; etc. That is why the number of irradiation pulses must be increased considerably

to determine the threshold value E_{th} and small Y values.

3. MATERIALS AND SPECIMENS

The materials studied in [6–9] were taken largely because they are considered as candidates for the use in reactors designed for thermonuclear synthesis. As was mentioned above, these materials were beryllium [6], tungsten, tungsten oxide, mixed tungsten–carbon layers (all of them described in [6, 7]), high strength reactor graphite MPG-6, highly oriented pyrolytic graphite (HOPG), polyacrylic carbon fibers UKN-400 (all of them considered in [8]), and subatomic carbon films on the surface of iron, niobium, tantalum, and uranium with the covering degree θ from 1 to 3 [9].

Needle-shaped beryllium specimens for the field ion microscopy analysis were obtained by electrochemical etching of small bars in concentrated phosphoric acid (H_3PO_4) at a dc voltage of 30–50 V. Tungsten specimens were produced from wires by electrochemical etching in a 1.5 N solution of NaOH at a dc voltage of 5–10 V. To obtain an oxide film on the tungsten surface, the tips were heated in the air to ~750°C. The W–C films were produced by collecting the products of the simultaneous sputtering of tungsten and graphite by 20 keV Ar^+ ions onto the needle-shaped tungsten specimens. The thicknesses of oxide and mixed layers and their irregularities and chemical composition were determined in [6] by a Sloan profilometer and by Auger electron analysis. The phase composition of the specimens was determined by X-ray structural analysis within the geometry of grazing beam incidence.

For reactor graphite MPG-6 [13], 1.0-cm-long 0.5×0.5-mm bars were first cut out from massive bars; then, these bars were sharpened either mechanically or by bombarding with C^+ ions. For pyrolytic graphite [14], thin layers parallel to the basic plane were first split off with a razor or Scotch tape from massive bars; then sharpened needles were split off from these layers. Finally, carbon-fiber specimens [15] were obtained from carbon fibers by direct cutting across their axis with a razor (fiber thickness was 7.0 μm). Then, the surfaces of the required curvature were obtained directly in the field ion microscope by their bombarding with image-gas ions at the reverse high-voltage polarity [16].

In [9], carbon films were deposited on the surface of needle-shaped specimens, previously produced from four materials chosen for substrates (Fe, Nb, Ta, U) by evaporating a carbon target with a pulse laser in vacuum. Herein, the total field emission current I_{fe} from the tip surface under a fixed (constant) potential was measured after each laser pulse. The I_{fe} value decreased as the substrate surface was coated with a carbon film ($\theta < 1$). The saturation of I_{fe} was supposed to correspond to the deposition of one atomic carbon layer ($\theta = 1$). The double number of laser pulses corresponded to $\theta = 2$ and so forth.

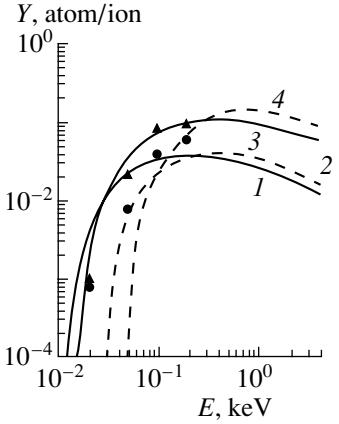

Fig. 2. Energy dependence of the yields of Be sputtering by D^+ and He^+ ions at room temperature. Data for (•) Be–D^+ and for (▲) Be–He^+ are taken from [6]. Theoretical calculations for (*1*) Be–D^+ and (*3*) Be–He^+ and averaged experimental data on (*2*) Be–D^+ and (*4*) Be–He^+ are taken from [2].

4. ENERGY THRESHOLDS OF SPUTTERING

Table 1 shows the threshold energies E_{th} of sputtering by different ions for the materials studied in [6–9] and in other experimental and theoretical studies. Table 2 shows similar values E_{th} for the subatomic carbon films of various thicknesses (with the covering degree θ from 1 to 3) on four metallic substrates. It follows from Table 1 that the E_{th} values measured by the novel method for pure beryllium sputtered with D^+ and He^+ ions are in satisfactory agreement with the calculations [19] and the JET experiments with Be irradiated by D^+ and He^+ ions at 923 K [2]. When Be is irradiated at room temperature, its threshold sputtering energy is substantially higher, which is likely caused by both the oxidation of the beryllium surface and an increase in the binding energy of oxides on this surface. In addition, Table 1 indicates that the E_{th} values for sputtering of W and WC mixture by D^+ ions are approximately identical and agree well with the previous measurements [2, 19, 20].

Our method gives a value of 65 eV for the threshold energy of tungsten oxide sputtering by deuterium ions, whereas $E_{th} \leq 18$ eV according to the mass spectroscopic measurement [19] in a chamber with a residual oxygen pressure of 8×10^{-5} torr. As was shown in [2], E_{th} is low, because the binding energy of tungsten oxide molecules with the surface is low

Table 1. Threshold energies of sputtering E_{th} [6–9]

No.	Material	Bombarding ions	T, K	E_{th}, eV		
				this method	experiment	theory
1	Be	D^+	78–373	<10	–	–
2	Be	D^+	923	–	10 [2, 17]	9.8 [2]
3	Be	D^+	293	–	26.2 [2]	–
4	Be	He^+	293	<10	44.5 [2]	30 [18]
5	Be	He^+	923	–	13.9 [2, 17]	13.9 [2,19]
6	W	D^+	293	160	175 [18], 178 [2]	201 [2], 160 [20]
7	W + C	D^+	78–293	150	–	–
8	WC	D^+		–	171 [2], 150 [18]	–
9	W oxide	D^+	293	65	<18 [19]	–
10	MPG-6	H^+	78–293	40	–	27.3 [2]
11	MPG-6	D^+	78–293	30	–	24.3 [2]
12	MPG-6	He^+	78–293	30	30.2 [2]	25.4 [2]
13	HOPG	H^+	78–293	40	–	–
14	HOPG	D^+, He^+	78–293	30	–	–
15	UKN-400	H^+, D^+, He^+	78– 293	20	–	–

($E_b = 0.3$ eV). In [7], an oxide film ~50 nm thick was formed on the tungsten surface. The binding energy E_b estimated similar to [19] is equal to ~1.1 eV. A considerable rise in the threshold energy obtained by the novel method can be also associated with distinctions between these two methods (mass spectroscopy and field ion microscopy). The novel method identifies only vacancies in tungsten; that is, it counts only sputtered tungsten atoms, whereas the mass-spectroscopic method records all sputtered surface atoms including adsorbed atoms and molecules.

Table 2. Threshold sputtering energies E_{th} measured by our method for subatomic carbon films on different metallic substrates

No.	Substrate material	Bombarding ions	θ	E_{th}, eV
1	Fe	H^+	1, 2, 3	30
2	Fe	He^+	1	20
3	Fe	He^+	2, 3	30
4	Nb	H^+	1, 2	50
5	Nb	H^+	3	40
6	Nb	He^+	1, 2, 3	40
7	Ta	H^+	1, 2, 3	40
8	Ta	He^+	1	30
9	Ta	He^+	2, 3	40
10	U	H^+	1	30
11	U	H^+	2, 3	40
12	U	He^+	1, 2, 3	30

The Auger electron analysis [7] for the mixed WC layer shows that W and C are distributed quite uniformly in the layer ~10^4 nm thick, and an admixture of oxygen on the surface is below 9.5 at. %. As a result of heating of tungsten in the air, the thickness of a WO layer on tungsten is equal to ~50 nm.

Table 1 also demonstrates that the energy thresholds of sputtering coincide for reactor graphite and pyrolytic graphite: $E_{th} \approx 40$ eV for H^+ ions and $E_{th} \approx 30$ eV for D^+ and He^+ ions. For UKN-400 carbon fibers, $E_{th} \approx 20$ eV for all three types of bombarding ions. The threshold energy E_{th} is lower for the carbon fibers, because their structure has specific features such as high porosity, lamination, and so forth. In addition, it is necessary to take into account the possible cluster nature of sputtering.

For the first time, E_{th} values were determined for MPG-6 graphite by the above experimental procedure, with bombarding by H^+ and D^+ ions; these values are only slightly higher than the theoretical values. For graphite bombarded by He^+ ions, field ion microscopy and mass spectroscopy provide virtually coinciding E_{th} values. This fact confirms the efficiency of the novel technique and allows us to consider data for other materials—for example, those for HOPG and UKN-400, which were obtained only with this technique—as completely reliable.

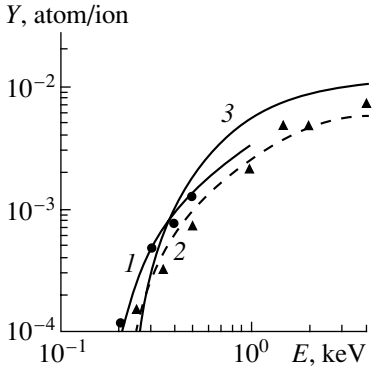

Fig. 3. Energy dependence of the yield of tungsten sputtered by D^+ ions. Curve *1* is plotted with (●) our data taken from [7], curve *2* is plotted with (▲) the experimental data taken from [2], and curve *3* corresponds to the theoretical calculations from [2].

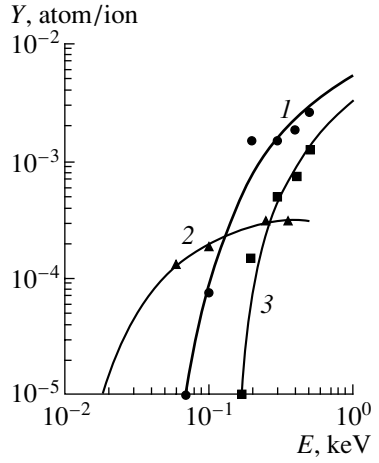

Fig. 4. Energy dependence of the sputtering yield of tungsten oxide on the tungsten specimen surface by D^+ ions. Curve *1* is plotted with (●) our data from [7], whereas curves *2* and *3* are plotted with the experimental data from [2] for (▲) tungsten at an oxygen pressure of 8×10^{-5} torr and (■) pure tungsten.

The results for the carbon–metal films (Table 2) indicate that the E_{th} values for the same θ values decrease when passing from Nb and Ta to Fe and U. At the same time, E_{th} depends only slightly on θ, if at all. The E_{th} values for the massive graphite specimens (MPG-6) and carbon films differ only slightly (see Table 1), although they must be different at first glance.

5. ENERGY DEPENDENCES OF SPUTTERING YIELDS IN THE PRETHRESHOLD REGION

Figure 2 shows the sputtering yields Y of beryllium irradiated by deuterium and helium ions (points) as measured for energies from 10 to 200 eV [6], (*1, 3*) as calculated in [2], and (*2, 4*) as averaged on the basis of experimental data taken from [19, 20]. As is seen, the sputtering yields measured for beryllium by field ion microscopy agree with computer simulation [2]. At the same time, the averaged experimental curves [19, 20] in the prethreshold energy region pass lower than theoretical curves because of the presence of a beryllium oxide film on the specimen surface. The production of vacancies in the energy region under study was observed indirectly, on the desorption and smeared field ion images, only in the first surface layer. Hence, sputtering of beryllium atoms in the energy region 10–200 eV occurs from the first monatomic layer on the surface.

The energy dependence of the yield of tungsten sputtered by deuterium ions is shown in Fig. 3: (curve *1*, circles) our data from [7], (curve *2*, triangles) experimental and (curve *3*) calculated data obtained in [2]. As is seen, the tungsten sputtering yields measured by different methods are close to each other and agree well with the theoretical curve. The same is true for the energy dependences of the sputtering yields for the resputtered W–C layer and WC layer.

Figure 4 shows (curve *1*, data from [7]) the energy dependence of the yield of tungsten oxide sputtered by deuterium ions, (curve *2*) the experimental data [2] for tungsten sputtered at an oxygen pressure of 8×10^{-5} torr, and (curve *3*) data for pure tungsten. For energies below 100 eV, the sputtering yields of tungsten irradiated at high oxygen pressure is substantially higher than the corresponding values measured by field ion microscopy. At $E \geq 350$ eV, the sputtering yields of tungsten oxide measured by mass spectroscopy (curve *2* in Fig. 4) approach the values for pure tungsten sputtered by deuterium ions (curve *3*). Therefore, when the sputtering yield increases up to 3×10^{-4} atom/ion under the experimental condition of [19], the oxide film on the tungsten surface has already been sputtered by D^+ ions. In the experiments with our field ion microscopic technique, the tungsten surface is covered by a thick tungsten oxide film; therefore, a higher sputtering yield is needed for the removal of this film.

Let us now consider the sputtering of carbon materials. Figure 5 shows the energy dependence of the yield of high-strength reactor graphite MPG-6 sputtered by H^+ ions (curve *1* for data from [8]), as well as the (curve *2*) theoretical and (curve *3*) experimental results taken from [2]. The experimental data differ from each other because they were obtained by different methods and for different types of carbon materials. However, these differences are not substantial in view of the features of the problem. The same is true for the energy dependences of the yields of MPG-6

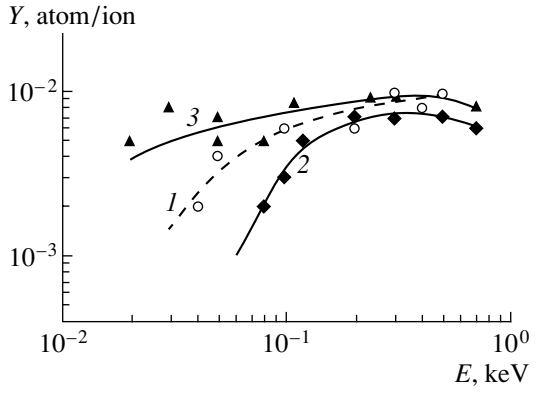

Fig. 5. Energy dependence of the yield of reactor graphite MPG-6 sputtered by H^+ ions. Curve *1* is plotted with (○) the experimental data from [8], curve *2* corresponds to (♦) the theoretical calculation from [2], and curve *3* is plotted with (▲) the experimental data from [2].

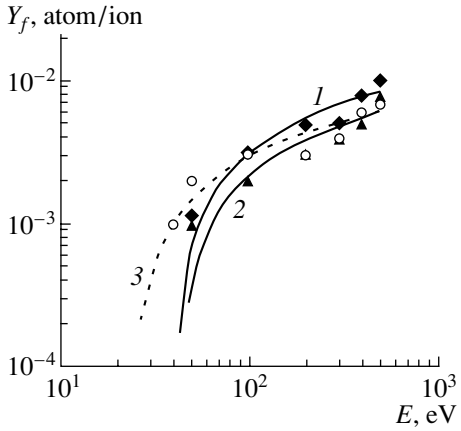

Fig. 7. Energy dependence of the sputtering yield of the carbon films on the Nb surface by H^+ ions: $\theta =$ (curve *1*, ♦) 1, (curve *2*, ▲) 2, and (curve *3*, ○) 3. Data are taken from [9].

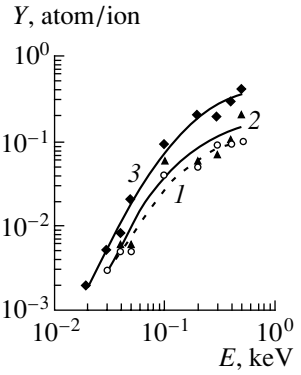

Fig. 6. Energy dependence of the yield of the following carbon materials sputtered by He^+ ions: (○, curve *1*) reactor graphite MPG-6, (▲, curve *2*) polyacrylonitrilic carbon fibers UKN-400, and (♦, curve *3*) highly oriented pyrolytic graphite. Data are taken from [8].

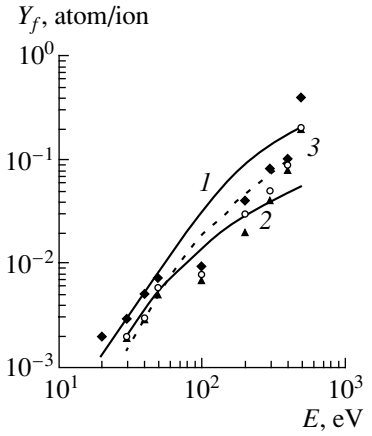

Fig. 8. The same as in Fig. 7, but for the carbon films that are deposited on the Fe surface and sputtered by He^+ ions.

sputtered by D^+ and He^+ ions [8], although, in the case of MPG-6 sputtering by D^+ ions, the differences of the experimental data are larger, particularly near the threshold of sputtering.

Figure 6 shows the energy dependences of the yield of the three carbon materials sputtered by He^+ ions. These dependences, as well as the similar dependences for carbon materials sputtered by H^+ and D^+ ions, clearly corroborate the above statement: carbon fibers are characterized by substantially higher sputtering yield Y and threshold energy $E_{\rm th}$ of sputtering. When materials are bombarded by hydrogen and deuterium ions, this difference is considerably larger than difference in the case of bombarding helium ions.

Figures 7–9 show the energy dependences of the sputtering yields $Y_{\rm f}$ of the subatomic carbon films of various thickness on various metallic substrates [9]. Figure 7 demonstrates the dependences for the carbon films that are deposited on niobium and sputtered by H^+ ions. Figure 8 shows the dependences for the carbon films that are deposited on iron and sputtered by He^+ ions. As is seen, the θ dependence of $Y_{\rm f}$ is immaterial, although in the case of sputtering by He^+, the $Y_{\rm f}$ values corresponding to $\theta = 1$ are higher than those for $\theta = 2$ and 3 (Fig. 8). In the case of film sputtering by H^+ ions, this is true only for relatively high energies of ions (Fig. 7).

Finally, Fig. 9 shows the energy dependences of $Y_{\rm f}$ obtained in [9] for the monatomic carbon films ($\theta = 1$) that are deposited on four different metallic substrates and bombarded by He^+ ions. As is seen, the $Y_{\rm f}$ values are close for the carbon films on all the metallic substrates used in [9]. In this case, $Y_{\rm f}$ in-

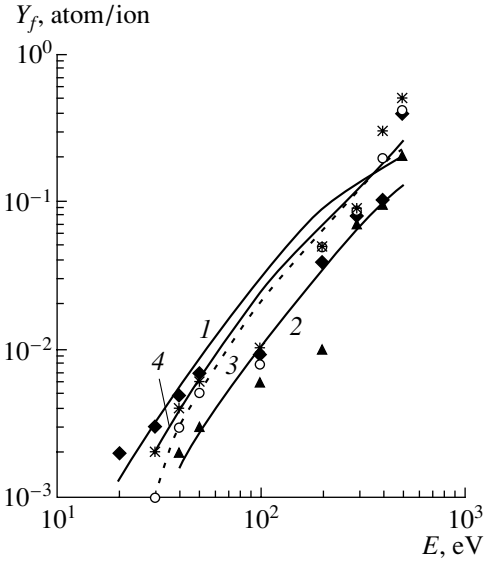

Fig. 9. Energy dependence of the sputtering yield of the monatomic carbon film ($\theta = 1$) that is deposited on the surfaces of (*1*, ♦) Fe, (*2*, ▲) Nb, (*3*, ○) Ta, and (*4*, ∗) U and sputtered by He^+ ions.

creases indistinctly when changing from Nb and Ta to U and Fe. In addition, it follows from the experimental data obtained in [9] that the film thickness $\theta = \theta^* = 3$ is limiting for cleaning of substrates by H^+ ions in the chosen bombarding energy range 2.0–10.0 keV, whereas $\theta^* = 4$ for He^+ ions.

Finally, the sputtering yields Y_f measured in [9] for the carbon films bombarded by H^+ ions are approximately an order of magnitude higher than the corresponding Y values for pure carbon. This difference is much smaller for He^+ ions. The difference in the Y_f values for carbon films bombarded by H^+ and He^+ ions with the same energies is substantially smaller than the difference for pure carbon.

6. CONCLUSION

First, the most important conclusion following from the results is that the novel technique proposed for precise atomic scale determination of the sputtering yields of conductive materials is very efficient. Its advantage over other methods is the possibility of cleaning the specimen surface from adsorbed atoms and molecules, oxide films, etc., directly inside a field ion microscope; i.e., one can work with the atomically clean surface of materials. Another advantage is the possibility of directly and indirectly observing each vacancy produced by bombarding ions on the specimen surface; i.e., each sputtered atom can be taken into account.

Particular results provide the following conclusions.

(1) The threshold energies of sputtering of pure beryllium by D^+ and He^+ ions are in satisfactory agreement with calculations [19] and experiments performed under similar conditions at 923 K [2]. At room temperature, the threshold energy of beryllium sputtering is higher due to oxidation and an increase in the binding energy of oxides on its surface.

(2) The threshold energies of sputtering of pure tungsten by deuterium ions are in satisfactory agreement with calculations [19], but are much lower than the corresponding values obtained by mass spectroscopy at room temperature [2].

(3) The threshold energy of tungsten sputtering by deuterium ions increases sharply and is equal to 65 eV.

(4) The energy dependences of the yield of sputtering of pure tungsten and a mixed tungsten–carbon layer by deuterium ions on tungsten agree with the previous data for W and WC [2].

(5) The sputtering yields and threshold energy E_{th} of carbon fibers are noticeably higher than the corresponding values of high-strength reactor graphite and highly oriented pyrolytic graphite. This difference is much more pronounced for bombarding hydrogen and deuterium ions than for helium ions.

(6) The energy thresholds of sputtering of carbon films by H^+ and He^+ ions decrease when changing from Nb and Ta to Fe and U, and thresholds for metal–carbon films are always lower than thresholds for pure carbon.

(7) The energy threshold of sputtering for $\theta \approx 1$ differs from the values for $\theta \geq 2$, and this difference is more pronounced for He^+ ions than for H^+ ions.

(8) In the taken range of bombarding ion energies (2.0–10.0 keV), the layer thickness $\theta = \theta^* = 3$ is limiting for cleaning of substrates by H^+ ions, and $\theta^* = 4$ for He^+ ions.

(9) The sputtering yields Y_f measured for carbon films bombarded with H^+ ions are about an order of magnitude higher than the corresponding Y values for pure carbon. This difference is noticeably smaller for He^+ ions. The Y_f values for carbon films bombarded with H^+ and He^+ ions of equal energies are less different than the corresponding values for pure carbon.

(10) Sputtering yields Y_f increase when changing from Nb and Ta to U and Fe, all other factors being the same.

(11) In the prethreshold region of the energies of bombarding ions, the energy dependences of the sputtering yields Y_f of the carbon films differ noticeably at $\theta \approx 1$ and $\theta \geq 2$ for both H^+ and He^+.

ACKNOWLEDGMENTS

I am grateful to my colleagues V.P. Babaev, M.I. Guseva, A.G. Zaluzhnyĭ, A.A. Zaluzhnyĭ, S.N. Korshunov, and N.E. Lazarev, who actively participated in the studies discussed in this paper, and to Yu.N. Devyatko for fruitful discussions of the results and concept of these studies.

This work was supported in part by the Russian Foundation for Basic Research (project no. 01-02-17934).

Postscript. Concluding this paper, I thank my lucky stars that led me to ITEP, where I met many outstanding scientists and splendid people with whom I shared common interests. Owing to the breadth of scientific interests of these scientists and their natural attraction to new original ideas, the radiation physics of condensed matter is actively developed at ITEP, where, at first sight, it is far from the basic themes. These scientists supported the development of experimental techniques even less traditional for ITEP such as atomic probe, field ion, scanning tunneling, and atomic force microscopy. Today, when ITEP has become one of the recognized world leaders in ultramicroscopic, atomic scale investigations in the radiation physics of condensed matter and in reactor materials science, I emphasize the particular services of Professor Yu.G. Abov in these achievements. His anniversary gives me, as his grateful disciple, a remarkable opportunity to express to him my gratitude and to wish him many years of creative activity.

REFERENCES

1. *Sputtering by Particle Bombardment,* Ed. by R. Behrisch (Springer-Verlag, New York, 1981, 1983; Mir, Moscow, 1984, 1986), Vols. I and II.
2. W. Ekstein, C. García-Rosales, J. Roth, and W. Ottenberger, Report IPP 9/82 (Max-Planck-Institut für Plasmaphysik, 1993).
3. E. W. Muller and T. T. Tsong, *Field Ion Microscopy. Principles and Applications* (Elsevier, New York, 1969).
4. A. L. Suvorov, *Field Ion Microscopy of Radiation Defects in Metals* (Énergoizdat, Moscow, 1982).
5. A. L. Suvorov, *Structure and Properties of Surface Atomic Layers of Metals* (Énergoatomizdat, Moscow, 1990).
6. M. I. Guseva, A. L. Suvorov, S. N. Korshunov, and N. E. Lazarev, J. Nucl. Mater. **266–269**, 222 (1999).
7. M. I. Guseva, A. L. Suvorov, S. N. Korshunov, and N. E. Lazarev, Zh. Tekh. Fiz. **69** (9), 137 (1999) [Tech. Phys. **44**, 1123 (1999)].
8. A. L. Suvorov, M. I. Guseva, S. N. Korshunov, *et al.*, Vopr. At. Nauki Tekh., Ser. Fiz. Radiats. Povrezhdeniĭ Radiats. Materialoved., No. 4 (78), 6 (2000).
9. A. L. Suvorov, V. P. Babaev, A. G. Zaluzhnyĭ, *et al.*, Zh. Tekh. Fiz. **73** (2002) (in press).
10. A. F. Bobkov, S. V. Zaĭtsev, V. A. Kasatkin, and A. L. Suvorov, Prib. Tekh. Éksp., No. 6, 188 (1985).
11. P. A. Bereznyak and V. V. Slezov, Radiotekh. Élektron. (Moscow) **17**, 354 (1972).
12. V. S. Fomenko, *Emission Properties of Materials: a Handbook* (Naukova Dumka, Kiev, 1981).
13. *Properties of Carbon Structural Materials: a Handbook,* Ed. by V. P. Sosedov (Metallurgiya, Moscow, 1975).
14. A. S. Fialkov, A. I. Baver, and N. M. Sidorov, Usp. Khim. **34** (1), 132 (1965).
15. A. A. Konkin, *Carbon and Other Heat-Resistant Fibrous Materials* (Khimiya, Moscow, 1974).
16. D. E. Dolin, A. A. Sosunov, A. L. Suvorov, and E. P. Sheshin, Zh. Tekh. Fiz. **60** (12), 115 (1990) [Sov. Phys. Tech. Phys. **35**, 1430 (1990)].
17. J. Roth, W. Eckstein, and M. Guseva, Fusion Eng. Des. **37**, 465 (1997).
18. J. Bohdansky, *Research Co-ordination Meeting on Plasma-Interaction Induced Erosion of Fusion Reactor Materials* (IAEA, Vienna, 1989).
19. J. Roth, J. Bohdansky, and W. Ottenberger, Report IPP 9/26 (Max-Planck-Institut für Plasmaphysik, 1979).
20. J. Roth, J. Bohdansky, and A. P. Martinelli, in *Proceedings of the First Conference on Ion Beam Modification of Materials, Budapest, 1978,* p. 1541.

Translated by E. Kozlovskiĭ

Physics of Atomic Nuclei, Vol. 65, No. 11, 2002, pp. 2029–2035. From Yadernaya Fizika, Vol. 65, No. 11, 2002, pp. 2089–2095.

NUCLEI

Neutron Transportation in a Closed Vessel*

V. K. Ignatovich[1], E. V. Lychagin[1], V. V. Nesvizhevsky[2], G. V. Nekhaev[1], A. Yu. Muzychka[1], and A. V. Strelkov[1]

Received March 4, 2002

Abstract—Results of the experiments on measurement of ultracold neutron (UCN) storage time in moving vessels are reported. A theory for change of the UCN spectrum in the vessel swinging on a long thread like a pendulum is presented. It is found that the average kinetic energy of the UCN increases proportionally to the first derivative of the acceleration but only during those quarters of a period in which the absolute magnitude of acceleration increases. The results of measurement and theoretical consideration of UCN storage time in a vessel struck by a hammer are also given. © *2002 MAIK "Nauka/Interperiodica".*

This is a toy science, and we dedicate it to the jubilee of the very serious scientist Yu.G. Abov. We hope that he will enjoy it.

1. INTRODUCTION

We started the investigation of the ultracold neutron (UCN) storage time in moving vessels in order to understand how many neutrons can be lost during transportation of UCN from a source to experimental hall directly in a vessel.

This problem arose in the very first experiment with UCN, in which neutrons were extracted from the reactor and delivered to the detector through a long metallic pipe called a neutron guide. It was noticed that the number of registered particles was too low. The lack of UCN was supposed to be due to their high losses in the tube, and it was decided to try to avoid these losses by direct transportation of UCN in a bottle.

At the beginning of the 1970s, two groups [1, 2] tried such a transportation of UCN from the active reactor core to the experimental hall in closed containers. However, these experiments failed. It was found to be too difficult to detect UCN in containers because the detector of UCN in the experimental hall was blocked by β–γ radiation from the radioactivity induced in the container construction materials when it was near the reactor core.

The first success was achieved only in [3], but the number of extracted UCN at that time was so small that this method did not attract much attention.

The interest in transportation of UCN in vessels was revived when a new way of production of UCN at powerful pulsed neutron sources was proposed. The new "dynamical convertor" [4] was expected to provide a high UCN density. In this method, a closed vessel without a window is shot directly towards the cloud of neutrons generated near the reactor core during the reactor pulse. If the vessel velocity is so high that the vessel walls are transparent even for the slowest neutrons, the neutron cloud easily goes through the walls into the bottle volume. At this very moment, the vessel must be suddenly stopped, and slow neutrons in the cloud become locked in the vessel.

After that, the trapped neutrons should be transported in the bottle to the experimental hall. Therefore, the problem of neutron transportation in containers became important in UCN physics again.

UCN density in the "dynamical convertor" was estimated to be 10^4 neutron/cm^3. However, it could not be measured near the reactor, and after transportation of the vessel for 1 min, the resulting density was measured to be only 25 neutron/cm^3. This discrepancy with expectation was supposed to be due to losses because of inaccurate transportation, as inaccurate transportation of a pail of water leads to splashing of the water out of the pail. If the vessel motion is accompanied with vibrations or stochastic accelerations, then the neutrons kicked by vibrating walls acquire high enough kinetic energy to become able to leave the vessel through the walls.

Since we were not able to measure UCN density in the vessel near the reactor core before transportation, we could not be sure that we indeed had a lot of neutrons there. Thus, we were obliged to study the effect of accelerations on neutron losses in the bottle. This was the motivation for the reported experiments.

*This article was submitted by the authors in English.

[1]Joint Institute for Nuclear Research, Dubna, Moscow oblast, 141980 Russia.

[2]ILL, Grenoble, France.

1063-7788/02/6511-2029$22.00

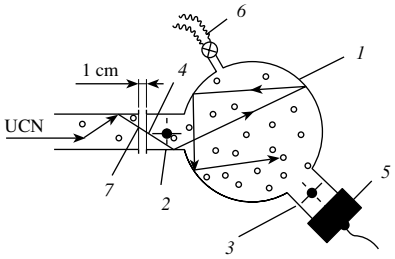

Fig. 1. Scheme of the experiment: (*1*) container, (*2*) entrance, (*3*) exit, (*4*) entrance window, (*5*) detector, (*6*) vacuum tube, and (*7*) Al foil.

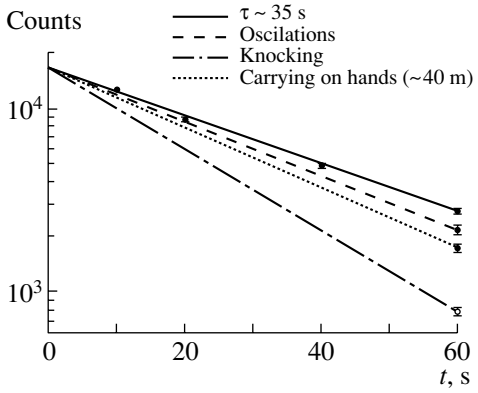

Fig. 2. Storage curve in the stationary vessel and the number of neutrons surviving in the bottle after 60 s, when the bottle was carried, oscillated, or struck with hammer twice per second.

2. DESCRIPTION OF THE EXPERIMENTS

It is evident that the motion of the bottle with a uniform velocity does not affect the neutron spectrum in it. Only accelerations are important. Thus, we need to estimate the effect of the vessel acceleration on the neutron spectrum and on the neutron storage time. To measure the effect of acceleration, we have to control acceleration and to know the number of trapped neutrons at the beginning before acceleration and the number of neutrons surviving after the trip with controlled motion. The measurement of UCN losses in the vessel without acceleration provides calibration for the data.

2.1. Description of the Installation

The experiments were carried out at the UCN port of the Steyerl turbine at ILL, Grenoble. The container in the experiment (Fig. 1) was a copper sphere (*1*) 39 cm in diameter and wall thickness of 1 mm. Two short neutron guides 10 cm in diameter were attached to it at the entrance (*2*) and at the exit (*3*). These neutron guides included turnable shutters. The entrance guide in front of the shutter was hermetically closed by entrance window (*4*), made of Al foil 0.1 mm in thickness. A UCN detector was attached to the exit neutron guide. The detector was a proportional ^{3}He counter (*5*) with Al window 10 cm in diameter and thickness of 0.1 mm.

The container was evacuated via a goffered tube (*6*) and a hole in the vessel wall down to the pressure of 10^{-3} mbar.

It was filled with neutrons at the end of the right turn of the neutron guide coming from the turbine, which we call "port." Its total cross section of area of 60 cm^2 was shut with an Al foil 0.1 mm in thickness (*7*). The flange construction allowed attachment of the container to the port, and there was a narrow gap 1 cm thick filled with atmospheric air left in between two Al windows of the bottle and the neutron guide. This gap at the entrance attenuates the UCN beam by 30%. The UCN density in the bottle filled through the two Al windows and the air in the gap between them was 4 times lower than in the bottle filled directly without them.

In order to fill the bottle with UCN, it was attached to the port for 30 s, which is several times longer than the filling constant (≈ 8 s). The storage curve, which gives the number of neutrons remaining in the bottle after exposition time t, is shown in Fig. 2. It can be approximated by the exponential $\exp(-t/\tau)$. The storage time τ in stationary vessel was found to be 35.0 ± 0.5 s.

2.2. Storage Time in Swinging Bottle

In order to investigate the effect of acceleration on UCN storage time, the vessel was set into different kinds of oscillatory motions of variable frequencies and amplitudes. One of them was swinging of the bottle suspended on a flexible wire (Fig. 3). The wire length was varied in order to get frequencies ν in the range $0.5 \le \nu \le 2$ Hz with the amplitude from 15 to 5 cm. The swinging continued for one minute. After that, the exit shutter (3) in Fig. 1 was opened and the remaining neutrons were counted. The results averaged over several measurements are shown in Fig. 2.

The parameters of oscillations and the storage times are shown in the table. The frequency ν is shown in the first column of the table, the amplitude x_0 is in the second column, and the product $\omega^3 x_0 = (2\pi\nu)^3 x_0$ is presented in the third column. This product characterizes the derivative of the oscillation acceleration. The storage time for a given oscillation is shown in the fourth column of the table. The storage time was calculated with the help of only two points: the first one immediately after filling (no exposition, $t = 0$), and the second one after exposition

Parameters of oscillations

ν, Hz	x_0, cm	$x_0\omega^3 \times 10^{-3}$, cm/s^3	τ, s	ξ_e	ξ_t
0	0	0	33.7 ± 0.5	1	
0.5	15	0.465	32.2 ± 0.4	0.95 ± 0.02	0.953
0.8	10	1.27	29.6 ± 0.5	0.88 ± 0.002	0.88
1.5	8	6.7	20.0 ± 0.2	0.59 ± 0.01	0.582
2	5	9.92	14.1 ± 0.2	0.418 ± 0.009	0.484

time $t = 60$ s. The fifth column of the table represents ratio of the storage time in the oscillating vessel to the storage time in the stationary one.

2.3. Storage of UCN in a Hammered Bottle

In addition to the measurement of storage time in the swinging bottle, we also measured it in the bottle struck by a hammer, and in the bottle carried by hand. Striking by a hammer models jerks during motion and sound vibration of the walls. Motion by hand gives smooth but uncontrollable accelerations.

Figure 2 gives the number of neutrons remaining in the stationary vessel after a one-minute exposition, during which time the vessel was periodically struck by a hammer. We see that the wall vibrations in such a case reduce the number of surviving neutrons by a factor of 4 compared to the calibration curve.

2.4. Carrying of the Bottle by Hand

When transported by hand, the vessel was carried for one minute at a velocity of ≈ 1 m/s. The route went first 3 m downward along a ladder and then horizontally for a distance of 40 m. After this travel, the exit shutter was opened and the number of neutrons remaining in the bottle was counted. Within statistical uncertainty, several measurements gave the same result. It shows that such a transportation decreases the number of neutrons left after 60 s by 40% compared to the calibration curve.

In the above-described experiment, the vessel was carried with the UCN detector permanently attached to it. The measurement with the vessel without the detector permanently attached gave the same result. In that case, the detector was attached to the vessel only at the end of the route. In this experiment, the exit shutter was always closed, and the remaining neutrons were counted through the same entrance shutter that was used for filling the vessel. In other words, the detector at the end of the route was attached to the same short guide (2) in Fig. 1, which was connected to the port at the filling stage.

The vacuum valve was closed before transportation, and the vessel was disconnected from the pump system. Within 6 min after disconnection, the pressure in the vessel usually increased from 1×10^{-3} to 2×10^{-3} mbar. We suppose that the residual gas in the vessel was air. From known characteristics of air ($p\tau = 18$ Torr s [5]), it was possible to estimate that increase in the residual gas pressure can decrease the storage time by ≤ 0.2 s only.

3. THEORETICAL CONSIDERATIONS

3.1. Effect of the Acceleration

Let us theoretically describe the effect of acceleration $\mathbf{a}(t)$ on the storage time. The most interesting case is related to small accelerations, when $at_f \ll v_l$, where $t_f = l_f/v$ is the neutron free-flight time between collisions with walls, v is the neutron velocity, $l_f = 4V/S$ is the free-flight path between two consecutive collisions with the walls, S is the total area of the walls, V is the volume of the vessel, $v_l = \sqrt{u}$ is the limiting velocity, and u is the optical potential of the container walls. The inequality $at_f \ll v_l$ means that acceleration only slightly changes the neutron velocity in the vessel.

Acceleration $\mathbf{a}$ in the reference frame of the vessel is equivalent to the "gravity" field. This field adds potential energy to particles. This energy is different in different parts of the vessel, so the spectrum of neutrons acquires additional total energy broadening $2mal$, where l is the largest diameter of the vessel in the direction $\mathbf{a}$ of the acceleration (see Fig. 4).

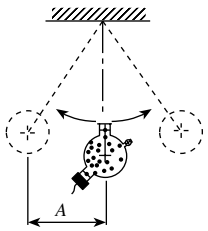

Fig. 3. Experiment with horizontal oscillations of the vessel.

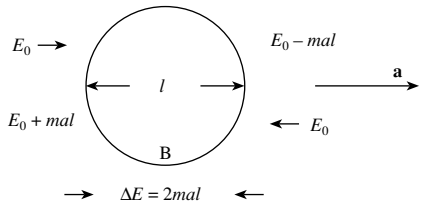

Fig. 4. Broadening of the neutron spectrum in an accelerated vessel. Before starting acceleration **a**, the particles in the bottle B had the same energy E_0. After switching on the acceleration, the particles moving upwards become slower, because they acquire potential energy mal, and the particles moving in the opposite direction become faster, because they lose potential energy mal.

Let us suppose that at the initial time there is no gravity at all, i.e., the vessel is in some inertial reference frame. In this case, the neutrons of some energy $E_0 = k_0^2$ are distributed isotropically and homogeneously over all the volume of the vessel.

After switching on the acceleration **a** along some axis $\mathbf{e}_z$, the neutrons in the vessel acquire the potential energy az, where z is the distance from the vessel bottom. Because of this suddenly added potential energy, the state with a homogeneous distribution of neutrons becomes a nonequilibrium one. Thus, irreversible processes start to act to transform the nonequilibrium state to an equilibrium one. These processes are provided by diffusive reflection from the walls.

In equilibrium, the particle density is no longer homogeneous in direction of **a**, which we suppose to be parallel to $\mathbf{e}_z$. At low z, particles have higher kinetic energy and higher density, and at higher z, they have lower kinetic energy and lower density. Such inhomogeneous distribution corresponds to higher total kinetic energy than in the initial state, and a gain in kinetic energy is achieved at the expense of potential energy.

If the acceleration does not change, the spectrum of particles after reaching equilibrium does not change anymore. If the acceleration increases, then the total kinetic energy also increases. However, if the acceleration decreases, then the kinetic energy does not change. We can easily understand this if we suppose that acceleration is completely switched off. In this case, particles completely lose their potential energy and become homogeneously distributed, but nothing happens with their kinetic energy. Every acceleration can be considered as a superposition of many infinitesimal accelerations. Thus, a decrease in total acceleration means that some of its infinitesimal parts become switched off.

Thus, if we consider slow swinging of the vessel with UCN as a pendulum on a long flexible wire, we conclude that at slow oscillations the total kinetic energy changes (increases and broadens) only at those quarters of periods when acceleration increases in absolute magnitude, and the most important factor for storage is not acceleration itself but its positive derivative.

Now, it is interesting to look at how the distribution of particles changes with the change in acceleration and what the equilibrium state in the accelerating vessel is. But before that, it is useful to discuss the question of what the "equilibrium state" is.

3.2. What is the Equilibrium State?

The equilibrium state is the state in which the angular distribution of particles is isotropic at every point in the vessel. This isotropic distribution corresponds to the maximal entropy at every point in the vessel

$$S = -\frac{k_\mathrm{B}}{4\pi}\int d\Omega \ln(1/4\pi) = k_\mathrm{B}\ln(4\pi),$$

where k_B is the Boltzmann constant and $d\Omega$ is an element of the solid angle.

In the equilibrium state, the density distribution is homogeneous in planes perpendicular to acceleration and inhomogeneous along the axis $\mathbf{e}_z||\mathbf{a}$. Along the acceleration direction, the density of the equilibrium state changes according to the rule

$$f(z,k^2) = f(0,k^2+az), \qquad (1)$$

where $f(0,k^2)$ is the energy distribution near the vessel bottom. We shall not prove (1) here, because it is proven in [5].

When $a = 0$, the distribution along z is constant; i.e., for N_0 neutrons with single energy $E_0 = k_0^2$ in a cylinder of height l with its axis along $\mathbf{e}_z$, the distribution is

$$f_0(z,k^2 : k_0^2) = \frac{N_0}{2\pi k_0 l}\delta(k^2 - k_0^2). \qquad (2)$$

In distribution (2), the number of particles and their energy are

$$N = \int f_0(z,k^2 : k_0^2)dzd^3k = N_0,$$

$$E = \int f_0(z,k^2 : k_0^2)dzk^2d^3k = k_0^2 N_0.$$

Now, we switch on the acceleration **a** and look for the distribution after the equilibrium is established. For simplicity, we shall consider the bottle in the form of a cylinder of height l along the axis $\mathbf{e}_z||\mathbf{a}$.

3.3. Equilibrium Distribution in Accelerated Bottle

We can find this distribution for arbitrary $f_0(z,k^2)$ that can exist before the acceleration is switched on. To do that, we use the following mathematical trick. We represent the previous distribution as

$$f_0(z,k^2) = \int\int \delta(z-z_1)\delta(k^2-k_1^2) f_0(z_1,k_1^2)\,dz_1\,dk_1^2 \tag{3}$$

and find the equilibrium distribution for an initial pointlike one

$$P_0(z:z_1,k^2:k_1^2) = \delta(z-z_1)\delta(k^2-k_1^2). \tag{4}$$

After the acceleration is switched on, the particles in distribution (4) acquire the fixed potential energy az_1, and their energy at every height z after isotropization becomes precisely defined. It permits us to find the equilibrium distribution immediately,

$$f_a(z:z_1,k^2:k_1^2) = C\delta(k^2+az-k_1^2-az_1), \tag{5}$$

where we used (1), the law of energy conservation, and choose the units for which $\hbar^2/2m = m = 1$. The constant C is determined by the particle conservation:

$$\int dz d^3k f_a(z:z_1,k^2:k_1^2) = \int dz d^3k P_0(z:z_1,k^2:k_1^2) = 2\pi k_1, \tag{6}$$

from which it follows that

$$C = \frac{3}{2}\frac{k_1 a}{(k_1^2+az_1)^{3/2}-(k_1^2+az_1-al)^{3/2}}.$$

In the limit $a \to 0$, we have $C \to 1/l$, and (5) transforms into a homogeneous distribution of the type (2).

The equilibrium function (5) must now be averaged over $f_0(z_1,k_1^2)dz_1dk_1^2$, and after this averaging, we obtain the equilibrium distribution for an arbitrary previous one.

According to (1), we need only to write the energy distribution near the bottom of the vessel,

$$f_a(0,k^2) = \frac{3}{2}\int \frac{k_1 a\delta(k^2-k_1^2-az_1)dz_1dk_1^2}{(k_1^2+az_1)^{3/2}-(k_1^2+az_1-al)^{3/2}} f_0(z_1,k_1^2) = \frac{3}{2}\int_0^l \frac{a dz_1\sqrt{k^2-az_1}}{(k^2)^{3/2}-(k^2-al)^{3/2}} f_0(z_1,k^2-az_1). \tag{7}$$

In particular, if $f_0(z,k^2)$ is identical to $f_a(z,k^2)$, we, after substitution into (7), obtain the identity $f_a(0,k^2) \equiv f_0(0,k^2)$.

Substitution of homogeneous distribution (2) into (7) gives

$$f_a(0,k^2) = \frac{3N}{4\pi l}\frac{\theta(k_0^2<k^2<k_0^2+al)}{k^3-(k^2-al)^{3/2}}, \tag{8}$$

where the θ function is equal to 1 or 0, when the inequality in its argument is satisfied or not. It is easy to check that the total number of particles and their total energy are the same as the ones obtained with homogeneous distribution (2).

3.4. Change in the Kinetic Energy in Accelerated Bottle

The most interesting is the total kinetic energy in the equilibrium state

$$K = \frac{3N}{4\pi l}\int dz d^3k \frac{k^2\theta(k_0^2<k^2+az<k_0^2+al)}{(k^2+az)^{3/2}-(k^2+az-al)^{3/2}} \tag{9}$$

$$= \frac{3N}{2l}\int_0^l dz \int_{k_0^2}^{k_0^2+al} \frac{du(u-az)^{3/2}}{u^{3/2}-(u-al)^{3/2}} = \frac{3N}{5la}\int_{k_0^2}^{k_0^2+al} du\,\frac{u^{5/2}-(u-al)^{5/2}}{u^{3/2}-(u-al)^{3/2}} = \frac{3Nk_0^4}{5la}\int_{1-\beta}^{1+\beta} du\,\frac{3u^2+\beta^2+2u\sqrt{u^2-\beta^2}}{2u+\sqrt{u^2-\beta^2}},$$

where $\beta = al/2k_0^2$. For small β, we have

$$\frac{Nk_0^4}{la}\int_{1-\beta}^{1+\beta} duu\left(1+\frac{\beta^2}{6u^2}\right) = \frac{Nk_0^2}{2\beta}\left[2\beta+\frac{\beta^3}{3}\right] = N\left[k_0^2+\frac{(al)^2}{24k_0^2}\right]. \tag{10}$$

This value gives an average increase in the particle energy for maximal acceleration a. However, we

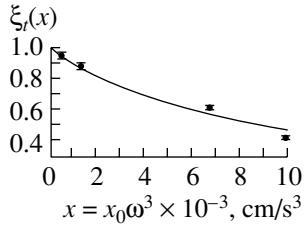

Fig. 5. Theoretical curve (12) and experimental points for experiment on change of storage time in swinging vessel.

should also take into account broadening of the spectrum distribution near the end of the bottle, because it is the most dangerous place where heated neutrons can escape through the wall. From (8), it follows that the broadening of the spectrum of kinetic energies near the bottom is al, and average kinetic energy is shifted by $3al/4$. This shift happens every half of a period, so the speed of energy increase is proportional to $al\omega$. This speed determines the storage time in the vessel, and, because $a = x_0\omega^2$, where x_0 is the amplitude of swinging, we can estimate the part of storage time due to heating of the spectrum as $\tau_v = u/lx_0\omega^3$.

3.5. Storage Time Dependence on Oscillations

If we denote storage time of the stationary vessel as $\tau_0 = t_f/\eta$, where η is the reduced loss coefficient in the stationary vessel at a single collision with the walls, then the storage time τ in the oscillating vessel is determined by the relation

$$\frac{1}{\tau} = \frac{1}{\tau_0} + \frac{1}{\tau_v}, \qquad (11)$$

from which it follows that the theoretical ratio $\xi_t = \tau/\tau_0$ can be represented as

$$\xi_t = \frac{\tau}{\tau_0} = \frac{\tau_v}{\tau_0 + \tau_v} = \frac{1}{1 + \alpha x_0\omega^3}, \qquad (12)$$

where α is some constant. It shows how quickly the equilibrium distribution is achieved. The main factor that influences it is the nonspecular or diffusive part of the reflection coefficient at a single collision with the walls. The parameter α must be found from the experiment.

The magnitude ξ_t is shown in sixth column of the table. The parameter α of (12) was obtained by equating the magnitude in the third line to the experimental value presented in the fifth column.

In Fig. 5, the experimental points and the theoretical curve are shown together. We see that our estimates are reasonable. Some disagreement with the experiment at large parameter $x_0\omega^3$ is understandable, because the theory is not yet complete. It is not evident that estimated losses due to oscillations can be added to losses without oscillations by means of expression (11). It is necessary to check whether the storage curve for the oscillating vessel is exponential or not, and if not, what its functional dependence on t is.

3.6. Vibrating Walls in a Hammered Bottle

The experiment with hammer impacts can also be described theoretically. Here, the impacts excite sound vibrations of the walls, and the losses are determined by collisions with the vibrating walls. If the amplitude of the wall vibration velocity is v_0, and the incident neutron has velocity $\mathbf{v}$, then the reflected one has velocity $\mathbf{u} = \mathbf{v} + 2\mathbf{e}_n v_0 \cos(\omega t)$, where $\mathbf{e}_n$ is a unit vector along the wall normal. After reflection, the energy becomes $E = u^2 = v^2 + 4vv_0 \cos(\omega t)\cos\theta + 4v_0^2\cos^2(\omega t)$, where θ is the angle of incidence. Averaging over angles and time gives the increase in energy in a unit time

$$\frac{dE}{dt} = Sn_0 v \int_0^1 2\cos\theta d\cos\theta \cdot 2v_0^2\cos^2\theta = n_0 S v v_0^2,$$

where S is the surface area of the bottle walls and n_0 is the neutron density. If we reduce losses to a single neutron, then $n_0 = 1/V$, where V is the bottle volume, and the rate of the neutron energy increase is

$$\frac{dE}{dt} = \frac{4}{t_f}v_0^2,$$

where t_f is the free-flight time between collisions with the walls. The storage time related to heating on sound, τ_s, can be defined as

$$\tau_s = E_l\frac{dt}{dE} = t_f\frac{v_l^2}{4v_0^2},$$

where $E_l = v_l^2$ is the limiting energy defined by optical potential of the walls. If the storage time without sound is τ_0, then the decrease in storage time due to the sound is

$$\xi = \frac{\eta}{\eta + 4v_0^2/v_l^2}.$$

If we excite the sound by hammer impacts, the average v_0^2 will be proportional to the number n of impacts during the storage; therefore,

$$K = \frac{1}{1 + \beta n},$$

where $\beta = 4v_0^2/v^2\eta$ is some constant.

4. CONCLUSION

UCN storage in vessels moving with varying acceleration is found to be an interesting problem worthy of theoretical and experimental investigations independently of a previous purely practical need to describe losses in the experiments [3, 6]. Of course, good understanding of UCN behavior in accelerating vessels will help to achieve a high density of neutrons in the bottles, filling them at reactor core, and carefully transporting them to the experimental hall. From the above considerations it immediately follows that comparatively "soft" transportation with accelerations $\omega^2 x_0$ not higher than 4 m/s^2 do not affect much the storage time of UCN. Frequent changes of acceleration are the most dangerous as well as impacts against the duct, which create sound vibrations of the walls. However, in order to achieve our main goal, i.e., to find the real number of neutrons accumulated near the reactor core in the experiments [3, 6], we need to reproduce the mode of the container transportation at a pulsed reactor in full detail.

Here, we considered mainly oscillatory motion of the vessel or its walls. It is interesting also to check how storage time can be affected by rotation of the vessel around its symmetry axis. If the storage time of UCN will decrease in rotating vessel, it will give valuable information on surface quality of the walls and on probability of diffusive scattering of UCN at a single collision with the walls.

REFERENCES

1. V. A. Anikolenko, A. V. Antonov, *et al.*, Kratk. Soobshch. Fiz., No. 11, 40 (1973); Preprint FIAN-92 (Moscow, 1973).
2. W. D. Trüstedt, A. Steyerl, and L. Köster, Bundesministerium für Bildung und Wissenshaft, Forschungsbericht K72-07, Jahrbericht 1970, Mai (1972).
3. A. V. Antonov, O. F. Galkin, *et al.*, Pis'ma Zh. Éksp. Teor. Fiz. **24**, 367 (1976) [JETP Lett. **24**, 352 (1976)].
4. B. V. Bagryanov, D. G. Kartashov, M. I. Kuvshinov, *et al.*, Yad. Fiz. **59**, 1983 (1996) [Phys. At. Nucl. **59**, 1911 (1996)].
5. V. K. Ignatovich, *The Physics of Ultracold Neutrons* (Clarendon, Oxford, 1990).
6. B. V. Bagryanov, D. G. Kartashov, M. I. Kuvshinov, *et al.*, Yad. Fiz. **62**, 844 (1999) [Phys. At. Nucl. **62**, 787 (1999)].

Physics of Atomic Nuclei, Vol. 65, No. 11, 2002, pp. 2036–2043. Translated from Yadernaya Fizika, Vol. 65, No. 11, 2002, pp. 2096–2104.

NUCLEI

Ternary-Fission Dynamics and Asymmetries in Reactions with Polarized Neutrons

V. E. Bunakov and F. Goennenwein[1)]

Institute of Nuclear Physics, Russian Academy of Sciences, Gatchina, Leningrad oblast, 188350 Russia

Received February 28, 2002

Abstract—We consider the results of experimental measurements of P-odd and P-even (left–right) and T-odd asymmetries of charged-particle emission in binary and ternary fission induced by polarized neutrons. We show what information on the ternary-fission mechanism can be obtained from a theoretical analysis of these data. © *2002 MAIK "Nauka/Interperiodica".*

1. EXPERIMENTAL DATA

In ternary fission, apart from two main fission fragments, a third light charged particle is emitted. The studies of parity-nonconservation effects in ternary fission began from the theoretical paper [1]. The following two mechanisms of the process were considered in this paper: the simultaneous emission of a third particle and fission fragments (three-body compound-nucleus decay) and double neck rupture, where a third particle (mainly α) is emitted after the first rupture of the neck from its remnants that still protrude from the fission "prefragments." Two types of P-odd effects were considered: the P-odd asymmetry of the fission fragments $\alpha_{\rm LF}^{\rm PNC}$ attributable to the P-odd correlation $(\boldsymbol{\sigma}_n \cdot \mathbf{p}_{\rm LF})$ and a similar asymmetry $\alpha_{\rm TP}^{\rm PNC}$ of the third particle resulting from the correlation $(\boldsymbol{\sigma}_n \cdot \mathbf{p}_{\rm TP})$. Here, the vector $\boldsymbol{\sigma}_n$ means the spin of the neutron that induces the (n, f) reaction and the vectors $\mathbf{p}_{\rm LF}$ and $\mathbf{p}_{\rm TP}$ are the momenta of the light fragment and the third particle, respectively. In what follows, all vectors are normalized to unity.

It was shown that, when the fragments and the third particle were emitted simultaneously,

$$\alpha_{\rm LF}^{\rm PNC} = \alpha_{\rm TP}^{\rm PNC} \leq \alpha_{\rm bin}^{\rm PNC} \qquad (1)$$

(the index "bin" means binary fission).

In the case of double neck rupture,

$$\alpha_{\rm LF}^{\rm PNC} = \alpha_{\rm bin}^{\rm PNC}, \quad \alpha_{\rm TP}^{\rm PNC} \approx 0. \qquad (2)$$

The physical meaning of these results is quite transparent. When the fragments and the third particle are emitted simultaneously, they are "peer" decay products of the same compound system, where the magnitude of the P-violation effects is determined by the same mixing of neighboring opposite-parity p and s resonances of the compound nucleus. In this "democratic" decay, $\alpha_{\rm LF}^{\rm PNC} = \alpha_{\rm TP}^{\rm PNC}$. The possible decrease in the effect compared to binary fission is associated with an additional phase that appears in three-body decay.

In the case of successive neck ruptures, the first rupture is virtually identical to that in binary fission and the magnitude of the effect for the fragments is determined by the same mixing of opposite-parity resonances of the fissioning compound nucleus. Therefore, the P-odd asymmetry of the fragments in binary and ternary fission is the same. However, the situation with the third particle differs greatly from the situation with the fragments, because, for this particle, $\alpha_{\rm TP}^{\rm PNC}$ is determined by the parity mixing of states of the "prefragments" emitting it. Even if they all were of the same order of magnitude as the mixing in the original fissioning nucleus, their signs would be random (because, in α decay, there are no analogs of the transient states in the fissioning nucleus). Consequently, $\alpha_{\rm TP}^{\rm PNC}$ would become infinitesimal when averaged over billions of the fragment states contributing to the α-particle emission.[2)]

The experimental results from [2–4] indicate that condition (2) is satisfied; i.e., the successive double neck rupture of the fissioning nucleus appears to be the third-particle emission mechanism. All the measurements mentioned above were made with a ^{233}U target. For the P-odd asymmetry of the third particle, the result was obtained in [2]:

$$\alpha_{\rm TP}^{\rm PNC} = (0.06 \pm 0.04) \times 10^{-3}.$$

[1)]Physikalishes Institut, Tuebingen, Germany.

[2)]Our explanation of the small value of $\alpha_{\rm TP}^{\rm PNC}$ differs from that given in [1]. Being clearer and correct, it leads to the same results.

1063-7788/02/6511-2036$22.00

For the achieved accuracy, it is virtually zero. In [3, 4], it was shown that $\alpha_{\rm LF}^{\rm PNC}$ and $\alpha_{\rm bin}^{\rm PNC}$ are equal, to within a factor of (1.05 ± 0.10).

Similar results were obtained in the recent measurements [5] carried out at the Laue–Langevin Institute (ILL) with a cold-neutron beam and a ^{233}U target. The effect measured in ternary fission was found to be

$$\langle \alpha_{\rm LF}^{\rm PNC} \rangle = (0.37 \pm 0.10) \times 10^{-3}.$$

It should be compared with the results from [6] obtained with the same neutron beam for binary fission:

$$\langle \alpha_{\rm bin}^{\rm PNC} \rangle = (0.400 \pm 0.017) \times 10^{-3}.$$

A new and noteworthy result of these latest experiments is also the fact that the asymmetry $\alpha_{\rm LF}^{\rm PNC}$ does not depend on the third-particle energy. Below, we will return to this fact. These experiments confirmed the previously obtained zero value of the P-odd asymmetry of the third particles, but with a lower accuracy: $\alpha_{\rm TP}^{\rm PNC} = (0.09 \pm 0.13) \times 10^{-3}$.

The above new results for ternary fission were obtained with an experimental setup in which the fragment detectors and the target were placed on the axis perpendicular to the neutron-beam direction and the third-particle detectors (semiconductor diodes) were located on the axis perpendicular to the plane formed by the beam direction and the fragment-detector axis. A more detailed description of the setup is given, for example, in [7]. When the P-odd effects were measured, the beam had a transverse polarization, for which the neutron spin was directed either toward the fragment detectors or toward the third-particle detectors, depending on whether the P-odd asymmetry of the fragments or of the third particles was measured. Another result of the recent experiments [5] obtained with the same setup is an estimate of the left–right asymmetry both for the fragments and for the third particles. Consider, for example, an experiment in which the neutron spin was directed along the fragment-detector axis. In this case, the left–right (LR) asymmetry of the third particles in ternary fission can be determined by comparing the counting in the third-particle detectors located at right angles to to the neutron spin and momentum $\mathbf{p}_n$. In this case, we measure the correlation

$$\mathbf{p}_{\rm TP} \cdot [\boldsymbol{\sigma}_n \times \mathbf{p}_n]. \qquad (3)$$

It determines the asymmetry of the third-particle emission toward the plane in which the neutron spin and momentum vectors lie. A close relationship of this P- and T-even correlation to the P-odd effects was pointed out long ago (see, e.g., [8] or [9]). This relationship is based on the fact that the correlation under consideration results from the interference of neighboring s and p resonances of the compound nucleus. It was measured several times for binary-fission fragments in reactions with thermal neutrons (see, e.g., [10–12]). In the ILL experiments with a cold-neutron beam and a ^{233}U target, the following result [12] was obtained:

$$\alpha_{\rm bin}^{\rm LR} = -(0.233 \pm 0.025) \times 10^{-3}.$$

In recent experiments [5] with the same beam, the left–right asymmetry of the third particles in ternary fission of a ^{233}U target has been measured,

$$\langle \alpha_{\rm TP}^{\rm LR} \rangle = -(0.08 \pm 0.08) \times 10^{-3}.$$

The value obtained shows that, within the statistical error limits, there is no left–right asymmetry of the third-particle emission. This result can be explained in the same way as the zero value of $\alpha_{\rm TP}^{\rm PNC}$ in terms of the double neck rupture mechanism.

Next, concurrently with the study of the P-odd effects in ternary fission, the left–right asymmetry of the fission fragments was analyzed. The data processing has not yet finished, but preliminary estimates give

$$\alpha_{\rm LF}^{\rm LR} = -(0.57 \pm 0.13) \times 10^{-3}.$$

By comparing these preliminary data with the above values of $\alpha_{\rm bin}^{\rm LR}$, we cannot unambiguously say whether the asymmetries in binary and ternary fission are equal or unequal. However, theoretical estimates in terms of the mechanism of successive double neck rupture yield equal values for these two asymmetries, and the experimental data, at least, are consistent with this result. It is important to note that, as in the case of P-violating effects for the fragments in ternary fission, the left–right asymmetry of the fragments does not depend on the third-particle energy. This can be seen from Fig. 1*a*.

Thus, the experiments indicate that the characteristics of the P-violating and left–right asymmetries are quite similar.

(1) The values of the effects for the fragments in binary and ternary fission are virtually equal; their

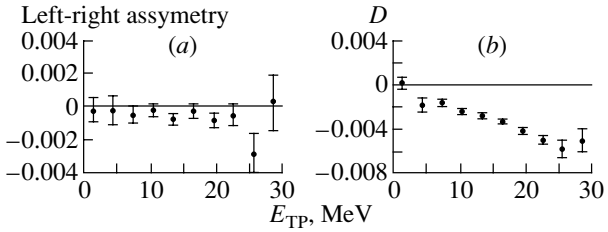

Fig. 1. Ternary fission of ^{233}U(n, f) by cold neutrons: (*a*) the left–right asymmetry of the fission fragments as a function of the third-particle energy; (*b*) T-odd correlation D as a function of the third-particle energy.

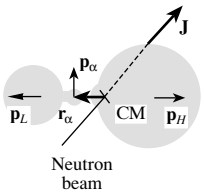

Fig. 2. A schematic view of the third-particle (α) emission in double neck rupture. CM marks the center-of-mass position of the fissioning system; $\mathbf{r}_\alpha$ and $\mathbf{p}_\alpha$ are the coordinate and momentum of the emitted α particle, respectively; **J** is the spin of the compound nucleus that captures a positive-helicity neutron.

values for the P-odd and left–right effects in the $^{233}\mathrm{U}(n,f)$ reaction with cold neutrons are on the order of 10^{-4}.

(2) In ternary fission, the P-odd and left–right effects for the fragments do not depend on the third-particle energy (see Fig. 1*a*).

(3) For the third particles, we failed to detect the P-odd and left–right effects with the available accuracy (i.e., their upper limit is approximately a factor of 5 lower than the measured effects for the fragments).

However, the most unexpected effect was detected with the setup [7] for longitudinally polarized neutrons: the light fragment flies to the left, while the third particle flies upward (see Fig. 2). Having measured the number of coincidences of the light fragments with the third particles N_+ in this geometry, we change the neutron helicity (or the direction of any of the momenta $\mathbf{p}_{\mathrm{LF}}$ or $\mathbf{p}_{\mathrm{TP}}$) and again measure the number of coincidences N_-. The difference $(N_+ - N_-)$ is related to the triple T-odd correlation of the form

$$\boldsymbol{\sigma}_n \cdot [\mathbf{p}_{\mathrm{LF}} \times \mathbf{p}_{\mathrm{TP}}]. \qquad (4)$$

Normalizing this difference yields the T-odd asymmetry D,

$$D = \frac{N_+ - N_-}{N_+ + N_-}. \qquad (5)$$

The measurement of this correlation was suggested in [13] by analogy with the β decay of a polarized neutron, in which the T-odd correlation

$$\boldsymbol{\sigma}_n \cdot [\mathbf{p}_e \times \mathbf{p}_\nu]$$

between the neutron spin and electron and neutrino momentum vectors was analyzed to test the T invariance.

The triple correlation was measured in the reaction of fission of $^{235}\mathrm{U}$ and $^{233}\mathrm{U}$ targets by cold neutrons. In both cases, the measurements were made for two main types of third particles (α and t). For ternary fission in the $^{233}\mathrm{U}(n,f)$ reaction, the following asymmetries D (averaged over the third-particle energy) were found:

$$\langle D\rangle_\alpha = -(2.52 \pm 0.14) \times 10^{-3}, \qquad (6)$$
$$\langle D\rangle_t = -(1.99 \pm 0.63) \times 10^{-3}.$$

For the $^{235}\mathrm{U}(n,f)$ reaction, the corresponding results are

$$\langle D\rangle_\alpha = +(0.83 \pm 0.11) \times 10^{-3}, \qquad (7)$$
$$\langle D\rangle_t = +(0.60 \pm 0.41) \times 10^{-3}.$$

Note that the effects for α particles and tritons are identical in sign and magnitude. Since, in contrast to the α particles, the tritons have a nonzero spin, these results apparently indicate that the measured correlations depend neither on the type of third particle nor on its spin.

Note also that this effect depends markedly on the third-particle energy (see Fig. 1*b*). In Eqs. (6) and (7), the measured values of D were obtained by averaging over the third-particle energy E_{TP} under the assumption of a linear E_{TP} dependence of D. Juxtaposing this dependence with the third-particle-energy independence of the P-violating and left–right asymmetries (see Fig. 1*a*), we are inclined to conclude that the nature of the P-odd and left–right asymmetries is similar (the interference and parity mixing of neighboring s and p resonances of the fissioning compound nucleus), while the origin of the triple correlation is associated with a completely different source.

Although the correlation (4) is formally a T-odd one, it was repeatedly pointed out (see, e.g., [14, 15]) that, in contrast to P violation, a nonzero T-odd correlation is directly related to the violation of T invariance only in the case of elastic scattering. In all inelastic processes like β and γ decay or fission, this relationship can be established only if this process can be described in the first Born approximation, and, even in this case, the relationship is severely masked by the effects of initial- or final-state interaction. Since the fission is associated with strong-interaction processes, it can hardly be described in the first Born approximation. Therefore, the possible explanation of the observed correlation should most likely be sought in the fission dynamics, but should not be considered to be an indication of the violation of T invariance. Below, we offer a possible qualitative version of this explanation.

2. THE MODEL TO EXPLAIN THE T-ODD TRIPLE CORRELATION

When a neutron with polarization P_n is absorbed by a target nucleus with spin I, a partially polarized compound resonance with the following polarization emerges:

$$P(J^+) = \{(2I+3)/[3(2I+1)]\}P_n \quad \text{for } J^+ = I+1/2,$$
$$P(J^-) = (-1/3)P_n \quad \text{for } J^- = I-1/2. \tag{8}$$

(Note that, for J^-, the polarization direction becomes opposite to the neutron polarization direction.)

Let us first consider, for simplicity, an isolated resonance (say, J^+). In that case, the probability of ternary fission induced by neutrons can be written as

$$W_{n,\mathrm{tf}} \sim \pi\lambda^2 \frac{2J^+ + 1}{3(2I+1)} \times \frac{\Gamma_n \Gamma_{\mathrm{tot}}}{(E - E(J^+))^2 + \Gamma_{\mathrm{tot}}^2/4}[w_{\mathrm{tf}} + P(J^+)w_{\mathrm{tf}}^P]. \tag{9}$$

Here, the factor in front of the square brackets is the cross section for the formation of the $\sigma(J^+)$ compound resonance in the reaction; λ is the neutron wavelength; Γ_n and Γ_{tot} are the neutron and total resonance widths, respectively; and w_{tf} and w_{tf}^P are the ternary fission probabilities for unpolarized and polarized nuclei, respectively.

We use the statistical approach to estimate the probability w_{tf}, because its validity in describing fission has been shown repeatedly. In this approach, the probability w_{tf} is defined by product of the level-density functions

$$\rho_i(A_i, E_{xi}^{\mathrm{sc}}, J_i) \sim \exp\left[2\sqrt{a_i(E_{xi}^{\mathrm{sc}} - E_{\mathrm{rot}}(J_i))}\right] \approx \exp\left[2\sqrt{a_i E_{xi}^{\mathrm{sc}}}\right], \tag{10}$$

where the indices $i = L, H$ denote a light or a heavy fragment, and A_i, E_{xi}^{sc}, and $E_{\mathrm{rot}}(J_i) = \hbar^2 J(J+1)/2\mathcal{J}_i$ are, respectively, the mass number, the internal excitation energy of the fragment at the time of scission, and its rotational energy. In general, E_{rot} does not exceed a few fractions of MeV, which allows us to disregard it compared to E_{xi}^{sc}.

To write the probability w_{tf}^P, we should use an expression for the level density $\rho_i(A_i, E_{xi}^{\mathrm{sc}}, M_i)$ with a fixed projection M_i of the total spin J_i onto the specified axis. According to (2.324) from [16], this expression is

$$\rho_i(A_i, E_{xi}^{\mathrm{sc}}, M_i) \sim \exp\left[2\sqrt{a_i(E_{xi}^{\mathrm{sc}} - \hbar^2 M_i^2/2\mathcal{J}_i)}\right] \approx \exp\left[2\sqrt{a_i E_{xi}^{\mathrm{sc}}}\left(1 - \hbar^2 M_i^2/4\mathcal{J}_i E_{xi}^{\mathrm{sc}}\right)\right]. \tag{11}$$

For positive neutron helicity and for the α-particle emission mechanism shown in Fig. 2, experiments are carried out in such a way that, when the third particle (let it be α) is emitted upward, its angular momentum $\mathbf{l}_\alpha = \mathbf{r}_\alpha \times \mathbf{p}_\alpha$ is parallel to the spin $J_z = M = J^+$ of the polarized system. The main idea of our approach is that, if the angular momentum $\mathbf{l}_\alpha$ of the escaping α particle is parallel to the polarized-system spin $J_z = M = J^+$, then the emitted α particle carries away part of the angular momentum of the original system, so that $M_f = M - l_\alpha$ in the final state. If, alternatively, the angular momentum l_α is antiparallel to M, then the system gains a recoil and increases its angular momentum to $M_f = M + l_\alpha$. Therefore, the emission of an α particle increases and decreases the level density of the final system for $w_{\mathrm{tf}}^{P\uparrow}$ (upward α emission) and $w_{\mathrm{tf}}^{P\downarrow}$ (downward emission), respectively.

Now, we can write the expression for D as

$$D = \frac{N_{\mathrm{par}} - N_{\mathrm{anti}}}{N_{\mathrm{par}} + N_{\mathrm{anti}}} = \frac{[w_{\mathrm{tf}}^{P\uparrow} - w_{\mathrm{tf}}^{P\downarrow}]P(J^+)}{2w_{\mathrm{tf}} + [w_{\mathrm{tf}}^{P\uparrow} + w_{\mathrm{tf}}^{P\downarrow}]P(J^+)}. \tag{12}$$

It is important to note that the double neck rupture mechanism discussed above assumes that an α particle is emitted by the neck remnants sticking out of the prefragment almost immediately after the first neck rupture. In terms of this mechanism, experimental data on the P-odd and left–right asymmetries indicate that the separation between the "prefragments" at the time of α-particle emission exceeds only slightly the range of nuclear forces (for strong and weak interactions). However, the long-range Coulomb forces of interaction between the fragments and the α particle are still strong enough for them to transfer energies and angular momenta. From this viewpoint, there is virtually no difference between the successive and simultaneous neck rupture mechanisms.

However, after the emission of an α particle, the initial spin polarization $P(J)$ of the compound nucleus $J = M$ changes, because it is transferred to the separating fragments and decreases due to the appearance of additional spins J_1 and J_2 in the fragments, which are known from experiments on γ-ray emission from them. These experiments show that the spins are $J_1 \approx J_2 \approx (5\text{–}8)\hbar$ and that they are oriented perpendicular to the fission axis. Recent experiments revealed [17] that the γ-ray-emission axis is not correlated with the direction of α-particle emission. These experimental results were justified in recent theoretical studies [18] of the orientation pumping mechanism of the fragment spins, which is

based on the uncertainty relation between the orientation angles of the deformed fragments relative to the fission axis and their spins. It was shown that, in most cases, this mechanism mainly contributes to the fragment spins, thereby replacing the other fragment-spin sources suggested previously (e.g., the bending mode of fission). Thus, it would be reasonable to assume that these "additional" fragment spins are oriented isotropically around the fission axis. The initial $J_z = M = J$ value would then be constant, while the fragment polarization would decrease compared to this value by the "factor of polarization transfer to the fragments," μ_{11}. These factors were included in implicit form in the fission probabilities $w_{\rm tf}^P$ in Eq. (9). The factors of polarization transfer to the fragments were calculated in [19] for the initial compound-nucleus polarization directed along the fission axis; their values ranged from -0.1 to $+0.1$, depending on various assumptions about the specific fission mechanisms. However, these calculations were performed by assuming that the helicity K (the nucleus-spin projection onto the fragment-separation axis) was a "good" quantum number, because the angular momentum L_f of the separating fragments was taken to be virtually zero. Recently, it has been shown [20] that, for the classical Bohr–Wheeler picture of fragment separation along the straight line coincident with the deformation axis of the fissioning nucleus to be preserved, L_f must be large enough. This can be easily understood, because only an infinite superposition of L_f values leads to the motion along a straight line in quantum mechanics. For any finite sum of L_f, the same uncertainty relation that was used in the above-mentioned paper [18] on the orientation pumping of spins gives a cone with an opening angle $\sim 1/L_f$.

Since the quantum numbers K "deteriorate" in the presence of a centrifugal barrier (the operator $\hat{K}$ does not commute with the operator $\hat{L}^2$; see, e.g., [21]) and since we need to calculate the transfer factors μ_{11} precisely in the region where this barrier is most pronounced, it would be good to estimate μ_{11} for our geometry in the L representation rather than in the K one. These calculations are being performed at present, while, for now, we hypothesize that the initial polarization (and the spin J) of the fissioning compound nucleus is equally distributed between the fragments and the angular momentum L_f of their relative motion. In this case, we obtain for the heavy and light fragments

$$\mu_{11} = \frac{J}{3J_1}. \tag{13}$$

Recall, for convenience, that $J = J_z = M$ is the spin of the polarized compound nucleus, while J_1 and J_2 are the spins introduced into the first and second fragments by mechanisms similar to orientation pumping or bending mode. Below, we assume that the contributions from the light and heavy fragments to the effect are

$$D = \frac{1}{2}(D_L + D_H). \tag{14}$$

Substituting now expressions (10), (11), (13), and (14) into (12) yields the contribution from the ith fragment to D:

$$D_i \approx \left\{ \left(\exp\left[-\frac{\hbar^2 (M_i - l_\alpha)^2 \sqrt{a_i}}{2\mathcal{J}_i \sqrt{E_{xi}^{\rm sc}}} \right] - \exp\left[-\frac{\hbar^2 M_i^2 \sqrt{a_i}}{2\mathcal{J}_i \sqrt{E_{xi}^{\rm sc}}} \right] \right) \Big/ \left(2 \left[1 + \left(\exp\left[-\frac{\hbar^2 (M_i - l_\alpha)^2 \sqrt{a_i}}{2\mathcal{J}_i \sqrt{E_{xi}^{\rm sc}}} \right] + \exp\left[-\frac{\hbar^2 M_i^2 \sqrt{a_i}}{2\mathcal{J}_i \sqrt{E_{xi}^{\rm sc}}} \right] \right) \mu_{11} P(J^+) \right] \right) \right\} \mu_{11} P(J^+) \tag{15}$$

Expanding the exponential functions in (15) into a series and disregarding the small second term in the denominator, we obtain

$$D_i \approx \frac{\hbar^2 M_i l_\alpha \sqrt{a_i}}{2\mathcal{J}_i \sqrt{E_{xi}^{\rm sc}}} \mu_{11} P(J^+). \tag{16}$$

Thus, the total effect for an isolated J^+ resonance is

$$D(J^+) \approx \frac{1}{2} \left[\frac{\hbar^2 M_L l_\alpha \sqrt{a_L}}{2\mathcal{J}_L \sqrt{E_{xL}^{\rm sc}}} + \frac{\hbar^2 M_H l_\alpha \sqrt{a_H}}{2\mathcal{J}_H \sqrt{E_{xH}^{\rm sc}}} \right] \times \mu_{11} P(J^+). \tag{17}$$

The same reasoning for an isolated compound J^- resonance leads to a similar expression,

$$D(J^-) \approx \frac{1}{2} \left[\frac{\hbar^2 M_L l_\alpha \sqrt{a_L}}{\mathcal{J}_L \sqrt{E_{xL}^{\rm sc}}} + \frac{\hbar^2 M_H l_\alpha \sqrt{a_H}}{\mathcal{J}_H \sqrt{E_{xH}^{\rm sc}}} \right] \times \mu_{11} P(J^-). \tag{18}$$

It can be easily seen from Eq. (8) and Fig. 2 that, in this case, the polarization $P(J^-)$ and the effect are negative.

Finally, taking into account the contributions of $\sigma(J^+)$ and $\sigma(J^-)$ to the total fission cross section, we obtain

$$D \approx \frac{\sigma(J^+)D(J^+) + \sigma(J^-)D(J^-)}{\sigma(J^+) + \sigma(J^-)}. \qquad (19)$$

Let us now consider the experimentally observed dependence of the effect on the final energy E_α of the escaping third particle.

The denominators in (17) and (18) contain the square roots of the internal excitation energies of the fragments at the time of scission, $\sqrt{E_{xi}^{\rm sc}}$. The mean total internal excitation energy $\langle E_x^{\rm sc}\rangle$ of the system at the scission point was estimated phenomenologically [22] from the even–odd difference between the fragment-charge yields as functions of the compound nucleus and its excitation energy. This estimation yielded $\langle E_x^{\rm sc}\rangle \approx 6$ MeV for uranium-isotope fission. Subsequently, this estimate was confirmed by theoretical calculations [23]. This energy arises from friction in the system when descending from the saddle point to the scission point. Next, recall the linear anticorrelation between the total excitation energy of the system and the third-particle energy E_α found in [24]. However, the total excitation energy includes both the internal excitation energy and the fragment deformation energy at the scission point. Therefore, the problem is to find the relation between $E_x^{\rm sc}$ and E_α. To this end, it would be reasonable to assume that the length and time of the descent mentioned above changes with the scission configuration. For the largest descent length, $E_x^{\rm sc}$ must be at a maximum ($E_{x,\max}^{\rm sc}$). In this case, the system will have the most elongated shape at the scission point. If ternary fission originates from this elongated configuration, then the α-particle energy (determined by the Coulomb repulsion from this configuration) will be at a minimum ($E_{\alpha,\min}$). In the opposite case of the shortest descent, the configuration at the scission point will be most compact, with the minimum value of $E_{x,\min}^{\rm sc}$ but with the maximum α-particle energy $E_{\alpha,\max}$. Assuming now a random distribution of $E_x^{\rm sc}$ about its mean value $\langle E_x^{\rm sc}\rangle = 6$ MeV and of E_α about its experimentally observed maximum in the α-particle spectrum $\langle E_\alpha\rangle = 16$ MeV as well as taking into account the above linear anticorrelation found in [24], we obtain a semiempirical formula for the anticorrelation:

$$E_x^{\rm sc} = E_{x,\max}^{\rm sc} - \frac{E_{x,\max}^{\rm sc}}{E_{\alpha,\max}}E_\alpha = \left(12 - \frac{12}{32}E_\alpha\right)\ [\text{MeV}]. \qquad (20)$$

For an equidistribution of $E_x^{\rm sc}$ between the two fragments, we have for each of them

$$E_x^{\rm sc} = \left(6 - \frac{6}{32}E_\alpha\right)[\text{MeV}]. \qquad (21)$$

Finally, substituting (21) into expressions (17)–(19) yields the following dependence of the triple-correlation coefficient D on the third-particle energy E_α:

$$D \sim 1/\sqrt{6 - 0.2E_\alpha}. \qquad (22)$$

The experimental data points are fitted by this expression in Fig. 3. Given the simplified assumptions used to derive Eqs. (20) and (21), the agreement may be considered to be satisfactory.

As we see from (19), for the triple correlation D to be calculated, the contributions of $\sigma(J^+)$ and $\sigma(J^-)$ to the fission cross section must be known. At present, this information is available only for the ^{235}U target [25]. Within the range of neutron energies concerned ($5 \le E_n \le 25$ meV), these contributions are $\sigma(J^+ = 4) = 553$ b and $\sigma(J^- = 3) = 323$ b.

In order to estimate D from (17) and (18), we must also estimate several other parameters, for example, the moment of inertia. The fragments are severely deformed immediately after the α-particle emission. This causes an increase in their moments of inertia almost up to rigid-body values (see, e.g., [26]) and an increase in their level-density parameters a_i. The estimates [27] based on microscopic calculations in the deformed Nilsson potential indicate that, near the scission point, these parameters can exceed the values for equilibrium deformations by a factor of 1.5–2. Therefore, we took rigid-body values for the moments of inertia $\mathcal{J}_i$ and doubled the "standard" values of $a_i \approx A_i/8$ in estimating D. Since an experimental comparison of the γ-ray emissions by the fragments in binary and ternary fission shows that the α particle of the ternary fission carries away no more than 10–15% of the fragment spin, we took $l_\alpha = 1\hbar$ for our estimates. Substituting all these values into expressions (17)–(19) and using formula (21), we obtain for ^{235}U

$$D \approx +1.5 \times 10^{-3}$$

at $E_\alpha = 16$ MeV, the maximum of the α-particle spectrum. Since we did not average our D over the α-particle spectrum (as was done when obtaining the experimental D), this value should be compared with the value of the experimental fit (see Fig. 3), i.e., with $+0.75 \times 10^{-3}$.

In the case of ^{233}U, where the contributions of the various compound-nucleus spins to the fission cross section are not known, we could obtain only limits for the effect by estimating $D(J^+ = 3)$ and $D(J^- = 2)$. It follows from these estimates that the effect for ^{233}U must be within the range from -2×10^{-3} to $+3 \times 10^{-3}$. The experimental fit for ^{233}U gives $D \approx -1.8 \times 10^{-3}$ at $E_\alpha = 16$ MeV (see Fig. 3).

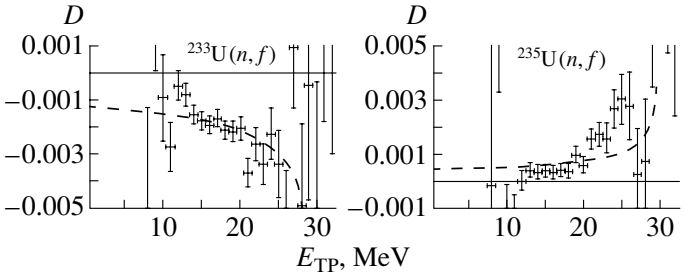

Fig. 3. Triple-correlation coefficients D for the $^{233}\mathrm{U}(n,f)$ and $^{235}\mathrm{U}(n,f)$ reactions as functions of the α-particle energy. The dashed curves represent the fits to the data obtained using the theoretical formula (22) (only one normalization constant was used for the fitting).

Thus, at present, we can assert that our approach yields a correct order-of-magnitude estimate for the effect (to within a factor of 2), satisfactorily reproduces its dependence on the third-particle energy, and gives the correct sign of the effect in the only case where the known contributions of the J^+ and J^- resonances to the fission cross section allow it to be calculated.

3. CONCLUSION

Recent experiments on the ILL reactor have shown that the P-odd and left–right asymmetries in ternary fission induced by cold polarized neutrons share several common features: the asymmetries are virtually identical in binary and ternary fission; the third-particle asymmetries are much smaller than those for the fragments (at the currently available accuracy, their values are compatible with zero ones); the asymmetries in ternary fission do not depend on the third-particle energy. All these features can be satisfactorily explained by the theory if the third particle is emitted in double neck rupture. The first rupture corresponds to binary fission and the subsequent second rupture ejects the third particle from the neck remnants and results in ternary fission. The P-odd and left–right asymmetries of the fragments are associated with the interference of neighboring s and p resonances of the compound nucleus. Note that the dependence of the asymmetries on the third-particle energy has not been studied previously. The absence of this dependence indicates that the system shape at the scission point spanning a wide range of deformations and determining the third-particle energy by its Coulomb repulsion does not affect the fragment asymmetry; i.e., the asymmetry is established well before the scission.

The study of the triple correlation between the spin of the fission-inducing neutron and the fragment and third-particle momenta was initially stimulated by the search for the violation of T invariance. However, the discovery of surprisingly large effects immediately cast doubt on the suggestion that the observed correlation could be related to the violation of T invariance. The theory has always indicated that the observation of T-odd correlations, in most cases, does not imply the violation of T invariance. Therefore, the problem of interpreting the new phenomenon arose. The key observation was the fact that, in contrast to the P-odd and left–right asymmetries, the triple correlation appreciably depended on the third-particle energy and, hence, on the configuration at the scission point. This suggested the interaction in the final state.

Here, we presented a viable model that accounts for this correlation. Its main idea was suggested in [28]. It uses the fact that, during the third-particle emission, the Coulomb interaction with the fission fragments results in the transfer of not only energy but also angular momentum. In the geometry of the experimental setup, the third-particle angular momentum either increases or decreases the internal angular momentum (spin) of the fragments for neutrons with positive or negative neutron helicities. This change causes a change in the fragment rotational energy that determines their level density. In the statistical model, this leads to a difference between the third-particle emission probabilities. For a reasonable choice of various parameters (like the fragment moments of inertia), the model yields a correct order-of-magnitude estimate for the effect. The model also satisfactorily reproduces the main feature of the triple correlation, its dependence on the third-particle energy.

ACKNOWLEDGMENTS

We are grateful to A. Barabanov, S. Kadmensky, M. Mutterer, G. Petrov, W. Furman, and P. Jesinger for useful advice and discussions. The work was supported by the INTAS (project no. 99-0229) and the Russian Foundation for Basic Research (project no. 99-02-17275).

REFERENCES

1. V. Bunakov and V. Gudkov, Z. Phys. A **321**, 277 (1985).
2. G. Petrov, G. Val'ski, *et al.*, Nucl. Phys. A **502**, 297 (1989).
3. A. V. Belozerov, G. V. Danilyan, *et al.*, Pis'ma Zh. Éksp. Teor. Fiz. **54**, 132 (1991) [JETP Lett. **54**, 132 (1991)].
4. F. Goennenwein *et al.*, Nucl. Phys. A **567**, 303 (1994).
5. P. Jesinger, A. Kötzle, F. Gönnenwein, *et al.*, Yad. Fiz. **65**, 662 (2002) [Phys. At. Nucl. **65**, 630 (2002)].
6. A. Koetzle *et al.*, Nucl. Instrum. Methods Phys. Res. A **440**, 750 (2000).
7. P. Jesinger *et al.*, Nucl. Instrum. Methods Phys. Res. A **440**, 618 (2000).
8. O. P. Sushkov and V. V. Flambaum, Usp. Fiz. Nauk **136**, 3 (1982) [Sov. Phys. Usp. **25**, 1 (1982)].
9. V. Bunakov and V. Gudkov, Nucl. Phys. A **401**, 93 (1983).
10. A. K. Petukhov, G. A. Petrov, *et al.*, Pis'ma Zh. Éksp. Teor. Fiz. **32**, 324 (1980) [JETP Lett. **32**, 300 (1980)].
11. V. A. Vesna, V. M. Lobashev, *et al.*, Pis'ma Zh. Éksp. Teor. Fiz. **31**, 704 (1980) [JETP Lett. **31**, 663 (1980)].
12. A. Alexandrovich, A. Gagarski, G. Petrov, *et al.*, Nucl. Phys. A **567**, 541 (1994).
13. K. Schreckenbach *et al.*, in *Time Reversal Invarince and Parity Violation in Neutron Reactions,* Ed. by C. Gould (World Sci., Singapore, 1994), p. 187.
14. R. Blin-Stoyle, *Fundamental Interactions and the Nucleus* (North-Holland, Amsterdam, 1973).
15. V. Bunakov and L. Pikelner, Prog. Part. Nucl. Phys. **39**, 337 (1997).
16. O. Bohr and B. R. Mottelson, *Nuclear Structure* (Benjamin, New York, 1969; Mir, Moscow, 1971), Vol. 1.
17. Yu. Kopach, M. Mutterer, *et al.*, Phys. Rev. Lett. **82**, 303 (1999).
18. I. Mikhailov and P. Quentin, Phys. Lett. B **462**, 7 (1999) .
19. A. L. Barabanov and D. P. Grechukhin, Yad. Fiz. **47**, 648 (1988) [Sov. J. Nucl. Phys. **47**, 411 (1988)].
20. S. Kadmensky, in *Proceedings of ISINN-9, Dubna, 2001*.
21. A. L. Barabanov and V. D. Furman, Z. Phys. A **357**, 411 (1997).
22. F. Goennenwein, in *The Nuclear Fission Process,* Ed. by C. Wagemans (CRC, Boca Raton, 1991), Chap. 8, p. 417.
23. F. Rejmund, A. Ignatyuk, *et al.*, Nucl. Phys. A **678**, 215 (2000).
24. P. Heeg, M. Mutterer, M. Panicke, *et al.*, in *Proceedings of Conference on 50 Years with Nuclear Fission, Gaithersburg, 1989* (American Nuclear Society, La Grange Park, 1989), Vol. 1, p. 299.
25. Yu. N. Kopach, A. B. Popov, V. I. Furman, *et al.*, Yad. Fiz. **62**, 900 (1999) [Phys. At. Nucl. **62**, 840 (1999)].
26. O. Bohr and B. R. Mottelson, *Nuclear Structure* (Benjamin, New York, 1975; Mir, Moscow, 1977), Vol. 2.
27. A. V. Ignatyuk, G. N. Smirenkin, and A. S. Tishin, Yad. Fiz. **15**, 1124 (1972) [Sov. J. Nucl. Phys. **15**, 622 (1972)].
28. V. E. Bunakov, Yad. Fiz. **65**, 648 (2002) [Phys. At. Nucl. **65**, 616 (2002)]; V. Bunakov and G. Petrov, in *Proceedings of ISINN-8, Dubna, 2000,* p. 100.

Translated by O. Chernavskaya

Physics of Atomic Nuclei, Vol. 65, No. 11, 2002, pp. 2044–2051. From Yadernaya Fizika, Vol. 65, No. 11, 2002, pp. 2105–2112.

NUCLEI

Resonance-Spin Memory in Low-Energy-Gamma-Ray Spectra from Sb, Tb, Ho, and Ta Odd–Odd Compound Nuclei*

U. Olejniczak[1], N. A. Gundorin[2], L. B. Pikelner[2], M. Przytuła[3], and D. G. Serov[2]

Received March 15, 2002

Abstract—The low-energy-gamma-ray spectra from neutron resonance capture with natural samples of Sb, Tb, Ho, and Ta were measured using the HPGe detector at the IBR-30 pulsed reactor at the JINR, Dubna. The resonance-spin-memory effect in the spectra from the odd–odd compound nuclei of ^{122}Sb, ^{169}Tb, and ^{166}Ho was found to be quite distinct. For the ^{182}Ta compound nucleus, it proved to be rather weak. © *2002 MAIK "Nauka/Interperiodica".*

1. INTRODUCTION

In the early days of neutron spectroscopy, the obtained experimental data exhibited a difference in the relative population of isomeric states from various neutron resonances in the same nuclide [1, 2]. The data analyzed by Draper *et al.* [3] allowed them to conclude that one can sometimes expect the population of the low-lying levels of the compound nucleus by cascade transitions to depend on the spin of the initial resonance state. The authors of [3] carried out an experiment designed to explain whether the differences in the low-energy-gamma-ray spectra from resonances in neutron capture with an indium target were significant. The spectra in the energy region up to 350 keV from three of the ^{115}In lowest resonances, 1.46, 3.86, and 9.1 eV with spins 5, 4, and 5, respectively, were different, but there was no clear correlation between the spectra and spins.

Domanic and Sailor [4] subsequently found experimental evidence that the ratios of the populations of the isomeric 70-keV level and the ground state of the ^{116}In compound nucleus for the resonance at 1.456 eV with spin 5 and for the resonance at 3.86 eV with spin 4 were quite different. They concluded that the difference by one in the spins of the initial resonance states significantly influenced the population ratios of the final low-lying levels. Thus, one could expect that the neutron-capture gamma-ray spectra for the two considered resonances should be clearly different.

Huizenga and Vandenbosch in their paper [5], which was devoted to the interpretation of isomeric cross-section ratios for radiative neutron capture, considered the question of whether the value of an isomeric ratio could provide some information about the spin of an initial resonance-capture state. They performed some calculations based on a simplified model of the cascade transition process assuming only dipole transitions and the application of the statistical model. The authors stated that the results of the calculations and the experimental data proved consistent enough to consider them as a guide to assign spins to the compound states formed in the resonance neutron capture. But they cautioned that the performed calculations were not appropriate for the cases where a statistical description was not valid.

The results of the studies outlined above show that, despite a large number of intermediate excited levels, which are accessible for transitions in cascade deexcitation, the memory of the spin of the initial resonance state is not lost completely, at least for some nuclei. The spin memory should be reflected in the difference between the low-energy-gamma-ray spectra consisting of the transitions between the low-lying levels populated by the cascades initiated from the resonance states of different spins.

The new method of the spin assignment of s-wave neutron resonances, proposed by Wetzel and Thomas [6], is based on the conclusions presented above. The essence of the method consists in the comparison of the intensity ratios for a properly chosen pair of low-energy transitions from many resonance gamma-ray spectra. The spin-memory effect manifests itself by grouping the intensity ratios around two different average values corresponding to the resonance spins $J_r = J_x \pm 1/2$, where J_x is the spin of a target nucleus. The authors of [6] tested their method on resonances with known spins, and, moreover, they as-

*This article was submitted by the authors in English.

[1]Department of Nuclear Physics, University of Lodz, Poland.
[2]Joint Institute for Nuclear Research, Dubna, Moscow oblast, 141980 Russia.
[3]The College of Computer Science, Lodz, Poland.

signed spin values to 18 resonances of ^{167}Er and ^{187,189}Os isotopes. All the resonance states investigated in [6] belong to even–even compound nuclei.

Shortly after [6], a number of experiments that employed the new method of spin assignment were carried out [7–11]. Therefore, apart from the investigations of the spin-memory effect for those eight isotopes studied by Wetzel and Thomas [6], that effect was also analyzed in neutron resonance reactions on the target isotopes ^{121,123}Sb [7], ^{169}Tm [8], ^{143,145}Nd [9], ^{115}In [10], and ^{175,176}Lu [11]. In one of the recent studies, the effect was helpful in the spin assignment for the resonances of the target isotope ^{109}Ag [12]. The prediction of the spin-memory effect on the basis of a theory or a rigorous model of the cascade transition process is rather difficult and might even prove impossible. The structures of excited nuclei are very complicated, and the description of the excited levels below the neutron separation energy is not precisely known. The early attempts at the theoretical analysis of that process were undertaken by Pönitz [13] and Sperber [14]. The obtained results showed how complicated the problem was, and that its solution must be found for each nuclide individually. Thus, one cannot tell a priori which pair of transitions reveals, by its intensity ratios, the existence of the spin-memory effect or whether it exists at all in the nuclide in question. Nevertheless, the information on its existence and size is important not only for the method of spin assignment in the neutron spectroscopy but also for the theory of the cascade transition process.

Some time ago, our attention was attracted by a remark that we found in the concluding part of the paper by Stolovy *et al.* [9]. The remark concerns the so-called indirect methods of resonance-spin determinations, to which the Wetzel–Thomas method belongs. The authors of [9] wrote that the methods "should not be used in the following cases: (1) if there is a high density of low-lying states with a wide variety of spins, so that the effect of the capture state spin is diluted (most odd–odd compound nuclei) ...." Despite this cautious reservation, some cases of certain odd–odd compound nuclei that reveal a quite considerable spin-memory effect have been described. Such nuclei are, for example, two antimony isotopes [7], thulium [8], indium [10], lutetium [11], and finally the silver-109 target isotope [12]. Are they exceptions only, or is it a rule?

To cast some additional light on the question, we chose the appropriate isotopes of terbium, holmium, and tantalum for the investigation. They are all excellent candidates for further investigations to the extent to which the suspected lack of the spin-memory effect in the nuclides specified above is justified. After resonance neutron capture, the nuclei of the selected natural elements become the odd–odd compound nuclei. They have a high density of low-lying levels, as they are middle-weight nuclei, as well as rather far from the magic nuclei. And as highly deformed nuclei, they have many low-lying bands of collective levels with a wide variety of spins [15]. The purpose of the present work was to detect experimentally the spin-memory effect in the three chosen nuclides, which have extremely favorable properties for the loss of spin memory in the cascade transition process.

2. EXPERIMENTAL ARRANGEMENT

The investigations of the resonance radiative neutron capture were performed at the pulsed reactor IBR-30 of the Laboratory of Neutron Physics, JINR, Dubna. The use of the time-of-flight method on a 60.5-m flight path for slow neutron spectrometry allowed the resolution of neutron energy $\Delta E = 1.9 \times 10^{-3} E^{1.5}$ to be achieved, where energy is in eV. The low-energy-gamma-ray spectra from the radiative capture were measured by a HPGe detector with the relative efficiency of 12% and 2.2-keV resolution at the 1332.5-keV gamma-ray ^{60}Co line.

The investigated plate samples were placed in the collimated neutron beam whose circular section was 5 cm in diameter at an angle of 45° to the beam direction and at a distance of 8 cm from the detector head. The detector was surrounded by a shield composed of 5-cm (CH/B-10) + 5-cm Pb + 1-cm Cu layers. To absorb the recycling neutrons with an energy below 0.17 eV, a cadmium sheet of 0.5-mm thickness was placed in front of the neutron collimator. The arrangement is shown schematically in Fig. 1.

Two parameters of the detector pulses, i.e., the time-of-flight of captured neutron and pulse-height of a detected gamma-ray photon, were analyzed by the computer data-acquisition system using a program of multidimentional measurement registration DELREN and were recorded in the memory. The obtained experimental data were located in 1024 time-of-flight and 8192 pulse-height channels. These data could be processed in an off-line procedure, which allows the selection of any required information that was accessible from the experiment.

The first measurement was treated as a test of the experimental arrangement. A natural antimony sample from Sb_2O_5 powder contained between thin aluminium sheets was used in that experiment. The spin-memory effect for antimony isotopes was investigated by Bhat *et al.* [7] and found to be very significant.

For the subsequent measurements, samples of natural terbium, holmium and tantalum were used in the form of metallic plates that had a thickness of 0.6, 0.5, and 0.11 mm, respectively.

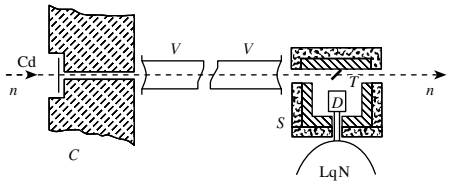

Fig. 1. Scheme of the horizontal section of the experimental arrangement: $(n-n)$ is neutron beam, Cd is cadmium filter, C is collimator, $(V-V)$ is vacuum beam tube, D is HPGe detector, S is detector shield, T is investigated sample, and LqN is liquid nitrogen container.

3. RESULTS OF MEASUREMENTS

3.1. Antimony

Natural antimony consists of two stable isotopes with mass numbers 121 and 123 and abundances of 57.21 and 42.79%, respectively. Their ground-state spins are $5/2^+$ for isotope 121, and $7/2^+$ for isotope 123. Thus, the s-wave resonances of the first isotope have spins 2^+ and 3^+, and those of the second one have spins 3^+ and 4^+. The resonance energies for both isotopes and spins of a number of low-energy resonances are given in [16]. The low-energy (<511 keV) gamma-ray spectra for some resonances were measured previously by Bhat *et al.* [7], and the spins of six resonances of ^{121}Sb were determined by the method outlined above.

The time-of-flight spectrum obtained from our experiment is shown in Fig. 2. The resonances of the lowest energies, i.e., 6.24 and 15.5 eV, belong to the $A = 121$ isotope and have spins of $J^{\uparrow} = 3^+$ and $J^{\downarrow} = 2^+$, respectively. The lowest and most prominent resonances belonging to the $A = 123$ isotope are at the energies of 21.4 and 105.0 eV and have spins of $J^{\uparrow} = 4^+$ and $J^{\downarrow} = 3^+$.

The gamma-ray spectra from the resonances at 6.24 and 15.5 eV are presented in Fig. 3. It is easy to notice that the intensity ratios of the neighboring peaks corresponding to the transition energies of 114.9 and 121.5 keV are evidently different in the spectra from the resonances of different spins.

The statistics of the counts in the spectra obtained from the resonances belonging to isotope 123 at the energies of 50.3 and 105 eV and spins 3^+ are poor. Nevertheless, the visible difference between the spectrum from the resonance with spin 4^+ at the energy of 21.4 eV and those spectra seems to show the occurrence of the spin-memory effect in the odd–odd compound nucleus of antimony-124.

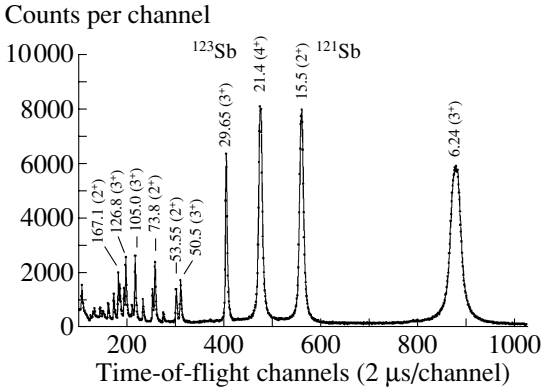

Fig. 2. Time-of-flight spectrum for the natural antimony sample. The resonances are labeled with their energies in eV and with their spins.

3.2. Terbium

Natural terbium is a monoisotope of mass number 159 and ground-state spin $3/2^+$; thus, its neutron capture s-wave resonances can take spin values 1^+ or 2^+.

The time-of-flight spectrum obtained from a 21-h measurement is shown in Fig. 4. In general, the resonances with spin 1^+ are visibly weaker than those with spin 2^+. For this reason, only three of them could be taken into account in the analysis.

The gamma-ray spectra from the neutron capture in the resonance energies are exceptionally dense line spectra in which many peaks overlap and are therefore difficult to analyze.

3.3. Holmium

Natural holmium is a monoisotope of mass number 165. The ground-state spin of its nuclei is $7/2^-$, and thus the spin of compound-nucleus states formed after resonance neutron capture can be 4^- or 3^-.

The data for the analysis were obtained from a 20-h measurement. In this case, it was possible to gain gamma-ray spectra from ten reasonably separate resonances, half of which had the former spin value and the other half the latter. Figure 5 presents a composite gamma-ray spectrum covering many resonances. Some of the spectral peaks are clearly separate and convenient for analysis, though some overlapping is observed too.

3.4. Tantalum

Natural tantalum consists of two isotopes with mass numbers 180 and 181. The abundance of the 180-isotope is insignificant (0.012%) and neglected

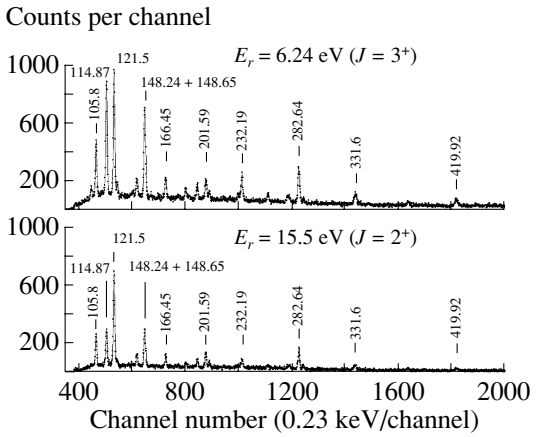

Fig. 3. The pulse-height spectra of the gamma radiation from neutron capture in the two lowest resonances in ^{121}Sb. The spectral peaks are labeled with the corresponding transition energies in keV.

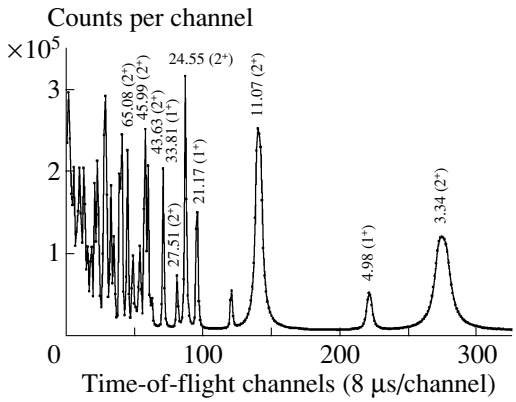

Fig. 4. The time-of-flight spectrum for the ^{159}Tb target (resonance energies in eV).

since its resonances in a measurement with a natural sample are not visible [16].

The spin of the 181-isotope ground state is $7/2^+$, and thus the spins of its s-wave resonances are 4^+ or 3^+. Figure 6 illustrates the time-of-flight spectrum for the radiative neutron capture with the tantalum sample. The highest resonance peak on the curve corresponds to double unresolved resonances with energies of 35.14 and 35.90 eV. They are nearly of the same strength, but their spins are different.

The pulse-height spectra from two of the lowest resonances (4.28 and 10.36 eV) with different spins are shown in Fig. 7. These spectra look very clear with their infrequent and distinctly separate peaks. In fact, however, the spectrum from the radiative neutron capture with the tantalum sample is much more complex with hundreds of peaks corresponding to less intensive radiative transitions in the tantalum-182 compound nucleus as demonstrated by Van den Cruyce *et al.* [17].

4. ANALYSIS OF EXPERIMENTAL DATA

The analysis designed to detect the existence of the spin-memory effect was conducted according to the manner presented by Wetzel and Thomas [6]. That method allows the avoidance of the need for troublesome normalization of the spectral data to the same resonance neutron flux, the energy-dependent efficiency of the gamma-ray detector, and the strength of the resonances (the "Hughes areas"). The idea of the method is to make comparisons of the intensity ratios for various resonances of a chosen pair of radiative transitions starting from the low-energy levels with spins J_a and J_b. In practice, instead of the transition intensities, the areas under the corresponding peaks of the gamma-ray spectra, S_a and S_b, are investigated in order to obtain the ratios $R_{ab} = S_a/S_b$. In the case of the occurrence of the spin-memory effect, the ratios R_{ab} obtained for a number of s-wave resonances are grouped around two separate average values $\langle R^{\uparrow}_{ab}\rangle$ and $\langle R^{\downarrow}_{ab}\rangle$ corresponding to resonances with spins $J^{\uparrow} = J_x + 1/2$ and $J^{\downarrow} = J_x - 1/2$ (if $J_x \neq 0$).

To quantify the strength of the effect, one can accept a quantity that is the quotient of the ratios: $Q_{ab} = \langle R^{\uparrow}_{ab}\rangle/\langle R^{\downarrow}_{ab}\rangle$. The other measure of the effect can be expressed as the percentage of the ratio difference $|\langle R^{\uparrow}_{ab}\rangle - \langle R^{\downarrow}_{ab}\rangle|$ from their average value $(\langle R^{\uparrow}_{ab}\rangle + \langle R^{\downarrow}_{ab}\rangle)/2$, namely,

$$\mathrm{SME} = 200|Q_{ab} - 1|/(Q_{ab} + 1)(\%).$$

The analysis of the data was performed using many possible pairs of transitions in the studied nuclides. The sought effect manifested itself in a clear

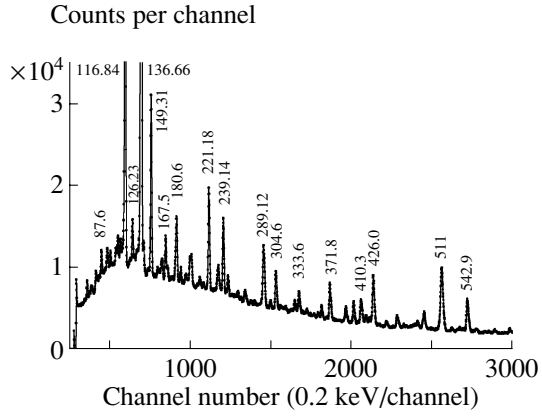

Fig. 5. The pulse-height spectrum of the gamma radiation from neutron capture in many resonances of ^{165}Ho (transition energies in keV).

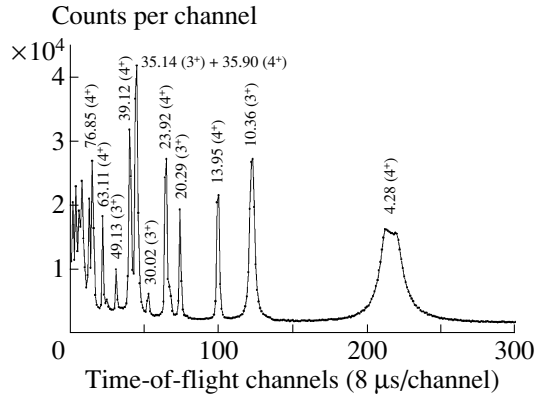

Fig. 6. The time-of-flight spectrum for the natural tantalum sample (resonance energies in eV).

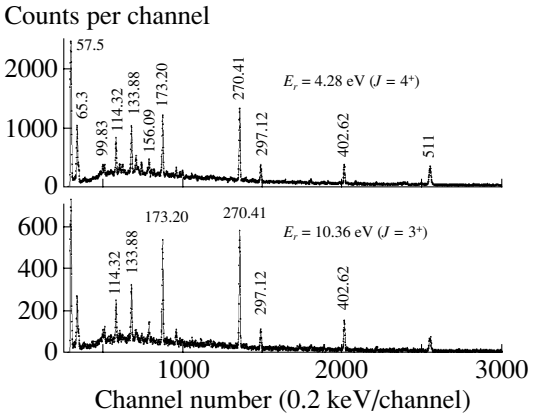

Fig. 7. The pulse-height spectra of the gamma rays from the two lowest resonances of ^{181}Ta with different spins (transition energies in keV).

and convincing manner in a rather small fraction of the analyzed cases. Only the most evident of them are presented below. The statistical features of R_{ab} values among resonances and their grouping around average values are illustrated graphically for those cases which are considered as convincing.

The results of the analysis of ten resonances of the antimony-121 target isotope are illustrated in Fig. 8*a*. Here, the strongest spin-memory effect was found for the pair of radiative transitions with the energies of 114.9 and 121.5 keV which started from the low-energy levels of the compound nucleus with the spins $J_a = 4^-$ and $J_b = 1^+$. The grouping of the R_{ab} ratios into two clearly separate classes corresponding to the resonance spins 2^+ and 3^+ is evident, and their fluctuations around the respective average values for resonance spins are contained in relatively narrow bands. The obtained value of $Q_{ab} = 2.57$. These results confirmed those from [7] and tested successfully our experimental arrangement and the applied method of analysis.

The analysis of the data for terbium was based on 46 combinations of transition pairs from the pulse-height spectra taken from ten resonances. Only three of them have spin 1^+, and the others have spin 2^+. The obtained values of Q_{ab} are between 1 and 1.92, and the highest SME = 63%. An example of a graphical illustration of the ratio grouping is shown in Fig. 8*b*. It corresponds to the transition pairs with the energies of 193.4 and 158.9 keV starting from the compound-nucleus levels with the energies and spins of 257.5 keV ($J_a = 4^-$) and 222.6 keV ($J_b = 0^+$). The spin-memory effect (61%) is unquestionable and rather strong.

In the analysis of the holmium data, the gamma-ray spectra from ten resonances were used, each half for either resonance spin. In nine pair combinations formed from eight transitions, the values of Q_{ab} that were obtained ranged from 1.18 to 1.97 with the corresponding values of SME ranging between 17 and 65%. A graphical illustration of the analysis results for the pair of transitions with the energies of 149.3 and 239.14 keV, which started from the levels of 329.8 keV ($J_a = 5^-$) and 430 keV ($J_b = 2^+$), is shown in Fig. 8*c*. The grouping of R_{ab} and their separation in the presented case are very clear.

For tantalum, the data from seven well-resolved resonances and from the peak composed of two unresolved resonances with different spins and the energies of 35.14 and 35.90 eV were analyzed. Fifteen pair combinations selected from six transitions were taken into account. The values obtained for Q_{ab} did not exceed 1.38, and the maximum SME was 32%. Three graphical illustrations corresponding to the highest values of Q_{ab} are presented in Fig. 9. To show the fluctuations of the individual values of R_{ab} ratios more clearly, the errors are omitted. The dashed lines around the average values of $R_{ab}^{\uparrow}$ and $R_{ab}^{\downarrow}$ (solid lines) denote the standard deviation band for the fluctuating ratios in a group of a given spin value. The position of the point corresponding to the double resonance (≈35 eV) in the middle between two groups (in all three illustrations!) results from different spins of the unresolved resonances and their nearly equivalent "weight" [16]. This verifies the accuracy of the measurement. The results of the analysis show a weak spin-memory effect in tantalum.

5. REMARKS AND CONCLUSIONS

To discuss and summarize the results, let us consider those obtained in other studies on spin-memory effect in low-energy-gamma-ray spectra and compare them for various compound nuclei. In the table, the characteristics of the spin-memory effect in

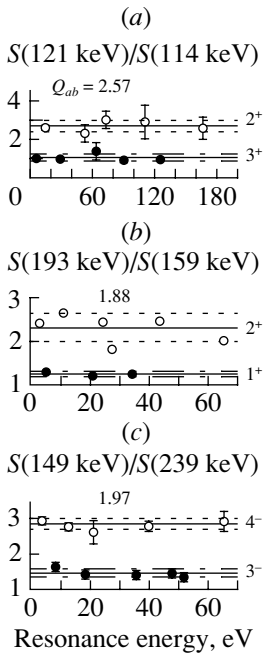

Fig. 8. (*a*) The ratios of the intensities of the 121.5-keV to 114.9-keV gamma rays vs. the resonance energy for the ^{121}Sb target. (*b*) The ratios of the intensities of the transition pair with energies of 193.4 and 158.9 keV vs. the resonance energy for the ^{159}Tb. (*c*) The ratios of the intensities of the transition pair with energies of 149.3 and 239.14 keV vs. the resonance energy for the ^{165}Ho. The solid lines are for the average ratios of the groups corresponding to different resonance spins. The dashed lines determine the standard deviation bands for each spin group of ratios.

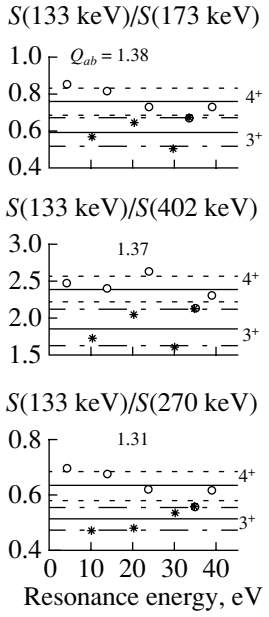

Fig. 9. The illustrations of the intensity ratio groupings for the resonances of ^{181}Ta. The cases of the highest values of Q_{ab} are shown.

the odd–odd compound nuclei (including our results) and in the even–even ones are gathered. Their comparison seems to suggest that, in general, the spin-memory effect in the odd–odd compound nuclei with "the high density of low-lying states with a wide variety of spins" is practically the same as in the even–even compound nuclei situated in their proximity. An increase in the effect in the close neighborhood of the magic number $Z = 50$ is observed (see In, Sb, Pd, and also Ag isotope, whose $Z = 47$, which was investigated by Zanini *et al.* [12]).

In the studies devoted to the even–even compound nuclei [6, 9], the SME values were obtained from the ratios of pair transitions from the lowest levels of the rotational band built on the ground state. Those transitions follow each other, and if not populated from side levels, they could diminish the effect. Therefore, it cannot be excluded that the maximum effect in the even–even compound nuclei can be stronger than those observed in the studies mentioned above. Some blurring of the effect can result from the manner of calculation of the areas needed for the evaluation of the R_{ab} ratios. The areas under the resonance peaks obtained from the time-of-flight spectra taken in energy windows corresponding to the transitions selected for the analysis also contain a certain contribution of some additional pulses from the recoil electrons generated in the Compton effect caused by high-energy capture photons. For this reason, the results for Nd isotopes would probably be higher than those given in [9].

Our results confirm the previously observed occurrence of the spin-memory effect in the odd–odd compound nuclei. The analysis done in this work shows that the observed strength of the effect depends on the selected pair of transitions starting from certain low-energy levels that differ much in their spins, J_a and J_b.

The presented effect could be considered as a good basis for spin assignment to neutron resonances as was shown in [6–12]. The measurement of the low-energy-capture-gamma-ray spectra for resonances using a modern germanium detector that cooperates with a time-of-flight neutron spectrometer is a relatively easy task. This method seems to be more sensitive than one based on the "ratio of single-to-coincidence counts" [18]. For example, the values of SME in the "coincidence method" expressed in percentage are below 30% for ^{106}Pd and below 15% for ^{178}Hf compound nuclei [18], while in the "ratio-of-intensities method" they are about 70 and 58%, respectively (see table). For the ^{96}Mo compound nucleus, they turned out to be the same and equal to

Characteristics of the spin-memory effect in compound nuclei from the resonance neutron capture

Compound nucleus			J_a, J_b	Q_{ab}	SME, %	Source of information
element	A	Z				
Odd–odd compound nuclei						
Sb	122	51	$4^-, 1^+$	2.57 ± 0.33	88	
Tb	160	65	$4^-, 1^+$	1.92 ± 0.28	63	
			$4^-, 0^+$	1.88 ± 0.27	61	
			$4^-, 1^-$	1.69 ± 0.24	51	
			$3^+, 0^+$	1.50 ± 0.14	40	
Ho	166	67	$5^-, 2^+$	1.97 ± 0.19	65	Our study
			$6^+, 2^+$	1.67 ± 0.13	50	
			$5^-, 3^-$	1.63 ± 0.22	48	
Ta	182	73	$4^+, 1^-$	1.38 ± 0.21	32	
			$4^+, 2^+$	1.37 ± 0.19	31	
			$4^+, 2^-$	1.31 ± 0.13	27	
In	116	49	5, 2	2.10	71	[10]
Sb	122	51	$4^-, 1^+$	~2.5	~86	[7]
Tm	170	69	3, 0	2.11 ± 0.36	71.4	[8]
Lu	176	71	5, 1	1.89 ± 0.04	61.6	[11]
Even–even compound nuclei						
Mo	96	42	4, 2	1.28 ± 0.08	24.6	[6]
Pd	106	46	4, 2	2.06 ± 0.09	69.3	[6]
Ba	136	56	4, 2	1.52 ± 0.24	41.3	[6]
Nd	144	60	4, 2	1.46 ± 0.04	37.4	[9]
Nd	146	60	4, 2	1.38 ± 0.04	31.9	[9]
Er	168	68	6, 4	1.75 ± 0.06	54.5	[6]
Hf	178	72	6, 4	1.82 ± 0.09	58.1	[6]
W	184	74	4, 2	2.06 ± 0.43	69.3	[6]
Os	188	76	4, 2	1.93 ± 0.60	63.5	[6]
Os	190	76	4, 2	1.73 ± 0.04	53.5	[6]

25%. In [19], the SME values obtained for the even–even compound nuclei of ^{162}Dy and ^{164}Dy on the basis of the former method do not exceed 13%, while, for the neighboring even–even compound nuclei investigated by the "ratio-of-intensities method," they are greater than 30% (table). However, it is necessary to note that the "coincidence method" uses the whole gamma-ray spectrum, which means an increase in the statistical precision of measurements.

The information obtained in the present work on the new nuclides that reveal the spin-memory effect can be useful not only for the spin-assignment method but also for the testing of the cascade transition process theory or models. The kinds of investigations that were employed can provide valuable data on relative populations of individual low-lying nuclear levels from deexcitation of neutron-capture resonance states.

REFERENCES

1. R. E. Wood, Phys. Rev. **95**, 453 (1954).
2. H. H. Landon and V. L. Sailor, Phys. Rev. **98**, 1267 (1955).
3. J. E. Draper, C. Fenstermacher, and H. L. Schultz, Phys. Rev. **111**, 906 (1958).
4. F. Domanic and V. L. Sailor, Phys. Rev. **119**, 208 (1960).
5. J. R. Huizenga and R. Vandenbosch, Phys. Rev. **120**, 1305 (1960).
6. K. J. Wetzel and G. E. Thomas, Phys. Rev. C **1**, 1501 (1970).
7. M. R. Bhat, R. E. Chrien, D. I. Garber, and O. A. Wasson, Phys. Rev. C **2**, 1115 (1970).

8. M. R. Bhat, R. E. Chrien, D. I. Garber, and O. A. Wasson, Phys. Rev. C **2**, 2030 (1970).
9. A. Stolovy, A. I. Namenson, J. C. Ritter, *et al.*, Phys. Rev. C **5**, 2030 (1972).
10. F. Corvi and M. Stefanon, Nucl. Phys. A **233**, 185 (1974).
11. L. Aldea, F. Bečvař, Huynh Thuong Hiep, *et al.*, Czech. J. Phys. B **28**, 17 (1978).
12. L. Zanini, F. Corvi, K. Athanassopulos, *et al.*, in *Proceedings of the 9th International Symposium on Capture Gamma-Ray Spectroscopy and Related Topics, Budapest, 1996,* Ed. by G. L. Molnár, T. Belgya, and Zs. Révay (Springer Hunharica Ltd., 1997), Vol. 1, p. 379.
13. W. P. Pönitz, Z. Phys. **197**, 262 (1966).
14. D. Sperber, Nucl. Phys. A **90**, 665 (1967); D. Sperber and J. W. Mandler, Nucl. Phys. A **113**, 689 (1968).
15. R. W. Hoff, in *Proceedings of the 8th International Symposium on Capture Gamma-Ray Spectroscopy, Fribourg, 1993,* Ed. by J. Kern (World Sci., Singapore, 1994), p. 132.
16. S. F. Mughabghab, M. Divadeenam, and N. E. Holden, *Neutron Cross Sections* (Academic, New York, 1981), Vol. 1, Part A; S. F. Mughabghab, *Neutron Cross Sections* (Academic, Orlando, 1984), Vol. 1, Part B; V. McLane, Ch. L. Dunford, and P. F. Rose, *Neutron Cross Section Curves* (Academic, New York, 1988), Vol. 2.
17. J. M. Van den Cruyce, G. Vandenput, L. Jacobs, *et al.*, Phys. Rev. C **20**, 504 (1979).
18. C. Coceva, F. Corvi, P. Giacobbe, and C. Carraro, Nucl. Phys. A **117**, 586 (1968).
19. E. N. Karzhavina, Kim Sek Su, A. B. Popov, and Kh. Faykov, Yad. Fiz. **22**, 3 (1975) [Sov. J. Nucl. Phys. **22**, 1 (1975)].

Physics of Atomic Nuclei, Vol. 65, No. 11, 2002, pp. 2052–2063. Translated from Yadernaya Fizika, Vol. 65, No. 11, 2002, pp. 2113–2124.

NUCLEI

Nuclear Relaxation via Paramagnetic Impurities

F. S. Dzheparov*, J.-F. Jacquinot[1)], and S. V. Stepanov*****

Institute of Theoretical and Experimental Physics,
Bol'shaya Cheremushkinskaya ul. 25, Moscow, 117259 Russia

Received March 6, 2002

Abstract—In the first part of this study, the kinetics of nuclear relaxation via paramagnetic impurities for systems of arbitrary space dimension d (including fractal ones) is calculated under the assumptions that are commonly adopted at present for three-dimensional objects. In the second part, a new mean-field-type theory is formulated that reproduces all the results of the first part for integral values of d and which is intended for describing the process at longer times, when the kinetics calculated in the first part is not correct and when a crossover to Balagurov–Vaks asymptotic behavior begins to develop. Solutions to the equations of the new theory are constructed at integral values of d. In order to obtain these solutions, a method is developed for calculating the low-energy and long-wave asymptotic behavior of the off-shell T matrix for potential scattering in the case of singular repulsive potentials. © *2002 MAIK "Nauka/Interperiodica".*

1. INTRODUCTION

Nuclear relaxation via paramagnetic impurities is the main relaxation process for nuclei of spin $I = 1/2$ in dielectric substances [1–5]. This process has been studied for a rather long time, especially in connection with the dynamical polarization of nuclei (see, for example, [4, 5]). Nevertheless, a number of interesting questions have not yet received adequate study. For example, the fact that long-time asymptotic behavior must be nonexponential in three-dimensional media [6] is not reflected in the theoretical literature on spin dynamics; moreover, no analysis has so far been performed for two- and one-dimensional systems, whereas experiments are already aimed at studying objects of fractal dimensions [7].

In this study, the theory developed in [1–5] to describe nuclear relaxation via paramagnetic impurities is generalized along two lines. In Section 2, a theory is formulated for an arbitrary spatial dimensionality d. In this form, it is applicable both to systems of integral dimension d and to fractal media. In Section 3, we propose a new theory of the mean-field-theory type. It is intended for describing the process in question for times at which the evolution of the nuclear polarization $p(t)$ begins to exhibit deviations from the initial stage (which is described by the theory given in Section 2) toward the Balagurov–Vaks asymptotic expression [6] $\ln p(t \to \infty) \propto t^{d/(d+2)}$. We note that, according to the existing theory [1–5], this evolution is given by $\ln p(t \to \infty) \propto t$ in three-dimensional media. The theory presented in Section 3 also provides new physical arguments in favor of the most important heuristic element underlying the old theory and its generalization in Section 2—the rearrangement of the expansion of $p(t)$ (in a series in powers of the paramagnetic-impurity density) into a cumulant form. We begin solving the equations of mean-field theory in Section 4 and, in Section 5, obtain explicit expressions for $p(t)$ in media of integral dimension $d \leq 3$. A T matrix is one of the key elements of the new theory. From the mathematical point of view, it is equivalent to the off-shell T matrix for the quantum-mechanical problem of scattering on a singular repulsive potential. Some auxiliary calculations associated with constructing low-energy and long-time asymptotic expressions for this matrix are given in the Appendices.

2. ANALYSIS IN THE LEADING ORDER OF THE CONCENTRATION EXPANSION

The process being discussed is usually described by the kinetic equation

$$\frac{\partial \tilde{p}(\mathbf{x},t)}{\partial t} = -\sum_z w_{zx}(\tilde{p}(\mathbf{x},t) - \tilde{p}(\mathbf{z},t)) \qquad (1)$$
$$-\sum_z n_z v_{zx}\tilde{p}(\mathbf{x},t), \quad \tilde{p}(\mathbf{x},0) = p_0,$$

where $\tilde{p}(\mathbf{x},t)$ is the polarization (more precisely, the projection of the nuclear spin onto the direction of a

[1)]SPEC CEA, Saclay, France.
*e-mail: dzheparov@itep.ru
**e-mail: jfjacq@drecam.saclay.cea.fr
***e-mail: sergey.stepanov@itep.ru

constant external magnetic field) of a nucleus occurring at a crystal site $\mathbf{x}$ and, if the angular dependence of dipole–dipole interaction is disregarded,

$$w_{xz} = \frac{w_0 r_0^6}{|\mathbf{x}-\mathbf{z}|^6}, \quad v_{zx} = \frac{v_0 r_0^6}{|\mathbf{x}-\mathbf{z}|^6} = \frac{C}{|\mathbf{x}-\mathbf{z}|^6}. \quad (2)$$

For vector indices, we hereafter use a Roman type instead of boldface in order to simplify the notation. The following conventions have been introduced in Eqs. (1) and (2): w_{xz} is the rate of flip-flop transitions for nuclear spins, r_0 is the spacing between nearest nuclei, v_{zx} is the rate of nuclear-spin relaxation at the site $\mathbf{x}$ under the effect of an electron paramagnetic impurity center (acceptor) situated at the site $\mathbf{z}$, and n_z is the corresponding occupation number ($n_z = 1$ if the site $\mathbf{z}$ is occupied by an acceptor; otherwise, $n_z = 0$); we also assume that $v_0 \gg w_0$. The distribution of acceptors is taken to be random and uncorrelated, in which case the mean value of the occupation number is $\langle n_z \rangle_c = c$, where c is the concentration of impurities, the occupations of different sites being independent [for example, $\langle n_x n_z \rangle_c = \delta_{xz} c + (1 - \delta_{xz}) c^2$]. Further, we will predominantly consider the continuous-medium limit, where all observables are expressed in terms of the impurity density $n = c/\Omega_c$, Ω_c being the volume of the unit cell of a crystal. In this limit, $c \to 0$, but variations of observables with time are finite.

In the standard formulation of the problem [1–5], the occupation numbers were not introduced; instead, an equivalent averaging over acceptor coordinates $\{\mathbf{R}\}$ was performed (by definition, $n_x = 1$ if $\mathbf{x} \in \{\mathbf{R}\}$, and $n_x = 0$ if $\mathbf{x} \notin \{\mathbf{R}\}$).

In the continual approximation, Eq. (1) reduces to

$$\frac{\partial \tilde{p}(\mathbf{x},t)}{\partial t} = D_0 \Delta \tilde{p}(\mathbf{x},t) - \sum_z n_z v_{zx} \tilde{p}(\mathbf{x},t) \quad (3)$$
$$= -\tilde{A}\tilde{p}(\mathbf{x},t), \quad D_0 = \frac{1}{2d}\sum_x x^2 w_{x0},$$

where d is the dimensionality of a medium; D_0 is the spin-diffusion coefficient; and the right-hand side of relation (3) defines the Hermitian operator $\tilde{A}$,

$$\tilde{A} = A_0 + \sum_z n_z V^z, \quad A_0 = -D_0 \Delta, \quad (4)$$
$$V^z_{xr} = \delta(\mathbf{x}-\mathbf{r}) v_{zr},$$

which is used below. In the following, we will consider only Eq. (3), since the conditions of its applicability are generally well satisfied, and set $p_0 = 1$.

For an observable, we will consider the total magnetization, which is proportional to the sample-averaged nuclear polarization. We have

$$p(t) = \frac{1}{\Omega}\int d^d x\, \tilde{p}(\mathbf{x},t) = \langle \bar{0}|G(t)|\bar{0}\rangle = \langle \bar{0}|\langle G(t)\rangle_c|\bar{0}\rangle, \quad (5)$$

where we have introduced the propagator $G_{xy}(t)$ satisfying Eq. (3) and the initial condition $G_{xy}(t=0) = \delta(\mathbf{x}-\mathbf{y})$ and where $|\bar{0}\rangle$ is a normalized vector whose components are $\langle \mathbf{x}|\bar{0}\rangle = 1/\sqrt{\Omega}$ (Ω is the crystal volume) and the symbol $\langle\cdots\rangle_c$ denotes, as before, averaging over the ensemble of impurities distributed at random.

For the problem specified by Eq. (3), the absence of a flux at the boundary Γ of the sample being considered, $D_0 \nabla \tilde{p}(\mathbf{x},t)|_\Gamma = 0$, is a natural boundary condition. In fact, however, an explicit form of boundary condition is immaterial for a macroscopic sample of characteristic dimension $R_s \gg \sqrt{D_0 t}$, where t is the observation time—it must only ensure that the operator $\tilde{A}$ is Hermitian. Below, this question is considered in greater detail.

Let us expand $p(t)$ in a series in the impurity concentration [8, 9]. To the first-order terms inclusive, we obtain

$$p(t) = \langle \bar{0}|G(t)|\bar{0}\rangle = \langle \bar{0}|G_0(t)|\bar{0}\rangle \quad (6)$$
$$+ n\int d^d r \langle \bar{0}|[G^{(1)}(t,\mathbf{r}) - G_0(t)]|\bar{0}\rangle + O(n^2)$$
$$= \exp(-M_0(t)(1+O(n^2))),$$

$$M_0(t) = n\int d^d r \langle \bar{0}|[G_0(t) - G^{(1)}(\mathbf{r},t)]|\bar{0}\rangle, \quad (7)$$

where $G_0(t)$ is the propagator in the absence of impurities and $G^{(1)}(t,\mathbf{r})$ is the propagator in the presence of one impurity center at the point $\mathbf{r}$ and where we have considered that $\langle \bar{0}|G_0(t)|\bar{0}\rangle = 1$. By virtue of translation invariance, we further have

$$M_0(t) = \frac{n}{\Omega}\int d^d r d^d x d^d y [G^{(0)}_{xy}(t) - G^{(1)}_{xy}(\mathbf{r},t)] \quad (8)$$
$$= n\int d^d x d^d y [G^{(0)}_{xy}(t) - G^{(1)}_{xy}(0,t)]$$
$$= n\Omega \langle \bar{0}|[G_0(t) - G^{(1)}(0,t)]|\bar{0}\rangle,$$

where $G^{(0)}_{xy} = (G_0)_{xy}$.

It is convenient to introduce the Laplace representation through the relation

$$f(\lambda) = \int_0^\infty dt\, e^{-\lambda t} f(t). \quad (9)$$

We now have $G_0(\lambda) = (\lambda + A_0)^{-1}$, $A_0 = -D_0\Delta$, and

$$M_0(\lambda) = n\Omega\left\langle\bar{0}\left|\left(\frac{1}{\lambda + A_0} - \frac{1}{\lambda + A_0 + V^0}\right)\right|\bar{0}\right\rangle \tag{10}$$

$$= n\Omega\langle\bar{0}|G_0(\lambda)T(\lambda)G_0(\lambda)|\bar{0}\rangle = \frac{n\Omega}{\lambda^2}\langle\bar{0}|T(\lambda)|\bar{0}\rangle,$$

where

$$T(\lambda) = V^0\frac{1}{1 + G_0(\lambda)V^0}, \quad (V^0)_{xy} = \delta(\mathbf{x} - \mathbf{y})v_{x0}.$$

Here, we have considered that $A_0|\bar{0}\rangle = 0$. From the representation in (10) and from the short-range character of the potential v_{x0}, it follows that $T(\lambda)$ is independent of the boundary conditions in the limit $\Omega \to \infty$. For actual calculations, it is convenient to represent $M_0(\lambda)$ in the form

$$M_0(\lambda) = \frac{n\Omega}{\lambda^2}\left\langle\bar{0}\left|V^0\frac{1}{\lambda + A_0 + V^0}(\lambda + A_0)\right|\bar{0}\right\rangle$$

$$= \frac{n\Omega}{\lambda}\left\langle\bar{0}\left|V^0\frac{1}{\lambda + A_0 + V^0}\right|\bar{0}\right\rangle = \frac{n\Omega}{\lambda}$$

$$\times\left\langle\bar{0}\left|V^0\frac{1}{(A_0 + V^0)(\lambda + A_0 + V^0)}(A_0 + V^0)\right|\bar{0}\right\rangle$$

$$= \frac{n\Omega}{\lambda}\left\langle\bar{0}\left|V^0\frac{1}{(A_0 + V^0)(\lambda + A_0 + V^0)}V^0\right|\bar{0}\right\rangle$$

$$= \frac{n\Omega}{\lambda}\sum_n\frac{|\langle n|V^0|\bar{0}\rangle|^2}{(\lambda + E_n)E_n}, \tag{11}$$

where $(A_0 + V^0)|n\rangle = E_n|n\rangle$. The results that are equivalent to those in formulas (6) and (11) are given in the monograph of Aleksandrov [3]. Our derivation followed the simpler and more rigorous approach developed in [10, 11].

In order to perform calculations according to formula (11), it is necessary to diagonalize the operator $A_0 + V^0$. It is obvious that $M_0(\lambda \to 0)$ and $M_0(t \to \infty)$ are determined by small values of E_n. Following [3], we can apply, in this region, the computational procedure developed in the theory of slow-particle scattering (scattering-length theory [12]). In the region of large λ and small t, it is convenient to use the method that is based on an expansion in powers of the diffusion coefficient and which was developed in [10, 11]. A satisfactory precision can be achieved with the aid of the representation

$$M_0(t) = M_\mathrm{F}(t) + M_1(t), \tag{12}$$

$$M_\mathrm{F}(t) = n\int d^dx(1 - \exp(-v_{x0}t)) = (\beta_\mathrm{F}t)^{d/s},$$

$$\beta_\mathrm{F} = C\left(n\frac{\sigma_d}{d}\Gamma\left(1 - \frac{d}{s}\right)\right)^{s/d},$$

where σ_d is the area of a unit d-dimensional sphere. In order to clarify some parametric dependences, we further assume that the potential has the form $v_{r0} = C/r^s$. Obviously, the dipole–dipole interaction (2) corresponds to $s = 6$. The first term on the right-hand side of (12) describes the initial, so-called Forster, part of relaxation, while $M_1(t)$ is the long-time asymptotic expression calculated on the basis of the representation in (11) and formally continued to arbitrary positive values of t [see Eqs. (15)–(17) below].

By virtue of the aforementioned arbitrariness in the choice of boundary condition, we can assume, in calculations by formula (11), that our sample has the shape of a sphere with the center at the origin of coordinates. The vector $|\bar{0}\rangle$ and the potential v_{x0} in Eqs. (10) and (11) are then invariant under rotations. In this section, it is therefore sufficient to take into account only the radial part of the Laplace operator. Accordingly, we set

$$\Delta = \Delta_r = \frac{1}{r^{d-1}}\frac{\partial}{\partial r}r^{d-1}\frac{\partial}{\partial r}. \tag{13}$$

In a spherically isotropic system, the variation of the polarization within the sphere $V(r)$ of radius r and surface $S = \sigma_d r^{d-1}$ due to a flux through the surface satisfies the equation

$$\frac{\partial}{\partial t}\int\limits_{V(r)} d^dxp(\mathbf{x}) = D_0\int\limits_S dS\frac{\partial}{\partial r}p(r) \tag{14}$$

$$= D_0\sigma_d r^{d-1}\frac{\partial}{\partial r}p(r).$$

Differentiating this relation with respect to r, we can see that the representation in (13) is consistent with the standard balance relation (14) at any d; therefore, formulas (11) and (13) determine $p(t)$ both for ordinary and for fractal systems.

If we consider the dimensionality of space as a continuous parameter, it follows from formulas (A.13)–(A.15) in Appendix A that, for $D_0t/b^2 \gg 1$, we have

$$M_1(t, d < 2) = \frac{2^{d-1}(2 - d)\sigma_d}{d\Gamma(2 - d/2)}n(D_0t)^{d/2}, \tag{15}$$

$$M_1(t, d = 2) = \frac{4\pi D_0nt}{\ln(4D_0t/(b^2e^{1+\gamma}))} \tag{16}$$

$$\times[1 + O(1/\ln^2(D_0t/b^2))],$$

$$\gamma = \int\limits_0^\infty dxe^{-x}\ln(1/x) = 0.5772,$$

$$M_1(t, d > 2) = M_1^{(0)}(t) + M_1^{(1)}(t), \tag{17}$$

$$M_1^{(0)}(t) = (d-2)\sigma_d n b^{d-2} D_0 t,$$
$$M_1^{(1)}(t) = \frac{2^{3-d}(d-2)}{(4-d)\Gamma(d/2)} \left(\frac{D_0 t}{b^2}\right)^{(4-d)/2} b^d n \sigma_d.$$

In formulas (16), the dependence on C and s is entirely absorbed in the scattering length

$$b = \left(\frac{C}{D_0}\right)^{1/(s-2)} \left(\frac{\Gamma(1-\frac{d-2}{s-2})}{\Gamma(1+\frac{d-2}{s-2})}\right)^{1/(d-2)} \times (s-2)^{-2/(s-2)}.$$

If $d < 2$, there is no b dependence at all, while, if $d = 2$, it is very weak.

It is formulas (15)–(17) that must be substituted into (12) at $s = 6$ and $d < 3$.

If, however, $s = 6$ and $d = 3$, we find, from (17), that

$$M_1^{(1)}(t, d=3, s=6) = \sqrt{\beta_1 t},$$
$$\beta_1 = 4\pi \left(\Gamma(3/4)/\Gamma(5/4)\right)^4 n^2 C.$$

But there is already a similar term in formula (12), $M_{\mathrm{F}}(t) = \sqrt{\beta_{\mathrm{F}} t}$, the corresponding constant having the close value of $\beta_{\mathrm{F}} = (16/9)\pi^3 n^2 C = 1.313\beta_1$. In this case, we must therefore discard the term $M_1^{(1)}(t)$ in calculations by formulas (12) and (17).

3. BASIC EQUATIONS OF MEAN-FIELD THEORY

Formulas (6) and (12) are inapplicable at rather long times t. In order to demonstrate this, we consider, following [6], the contribution to $p(t \to \infty)$ from large regions containing no acceptors. In these regions, absorption occurs only at the boundary. The corresponding solution to the diffusion equation in a spherical region of radius R is proportional to $\exp(-\kappa D_0 t/R^2)$, where $\kappa \propto 1$. The probability that such a sphere exists is proportional to $\exp(-nV(R))$, where $V(R) = (\sigma_d/d)R^d$. Therefore, we have

$$p(t \to \infty) \propto n \int_0^\infty d^d R \exp(-\kappa D_0 t/R^2 - nV(R)) \propto \exp(-(Bt)^{d/(d+2)}), \quad (18)$$

where B is a constant that is determined by geometry, the density of acceptors, and the diffusion coefficient. Under the integral sign, we have omitted here immaterial terms that involve a power-law dependence on R. A more rigorous derivation of the asymptotic expression (18) is given in [13, 14].

It does not seem that the problem of the crossover between the dependence in (6) and the asymptotic expression (18) has received adequate study. In the numerical calculations presented in [15], there is an indication that the asymptotic expression (18) is realized for $p(t) < 10^{-11}$. In view of this, it is natural to expect that the crossover region is rather wide, so that it would be of interest to construct an adequate theory for it. Approaches of the mean-field-theory type that, for the problems in question, are known as the coherent-potential method (see, for example, [16]) or the effective-medium (coherent-medium) method [9] could form a basis of an appropriate candidate for such a theory. They are constructed in the Laplace representation for the propagator and, in view of the algebraic structure of the equations and the results, are likely to produce formulas that cannot be considered as a natural continuation of relations (6), (7), (12), and (15)–(17) to the region of long times t. We can, however, realize a similar construction directly in the t representation, sidestepping this difficulty.

For this purpose, we represent the propagator $G(t)$ in the form

$$G(t) = \langle \exp(-(A_0 + V)t)\rangle_c = \exp(-B(t)), \quad (19)$$
$$B(t) = A_0 t + M(t),$$

$$V = \sum_z n_z V^z, \quad V^z_{xr} = \delta(\mathbf{x} - \mathbf{r}) v_{xz}. \quad (20)$$

The operator $M(t)$, which is as-yet undefined, can be written in the form $M(t) = \sum_z M^z(t)$ similar to the form of V in (20). It can be said that the operators $M^z(t)$ must adequately describe the effect of acceptors in the so-called effective medium that appears upon averaging over the configurations of acceptors. It is therefore natural to assume that, on average, the propagator $G(t)$ undergoes no changes if one of the sites of the effective medium is replaced by an actual one and if the result is thereupon averaged over the distribution of acceptors; that is,

$$G(t) = \langle \exp(-A_0 t - M(t) + M^z(t) - n_z V^z t)\rangle_c. \quad (21)$$

Relations (19)–(21) form a closed set of nonlinear operator equations.

Corrections to the effective-medium propagator obtained in this way can be determined, at least in principle, on the basis of formal concentration and T-matrix expansions [9], which, being appropriately formulated in the time representation, lead to an alternative derivation of Eq. (21) as the condition requiring that the first term in the formal concentration expansion vanish or as the condition requiring that

the single-particle scattering T matrix in the effective medium vanish on average.

Let us simplify Eq. (21). The identity $f(n_z) = f(0) + n_z(f(1) - f(0))$ is valid for an arbitrary function $f(x)$. Taking this identity into account, we can reduce the right-hand side of Eq. (21) to a linear form in n_z and straightforwardly calculate the expectation value $\langle\cdots\rangle_c$. In this way, we obtain the equation

$$c[e^{-B(t)-V^z t+M^z(t)} - e^{-B(t)+M^z(t)}] = e^{-B(t)} - e^{-B(t)+M^z(t)}. \quad (22)$$

The operator M^z is proportional to c and is therefore small, but the operator $M = \sum_z M^z$ is not small. In view of this, we retain only the leading terms in c on the left- and on the right-hand side of (22). This yields

$$c[e^{-B(t)-V^z t} - e^{-B(t)}] = -\int_0^1 d\xi e^{-\xi B(t)} M^z e^{-(1-\xi)B(t)}. \quad (23)$$

Performing summation over z and taking into account translation invariance, we now find that $M(t)$ satisfies the equation

$$M(t)e^{-B(t)} = c\sum_z [e^{-B(t)} - e^{-B(t)-V^z t}]. \quad (24)$$

4. SIMPLIFICATION OF THE EQUATIONS OF MEAN-FIELD THEORY

Equation (24) still remains very complicated. It is natural to perform further transformations in order to reduce it to a form that admits, upon some generalizations, the application of the technique used above to calculate $M_0(t)$.

We set

$$M(t) = (m_0(t) + m_1(t))t, \quad (m_0(t))_{xz} = \delta_{xz} m_0(t), \quad (25)$$

where, as m_0, we have singled out that part of M which is proportional to an identity operator. Making the Laplace transformation, we can now rewrite (24) in the mixed t–λ representation as

$$(m_0 + m_1)te^{-At} = c\int_{C_M} \frac{d\lambda\, e^{\lambda t}}{2\pi i} \sum_r \left(\frac{1}{\lambda + A} - \frac{1}{\lambda + A + V^r}\right) = c\int_{C_M} \frac{d\lambda\, e^{\lambda t}}{2\pi i} \sum_r \frac{1}{\lambda + A} V^r \frac{1}{\lambda + A + V^r} = c\int_{C_M} \frac{d\lambda\, e^{\lambda t}}{2\pi i} G(\lambda) \sum_r T^r(\lambda) G(\lambda), \quad (26)$$

where the Mellin integration contour C_M goes along the straight line from $\epsilon - i\infty$ to $\epsilon + i\infty$ and where we have introduced the operators $A = A(t) = A_0 + m_1(t)$ and $G = (\lambda + A)^{-1}$ and the single-particle scattering T matrix in the form

$$T^r = V^r \frac{1}{1 + G(\lambda)V^r} = \frac{1}{1 + V^r G(\lambda)} V^r. \quad (27)$$

In these relations and in what follows, we do not indicate, if this is not necessary, the explicit time dependence in operators—for example, in A, G, and T^r—and in the corresponding eigenvalues.

The operators M and A are translation-invariant; calculating the diagonal element of Eq. (26) for the state $|\mathbf{k}\rangle$, where

$$\langle \mathbf{x}|\mathbf{k}\rangle = \frac{1}{\sqrt{\Omega}} \exp(i\mathbf{k}\cdot\mathbf{x}),$$

we therefore obtain

$$(m_0 + m_1(k))te^{-A(k)t} = c\int_{C_M} \frac{d\lambda\, e^{\lambda t}}{2\pi i} G^2(\lambda, k) \sum_r T^r(\lambda, k) = n\int_{C_M} \frac{d\lambda\, e^{\lambda t}}{2\pi i} G^2(\lambda, k) \Omega T^0(\lambda, k), \quad (28)$$

where $T^r(\lambda, k) = \langle \mathbf{k}|T^r|\mathbf{k}\rangle$ and $m_1(k)$, $A(k)$, and $G(\lambda, k) = (\lambda + D_0 k^2 + m_1(k))^{-1}$ are eigenvalues of the operators m_1, A, and G, respectively, these eigenvalues depending only on $k = |\mathbf{k}|$ by virtue of spherical symmetry. In the last relation in (28), we have performed a transition to the continuous-medium limit and have taken into account the property of translation invariance, which entails the relations $T^r_{xz} = T^0_{\mathbf{x}-\mathbf{r},\mathbf{z}-\mathbf{r}}$ and $T^r(\lambda, k) = T^0(\lambda, k)$.

Introducing the function

$$T(\lambda, k) = \Omega T^0(\lambda, k) = \langle \phi_{\mathbf{k}}|T^0|\phi_{\mathbf{k}}\rangle, \quad (29)$$

where

$$\langle \mathbf{x}|\phi_{\mathbf{k}}\rangle = \sqrt{\Omega}\langle \mathbf{x}|\mathbf{k}\rangle = \phi_{\mathbf{k}}(\mathbf{x}) = \exp(i\mathbf{k}\cdot\mathbf{x}), \quad (30)$$

we can represent the basic equation of the mean-field theory in the form

$$(m_0 + m_1(k))te^{-A(k)t} = c\int_{C_M} \frac{d\lambda\, e^{\lambda t}}{2\pi i} G^2(\lambda, k) T(\lambda, k). \quad (31)$$

Equation (31) has much in common with relations (10) and (11) and reduces to them at $m_1 = 0$

and $k = 0$. In order to solve this equation at $m_1 \neq 0$, it is necessary to find a convenient method that would make it possible to calculate the matrix element $T^0(\lambda, k)$ with allowance for $O(k^2)$ terms inclusive if the vector $|\bar{0}\rangle$ in (11) is replaced by the vector $|\mathbf{k}\rangle$. To this accuracy, we have

$$\langle \mathbf{k}|m_1(t)|\mathbf{k}\rangle = m_1(k,t) = D_1(t)k^2, \qquad (32)$$

and the role of m_1 reduces to renormalizing the diffusion coefficient:

$$D_0 \to D(t) = D_0 + D_1(t). \qquad (33)$$

5. SOLVING THE EQUATIONS OF MEAN-FIELD THEORY

Below, we use the asymptotic behavior of $T(\lambda, k)$ for $\lambda \to 0$ and for $k \to 0$. The corresponding asymptotic expressions are given in Appendix B at integral values of d.

Solving the Equations of Mean-Field Theory at $d = 3$

Taking into account relation (A.29) from Appendix B, we can recast Eqs. (31) and (33) into the form

$$(m_0 + m_1(k))te^{-A(k)t} = n \int\limits_{C_M} \frac{d\lambda\, e^{\lambda t}}{2\pi i} \qquad (34)$$

$$\times\, G^2(\lambda, k) \cdot 4\pi Db\left(1 + b\sqrt{\frac{\lambda}{D}} + \frac{\lambda\xi}{2D}b^2 + \xi(kb)^2\right),$$

where $\xi = 2/3$ and where, on the right-hand side, we have retained only two leading terms in $b\sqrt{\lambda/D}$ (this corresponds to taking into account two leading terms of an expansion in $t^{-1/2}$). Expanding both sides of Eq. (34) in series in k^2 and comparing the coefficients of k^0 and k^2, we obtain a set of equations for $m_0(t)$ and $D_1(t)$ in the form

$$m_0(t) = R + 2\sqrt{\frac{\alpha R}{t}}, \qquad (35)$$

$$D_1 = -D\left(\frac{2}{3}\sqrt{\alpha R t} - 2\pi\xi\alpha\right), \qquad (36)$$

where

$$R = 4\pi nDb, \quad \alpha = 4nb^3. \qquad (37)$$

Upon introducing the new unknown variable $x = \sqrt{D_0/D}$, we then arrive at the equation

$$x^3 - (1 - 2\pi\xi\alpha)\, x = \frac{2}{3}\sqrt{\alpha R_0 t}, \quad R_0 = 4\pi nD_0 b. \qquad (38)$$

The root issuing from the value of $x(t = 0) = 1 + O(\alpha)$ is physical. At long times, we have $x^2(R_0 t \to \infty) = D_0/D \to (4\alpha R_0 t/9)^{1/3}$. On the whole, this solution has the form

$$x(t) = 2^{-1/3}\left[(\phi(t) + \chi(t))^{1/3} + (\phi(t) - \chi(t))^{1/3}\right], \qquad (39)$$

$$\phi(t) = \frac{2}{3}\sqrt{\alpha R_0 t},$$

$$\chi(t) = \sqrt{\phi^2(t) - 4\left(\frac{1 - 2\pi\xi\alpha}{3}\right)^3}.$$

The above relation is one of the representations of the Cardano formulas. It is of importance that the point at which $\chi(t) = 0$ is regular for the function $x(\phi)$ since its derivative $x'(\phi)$ is bounded at this point.

Thus, we arrive at the conclusion that, for three-dimensional systems, our mean-field theory predicts new kinetics; that is,

$$p(t) = \exp(-R(t)t) = \exp(-R_0 t/x(t)). \qquad (40)$$

For $\alpha R_0 t \ll 1$, this kinetics coincides with the previous result described in Section 3; with increasing time, it behaves as $\ln(1/p(t \to \infty)) \propto t^{2/3}$, which is much closer to the Balagurov–Vaks asymptotic expression $\ln(1/p_{BV}(t)) \propto t^{3/5}$ than to the previous result of the form $\ln(1/p_{old}(t)) = Rt$.

Solving the Equations of Mean-Field Theory at $d = 1$

In this case, the analysis is perfectly analogous to that in the three-dimensional case. Substituting (A.39) into (31) and (33) and comparing the coefficients of k^0 and k^2, we obtain

$$p(t) = \exp(-m_0(t)t) = \exp\left(-4n\sqrt{\frac{D(t)t}{\pi}}\right), \qquad (41)$$

the effective diffusion coefficient $D(t) = D_0/x^2(t)$ being determined from the equation

$$x^3 - x(1 - 4nb) = \chi(t), \quad \chi(t) = \frac{4n}{3}\sqrt{\frac{D_0 t}{\pi}}. \qquad (42)$$

At short t, the physical solution to the above equation issues from $x = (1 - 4nb)^{1/2}$, while, at long times, we have $x(t \to \infty) = \chi^{1/3}(t) \propto t^{1/6}$. At arbitrary values of t, the solution has the form

$$x(t) = 2^{-1/3}\left[(\chi(t) + \xi(t))^{1/3} + (\chi(t) - \xi(t))^{1/3}\right], \qquad (43)$$

$$\xi(t) = \sqrt{\chi^2(t) - 4\left(\frac{1 - 4nb}{3}\right)^3}.$$

For $t \to \infty$, the kinetics specified by Eqs. (41) parametrically coincides with the Balagurov–Vaks kinetics, the numerical value of the exponent in (41) being $4/(3^{2/3}\pi) = 0.61$ of the exact value.

Solving the Equations of Mean-Field Theory at $d = 2$

Substituting formula (A.32) into Eqs. (31) and (33) and comparing the coefficients of k^0 and k^2, we arrive at the relations

$$m_0(t)t = 4\pi nD \int\limits_{C_M} \frac{d\lambda}{2\pi i} e^{\lambda t}/(\lambda^2 \ln(1/(b_1\sqrt{\lambda/D}))), \tag{44}$$

$$D_1 - Dm_0(t)t = -\frac{2\pi Dn}{t} \times \int\limits_{C_M} \frac{d\lambda}{2\pi i}\frac{e^{\lambda t}}{\lambda^2}\left(\frac{4D}{\lambda \ln(D/b_1^2\lambda)} + \frac{b^2}{2\lambda^2}\right), \tag{45}$$

where $b_1 = be^{\gamma}/2$.

By using expressions (A.37) and (A.38) for the long-time asymptotic behavior of the integrals involved, we find from (44) and (45) that

$$m_0(t)t = \frac{4\pi Dnt}{\ln(4Dt/(b^2e^{1+\gamma}))}[1 + O(1/\ln^2(Dt/b^2))] \tag{46}$$

and that the effective diffusion coefficient $D(t) = D_0/x(t)$ is determined by the equation

$$x = \frac{1}{2}\left[1 - \alpha_2 + \left((1-\alpha_2)^2 + \frac{2R_2t}{\ln(R_2t/(\alpha_2e^{1+\gamma})) - \ln x}\right)^{1/2}\right], \tag{47}$$

$$R_2 = 4\pi D_0 n, \qquad \alpha_2 = \pi n b^2.$$

In the limit $t \to \infty$, these relations lead to kinetics in the form

$$\ln p(t) \to -(4\pi D_0 nt/\ln(D_0 nt))^{1/2}, \tag{48}$$

while the Balagurov–Vaks asymptotic expression reads

$$\ln p_{BV}(t) \to -x_0(4\pi D_0 nt)^{1/2}, \tag{49}$$

where $x_0 = 2.40$ is the first zero of the function $J_0(x)$.

6. CONCLUSION

The results of our study open possibilities for planning new experimental investigations of nuclear relaxation via paramagnetic impurities both in low-dimensional systems on the basis of formulas (12) and (15)–(17) and in three-dimensional systems on the basis of formulas (37)–(40). Natural lines of subsequent theoretical investigations include a microscopic analysis of the applicability range of the new mean-field theory constructed in this study and attempts at refining it, as well as the calculation of corrections for low-dimensional systems due to the fact that actual physical objects are three-dimensional.

ACKNOWLEDGMENTS

We are grateful to Yu.G. Abov and M. Goldman and to the participants of the Moscow Seminar on Magnetic Resonance and of the Seminar of the Institute of Theoretical and Experimental Physics on Low-Energy Physics for stimulating discussions.

This work was supported in part by the Russian Foundation for Basic Research (project nos. 99-02-17440 and 00-15-96656) and by a grant from the Ministry for Foreign Affairs of France.

APPENDIX A

Calculation of the Matrix Element $\langle\bar{0}|T^0|\bar{0}\rangle$ for a Space of Arbitrary Dimensionality

From relations (10) and (11), it follows that

$$\langle\bar{0}|T|\bar{0}\rangle = \lambda\sum_n \frac{|\langle\bar{0}|V^0|n\rangle|^2}{E_n(\lambda + E_n)}. \tag{A.1}$$

Employing the method developed in [3, 12] for the three-dimensional case, we will further construct low-energy eigenstates of the operator $A_0 + V^0$ at an arbitrary dimensionality d. The equations of the eigenvalue problem can be represented in the form

$$(-D_0\Delta_r + v_{r0})\,\psi_n(r) = E_n\psi_n(r), \qquad v_{r0} = C/r^s, \quad \psi_n(r) = \langle r|n\rangle. \tag{A.2}$$

Let us introduce the point ρ specified by the condition $v_{\rho 0} = E_n$. We neglect the right-hand side of Eq. (A.2) in the region $r < \rho$ and the potential C/r^s in the region $r > \rho$. As a result, we arrive at the equation

$$(-D_0\Delta_r + \bar{v}_{r0})\,\psi_n(r) = \vartheta(r \geq \rho)E_n\psi_n(r), \qquad \bar{v}_{r0} = \vartheta(r < \rho)v_{r0}, \tag{A.3}$$

where $\vartheta(\xi)$ is the Heaviside step function.

The solution that is regular at the point $r = 0$ and which is normalized by the condition $\langle n|n\rangle = 1$ can

now be expressed in terms of the Bessel functions $K_\nu(x)$ and $J_\mu(x)$ as

$$\psi_n(r) = \vartheta(r<\rho)\psi_n^<(r) + \vartheta(r\geq\rho)\psi_n^>(r), \quad \text{(A.4)}$$

$$\psi_n^<(r) = \frac{a_n}{N_n} r^{-\mu} K_\nu\left(\frac{2}{s-2}\left(\frac{\beta_0}{r}\right)^{(s-2)/2}\right),$$

$$\nu = \frac{d-2}{s-2}, \qquad \mu = \frac{d-2}{2},$$

$$\psi_n^>(r) = \frac{1}{N_n}(q_n r)^{-\mu}\left(J_\mu(q_n r) + \xi_n J_{-\mu}(q_n r)\right),$$

where $\beta_0 = (C/D_0)^{1/(s-2)}$ and N_n is a normalization factor. The parameters a_n and ξ_n are determined from the condition requiring that the logarithmic derivative $\psi_n'(r)/\psi_n(r)$ be continuous at $r=\rho$. The eigenvalues $E_n = D_0 q_n^2$ are determined from the boundary condition that is imposed here in the form standard for our problem—that is, by requiring that the flux at the external surface of a sphere vanish:

$$\partial\psi_n(r)/\partial r|_{r=R} = 0. \quad \text{(A.5)}$$

It is sufficient to match the solutions at the point ρ [12] by using two leading terms of the asymptotic expansion in small β_0/r (for K_ν) and in small $q_n r$ (for J_μ and $J_{-\mu}$). In the final results, the parameter $C = v_0 r_0^s$ can be eliminated by expressing it in terms of the so-called scattering length b, which is defined as the minimal length at which the function $\psi_n^>(r)$ formally continued to the region of small r vanishes. From (A.4), it follows that b is the only parameter specifying $\psi_n^>(r)$. The theory is self-consistent in the region $q_n b \ll 1$.

Upon implementing this program, we obtain

$$a_n = \frac{2^{1-\mu}\sin\pi\nu}{\pi(s-2)^\nu}\,\frac{\Gamma(1-\nu)}{\Gamma(d/2)}\beta_0^\mu,$$

$$\xi_n = -\left(\frac{q_n b}{2}\right)^{2\mu}\frac{\Gamma(1-\mu)}{\Gamma(1+\mu)},$$

$$b = (s-2)^{-\nu/\mu}(\Gamma(1-\nu)/\Gamma(1+\nu))^{1/(2\mu)}\beta_0, \quad \text{(A.6)}$$

$$\beta_0 = (C/D_0)^{1/(s-2)}.$$

In the case of $d\geq 2$, there are two types of solutions:

(i) one singular solution $\psi_0^>(r)$ in which $q_0 R \ll 1$ and $q_0^2 = 4\mu(1+\mu)b^{2\mu}/R^{2+2\mu}$,

$$\psi_0^>(r) = \frac{1}{2^\mu\Gamma(d/2)N_0} \quad \text{(A.7)}$$

$$\times\left(1-\left(\frac{b}{r}\right)^{2\mu}\left(1-\frac{1}{1-\mu}\left(\frac{q_0 r}{2}\right)^2\right)\right),$$

$$N_0^2 = \frac{\sigma_d R^d}{2^{2\mu} d\Gamma^2(d/2)};$$

(ii) a set of regular solutions $\psi_n^>(r)$ at integral values of $n>0$, with the normalization factor being given by

$$N_n^2 = \frac{\sigma_d R}{\pi q_n^{1+2\mu}}(1+\xi_n^2+2\xi_n\cos\pi\mu), \quad \text{(A.8)}$$

where one can set $q_n = \pi n/R$ without loss of generality. The last relation is valid by virtue of the fact that, as will be seen upon calculating the matrix element $\langle\bar{0}|V^0|n\rangle$, the contribution of any finite number of the first terms in the sum in (11) over regular solutions decreases in proportion to $1/R$ for finite t and $R\to\infty$. It is natural that, in this case, the sum can be replaced by an integral with respect to q_n.

For $d<2$, there exist only regular solutions normalized as in (A.8) and the sum over the states involved can be replaced by an integral.

In order to calculate the matrix element $\langle\bar{0}|V^0|n\rangle$, we recast Eq. (A.3) into the form

$$\bar{v}_{r0}\psi_n(r) = (\vartheta(r\geq\rho)E_n + D_0\Delta_r)\,\psi_n(r). \quad \text{(A.9)}$$

In view of spherical symmetry, we have

$$\langle\bar{0}|V^0|n\rangle = \frac{\sigma_d}{\Omega^{1/2}}\int_0^\infty dr r^{d-1}\bar{v}_{r0}\psi_n(r), \quad \text{(A.10)}$$

while, by virtue of Eq. (A.9), the integral in (A.10) can be represented as

$$\int_0^\infty dr r^{d-1}\bar{v}_{r0}\psi_n(r) = \int_0^\rho dr r^{d-1} v_{r0}\psi_n(r) \quad \text{(A.11)}$$

$$= \int_0^\rho dr r^{d-1} D_0\Delta_r\psi_n(r)$$

$$= D_0\int_0^\rho dr\frac{\partial}{\partial r}r^{d-1}\frac{\partial}{\partial r}\psi_n(r) = D_0\rho^{d-1}\frac{\partial}{\partial\rho}\psi_n^>(\rho).$$

In order to obtain the final result, it is sufficient to substitute the asymptotic expression for $\psi_n^>(\rho)$ in the region $q_n\rho\ll 1$ into the last expression. The result is

$$\langle\bar{0}|V^0|n\rangle = \frac{2\mu D_0\sigma_d b^{2\mu}}{2^\mu\sqrt{\Omega}N_n\Gamma(1+\mu)}. \quad \text{(A.12)}$$

By substituting the expressions obtained for E_n and $\langle\bar{0}|V^0|n\rangle$ into the sum over states on the right-hand side of (11) or (A.1), we find that, in the limit $R\to\infty$, the singular term at $n=0$ makes a finite contribution; the contribution of each regular solution tends to zero—only the total sum over the regular

solutions is finite and can be replaced by an integral. As a result, we arrive at

$$M_1(t) = \vartheta(d>2)(d-2)\sigma_d n D_0 t b^{d-2} + M_2(t), \tag{A.13}$$

$$M_2(t) = 2^{d-2}(d-2)^2\frac{\sigma_d}{\Gamma^2(2-d/2)}b_0^d n\chi(D_0 t/b_0^2, d), \tag{A.14}$$

$$\chi(a,d) = \int_0^\infty \frac{dx}{x^3}\frac{1-\exp(-ax^2)}{x^{d-2}+x^{2-d}-2\cos(\pi(d-2)/2)},$$

$$b_0 = \frac{b}{2}\left(\frac{\Gamma(2-d/2)}{\Gamma(d/2)}\right)^{1/(d-2)},$$

$$b = \left(\frac{C}{D_0}\right)^{1/(s-2)}\left(\frac{\Gamma(1-\dfrac{d-2}{s-2})}{\Gamma(1+\dfrac{d-2}{s-2})}\right)^{1/(d-2)} \times (s-2)^{-2/(s-2)},$$

where b is the scattering length and $s=6$ is the exponent in the dependence of v_{x0} on the distance [see Eq. (2)]. At $d=2$, it follows from (A.13) and (A.14) that

$$M_1(t,d=2) = M_2(t,d=2) = 2\pi b_0^2 n \tag{A.15}$$
$$\times \int_0^\infty \frac{dx}{x^3}\frac{1-\exp(-x^2 D_0 t/b_0^2)}{\ln^2 x + \pi^2/4}.$$

APPENDIX B

Calculation of the Matrix Element $\langle k|T^0|k\rangle$ for $kb \ll 1$

The calculation presented in this section differs substantially from the analysis performed in Appendix A for the following reasons:

(i) The states $\langle \mathbf{x}|\phi_{\mathbf{k}}\rangle = \exp(i\mathbf{k}\cdot\mathbf{x})$ are anisotropic. There is no natural generalization of the Laplace operator to an arbitrary dimensionality d in this case; in the following, we therefore restrict our consideration to integral values of d not greater than three. In order to calculate $T(\lambda,k)$ to k^2 terms inclusive, it is sufficient to take into account the isotropic and the vector component in the expansion of $\exp(i\mathbf{k}\cdot\mathbf{x})$ in terms of representations of the groups of rotations. Taking into account the isotropy of the potential $V^0(r)$ and introducing the operator π_l of projection onto l states that are characterized by a specific parity and the total orbital angular momentum, we accordingly obtain the partial-wave expansion in the form

$$T(\lambda,k) = \langle\phi_{\mathbf{k}}|T^0|\phi_{\mathbf{k}}\rangle = \sum_{l=0}^\infty \langle\phi_{\mathbf{k}}|T_l^0|\phi_{\mathbf{k}}\rangle \tag{A.16}$$
$$= \sum_{l=0}^\infty T_l(\lambda,k) = T_0 + T_1 + o(k^2),$$

where

$$T_l(\lambda,k) = \langle\phi_{\mathbf{k}}|T_l^0|\phi_{\mathbf{k}}\rangle, \quad T_l^0 = \pi_l T^0, \tag{A.17}$$
$$[\pi_l, T^0] = 0.$$

(ii) The operator $A = A_0 + m_1(t)$ is nonlocal since the matrix element $(m_1)_{xy} = (m_1)_{x-y,0}$ is smeared in $|\mathbf{x}-\mathbf{y}|$, with the characteristic size of smearing being b. For standard potentials of the form $v_{r0} \propto 1/r^s$, we are unable, in this case, to calculate the resolvent $(\lambda + A + V^0)^{-1}$ on the basis of the representation

$$T^0 = \frac{1}{1+V^0 G(\lambda)}V^0 = (\lambda+A)\frac{1}{\lambda+A+V^0}V^0. \tag{A.18}$$

It is therefore natural to consider some model potential that simulates an actual potential quite reliably. For this purpose, we replace v_{r0} by a stepwise square-well potential $u(r)$,

$$v_{r0} \to u(r) = u_0\vartheta(r<b), \tag{A.19}$$

assuming that $u_0 \to \infty$ and that the scattering length b was determined by using the true potential v_{r0}. In addition, we set $m_1(t) = -D_1(t)\Delta$.

The method formulated in item (ii) fully reproduces the results obtained in Appendix A for the case of $k=0$ and the results presented in Section 2 for moderately long times (asymptotic behavior in the intermediate region). In deriving the long-time Balagurov–Vaks asymptotic behavior, the explicit form of the potential v_{r0} was not used; therefore, the above substitution (A.19) cannot lead to a significant change in the description of the crossover between the intermediate and the long-time asymptotic behavior. Yet another argument in favor this substitution consists in that it does not lead to qualitative changes in the numerical coefficients of k^2 in the formulas for $T(\lambda,k)$ that are obtained below; in addition, the basic results in Section 5 depend only slightly on these coefficients—they are determined, to a much greater extent, by the structure of the basic Eq. (31) of our mean-field theory.

As previously, we define the function $T(\lambda,k)$ as an analytic continuation from a region near the positive semiaxis of the complex variable λ.

Three-Dimensional Systems

For the sake of definiteness, we will now consider the three-dimensional case. We expand a plane wave in the eigenfunctions $Y_{lm}(\mathbf{r})$ of the angular part of the Laplace operator [12]; that is,

$$e^{i\mathbf{k}\cdot\mathbf{r}} = 4\pi\sum_{l=0}^{\infty}(-i)^l\sum_{m=-l}^{l}Y^*_{lm}(\mathbf{k})Y_{lm}(\mathbf{r})\phi_l(kr), \tag{A.20}$$

$$\phi_l(kr) = \left(\frac{r}{k}\right)^l\left(\frac{1}{r}\frac{d}{dr}\right)^l\frac{\sin kr}{kr},$$

where $Y_{lm}(\mathbf{r})$ is an ordinary spherical harmonic that depends only on the direction of the vector $\mathbf{r}$. With the aid of expansion (A.16) and relations (A.18) and (A.20), we obtain

$$T_l(\lambda,k) = 4\pi(2l+1)\Theta_l(\lambda,k), \tag{A.21}$$

$$\Theta_l(\lambda,k) = \langle\phi_l(k)|T_l|\phi_l(k)\rangle = \langle\phi_l(k)|F_l(\lambda,k)\rangle$$
$$= \int_0^\infty r^2dr\phi_l(kr)F_l(\lambda,k,r),$$

$$T_l = (1+UG_l(\lambda))^{-1}U = (\lambda+A_l)(\lambda+A_l+U)^{-1}U,$$
$$\langle r|\phi_l(k)\rangle = \phi_l(kr),$$

where $F_l(\lambda,k,r) = \langle r|F_l(\lambda,k)\rangle$ and $|F_l(\lambda,k)\rangle = T_l|\phi_l(k)\rangle$. In (A.21), we have introduced the operators

$$A_l = -D(\Delta_r - l(l+1)r^{-2}),$$
$$\langle r|U|r_1\rangle = \delta(r-r_1)r^{-2}u(r)$$

and applied the standard scalar product in the space of functions depending on radial variables:

$$\langle f|g\rangle = \int_0^\infty r^2drf^*(r)g(r). \tag{A.22}$$

Upon introducing the function

$$Q_l(\lambda,k,r) = \langle r|(\lambda+A_l+U)^{-1}U|\phi_l(k)\rangle, \tag{A.23}$$

we arrive at

$$F_l(\lambda,k,r) = (\lambda+A_l)Q_l(\lambda,k,r), \tag{A.24}$$

where $Q_l(\lambda,k,r)$ satisfies the equation

$$(\lambda+A_l+u(r))Q_l(\lambda,k,r) = u(r)\phi_l(kr) \tag{A.25}$$

and the standard conditions requiring that the solution $Q_l(r)$ in question be bounded for all r; vanish for $r\to\infty$; and be continuous, along with its derivative $\partial Q_l(r)/\partial r$, at finite u_0. A standard calculation revealed that, in the limit $u_0\to\infty$, we have

$$Q_l(\lambda,k,r) = \vartheta(r\le b)\phi_l(kr) \tag{A.26}$$
$$+\,\vartheta(r\ge b)\chi_l(\varepsilon r)\phi_l(kb)/\chi_l(\varepsilon b),$$

where $\varepsilon = (\lambda/D)^{1/2}$ and

$$\chi_l(\varepsilon r) = \left(\frac{r}{-\varepsilon}\right)^l\left(\frac{1}{r}\frac{d}{dr}\right)^l\frac{\exp(-\varepsilon r)}{\varepsilon r},$$
$$(\lambda+A_l)\chi_l(\varepsilon r) = 0.$$

Combining formulas (A.21), (A.24), and (A.26), we arrive at the relation

$$\Theta_l(\lambda,k) = (\lambda+Dk^2)\int_0^b r^2dr\phi_l^2(kr) \tag{A.27}$$
$$-\,Db^2\phi_l^2(kb)\frac{\partial}{\partial b}\ln\frac{\chi_l(\varepsilon b)}{\phi_l(kb)}.$$

In perfect analogy, we can prove that an off-diagonal element can be represented as

$$\langle\phi_{\mathbf{p}}|T_l^0|\phi_{\mathbf{k}}\rangle = 4\pi(2l+1)P_l(\mathbf{p}\cdot\mathbf{k}/pk) \tag{A.28}$$
$$\times\left[(\lambda+Dk^2)\int_0^b r^2dr\phi_l(pr)\phi_l(kr)\right.$$
$$\left.-\,Db^2\phi_l(pb)\phi_l(kb)\frac{\partial}{\partial b}\ln\frac{\chi_l(\varepsilon b)}{\phi_l(kb)}\right],$$

where $P_l(\xi)$ is a Legendre polynomial. It can be shown that the representation in (A.28) satisfies the symmetry condition $\langle\phi_{\mathbf{p}}|T_l^0|\phi_{\mathbf{k}}\rangle = \langle\phi_{\mathbf{k}}|T_l^0|\phi_{\mathbf{p}}\rangle$.

By expanding expression (A.27) in a series in the small parameters kb and $\varepsilon b = b\sqrt{\lambda/D}$, we derive the desired asymptotic expansions in the form

$$\Theta_0(\lambda,k) = Db(1+\varepsilon b+\frac{1}{3}\varepsilon^2b^2-\frac{1}{3}k^2b^2+\cdots),$$
$$\Theta_1(\lambda,k) = Dk^2b^3/3+\cdots, \tag{A.29}$$
$$T(\lambda,k) = 4\pi Db\left(1+\varepsilon b+\frac{1}{3}\varepsilon^2b^2+\frac{2}{3}k^2b^2+\cdots\right).$$

Two-Dimensional Systems

The above calculation can easily be generalized to the case of an arbitrary dimensionality. At $d=2$, the expansion of a plane wave can be written as

$$\exp(i\mathbf{k}\cdot\mathbf{r}) = J_0(kr)+2\sum_{n=1}^{\infty}i^n\cos(n\varphi)J_n(kr), \tag{A.30}$$

where φ is the angle between the vectors $\mathbf{k}$ and $\mathbf{r}$ and $J_n(\xi)$ is a Bessel function. Accordingly, we have

$$T(\lambda,k) = \langle\phi_{\mathbf{k}}|T^0|\phi_{\mathbf{k}}\rangle \tag{A.31}$$

$$= 2\pi\left[\Theta_0(\lambda,k) + 2\sum_{n=1}^{\infty}\Theta_n(\lambda,k)\right],$$

$$\Theta_n(\lambda,k) = (\lambda + Dk^2)\int_0^b rdrJ_n^2(kr)$$
$$- DbJ_n^2(kb)\frac{\partial}{\partial b}\ln\frac{K_n(\varepsilon b)}{J_n(kb)},$$

where $K_n(\varepsilon r)$ is a Bessel function of an imaginary argument; this function satisfies the equation $(\lambda + Dk^2)K_n(\varepsilon r) = 0$ and the condition of vanishing at infinity [it decreases in just the same way as $\chi_l(\varepsilon r)$ in (A.26)]. By using these relations and the standard asymptotic formulas for $J_n(\xi \to 0)$ and $K_n(\xi \to 0)$, we obtain

$$T(\lambda,k) = 2\pi D[(\ln 2 - \gamma - \ln(\varepsilon b))^{-1} + k^2b^2/2 \quad \text{(A.32)}$$
$$+ O(k^2b^2/\ln(\varepsilon b)) + O(1/\ln^3(\varepsilon b)) + O(k^3b^3)].$$

An analysis of the equations of our mean-field theory for two-dimensional systems is somewhat more complicated than at $d = 3$ and $d = 1$ because of the presence of logarithms in the integrands. For this reason, we derive below some auxiliary formulas.

We begin by considering the integral

$$Z_1(t) = \int_{C_M}\frac{d\lambda}{2\pi i}\frac{\exp(\lambda t)}{\lambda\ln(1/\lambda)}. \quad \text{(A.33)}$$

In order to analyze its asymptotic behavior for $t \to \infty$, the integration contour can be bent to the left and disposed along the negative semiaxis λ in such a way that it circumvents the cut of the function $\ln\lambda$ along this axis. As the result, we have

$$Z_1(t) = \int_0^{\infty} dx\exp(-xt)/[x(\ln^2 x + \pi^2)] \quad \text{(A.34)}$$
$$= \frac{1}{\pi}\left[\frac{\pi}{2} - \int_0^{\infty} dxe^{-x}\arctan\left(\frac{1}{\pi}(\ln t - \ln x)\right)\right].$$

The last representation was obtained by taking the preceding integral by parts; it is convenient for analyzing $Z_1(t \to \infty)$ by expanding the integrand in a series in powers of $1/\ln t$. This yields

$$Z_1(t) = (\ln t + \gamma)^{-1}(1 + O(1/\ln^2 t)). \quad \text{(A.35)}$$

Let now consider the integral

$$Z_2(t) = \int_{C_M}\frac{d\lambda}{2\pi i}\frac{\exp(\lambda t)}{\lambda^2\ln(1/\lambda)}. \quad \text{(A.36)}$$

It is obvious that, in calculating $Z_2(t = 0)$, the integration contour can be closed on the right, whereupon the result is determined by the only pole of the integrand at $\lambda = 1$. We then have $Z_2(0) = 1$. It follows that

$$\Delta Z_2(t) = Z_2(t) - Z_2(0) \quad \text{(A.37)}$$
$$= \int_{C_M}\frac{d\lambda}{2\pi i}\frac{\exp(\lambda t) - 1}{\lambda^2\ln(1/\lambda)} = \int_0^t d\tau Z_0(\tau)$$
$$= \frac{t}{\ln t + \gamma - 1}(1 + O(1/\ln^2 t)).$$

In a similar way, we can represent $Z_3(t)$ in the form

$$Z_3(t) = \int_{C_M}\frac{d\lambda}{2\pi i}\frac{\exp(\lambda t)}{\lambda^3\ln(1/\lambda)} \quad \text{(A.38)}$$
$$= \int_0^t d\tau Z_2(\tau) + 1$$
$$= \frac{t^2}{2(\ln t + \gamma - 3/2)}(1 + O(1/\ln^2 t)).$$

One-Dimensional Systems

In this case, the decomposition of a plane wave in the components that are even and odd under the inversion of the coordinate axis x,

$$\exp(ikx) = \cos(kx) + i\sin(kx),$$

leads to the general formula

$$T(\lambda,k) = 2\left\{(\lambda + Dk^2)\int_0^b dr(\cos^2(kr) + \sin^2(kr)) - D\left[\cos^2(kb)\frac{\partial}{\partial b}\ln\frac{\exp(-\varepsilon b)}{\cos(kb)}\right.\right. \quad \text{(A.39)}$$
$$\left.\left. + \sin^2(kb)\frac{\partial}{\partial b}\ln\frac{\exp(-\varepsilon b)}{\sin(kb)}\right]\right\} = 2D[\varepsilon + (\varepsilon^2 + k^2)b].$$

REFERENCES

1. A. Abragam, *The Principles of Nuclear Magnetism* (Clarendon, Oxford, 1961; Inostrannaya Literatura, Moscow, 1963).
2. G. Khutsishvili, Usp. Fiz. Nauk **87**, 211 (1965) [Sov. Phys. Usp. **8**, 743 (1965)].
3. I. V. Aleksandrov, *Theory of Magnetic Relaxation* (Nauka, Moscow, 1975).
4. V. A. Atsarkin, *Dynamical Polarization of Nuclei* (Nauka, Moscow, 1980).
5. A. Abragam and M. Goldman, *Nuclear Magnetism: Order and Disorder* (Clarendon, Oxford, 1982; Mir, Moscow, 1984), Vols. 1, 2.
6. V. Ya. Balagurov and V. T. Vaks, Zh. Éksp. Teor. Fiz. **65**, 1939 (1973) [Sov. Phys. JETP **38**, 968 (1973)].
7. T. Tabti, M. Goldman, J.-F. Jacquinot, *et al.*, J. Chem. Phys. **107**, 9239 (1997).
8. F. S. Dzheparov, V. S. Smelov, and V. E. Shestopal, Pis'ma Zh. Éksp. Teor. Fiz. **32**, 51 (1980) [JETP Lett. **32**, 47 (1980)].
9. F. S. Dzheparov, Zh. Éksp. Teor. Fiz. **99**, 982 (1991) [Sov. Phys. JETP **72**, 546 (1991)].
10. Yu. G. Abov, M. I. Bulgakov, S. P. Borovlev, *et al.,* Izv. Akad. Nauk SSSR, Ser. Fiz. **52**, 1699 (1988).
11. Yu. G. Abov, M. I. Bulgakov, S. P. Borovlev, *et al.,* Zh. Éksp. Teor. Fiz. **99**, 962 (1991) [Sov. Phys. JETP **72**, 534 (1991)].
12. L. D. Landau and E. M. Lifshitz, *Course of Theoretical Physics,* Vol. 3: *Quantum Mechanics: Non-Relativistic Theory* (Nauka, Moscow, 1989, 4th ed.; Pergamon, Oxford, 1977, 3rd ed.).
13. L. A. Pastur, Teor. Mat. Fiz. **32**, 88 (1977).
14. M. Donsker and S. Varadhan, Commun. Pure Appl. Math. **28**, 525 (1975).
15. S. Havlin, M. Dishon, J. E. Kiefer, and G. H. Weiss, Phys. Rev. Lett. **53**, 407 (1984).
16. J. M. Ziman, *Models of Disorder: the Theoretical Physics of Homogeneously Disordered Systems* (Cambridge Univ. Press, Cambridge, 1979; Mir, Moscow, 1982).

Translated by A. Isaakyan

Physics of Atomic Nuclei, Vol. 65, No. 11, 2002, pp. 2064–2069. From Yadernaya Fizika, Vol. 65, No. 11, 2002, pp. 2125–2130.

ELEMENTARY PARTICLES AND FIELDS

Study of the $K^- \to e^-\nu\pi^0$ Decay*

I. V. Ajinenko[1], S. A. Akimenko[1], G. A. Akopdzhanov[1], K. S. Belous[1], G. I. Britvich[1], I. G. Britvich[1], A. P. Filin[1], V. N. Govorun[1], A. V. Inyakin[1], V. A. Khmelnikov[1], A. S. Konstantinov[1], V. F. Konstantinov[1], I. Ya. Korolkov[1], V. M. Leontiev[1], V. P. Novikov[1], V. F. Obraztsov[1], V. A. Polyakov[1], V. I. Romanovsky[1], V. M. Ronjin[1], V. A. Senko[1], N. A. Shalanda[1], M. M. Shapkin[1], V. I. Shelikhov[1], N. E. Smirnov[1], A. A. Sokolov[1], O. G. Tchikilev[1], E. V. Vlasov[1], O. P. Yushchenko[1], V. N. Bolotov[2], S. V. Laptev[2], A. Yu. Polyarush[2], V. E. Postoev[2], S. V. Yashchenko[3], B. Zh. Zalikhanov[3], and V. Z. Serdyuk[3]

Received April 11, 2002

Abstract—The decay $K^- \to e^-\nu\pi^0$ has been studied using in-flight decays detected with the ISTRA+ setup working at the 25-GeV negative secondary beam of the U-70 PS. About 130K events were used for the analysis. The λ_+ parameter of the vector form factor has been measured: $\lambda_+ = 0.0293 \pm 0.0015(\text{stat.}) \pm 0.002(\text{syst.})$. The limits on the possible tensor and scalar couplings have been derived: $f_T/f_+(0) = -0.045 \pm 0.060(\text{stat.})$ and $f_S/f_+(0) = -0.019^{+0.025}_{-0.016}(\text{stat.})$. © *2002 MAIK "Nauka/Interperiodica".*

1. INTRODUCTION

The decay $K \to e\nu\pi^0(\mathrm{K}_{e3})$ is known to be a promising one to search for an admixture of scalar (S) or tensor (T) interactions to the Standard Model (SM) $V - A$. This topic has been attracting significant interest in recent years, and, moreover, some previous experiments with charged and neutral kaon beams have reported indications for some anomalous S and T signals [1, 2]. On the other hand, a recent KEK [3, 4] experiment with stopped K^+ beam has reported negative results of the searches.

In our analysis, we present a new search for S and T couplings based on the statistics of about 130K K_{e3} events. Another result of our study is the measurement of the $V - A$ $f_+(t)$ form-factor slope λ_+.

2. EXPERIMENTAL SETUP

The experiment is performed at the IHEP 70-GeV proton synchrotron U-70. The experimental apparatus ISTRA+ is the result of the modification of ISTRA-M [5], which, in turn, evolved from ISTRA, which yielded important results on π^- and K^- decays in the late 1980s [6]. The setup is located in the 4-A negative unseparated secondary beam. The beam momentum in the measurements is ~25 GeV with $\Delta p/p \sim 2\%$. The admixture of K^- in the beam is ~3%. The beam intensity is $\sim 3 \times 10^6$ per 1.9 s U-70 spill. A schematic view of the detector is shown in Fig. 1. The momentum of the beam particle deflected by M_1 is measured by BPC_1–BPC_4 PCs with 1-mm wire step; the kaon identification is done by $\check{C}_0$–$\check{C}_2$ threshold $\check{C}$ counters. The 9-m-long evacuated decay volume is surrounded by eight lead glass rings LG_1–LG_8 used to veto low-energy photons. The same role is played by SP_2 is a 72-cell lead-glass calorimeter. The decay products deflected in M_2 with a 1-T m field integral are measured with 2-mm-step proportional chambers PC_1–PC_3, 1-cm-cell drift chambers DC_1–DC_3, and finally with 2-cm-diameter drift tubes DT_1–DT_4. A wide-aperture threshold Cherenkov counter $\check{C}_3$ is filled with He and used to trigger the electrons. The counter $\check{C}_4$ was not used in the present experiment. SP_1 is a 576-cell lead-glass calorimeter, followed by HC—a scintillator-iron sampling hadron calorimeter, subdivided into seven longitudinal sections 7×7 cells each. MH is an 11×11 cell scintillating hodoscope, used to solve the ambiguity for multitrack events and improve the time resolution of the tracking system, MuH is a 7×7 cell muon hodoscope. The

*This article was submitted by the authors in English.

[1]Institute for High Energy Physics, Protvino, Moscow oblast, 142284 Russia.

[2]Institute for Nuclear Research, Russian Academy of Sciences, pr. Shestidesyatiletiya Oktyabrya 7a, Moscow, 117312 Russia.

[3]Joint Institute for Nuclear Research, Dubna, Moscow oblast, 141980 Russia.

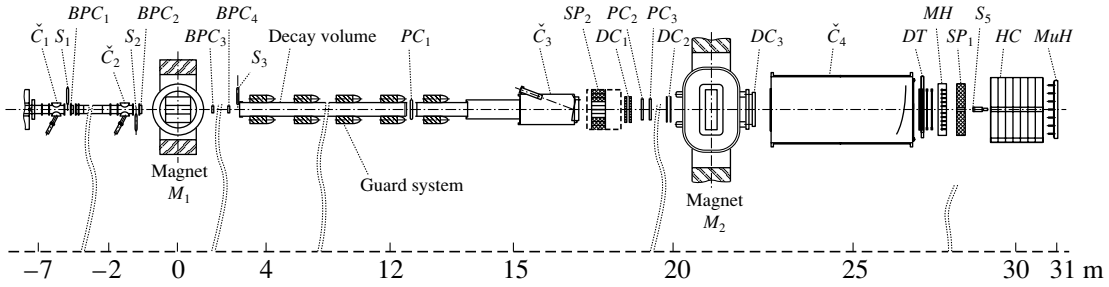

Fig. 1. The layout of the ISTRA+ setup.

trigger is provided by S_1–S_5 scintillation counters, $\check{C}_0$–$\check{C}_2$ Cherenkov counters, and the analog sum of amplitudes from the last dinodes of the SP_1 and is very loose:

$$T = S_1 \cdot S_2 \cdot S_3 \cdot \bar{S}_4 \cdot \check{C}_0 \cdot \bar{\check{C}}_1 \cdot \bar{\check{C}}_2 \cdot \bar{S}_5 \cdot \sum(SP_1).$$

Here, S_4 is a scintillator counter with a hole to suppress beam halo; S_5 is a counter downstream of the setup at the beam focus; $\sum(SP_1)$—a requirement for the analog sum of amplitudes from SP_1 to be larger than ~ 700 MeV—a MIP signal. The last requirement serves to suppress the $K \to \mu\nu$ decay. Some complementary triggers: the electron trigger $T_e = S_1 \cdot S_2 \cdot S_3 \cdot \bar{S}_4 \cdot \bar{S}_5 \cdot \check{C}_3$ and prescaled "decay" trigger $T_d = S_1 \cdot S_2 \cdot S_3 \cdot \bar{S}_4 \cdot \bar{S}_5$ were used to cross-check the efficiency of the main one.

The main difference between ISTRA-M and ISTRA+ is in the electronics and DAQ: all the CAMAC-based electronics was changed by IHEP-developed MICC [7] ECL-based electronics. ISTRA+ has now 12 MICC crates with ADCs, TDCs, and latches. The DAQ, described in some detail in [8], is based on IHEP-developed VME master V-08 [9], which writes the MICC stream into standard VME memory. Between the spills, the information is written to the PC through the BIT-3 VME–PCI interface. The saturated event rate is ~6500 of 1 Kb events per 1.9 s spill.

3. EVENT SELECTION

During physics runs in November–December 1999 and March–April 2001, 206M and 363M events were logged on tapes. This information is supported by about 100M MC events generated with GEANT 3 [10]. MC generation includes a realistic description of the setup including decay volume entrance windows, track chamber windows, gas, sensing wires and cathode structure, Cherenkov counters, mirrors and gas, shower generation in EM calorimeters, etc.

The usual first step of the data processing is the EM calorimeter calibration, using special runs with 10-GeV electrons; track system alignment, HCAL; and guard system calibration with muon-beam runs. The data processing starts with the beam-particle reconstruction in BPC_1–BPC_4; then the secondary tracks are looked for in PC_1–PC_3, DC_1–DC_3, and DT_1–DT_4; and events with one good negative track are selected. The decay vertex is searched for, and a cut is introduced on the matching of incoming and decay track. The next step is to look for showers in

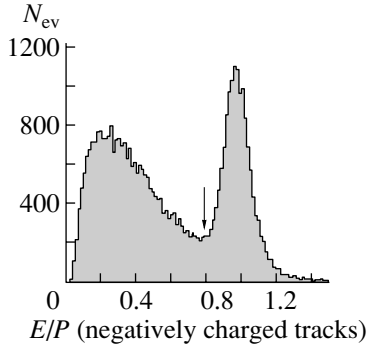

Fig. 2. The E/p plot is the ratio of the energy of the associated cluster in ECAL to the momentum of the charged track. The arrow shows the cut used for the electron separation.

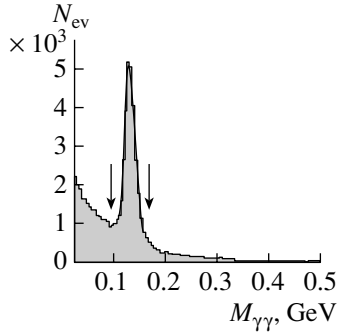

Fig. 3. The $\gamma\gamma$ mass spectrum for the events with the identified electron and two extra showers. Arrows indicate the cut values.

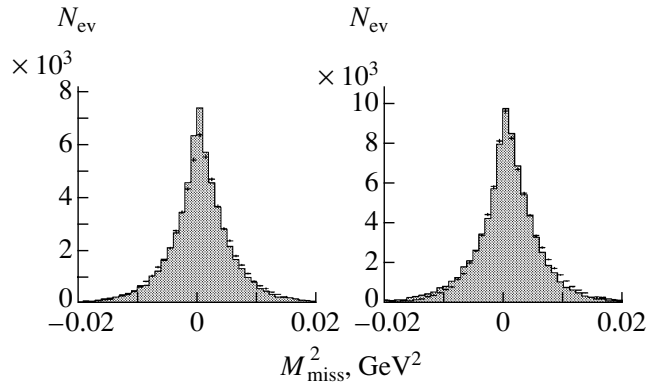

Fig. 4. The missing 4-momentum squared $(P_K - P_e - P_{\pi^0})^2$ for the selected events for 1999 run (left) and 2001 run (right). The points with errors are the data; the histograms are MC.

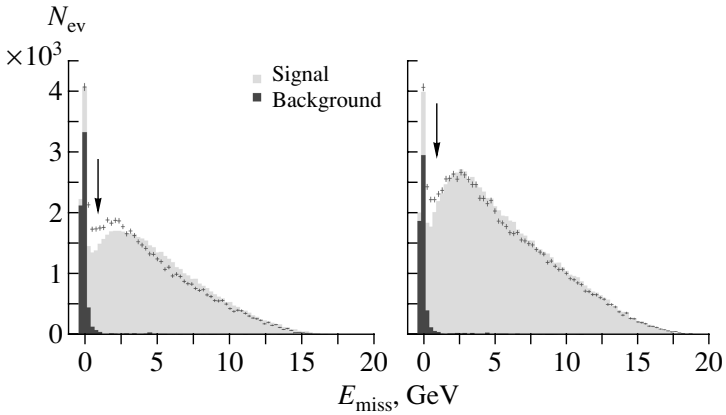

Fig. 5. The missing energy for the $e\pi^0$ events for 1999 run (left) and 2001 run (right). The points with errors are the data; the histograms are MC. The dark (gray) peak at zero value corresponds to the MC-predicted $K \to \pi^-\pi^0$ background. The arrow indicates the cut value.

the SP_1 calorimeter. A method of shower parameter reconstruction based on the MC-generated patterns ($\sim$2000 3×3 patterns) of showers is used. The matching of the charged track and a shower in the SP_1 is done on the basis of the difference between the track extrapolation and the shower coordinates. The electron identification is done using the E/P ratio of the energy of the shower associated with the track and the track momentum (see Fig. 2). The selection of events with the two extra showers results in the $M_{\gamma\gamma}$ spectrum shown in Fig. 3. The π^0 peak has a mass of $M_{\pi^0} = 134.8$ MeV and a resolution of 8.6 MeV. Another important variable for the $K^- \to e^-\nu\pi^0$ selection is the missing mass squared $(P_K - P_e - P_{\pi^0})^2$, where P are the corresponding 4-momenta (see Fig. 4). The cut is ± 0.01 GeV^2.

The further selection is done by the requirement that the event passes the $2C$ $K \to e\nu\pi^0$ fit. At the same time, a similar $2C$ fit $K \to \pi^-\pi^0$ should fail. The missing energy $E_K - E_e - E_{\pi^0}$ after this selection is shown in Fig. 5. The peak at low $E_{\rm miss}$ corresponds to the remaining $K^- \to \pi^-\pi^0$ background. The corresponding cut is $E_{\rm miss} > 1$ GeV. The surviving background is estimated from MC to be less than 3%.

The detailed data-reduction information is shown in Table 1.

4. ANALYSIS

The event selection described in the previous section results in selected 54K events in the 1999 data and 79K events in the 2001 data. The distribution of the events over the Dalitz plot is shown in Fig. 6. The variables $y = 2E_e/M_K$ and $z = 2E_{\pi^0}/M_K$, where E_e, E_{π^0} are the energies of the electron and π^0 in the kaon c.m.s., are used. The background events, as MC shows, occupy the peripheral part of the plot.

The most general Lorentz-invariant form of the matrix element for the decay $K^- \to l^-\nu\pi^0$ is [11]

$$M = \frac{G_F V_{us}}{2}\bar{u}(p_\nu)(1+\gamma^5) \qquad (1)$$

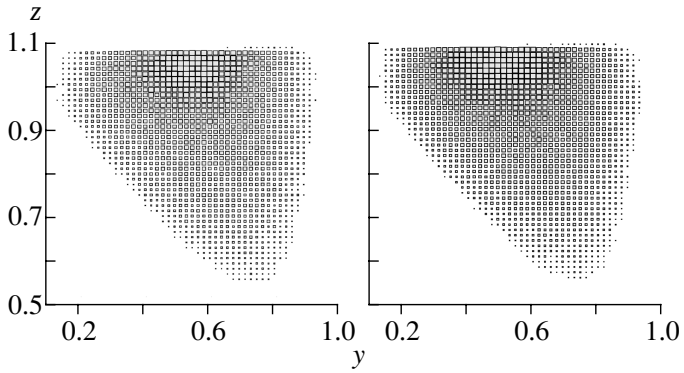

Fig. 6. Dalitz plots ($y = 2E_e/M_K$, $z = 2E_{\pi^0}/M_K$) for the selected $K \to e\nu\pi^0$ events after the $2C$ fit: (left panel) 1999 statistics and (right panel) 2001 statistics.

$$\times \left[2m_K f_S - [(P_K + P_\pi)_\alpha f_+ + (P_K - P_\pi)_\alpha f_-]\gamma^\alpha + i\frac{2f_T}{m_K}\sigma_{\alpha\beta}P_K^\alpha P_\pi^\beta \right] v(p_l).$$

It consists of scalar, vector, and tensor terms; f_S, and f_T, $f_\pm$ are functions of $t = (P_K - P_\pi)^2$. In the SM, the W-boson exchange leads to the pure vector term. The "induced" scalar and/or tensor terms due to EW radiative corrections are negligibly small; i.e., the nonzero scalar/tensor form factors indicate physics beyond the SM.

The term in the vector part, proportional to f_-, is reduced (using the Dirac equation) to a scalar form factor. In the same way, the tensor term is reduced to a mixture of scalar and vector form factors. The redefined V, S and the corresponding Dalitz plot density in the kaon rest frame ($\rho(E_\pi, E_l)$) are [12]

$$\rho(E_\pi, E_l) \sim A|V|^2 + B\mathrm{Re}(V^*S) + C|S|^2; \tag{2}$$

$$V = f_+ + (m_\mu/m_K)f_T,$$

$$S = f_S + (m_\mu/2m_K)f_- + \left(1 + \frac{m_\mu^2}{2m_K^2} - \frac{2E_\mu}{m_K} - \frac{E_\pi}{m_K}\right) f_T,$$

$$A = m_K(2E_\mu E_\nu - m_K\Delta E_\pi) - m_\mu^2\left(E_\nu - \frac{1}{4}\Delta E_\pi\right),$$

$$B = m_\mu m_K(2E_\nu - \Delta E_\pi),$$

$$C = m_K^2\Delta E_\pi, \quad \Delta E_\pi = E_\pi^{\max} - E_\pi, \quad E_\pi^{\max} = \frac{m_K^2 - m_\mu^2 + m_\pi^2}{2m_K}.$$

In case of K_{e3} decay, one can neglect the terms proportional to m_l, m_l^2. Then, assuming linear dependence of f_+ on t, $f_+(t) = f_+(0)(1 + \lambda_+ t/m_\pi^2)$, and real constants f_S, f_T, we get

$$\rho(E_\pi, E_e) \sim m_K(2E_eE_\nu - m_K\Delta E_\pi) \times (1 + \lambda_+ t/m_\pi^2)^2 + m_K^2\Delta E_\pi \times \left(\frac{f_S}{f_+(0)} + \left(1 - \frac{2E_e}{m_K} - \frac{E_\pi}{m_K}\right)\frac{f_T}{f_+(0)}\right)^2. \tag{3}$$

The procedure for the experimental extraction of the parameters λ_+, f_S, and f_T starts from the subtraction of the MC-estimated background from the Dalitz plots of Fig. 6. The background normalization was determined by the ratio of the real and generated $K^- \to \pi^-\pi^0$ events. Then, the Dalitz plots were subdivided into 20×20 cells. The background-subtracted distribution of the numbers of events in the cells (i, j) over Dalitz plots, for example, in the case of simultaneous extraction of λ_+ and $f_S/f_+(0)$, was fitted with the function

$$\rho(i,j) \sim W_1(i,j) + W_2(i,j)\lambda_+ + W_3(i,j)\lambda_+^2 + W_4(i,j)\left(\frac{f_S}{f_+(0)}\right)^2. \tag{4}$$

Here, W_k are MC-generated functions, which are built up as follows: The MC events are generated with constant density over the Dalitz plot and recon-

Table 1. Event-reduction statistics (the main steps are shown for the 1999 and 2001 runs)

Run	1999	2001
$N_{\rm ev}$ on tapes	206 544 909	363 002 105
Beam track reconstructed	$159\,459\,629 = 77\%$	$268\,564\,958 = 74\%$
One secondary track found	$81\,166\,929 = 41\%$	$134\,227\,095 = 37\%$
Written to DST	$70\,015\,610 = 34\%$	$107\,215\,783 = 30\%$
e^- identified	1 300 958	1 998 719
Two showers reconstructed	252 177	361 621
π^0 identified	186 850	251 489
$\lvert M^2_{\rm miss}\rvert < 0.01$ GeV^2	96 652	144 642
$K \to \pi^-\pi^0$ rejected	79 660	117 566
$K \to e\nu\pi^0$ accepted	65 208	97 585
$E_{\rm miss} > 1$ GeV	54 009	79 248

Table 2. Results of the fit

	1999	2001	1999 + 2001
λ_+	$0.0271^{+0.0023}_{-0.0023}$	$0.0310^{+0.0019}_{-0.0019}$	$0.0293^{+0.0015}_{-0.0015}$
λ_+	$0.0270^{+0.0023}_{-0.0023}$	$0.0310^{+0.0019}_{-0.0019}$	$0.0293^{+0.0015}_{-0.0015}$
$f_T/f_+(0)$	$-0.039^{+0.088}_{-0.085}$	$-0.049^{+0.080}_{-0.075}$	$-0.045^{+0.060}_{-0.057}$
λ_+	$0.0268^{+0.0024}_{-0.0027}$	$0.0304^{+0.0022}_{-0.0024}$	$0.0289^{+0.0017}_{-0.0018}$
$f_S/f_+(0)$	$-0.014^{+0.034}_{-0.026}$	$-0.022^{+0.035}_{-0.019}$	$-0.019^{+0.025}_{-0.016}$
χ^2/ndf	1.7	1.3	1.5
$N_{\rm bins}$	225	228	

structed with the same program as for the real events. Each event carries the weight w determined by the corresponding term in (3), calculated using the MC-generated values for y and z. The radiative corrections according to [13] were taken into account. Then, W_k is constructed by summing up the weights of the events in the corresponding Dalitz plot cell. This procedure allows one to avoid the systematic errors due to the "migration" of the events over the Dalitz plot because of the finite experimental resolution.

5. RESULTS

The results of the fit are summarized in Table 2. The combination of the two runs is done by a simultaneous fit. The first line corresponds to the pure $V - A$ SM fit. In the second line, the tensor and, in the third, the scalar terms are added to the fit. All the errors presented are from the MINOS procedure of the MINUIT program [14] and are larger than the Gaussian ones. At present, we estimate an additional systematic error in λ_+ to be ± 0.002. The estimate is done by comparing two runs, which differ a lot in amount of matter in the beam-line and detector configuration and by varying cuts, cell size during the fit of the Dalitz plots, etc.

The comparison of our results with the most recent $K^\pm$ data [1, 3, 4] shows that our statistics, at present, are the highest in the world and the statistical errors are somewhat smaller than in [1, 3] and comparable with [4]. We do not confirm the observation of a significant f_S and f_T in [1]. Our data are in good agreement with [3, 4] and with the theoretical calculations for λ_+ ($\lambda_+ = 0.031$) [15], done in the context of chiral perturbation theory.

6. SUMMARY AND CONCLUSIONS

The K^-_{e3} decay has been studied using in-flight decays of 25-GeV K^- detected by the ISTRA+ mag-

netic spectrometer. Due to the high statistics, adequate resolution of the detector, and good sensitivity over all the Dalitz plot space, the measurement errors are significantly reduced as compared with the previous measurements. The λ_+ parameter of the vector form actor has been measured to be

$$\lambda_+ = 0.0293 \pm 0.0015(\text{stat.}) \pm 0.002(\text{syst.}).$$

The limits on the possible tensor and scalar couplings have been derived:

$$f_T/f_+(0) = -0.045^{+0.060}_{-0.057},$$
$$f_S/f_+(0) = -0.019^{+0.025}_{-0.016}.$$

ACKNOWLEDGMENTS

It is a honor for the ISTRA+ collaboration to present this article for the special issue of *Physics of Atomic Nuclei* on occasion of the 80th anniversary of Yu.G. Abov.

The INR part of the collaboration was supported by the Russian Foundation for Basic Research, project no. 00-02-16074.

REFERENCES

1. S. A. Akimenko *et al.*, Phys. Lett. B **259**, 225 (1991).
2. R. J. Tesarek, hep-ex/9903069.
3. S. Shimizu *et al.*, Phys. Lett. B **495**, 33 (2000).
4. A. S. Levchenko *et al.*, hep-ex/0111048.
5. V. N. Bolotov *et al.*, IHEP 95-111 (Protvino, 1995).
6. V. N. Bolotov *et al.*, Yad. Fiz. **44**, 108, 117 (1986) [Sov. J. Nucl. Phys. **44**, 68, 73 (1986)]; **45**, 1652 (1987) [**45**, 1023 (1987)].
7. Yu. B. Bushnin *et al.*, IHEP 88-47 (Serpukhov, 1988); V. A. Medovikov *et al.*, IHEP 99-60 (Protvino, 1999); A. N. Isaev *et al.*, Prib. Tekh. Eksp., No. 3, 41 (2000); M. M. Vasiliev *et al.*, Prib. Tekh. Eksp., No. 5, 45 (2000).
8. A. P. Filin *et al.*, in *Proceedings of the CHEP 2001 Conference, Bejing, 2001*.
9. V. N. Govorun *et al.*, IHEP Preprint (in preparation).
10. R. Brun *et al.*, CERN-DD/EE/84-1.
11. H. Steiner *et al.*, Phys. Lett. B **36B**, 521 (1971).
12. M. V. Chizhov, hep-ph/9511287.
13. E. S. Ginsberg, Phys. Rev. **162**, 1570 (1967).
14. F. James and M. Roos, CERN D506 (1989).
15. J. Gasser and H. Leutwyler, Nucl. Phys. B **250**, 517 (1985).

Physics of Atomic Nuclei, Vol. 65, No. 11, 2002, pp. 2070–2076. From Yadernaya Fizika, Vol. 65, No. 11, 2002, pp. 2131–2137.

ELEMENTARY PARTICLES AND FIELDS

Search for Exotic Baryons with Hidden Strangeness in Proton Diffractive Production at the Energy of 70 GeV*,**

Yu. M. Antipov[1)], A. V. Artamonov[1)], V. A. Batarin[1)], O. V. Eroshin[1)], S. V. Golovkin[1)], Yu. P. Gorin[1)], V. N. Govorun[1)], A. N. Isaev[1)], A. P. Kozhevnikov[1)], V. P. Kubarovsky[1)], V. F. Kurshetsov[1)], L. G. Landsberg[1)], V. A. Medovikov[1)], V. V. Molchanov[1)], V. A. Mukhin[1)], D. I. Patalakha[1)], S. V. Petrenko[1)], A. I. Petrukhin[1)], V. A. Senko[1)], N. A. Shalanda[1)], A. N. Sytin[1)], V. S. Vaniev[1)], D. V. Vavilov[1)], V. A. Victorov[1)], V. I. Yakimchuk[1)], S. A. Zimin[1)], V. Z. Kolganov[2)], G. S. Lomkatsi[2)], A. F. Nilov[2)], and V. T. Smolyankin[2)]

The SPHINX Collaboration

Received April 11, 2002

Abstract—The first preliminary results from the upgraded SPHINX spectrometer, working in the proton beam with the energy of 70 GeV of the IHEP accelerator, are presented. The data for the reaction $p + N \to [\Sigma^0 K^+] + N$ based on new statistics are in good agreement with our previous data and strongly support the existence of the $X(2000)$ state (with an increase in statistics for this state by a factor of ~ 5). We also observed radiative decay of $\Lambda(1520) \to \Lambda\gamma$. The significant increase in statistics for many diffractive-production reactions will allow us to study them in great detail. © *2002 MAIK "Nauka/Interperiodica".*

1. EXOTIC BARYONS AND THEIR PRODUCTION PROCESSES

Extensive studies of the diffractive baryon production and search for cryptoexotic pentaquark baryons with hidden strangeness ($B_\phi = |qqqs\bar{s}\rangle$; here, $q = u, d$ quarks) are being carried out by the SPHINX collaboration at the IHEP accelerator. This program was described in detail in reviews [1, 2].

The cryptoexotic B_ϕ baryons do not have external exotic quantum numbers, and their complicated internal valence-quark structure can be established only indirectly, by examination of their dynamic properties, which can be quite different from those for ordinary $|qqq\rangle$ baryons. Examples of such anomalous features are listed below (see [1, 2] for more details):

(i) The dominant OZI-allowed decay modes of B_ϕ baryons are the ones with strange particles in the final state (for ordinary baryons, such decays have branching ratios at the percent level).

(ii) Cryptoexotic B_ϕ baryons can possess both large masses ($M > 1.8$–2.0 GeV) and narrow decay widths ($\Gamma \leq 50$–100 MeV). This is due to a complicated internal color structure of these baryons which leads to a significant quark rearrangement of color clusters in the decay process and due to a limited phase space for the OZI-allowed $B \to YK$ decays. At the same time, typical decay widths for the well-established $|qqq\rangle$ isobars with similar masses are ≥ 300 MeV.

As was emphasized in a number of papers (see reviews [1, 2] and the references therein), diffractive production processes with Pomeron exchange offer new tools in searches for the exotic hadrons. In modern notion, the Pomeron is a multigluon system that allows for the production of exotic hadrons in gluon-rich diffractive processes.

The Pomeron exchange mechanism in diffractive production reactions can induce coherent processes on the target nucleus. In such processes, the nucleus acts as a whole. Owing to the difference in the absorptions of single-particle and multiparticle objects in nuclei, coherent processes could serve as an effective tool for separation of a resonance against a nonresonant multiparticle background.

The SPHINX spectrometer was working in the proton beam of the IHEP accelerator with the energy

*This article was submitted by the authors in English.

[1)]Institute for High Energy Physics, Protvino, Moscow oblast, 142284 Russia.

[2)]Institute of Theoretical and Experimental Physics, Bol'shaya Cheremushkinskaya ul. 25, Moscow, 117259 Russia.

**The extended version of the talk given by V.F. Kurshetsov at the conference "Hadron-2001" (Protvino, IHEP, August 2001).

$E_p = 70$ GeV and intensity $I \simeq (2-3) \times 10^6$ protons/spill. The experiments on the SPHINX facility can be divided into two stages:

(a) First-generation measurements—with "old" SPHINX setup (the runs of 1990–1994). The main results of these measurements were published between 1994 and 2000 [3–15]. The most sensitive data were obtained in 1999–2000 [14, 15] (previous data).

(b) Second-generation measurements—with completely upgraded SPHINX setup. With the modified setup, more than 10^9 events were recorded from 1996 to 1999. Preliminary results of these measurements will be presented at the conference "Hadron-2001" for the first time (new data).

The "old" SPHINX and upgraded one had the same structure, but after the upgrade the facility was equipped with a new tracking system, new hodoscopes, hadron calorimeter and modernized RICH spectrometer, new electronics, DAQ, and online computers (which increased the maximum flux of data per spill by an order of magnitude). As the result of this upgrade, we have obtained a practically new setup.

Let us briefly summarize some results of the searches for cryptoexotic baryon states that were obtained earlier in the experiments of the SPHINX collaboration.

2. MAIN RESULTS OF THE PREVIOUS MEASUREMENTS ON THE SPHINX FACILITY

In the previous measurements on the SPHINX spectrometer, several unusual baryonic states were observed in the study of diffractive-production reactions (see [1–6, 9, 10, 14, 15]). The most interesting information was obtained in the study of the reaction

$$p + N(\mathrm{C}) \to [\Sigma^0 K^+] + N(\mathrm{C}) \qquad (1)$$

(here, C corresponds to the coherent reaction on carbon nuclei). The key element of the analysis of this reaction is the selection of $\Sigma^0 \to \Lambda\gamma$ decay, which is a rather complicated problem due to the soft character of the photon spectrum in the laboratory frame ($E_\gamma < 6$ GeV) and significant background. A detailed GEANT-based Monte Carlo simulation of the setup was done for efficiency calculations and cross-section evaluations.

The reaction (1) was studied in our previous works [6, 9] and [14] in different experimental and kinematic conditions, with successively improved separation of the Σ^0 signal due to improvement in the measurements and data analysis. The results of all these studies are in good agreement, which support our conclusion of the observation of two new baryonic states:

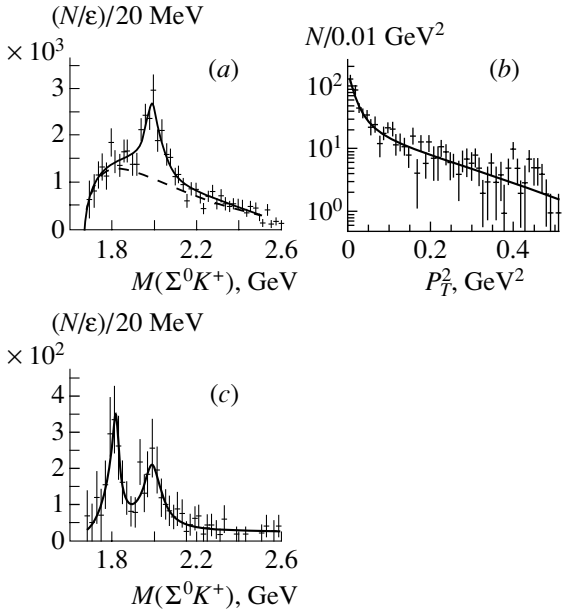

Fig. 1. Distributions for diffractive reaction $p + N \to [\Sigma^0 K^+] + N$: ($a$) corrected mass spectrum $M(\Sigma^0 K^+)$ for all P_T^2 (soft-photon cut); (b) transverse-momentum distribution dN/dP_T^2; and (c) corrected mass spectrum $M(\Sigma^0 K^+)$ for the region of very small $P_T^2 < 0.01$ GeV^2 (strong-photon cut).

(a) the state $X(2000)^+ \to \Sigma^0 K^+$ with the mass $M = 1989 \pm 6$ MeV and the width $\Gamma = 91 \pm 20$ MeV;

(b) the state $X(1810)^+ \to \Sigma^0 K^+$ with $M = 1807 \pm 7$ MeV and $\Gamma = 62 \pm 19$ MeV.

The effective mass spectrum $M(\Sigma^0 K^+)$ in reaction (1) for all values of the square of transverse momentum (P_T^2) is presented in Fig. 1a. The peak of $X(2000)$ is seen very clearly in this spectrum with a good statistical significance. Thus, the reaction

$$p + N \to X(2000) + N \qquad (2)$$

is well separated in the SPHINX data. We estimated the cross section for $X(2000)$ production in (2):

$$\sigma[p + N \to X(2000) + N] \cdot \mathrm{BR}[X(2000) \to \Sigma^0 K^+] = 95 \pm 20 \text{ nb/nucleon} \qquad (3)$$

(assuming $\sigma \propto A^{2/3}$, e.g., for the effective number of nucleons in carbon nucleus equal to 5.24). The parameters of the $X(2000)$ peak are not sensitive to different photon cuts (see Table 1).

The transverse momentum distribution dN/dP_T^2 for reaction (2) is shown in Fig. 1b. From this distribution, the coherent diffractive-production reaction on carbon nuclei is identified as a diffractive peak with

Table 1. Data on $M(\Sigma^0 K^+)$ in reaction $p+N \to [\Sigma^0 K^+]+N$, $\Sigma^0 \to \Lambda\gamma$ with different photon cuts [14] (for all P_T^2)

Photon cut	Soft	Intermediate	Strong
N events in $X(2000)$ peak	430 ± 89	301 ± 71	190 ± 47
Correction factor for photon efficiency	1.0	1.4	2.25
Parameters of $X(2000)$			
M (MeV), weighted spectrum	1986 ± 6	1991 ± 8	1988 ± 6
Γ (MeV), weighted spectrum	98 ± 20	96 ± 26	68 ± 21
$\sigma[p+N \to X(2000)+N] \cdot \mathrm{BR}[X(2000) \to \Sigma^0 K^+]$ (nb/nucleon)	100 ± 19	93 ± 25	91 ± 21

the slope $b \simeq 63 \pm 10$ GeV^{-2}. The cross section for coherent reaction is determined as

$$\sigma[p+\mathrm{C} \to X(2000)+\mathrm{C}]_{\mathrm{coh}} \cdot \mathrm{BR}[X(2000)^+ \to \Sigma^0 K^+] = 260 \pm 60 \ \mathrm{nb/(C\ nucleus)}. \quad (4)$$

The errors in (3) and (4) are statistical only. Additional systematic errors are about $\pm 20\%$ due to uncertainties in the cuts, in the Monte Carlo efficiency calculations, and in the absolute normalization. In the study of coherent reaction (1) (with $P_T^2 < 0.075$ GeV^2) in the mass spectrum $M(\Sigma^0 K^+)$, we observed not only the peak of $X(2000)$, but also another state $X(1810)$. Study of the yield of $X(1810)$ as function of P_T^2 demonstrates that this state is produced only in the region of very small P_T^2 ($\lesssim 0.01$ GeV^2), where it is well defined (see Fig. 1*c*). From this data, parameters of $X(1810)$ are determined, as well as the coherent cross section

$$\sigma[p+\mathrm{C} \to X(1810)+\mathrm{C}]_{P_T^2<0.01\ \mathrm{GeV}^2} \times \mathrm{BR}[X(1810)^+ \to \Sigma^0 K^+] = 215 \pm 44 \ \mathrm{nb}. \quad (5)$$

In the mass spectrum $M(\Sigma^0 K^+)$ in Fig. 1*a*, there is only a slight indication for $X(1810)$ structure, which is seen very clearly in coherent reaction (1). This difference is caused by a large background in this region for the events in Fig. 1*a* (for all P_T^2 values).

To explain the production of the $X(1810)$ state only at a very small P_T^2, the hypothesis of the electromagnetic production of this state in the Coulomb field of the carbon nucleus was proposed [16], and it seems not to be in contradiction with the experimental data.

2.1. X(2000) as a Candidate for Pentaquark Baryon

In a comparative study of coherent reactions $p+\mathrm{C} \to [p\pi^+\pi^-]+\mathrm{C}$ and $p+\mathrm{C} \to [\Delta^{++}\pi^-]+\mathrm{C}$ under the same kinematics as $p+\mathrm{C} \to [\Sigma^0 K^+]+\mathrm{C}$, a search for other decay modes of $X(2000)$ was performed. No peaks in a 2-GeV mass range were observed in $M(p\pi^+\pi^-)$ and $M(\Delta^{++}\pi^-)$ mass spectra, and lower limits for the ratios

$$R[X(2000)] = \mathrm{BR}\{X(2000) \to [\Sigma K]\}/\mathrm{BR}\{X(2000) \to [\Delta\pi]; [p\pi^+\pi^-]\} \gtrsim 1 \quad (6)$$

were obtained. Thus, two unusual properties of the $X(2000)$ state were found:

(i) Anomalously large branching ratios for decay channels with strange-particle emission ($R[X(2000)] \gtrsim 1$). At the same time, R does not exceed a few percent for ordinary isobars.

(ii) Small enough decay width of the heavy $X(2000)$ state. For well established isobars in this mass region, $\Gamma \gtrsim 300$–400 MeV.

These anomalous dynamical properties of the $X(2000)$ baryon are the reasons to consider it as a serious candidate for pentabaryon with hidden strangeness $|X(2000) = |uuds\bar{s}\rangle$ (see more details in [2] and [6]).

2.2. The Reality of X(2000)

We have obtained some additional data to support the reality of the $X(2000)$-baryon state:

(i) In the experiments with the SPHINX setup, we studied the reaction

$$p+N(C) \to [\Sigma^+ K^0]+N(\mathrm{C}). \quad (7)$$

In spite of limited statistics, we observed the $X(2000)$ peak and the indication for $X(1810)$ structure in this

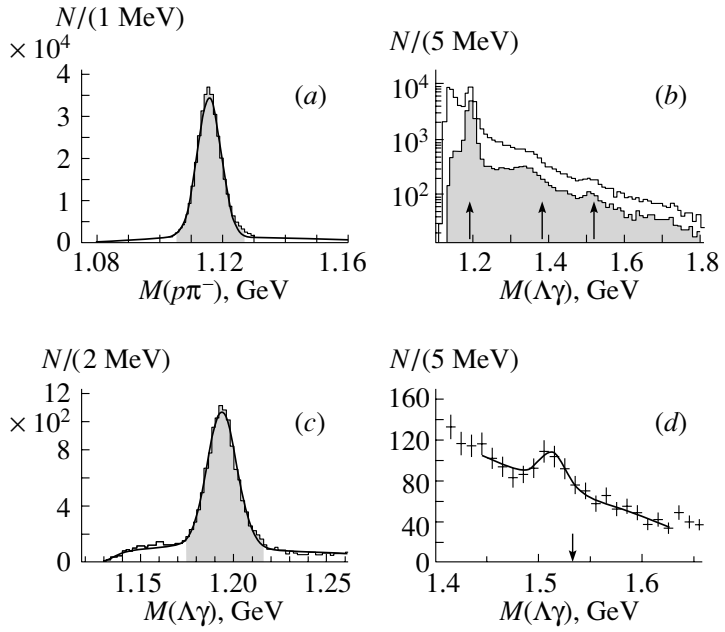

Fig. 2. (*a*) Effective-mass distribution $M(p\pi)$ for the reaction (9); (*b*) effective-mass distribution $M(\Lambda\gamma)$ for the reaction (10): (unshaded histogram) all events and (shaded histogram) soft-photon cut; the arrows show the positions of $\Sigma^0(1192)$, $\Sigma^0(1385)$, and $\Lambda(1520)$; (*c*) and (*d*): the same as (*b*) but in the regions of $\Sigma^0(1192)$ and $\Lambda(1520)$ (soft-photon cut). All the data are preliminary.

reaction, which are quite compatible with the data for reaction (1) [15].

(ii) In the experiment at the SELEX (E781) spectrometer [17] with the Σ^--hyperon beam of the Fermilab Tevatron, the diffractive-production reaction

$$\Sigma^- + N \to [\Sigma^- K^+ K^-] + N \qquad (8)$$

was studied at the beam momentum $P_{\Sigma^-} \simeq 600$ GeV. In the invariant-mass spectrum $M(\Sigma^- K^+)$ for this reaction, a peak with parameters $M = 1962 \pm 12$ MeV and $\Gamma = 96 \pm 32$ MeV was observed (see [2, 18]). The parameters of this structure are very close to the parameters of $X(2000)$. Thus, the real existence of the $X(2000)$ baryon seems to be supported by the data from another experiment and in another process.

3. PRELIMINARY RESULTS FROM UPGRADED SPHINX FACILITY

Let us now present some preliminary results from the upgraded spectrometer, the final version of which includes

a wide-aperture magnetic spectrometer with proportional chambers, drift tubes, and scintillator hodoscopes;

multichannel lead-glass γ spectrometer with 1052 counters $5\times5\times42$ cm^3;

system of Cherenkov counters for identification of secondary particles (including RICH spectrometer with photomatrix of 736 small phototubes—the first RICH device of this type (see [3, 19]);

Table 2. Estimated increase in statistics for diffractive-production reactions with the upgraded SPHINX facility (relative to the previous data)

Reaction	Relative factor
$p + N \to [\Sigma^0 K^+] + N$	5–7
$\to [\Sigma^+ K^0] + N$	10–15
$\to [\Sigma^*(1385) K^+] + N$	5–7
$\to [p\eta] + N$	∼15
$\to [p\eta'] + N$	∼15

Table 3. Number of events with different topology of photons for the reaction $p + N \to [\Lambda K^+] + n\gamma + N$ (∼70% of data)

Reaction	Number of events
$p + N \to [\Lambda K^+] + 0\gamma + N$	171K
$\to [\Lambda K^+] + 1\gamma + N$	57K
$\to [\Lambda K^+] + 2\gamma + N$	31K
$\to [\Lambda K^+] + 3\gamma + N$	12K
$\to [\Lambda K^+] + \text{any } \gamma + N$	322K

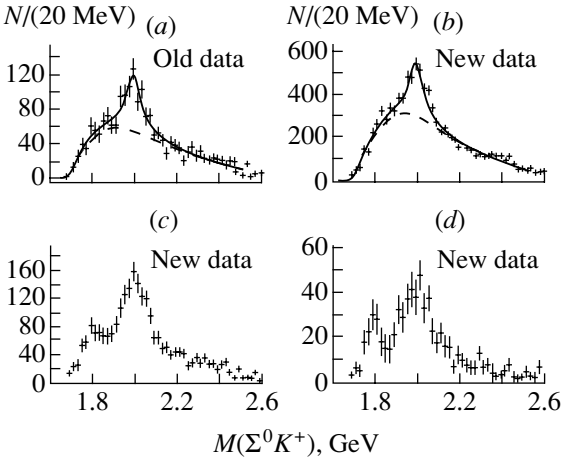

Fig. 3. Invariant-mass spectra $M(\Sigma^0 K^+)$ in the diffractive reaction $p + N \to [\Sigma^0 K^+] + N$ (with soft-photon cut): (*a*) old data, all P_T^2; (*b*) new data, all P_T^2; (*c*) new data, $P_T^2 \leq 0.75$ GeV^2, $P_{K^+} \leq 25$ GeV; and (*d*) new data, $P_T^2 \leq 0.01$ GeV^2, $P_{K^+} \leq 25$ GeV. The data in (*b*), (*c*), and (*d*) is preliminary.

hadron calorimeter with 96 total-absorption detectors;

guard system of scintillator counters and lead-scintillator sandwiches for separation of exclusive reactions;

trigger and front-end electronics, DAQ, and fast on-line computers.

The new front-end electronics and DAQ system allowed us to record up to ~3000 triggers per 10-s accelerator cycle. This, in turn, gave us the possibility of discarding old trigger requirements and introducing new types of triggers. During the runs from 1996 to 1999, more than 10^9 events were recorded, corresponding to approximately 10^{12} protons passing through (C/Cu) target.

3.1. Status of New Data Processing

Up to now, almost 70% of have been were processed by a tracking reconstruction program that was completely rewritten. We also finished the preliminary calibration of the RICH and γ detector. These detectors were used in the analysis, but there is room for improvement. The new GEANT-based Monte Carlo program is under development. Based on preliminary analysis, we can estimate the possible increase in statistics for some reactions studied with the "old" SPHINX (see Table 2).

Two new types of triggers were introduced in the runs with the upgraded SPHINX. One of them (meson trigger) was designed to continue our investigations of quasiexclusive meson production in the deep-fragmentation region [13]. The other (multiparticle trigger) was developed to search for possible narrow exotic baryons, in particular, for $Z^+(1530), Z^+ \to nK^+(pK^0)$, predicted in [20, 21]. The data from these types of triggers have also passed the track reconstruction stage, and preliminary results will be available in the near future.

3.2. The Reactions with Λ(1115) in the Final State

Currently, we are concentrating on studying the reactions with $\Lambda(1115)$ in the final state

$$p + N \to [\Lambda K^+] + n\gamma + N, \quad \Lambda \to p\pi^-. \qquad (9)$$

The identification of Λ in reaction (9) (and, more generally, the identification of the ΛK^+ system in the final state) was done using the combined information from RICH and the tracking system. This results in a very clean signal for Λ, presented in Fig. 2*a*.

The decomposition of the sample (9) into reactions with a different number of photons ($E_\gamma \geq 1$ GeV) is presented in Table 3.

Further discussion will be devoted to the reaction with a single photon in the final state

$$p + N \to [\Lambda K^+] + \gamma + N. \qquad (10)$$

The general spectrum of the $\Lambda\gamma$ effective mass for this reaction is shown in Fig. 2*b* for all events and the events with special cuts for the selection of "real" photons. There are three distinct structures in this distribution: the decay $\Sigma^0(1192) \to \Lambda\gamma$, the decay $\Sigma^0(1385) \to \Lambda\pi^0$ with one missing photon, and the decay $\Lambda(1520) \to \Lambda\gamma$. The signal for Σ^0 is shown in more detail in Fig. 2*c* and for $\Lambda(1520)$ in Fig. 2*d*.

3.3. X(2000) and X(1810) in the New Data

Using the cuts shown in Fig. 2*c,* reaction (1) in the data from the upgraded SPHINX spectrometer was finally selected. The results are presented in Fig. 3 together with the distribution from previous data.

Note that the effective-mass distribution $M(\Sigma^0 K^+)$ from the first-generation experiment (Fig. 3*a*) is not corrected for the efficiency, thus allowing it to be compared directly with the same distribution from new data (Fig. 3*b*). The distributions are very similar to the evident increase in statistics from new data and can be easily fitted by the same function. In fact, the fit of the distribution in Fig. 3*b* was done using the parameters of $X(2000)$ from the previous one with two free parameters for normalization. The effective-mass distributions $M(\Sigma^0 K^+)$ with our standard P_T^2 cuts are shown in Fig. 3*c* (coherent region) and Fig. 3*d* (the region of very small P_T^2). Note that, in the last two figures, an additional cut on

the kaon momentum $P_{K^+} \leq 25$ GeV was introduced to ensure the identification capabilities of RICH. As can be seen from the comparison of Figs. 1 and 3, the results for the reaction $p + N \to [\Sigma^0 K^+] + N$ based on new statistics are in good agreement with our previous data and strongly support the existence of the $X(2000)$ state (with an increase in statistics for this state by a factor of ~ 5).

With new statistics, we hope to obtain quantitative information for the $X(2000)$ state (cross sections, angular decay distributions, quantum numbers, branching ratios for different channels) and study the features of $X(1810)$ production in the small-P_T^2 region with C and Cu targets.

3.4. Prospects for Measuring the Radiative Width for $\Lambda(1520) \to \Lambda\gamma$ and $\Lambda(1520) \to \Sigma^0\gamma$

Up to now, direct measurements of the electromagnetic decays of hyperons have been made only for two states—the well-known decay $\Sigma^0 \to \Lambda\gamma$ and the decay

$$\Lambda(1520) \to \Lambda\gamma. \qquad (11)$$

The current PDG value for this decay is based on a very old bubble-chamber experiment [22]. The photon from the decay (11) in this experiment was not detected directly, and the missing-mass method was used in studying the reaction

$$K^- + p \to \Lambda + \text{neutral particles}. \qquad (12)$$

The result for the radiative width of the decay (11)

$$\Gamma[\Lambda(1520) \to \Lambda\gamma] = 125 \pm 22 \text{ keV} \qquad (13)$$

is in contradiction to the more recent (unpublished) result [23]

$$\Gamma[\Lambda(1520) \to \Lambda\gamma] = 33 \pm 11 \text{ keV}. \qquad (14)$$

As can be seen from Fig. 2*d*, we definitely observe the decay (11) in our data. Thus, the prospects for measuring this decay with a reasonable accuracy seem to be very good. Note that different models give a value for the width in the range 32–215 keV.

The decay $\Lambda(1520) \to \Sigma^0\gamma$ is connected to the decay $\Lambda(1520) \to \Lambda\gamma$ by $SU(3)$ symmetry. It was never measured directly, and the PDG value for the width of this decay is $SU(3)$ + phase-space calculation using (13) as an input. The prospects for singling out this decay in our data is unclear and is currenty under study.

For a detailed review of the situation with radiative decays of hyperons, see [24].

4. CONCLUSIONS

In the experiments with the "old" SPHINX, we investigated the reaction $p + N \to [\Sigma^0 K^+] + N$ and observed the new baryon state $X(2000) \to \Sigma^0 K^+$ with $M = 1989 \pm 6$ MeV, $\Gamma = 91 \pm 20$ MeV and with anomalous dynamical properties. This $X(2000)$ state is a serious candidate for pentaquark baryon with hidden strangeness $|uuds\bar{s}\rangle$.

In the new runs with the completely upgraded SPHINX facility (practically new setup), large statistics for many proton-induced reactions were obtained. The first preliminary results for the reaction $p + N \to [\Sigma^0 K^+] + N$ based on new statistics are in good agreement with our previous data and strongly support the existence of the $X(2000)$ state (with an increase in statistics for this state by a factor of ~ 5).

Radiative decay of $\Lambda(1520) \to \Lambda + \gamma$ is observed in the new statistics. There is also hope that we can see the decay $\Lambda(1520) \to \Sigma^0\gamma$. The data on these decays can be very important for the investigation of the mechanisms of the $SU(3)$-symmetry breaking.

We have a large program for further analysis of new statistics and, first of all, for quantitative data on several interesting objects that were indicated in our old measurements.

ACKNOWLEDGMENTS

It is a great pleasure for us to thank Yu.G. Abov for his interest and encouraging support of our work throughout more than a decade of experiments at the SPHINX facility.

This work was supported in part by the Russian Foundation for Basic Research, project nos. 99-02-18251 and 02-02-16086.

REFERENCES

1. L. G. Landsberg, Usp. Fiz. Nauk **164**, 1129 (1994) [Phys. Usp. **37**, 1043 (1994)]; V. F. Kurshetsov and L. G. Landsberg, Yad. Fiz. **57**, 2030 (1994) [Phys. At. Nucl. **57**, 1954 (1994)]; L. G. Landsberg, Yad. Fiz. **60**, 1541 (1997) [Phys. At. Nucl. **60**, 1397 (1997)].
2. L. G. Landsberg, Phys. Rep. **320**, 223 (1999); Yad. Fiz. **62**, 2167 (1999) [Phys. At. Nucl. **62**, 1999 (1999)].
3. SPHINX Collab. (D. V. Vavilov *et al.*), Yad. Fiz. **57**, 241 (1994) [Phys. At. Nucl. **57**, 227 (1994)]; SPHINX Collab. (M. Ya. Balatz *et al.*), Z. Phys. C **61**, 220 (1994).
4. SPHINX Collab. (M. Ya. Balatz *et al.*), Z. Phys. C **61**, 399 (1994).
5. SPHINX Collab. (D. V. Vavilov *et al.*), Yad. Fiz. **57**, 253 (1994) [Phys. At. Nucl. **57**, 238 (1994)].
6. SPHINX Collab. (L. G. Landsberg *et al.*), Nuovo Cimento A **107**, 2441 (1994).

7. SPHINX Collab. (D. V. Vavilov *et al.*), Yad. Fiz. **57**, 1449 (1994) [Phys. At. Nucl. **57**, 1376 (1994)]; **58**, 1426 (1995) [**58**, 1342 (1995)].
8. SPHINX Collab. (S. V. Golovkin *et al.*), Z. Phys. C **68**, 585 (1995).
9. SPHINX Collab. (S. V. Golovkin *et al.*), Yad. Fiz. **59**, 1395 (1996) [Phys. At. Nucl. **59**, 1336 (1996)].
10. SPHINX Collab. (V. A. Bezzubov *et al.*), Yad. Fiz. **59**, 2199 (1996) [Phys. At. Nucl. **59**, 2117 (1996)].
11. L. G. Landsberg, in *Proceedings of the Seventh International Conference on Hadron Spectroscopy, "Hadron-97," Upton, N.Y., 1997,* Ed. by S.-U. Chung and H. J. Willutzki, p. 725.
12. V. A. Victorov *et al.*, Yad. Fiz. **59**, 1229 (1996) [Phys. At. Nucl. **59**, 1175 (1996)]; SPHINX Collab. (M. Ya. Balatz *et al.*), Yad. Fiz. **59**, 1242 (1996) [Phys. At. Nucl. **59**, 1186 (1996)]; SPHINX Collab. (S. V. Golovkin *et al.*), Z. Phys. A **359**, 435 (1997).
13. SPHINX Collab. (S. V. Golovkin *et al.*), Z. Phys. A **359**, 327 (1997).
14. SPHINX Collab. (S. V. Golovkin *et al.*), Eur. Phys. J. A **5**, 409 (1999).
15. SPHINX Collab. (D. V. Vavilov *et al.*), Yad. Fiz. **63**, 1469 (2000) [Phys. At. Nucl. **63**, 1391 (2000)].
16. D. V. Vavilov *et al.*, Yad. Fiz. **62**, 501 (1999) [Phys. At. Nucl. **62**, 459 (1999)].
17. R. Edelstein *et al.*, Fermilab Proposal E781 (1987, revised in 1993).
18. L. G. Landsberg, in *Proceedings of the 4th Workshop on Small-X and Diffractive Physics, Fermilab, Batavia, 1998,* p. 189; in *Proceedings of "Hyperon-99," Fermilab, Batavia, 1999,* p. 29.
19. A. Kozhevnikov, V. Kubarovsky, V. Molchanov, *et al.*, Nucl. Instrum. Methods Phys. Res. A **433**, 164 (1999).
20. D. Diakonov, V. Petrov, and M. V. Polyakov, Z. Phys. A **359**, 305 (1997); hep-ph/9703373.
21. H. Weigel, *Talk at the 7th Conference on Intersections between Particle and Nuclear Physics, CIPANP 2000, Quebec City, Quebec, Canada, 2000,* hep-ph/0006191.
22. T. S. Mast, M. Alston-Garnjost, R. O. Bangerter, *et al.*, Phys. Rev. Lett. **21**, 1715 (1968).
23. R. Bertini *et al.*, *Contribution to PANIC-10, Heidelberg, 1984;* R. Bertini, Nucl. Phys. B **279**, 49 (1987).
24. L. G. Landsberg, Yad. Fiz. **59**, 2161 (1996) [Phys. At. Nucl. **59**, 2080 (1996)].

Physics of Atomic Nuclei, Vol. 65, No. 11, 2002, pp. 2077–2091. Translated from Yadernaya Fizika, Vol. 65, No. 11, 2002, pp. 2138–2152.

ELEMENTARY PARTICLES AND FIELDS

Neutrino Crown of a Protoneutron Star in the Process of Collapse: Physical Formulation of the Problem

V. S. Imshennik

Institute of Theoretical and Experimental Physics,
Bol'shaya Cheremushkinskaya ul. 25, Moscow, 117259 Russia

Received March 26, 2002

Abstract—A spherically symmetric gravitational collapse of the iron core of a star develops in the form of a hydrodynamic process, where the role of intrinsic neutrino radiation ever increases. The early stage of the collapse has a homological character within the interior of the core, but there is a delay in exterior layers. Hydrodynamic calculations reveal that, at the late stage of the collapse (it is the stage within which the majority of neutrinos are emitted), a structure is formed that consists of a neutron-star germ nontransparent to neutrinos and exterior layers accreting onto it, which are, on the contrary, transparent to neutrinos. They are separated by a semitransparent layer occurring between the front of the accretion shock wave and the germ surface forming a neutrinosphere. By using a typical quasistationary character of this layer, which is referred to as the neutrino crown of a protoneutron star, a stationary model is developed here that supplements hydrodynamic calculations of the collapse process, which are rather rough within this model. In particular, these calculations reveal the crucial significance of the semitransparent crown for a possible transition of the collapse into an explosion having a scale of a supernova explosion. If there is no such possibility, the same crown determines the important properties of a quiet collapse that are associated with the development of convective instability, etc., in it. The model formulated here, which is comparatively simple (in relation to hydrodynamic calculations) owing to an adequate physical formulation of problem, is intended for analyzing special features of the crown. This formulation of the problem demonstrates some new possibilities of neutrino hydrodynamics, which is an analog of the well-known radiative hydrodynamics involving photons instead of neutrinos.

1. INTRODUCTION

The modern hydrodynamic theory of the collapse of the iron cores of stars that, from the very beginning of their existence, have a rather large mass ($M_{\rm ms} \geq 10M_\odot$) within the main sequence developed on the basis of a one-dimensional (spherically symmetric) numerical simulation of the collapse of such cores of stars in their self-consistent gravitational field with allowance for quite a complicated equation of state of nuclear matter [1–3] undergoing the neutronization under the effect of conventional nuclear β transformations and intrinsic neutrino radiation [4]. The contribution of this radiation during collapse increases very fast as the characteristic densities and temperatures increase and appears to be the main mechanism through which the collapsing core of a star loses energy and lepton charge. Upon approximately two decades of development, the one-dimensional hydrodynamic theory of collapse of the iron cores of stars arrived at specific conclusions that were formulated, for example, in the review article of Imshennik and Nadyozhin [5]. One qualitative conclusion of this theory is that collapse is of a nonhomological character. At its first (early) stage, there occurs a homological collapse (the radial distribution of the velocity of fall being linear) of the interior of the core, the core mass being $M_c \leq 1M_\odot$; at the same time, the exterior part of mass $M_e = M_{\rm Fe} - M_c$ ($M_{\rm Fe}$ is the iron-core mass) is noticeably delayed, collapsing with a decreasing velocity of fall. At a mass equal to M_c, the linear law of velocity is violated, the velocity reaching its maximum absolute value there. Before this exterior part collapses to the very end, the interior core of mass M_c already stops, forming a protoneutron star (PNS). It can be assumed that the collapse is terminated under the concerted effect of two factors: (i) the relative attenuation of neutrino-energy losses due to nontransparency of the PNS interior to intrinsic neutrino radiation at characteristic central matter densities of $\rho_c \gtrsim 10^{12}$ g/cm^3 and temperatures of $T_c \gtrsim 5 \times 10^{10}$ K and (ii) a considerable growth of the pressure in a free-nucleon gas that is the product of the dissociation of nuclides belonging to the iron peak of elements ($^{56}{\rm Fe} \to 26^1p + 30^1n$) and which is formed under the above physical conditions.

We note that, strictly speaking, this pattern of collapse is applicable to the collapse of the most mas-

1063-7788/02/6511-2077$22.00

sive iron cores for which $M_{\rm Fe} \simeq 2M_\odot$ and which are accordingly formed in the most massive stars with $M_{\rm ms} \simeq 25M_\odot$. In less massive objects, the collapse process occurs at lower characteristic temperatures and involves the emergence of a noticeable number of nuclides including exotic ones that are highly enriched in neutrons (under the conditions of developing neutronization). The equation of state of matter becomes more complicated upon taking into account the contribution of these nuclides, which are in fact unknown, and effects of nonideality in cold nuclear matter that are due to attractive nuclear forces and the repulsion of particles. A qualitative comparison of numerical models corresponding to "cold collapse" of this type with "hot collapse" peculiar to the most massive stars was performed in [6] (that the collapse of the 1987A PSN core—it preceded the famous explosion of the SN 1987A supernova—belongs to the latter type is a circumstance of paramount importance). In this study, we will predominantly restrict ourselves to the case of rather massive iron cores, which is described by a simpler equation of state and which can be applied in interpreting SN 1987A.

Thus, we can state that, instead of the volume process of neutrino-energy losses upon PNS formation, the surface process of energy losses begins, which is accompanied by the formation of a neutrinosphere, an analog of a photosphere in conventional stars within the main sequence, such as our Sun. As soon as a neutrinosphere is formed, the PNS can be considered as a neutrino star, but its existence is short-term: as was shown within the hydrodynamic theory of collapse [7], the lifetime of such a neutrino star is approximately 10 s, the neutrino signal from the collapsing iron core of a star being of approximately the same duration. As applied to SN 1987A, the description of the evolution of such a neutrino star, together with its neutrinosphere, was motivated by the detection of a neutrino signal in [8]. This is the way in which the second (later) stage of the collapse develops, which is accompanied by the accretion of the exterior part of the iron core to the PNS, its mass M_e being on the same order of magnitude as the collapsing-core mass M_c at the early stage since the theory of massive-star evolution predicts the following interval for iron-core masses: $1.2M_\odot < M_{\rm Fe} < 2M_\odot$ [5, 6]. This stage of collapse is the most peculiar in that, upon the abrupt stopping of a PNS, a strong shock wave is formed; within its narrow front, the accreting flux of matter of the iron-core periphery (cold iron gas) is decelerated and is predominantly converted into a hot gas of free nucleons. As is shown within hydrodynamic theory, the front of this accretion shock wave (ASW) moves relatively slow in space, occurring somewhere close to the neutrinosphere above it. If we denote by $r_{\nu 0}$ the radius of the neutrinosphere and by $r_{\rm sw}$ the radius of the ASW front, $r_{\rm sw} \gtrsim r_{\nu 0}$.

The following circumstances are favorable for a theoretical consideration. First, the accretion velocity at the ASW front in an iron gas is close to the free-fall velocity v_0 in the gravitational field of a PNS of mass M_0,

$$v_0 = -\left(\frac{2GM_0}{r_{\rm sw}}\right)^{1/2}, \qquad (1)$$

while the density ρ_0 is related to the rate of growth of the PNS mass, $\dot{M}_0$, by the simple equation

$$\rho_0 = -\frac{\dot{M}_0}{4\pi r_{\rm sw}^2 v_0} \qquad (\dot{M}_0 > 0). \qquad (2)$$

Second, the quasistationarity condition holds; in fact, this condition is already assumed in relations (1) and (2), its particular cases being represented by the requirements $M_0 = {\rm const}$ and $\dot{M}_0 = {\rm const}$. If we supplement these two with the requirement that all the parameters of a PNS, including the parameters of neutrino radiation from the neutrinosphere, be quasistatioinary, we can expect that a quasistationary solution will exist in the entire spherical layer between the neutrinosphere and the ASW front—that is, in the following range of radius values: $r_{\nu 0} < r < r_{\rm sw}$. It is this spherical layer that will be referred to below as the crown of a protoneutron star (or, for the sake of brevity, CPNS). It should be recalled that, according to the aforesaid, the equivalent term of a neutrino-star crown is also legitimate for it. Burrows *et al.* [9] were the first to notice this property of the second (later) stage of collapse of the iron core of a star. Those authors obtained the corresponding quasistationary solution, but they employed some additional simplifications, which are partly unjustified [10] (see below). In fact, the very existence of such a solution follows from the relationship between the characteristic lifetimes of a CPNS and a PNS. We will now consider this point in some detail. By using the neutrino-thermal-conductivity approximation to describe the transport of neutrino radiation [11], it was shown, for the first time, within the hydrodynamic theory of collapse [7] that the time of diffusion of intrinsic-radiation neutrinos through a PNS is $t_{\rm PNS} \sim 1$ s. We note that the characteristic time of accretion of the exterior layer of the iron core—as a matter of fact, it is unambiguously related to the neutrino-radiation-diffusion time [7]—is on the same order of magnitude. On the other hand, the characteristic CPNS time $t_{\rm CPNS}$ is obviously about the ratio $r_{\rm sw}/v_0 \sim 3 \times 10^6/10^{10} \sim 3 \times 10^{-4}$ s since $r_{\rm sw} \sim 3 \times 10^6$ cm and $v_0 \sim 10^{10}$ cm/s [7]. The last value is obtained upon substituting $M_0 = 1M_\odot$ and $r_{\rm sw} = 2.7 \times 10^6$ cm into (1). It should be noted that

the PNS radius $r_{\nu 0}$ significantly exceeds the known radius of cold neutrino stars, $\sim 10^6$ cm [12]; for our rough estimates, we set $r_{\rm sw} \sim r_{\nu 0}$. Thus, the strong inequality $t_{\rm PNS} \gg t_{\rm CPNS}$—that is, the quasistationarity condition for a CPNS—is indeed satisfied.

2. QUALITATIVE CONSIDERATION OF A STATIONARY CPNS

For the solution to the problem of the CPNS structure to be stationary, it is necessary that not only the parameters $r_{\nu 0}$, M_0, and $\dot{M}_0$, which were discussed above in detail, but also the radius of the ASW front, $r_{\rm sw}$, be constant. This immobility of the shock front is emphasized, in fluid dynamics, by the term "attached shock," along with an ASW. Thus, we are going to address the problem of determining the stationary structure of a CPNS, which is a spherical layer between the neutrinosphere ($r = r_{\nu 0}$) and the ASW front ($r = r_{\rm sw}$). The solution to this problem is determined by appropriate boundary conditions at the internal and external boundaries, the inequality $r_{\nu 0} < r_{\rm sw}$ being satisfied. It is obvious that the well-known Hugoniot conditions at the ASW front [13] as formulated for the case of an attached shock whose thickness is negligible serve as external boundary conditions. The Hugoniot conditions determine all physical quantities behind the ASW front if, in front of it, the values of the density ρ_0 and the velocity v_0 are specified according to relations (2) and (1) at given values of the parameters M_0, $\dot{M}_0$, and $r_{\rm sw}$. The shock must then be considered to be strong—that is, the pressure and the specific internal energy in front of the ASW front must be disregarded for cold iron gas (this was mentioned above in discussing the results of hydrodynamic theory). In order to obtain internal boundary conditions, we may assume that neutrino radiation from a neutrinosphere corresponds to the generalization of blackbody photon radiation to the case of the Fermi–Dirac statistics of neutrinos and antineutrinos. The density of neutrino-radiation-energy flux can then be represented in the form (see a detailed derivation in Section 3) [11]

$$F_{\nu\bar{\nu}} = \frac{\pi c}{4(ch)^3} T_{\nu\rm eff}^4 \left(\psi_{\nu\rm eff}^4 + 2\pi^2 \psi_{\nu\rm eff}^2 + \frac{7\pi^4}{15} \right), \quad (3)$$

where, for the parameters of neutrino radiation, we take the effective temperature $T_{\nu\rm eff}$ (here, in erg) and the effective dimensionless chemical potential (the ratio of the dimensional chemical potential to temperature) for neutrinos, $\psi_{\nu\rm eff}$. It can easily be seen from (3) that, at $\psi_{\nu\rm eff} = 0$, $(\pi c/4(ch)^3)(7\pi^4/15) = 7\sigma_{\rm SB}^*/8$, where $\sigma_{\rm SB}^*$ is the usual Stefan–Boltzmann constant for temperature taken in energy units; that is,

$$\sigma_{\rm SB}^* = \sigma_{\rm SB} k_{\rm B}^{-4} = \frac{2\pi^5 c}{15(ch)^3}, \quad (4)$$

where $k_{\rm B}$ is Boltzmann's constant and $\sigma_{\rm SB}$ is the Stefan–Boltzmann constant. In the important particular case being considered ($\psi_{\nu\rm eff} = 0$), formula (3) is the Fermi–Dirac generalization of the known formula for blackbody photon radiation at the same effective temperature $T_{\nu\rm eff}$. In the general case, including that of $\psi_{\nu\rm eff} \neq 0$, it is implied in Eq. (3) that the antineutrino chemical potential is given by $\psi_{\bar{\nu}\rm eff} = -\psi_{\nu\rm eff}$, as it is for neutrino radiation under equilibrium blackbody conditions [11]. In formulating the internal boundary condition, the preassignment of some more functions of the local parameters $T_{\nu 0}$ and $\psi_{\nu 0}$ at $r = r_{\nu 0}$ plays the role of an input. In the following, it will be shown that they are unambiguously determined by the effective values of the temperature and the chemical potential, $T_{\nu\rm eff}$ and $\psi_{\nu\rm eff}$, at the PNS neutrinosphere (see Section 6).

We begin our analysis by assessing the characteristic value of $T_{\nu\rm eff}$ on the basis of the estimate known for the integral of the neutrino emissivity with respect to time, $L_{\nu\bar{\nu}} t_{\rm PNS}$—it is equal to the total PNS binding energy of about 10^{53} erg [12].[1)] In doing this, we will also employ the obvious relation $L_{\nu\bar{\nu}} = 4\pi r_{\nu 0}^2 F_{\nu\bar{\nu}}$, where $F_{\nu\bar{\nu}}$ is given in (3) with $\psi_{\nu\rm eff} = 0$ and $t_{\rm PNS} = 1$ s (see above). Using the value of $r_{\nu 0} = 10^6$ cm and

[1)] In fact, we must use here one-third of the total binding energy if we consider that the radiation energy is distributed among three neutrino flavors (ν_e, ν_μ, and ν_τ) in approximately equal shares. A simplified physical formulation of the problem of the CPNS structure involves only electron neutrinos. There arises the question of assessing the significance of other neutrino flavors (μ and τ). One can arrive at the conclusion [7, 14–16] that, despite the distribution of energy fluxes in equal shares among all neutrino flavors, the contribution of ν_μ and ν_τ (and of $\bar{\nu}_\mu$ and $\bar{\nu}_\tau$) is of secondary importance in the hydrodynamics of collapse in relation to the electron-neutrino contribution even within a PNS. Yet, the problem of this contribution is uncertain to some extent because of paucity of required data and calls for a further investigation. Nevertheless, we can adduce some additional physical arguments concerning the CPNS problem. The delay of the emergence of nontransparency to muon and tau neutrinos proves to be insignificant [17]. Obviously, the flux of such neutrinos will then come from other neutrinospheres that are exterior with respect to that considered here; the effective temperatures of those neutrinos will be somewhat higher, but their relevant parameters will only be slightly different from the values for the electron flavor: $T_{\nu_\mu\rm eff} \gtrsim 5$ MeV and $r_{\nu_\mu 0} \lesssim 10^6$ cm (see [5] and references therein). This means that the interaction of such soft neutrinos with nucleons of the crown will be suppressed by the high threshold for muon and τ-lepton production (a few hundred MeV), their concentrations in the crown being negligible at low characteristic temperatures of $T_{\nu_\mu\rm eff} \lesssim 5$ MeV.

substituting $\sigma^*_{SB} = 1.5 \times 10^{59}$ from (4) into (3), we then arrive at $T_{\nu\text{eff}} \simeq 0.6 \times 10^{-5}$ erg $\simeq 4$ MeV, which is in reasonable agreement with the results obtained from hydrodynamic theory in [8] ($T_{\nu\text{eff}} \simeq 5.5$ MeV) and in [9, 10] ($T_{\nu\text{eff}} \simeq 4.5$ MeV). It should be noted that the last values of the effective temperature are characteristic of a time interval covering a considerable part of the late stage of collapse. These values (which are close to each other) are established within some rather short time interval immediately after the emergence of the nontransparency effect and the formation of a PNS, together with its neutrinosphere. In subsequently solving the problem of the CPNS structure, we will assume that the parameters $T_{\nu\text{eff}}$ and $\psi_{\nu\text{eff}}$ are preset, along with $r_{\nu 0}$, whereupon the energy-flux density $F_{\nu\bar{\nu}}$ appearing in (3) and the neutrino emissivity $L_{\nu\bar{\nu}}$ become specified. It should be emphasized that the inclusion of nonzero values of the parameter $\psi_{\nu\text{eff}}$ is of fundamental importance since this means the dominance of neutrino radiation if $\psi_{\nu\text{eff}} > 0$ or the dominance of antineutrino radiation if $\psi_{\nu\text{eff}} < 0$. In hydrodynamic theory [7, 8], $\psi_{\nu\text{eff}} \simeq 0.15$, which is interpreted on the basis of the conjecture that matter still continues to undergo neutronization in the interior of a PNS (see also [4]).

The problem of the CPNS structure is significantly simplified owing to two assumptions concerning the composition of matter and the properties of the electron–positron (e^-, e^+) component: (i) The baryon component of matter consists only of free nucleons n and p in the form of Boltzmann gases. (ii) The lepton component involves only e^- and e^+ in the form of ultrarelativistic Fermi–Dirac gases, their degree of degeneracy being arbitrary. It is obvious that, adopting these assumptions, we neglect the contribution of various nuclides to the baryon component and the contribution of neutrino–antineutrino gases ($\nu, \bar{\nu}$) to the lepton component. That it is legitimate to consider the lepton component in the ultrarelativistic approximation and the baryon component in the Boltzmann approximation follows from the above estimates of characteristic accretion velocities ($v_0 \sim 10^{10}$ cm/s) and the temperatures of matter, T_0, which are on the same order of magnitude as the effective temperature of neutrino radiation ($T_{\nu\text{eff}} \sim 4$ MeV). Further, it is reasonable to estimate the characteristic densities ρ_0 in front of the ASW front; in doing this, we assume, in accordance with hydrodynamic theory, that the accretion rate $\dot{M}_0$ lies in the range $0.1M_\odot/\text{s} < \dot{M}_0 < 10M_\odot/\text{s}$. At $M_0 = 1M_\odot$ and $r_{sw} = 2.7 \times 10^6$ cm (see above), we then find from (2) that ρ_0 lies in the range $2.2 \times 10^8 < \rho_0 < 2.2 \times 10^{10}$ g/cm^3. These densities are much lower than the nuclear-matter density (2.7×10^{14} g/cm^3); therefore, we can ignore nonideality effects in the baryon component at the above rather high temperatures T_0. On the other hand, we note that the characteristic densities are so high that the photon contribution to the properties of matter is insignificant; however, this contribution, which is extremely simple, will be taken into account in the following. As to the contribution of ν and $\bar{\nu}$ to the properties of the lepton component, it is small if for no other reason than the smallness of characteristic neutrino concentrations in relation to the concentrations of e^- and e^+.[2)] Indeed, the neutrino and antineutrino concentrations are $n_\nu \sim n_{\bar{\nu}} \sim F_{\nu,\bar{\nu}}(r^2_{\nu 0}/r^2_{sw})(3cT_{\nu\text{eff}})^{-1} \sim 10^{33}$ cm^{-3}, while the electron and positron concentrations are estimated at $n_{e^-} \sim n_{e^+} \sim 10\rho_0(m_0)^{-1} \sim 10^{34}$ cm^{-3} even without allowing for a considerable degree of electron degeneracy. In these estimates, it is assumed that $F_{\nu,\bar{\nu}} \sim 10^{40}$ erg/cm^2, $T_{\nu\text{eff}} \sim 10^{-5}$ erg, and $3r_{\nu 0} \sim r_{sw}$ and that the characteristic compression behind the ASW front is approximately tenfold at $\rho_0 \sim 10^9$ g/cm^3. For the sake of simplicity, these concentrations of ν and $\bar{\nu}$ are identified with the concentrations of neutrinosphere ν and $\bar{\nu}$ in the vicinity of the ASW front.

As was indicated above, the thickness of the ASW front is negligible in relation to other scales of length, such as $r_{\nu 0}$ and r_{sw}. However, it is assumed that, within this thickness, there occurs the dissociation of iron-gas nuclides into free nucleons, the energy required for this endothermic process, which must of course be taken into account in the Hugoniot conditions at the ASW front, having a well-known enormous value of about 8.80 MeV/nucleon. At the above characteristic values of the matter temperature T_0, the dissociation process in question is predominantly completed within the front thickness, so that our input assumption on the composition of the baryon component is justified. Nevertheless, matter does not undergo a noticeable neutronization within the front thickness since neutronization processes are induced by weak interactions in reactions involving the β transformations of nuclei. For this reason, the relationship between n and p in the Hugoniot conditions is taken to be identical to that which is peculiar to iron-gas nuclides.

In view of the fact that the complete hydrodynamic theory of the late stage of iron-core collapse must include solving the quasistationary problem of the CPNS structure, there arises the question of whether it is necessary to consider this problem, especially with the above considerable simplifications

[2)] In [11], it was rigorously proven, however, that there is virtually no energy–momentum transfer to crown matter from neutrinosphere radiation specified by blackbody intensities—only a small fraction of this radiation is transferred to the crown and is absorbed there (see Section 3).

in its physical formulation. In my opinion, it is reasonable to do this, provided that the formulation of the quasistationary problem in question is thoroughly validated. Further, the region that is semitransparent to neutrino radiation and which surrounds the neutrinosphere is well known to be precisely the region that is rather roughly described in hydrodynamic theory, especially at its early stage [7]. Strictly speaking, it is necessary to solve numerically very involved transport equations [3]. Even now, this can in fact be achieved only in individual calculations of record volume that are handicapped by the paucity of data on neutrino interactions with matter of complex chemical composition [18, 19]. It is extremely difficult to analyze the physical meaning of numerical results and to determine the conditions of convective instability of these solutions, which plays a crucial role in the development of the neutrino-convective mechanism of the explosion of collapsing supernovae [14–16].

The physical formulation of the quasistationary hydrodynamic problem of the CPNS structure is presented in this article with allowance for neutrino radiation from the neutrinosphere of a PNS. First of all, a set of hydrodynamic equations is derived that contains, on the right-hand sides, changes that direct and inverse β processes induce in (i) energy and (ii) the lepton charge, these changes being given in the form of terms integrated over the spectrum of ν and $\bar{\nu}$. After that, boundary conditions at the external (ASW) and the internal (neutrinosphere) boundary of the CPNS are formulated and validated. The radius of the internal boundary is preset ($r = r_{\nu 0}$) along with all parameters characterizing neutrino radiation from the neutrinosphere ($T_{\nu\mathrm{eff}}, \psi_{\nu\mathrm{eff}}$), while the radius of the external boundary ($r = r_{\mathrm{sw}}$) is an eigenvalue of the problem under consideration. This eigenvalue is determined by requiring fulfillment of the internal boundary condition for the matter temperature ($T = T_{\nu 0}$), which is unambiguously related to the above parameters of neutrino radiation. The physical formulation of the problem is based on the assumption that the optical thickness of the CPNS structure along the radius is rather small (semitransparency). Strictly speaking, this assumption can be checked upon numerically solving the problem, and this would demonstrate that the sought solution exists.

3. EQUATIONS OF NEUTRINO HYDRODYNAMICS FOR THE CPNS STRUCTURE

Below, we present four stationary (hereafter, we omit the prefix "quasi") equations of neutrino hydrodynamics for the spherically symmetric case, describing gravitational interaction in the simplest way—that is, in the Newton approximation and with allowance for only the internal PNS mass M_0 (this is the so-called Roche approximation for the case where the CPNS mass is disregarded). These equations are given in the usual order: the continuity equation for the baryon charge (n, p), the equation of motion, the equation for energy in the entropy form, and the equation for the lepton charge (e^-, e^+). Specifically, we have

$$\rho v = -\frac{\dot{M}_0}{4\pi r^2}, \tag{5}$$

$$v\frac{dv}{dr} + \frac{1}{\rho}\frac{dp}{dr} + \frac{GM_0}{r^2} = 0, \tag{6}$$

$$\frac{d}{dr}\left(\frac{E}{\rho}\right) + p\frac{d}{dr}\left(\frac{1}{\rho}\right) = \frac{H - C}{v}, \tag{7}$$

$$\frac{dY_e}{dr} = \frac{P - Q}{v}, \tag{8}$$

where $\rho = m_0(n_n + n_p)$ (m_0 is the atomic-weight unit on the $^{12}\mathrm{C} = 12$ scale) is the baryon density of matter; v is the hydrodynamic velocity; p is pressure; E is the internal-energy density; and Y_e is a specific lepton charge, $Y_e = (n_{e^-} - n_{e^+})/(n_n + n_p)$, which is unambiguously related to the ratio of the neutron and the proton concentration, $\theta = n_n/n_p$. By using these equations and the mandatory electric-neutrality condition $n_{e^-} - n_{e^+} = n_p$ for matter, we can derive the simple relations

$$Y_e = (1 + \theta)^{-1}, \quad n_p = \frac{\rho}{m_0}Y_e, \quad n_n = \frac{\rho}{m_0}(1 - Y_e). \tag{9}$$

Some comments on the set of Eqs. (5)–(8) are in order. By the matter density ρ, the continuity Eq. (5) implies the baryon density of matter—more precisely, its baryon charge. In Eq. (6) (the equation of motion), we have discarded small terms corresponding to momentum transfer from absorbed neutrinosphere ν and $\bar{\nu}$ to matter, since the relative contribution of this effect with respect to the energy transfer is about v/c, where there appears the velocity behind the ASW front, $|v| \ll |v_0|$—this relative contribution is indeed small since $|v|/c \ll 1$ (see Section 2). On the contrary, effects associated with the absorption of the aforementioned neutrinos are taken into account in Eqs. (7) and (8) (equations for energy and the lepton charge, respectively), where they are represented by the integral term H on the right-hand side of (7) and the integral term P on the right-hand side of (8). In addition to inverse β processes for neutrinosphere ν and $\bar{\nu}$, these equations allow for direct β processes induced by the intrinsic radiation of ν and $\bar{\nu}$ in CPNS matter. The corresponding integral terms are C in

(7) and Q in (8). The effects of inelastic neutrino–electron scattering are completely disregarded because their mathematical description is cumbersome; moreover, their order-of-magnitude estimate obviously does not exceed that of the absorption effect.[3] In passing, we note that, for the lepton charge Y_e defined above, Eq. (8) does not imply the disregard of the neutrino lepton charge—the equation is written exactly for the entire set of β processes. Only in the equation of state for matter—that is, in the equation relating p and E—will we neglect the contribution of the neutrino lepton charge (see Section 4 below).

In the explicit expressions for the above integral terms, the ultrarelativistic approximation is valid for the lepton component of matter. This approximation implies fulfillment of the strong inequalities $m_ec^2 \ll T \lesssim T_{\nu\mathrm{eff}}$ and $(m_n - m_p)c^2 = 2.53 m_ec^2 \ll T \lesssim T_{\nu\mathrm{eff}}$; of these, the second will suffice. In the ultrarelativistic approximation, these terms are explicitly given by

$$H = \frac{T_{\nu\mathrm{eff}}}{m_0}[(1-Y_e)W_{a'}^{(1)} + Y_eW_{b'}^{(1)}], \qquad (10)$$
$$C = \frac{T}{m_0}[Y_eW_a^{(1)} + (1-Y_e)W_b^{(1)}],$$

$$P = (1-Y_e)W_{a'}^{(0)} - Y_eW_{b'}^{(0)}, \qquad (11)$$
$$Q = Y_eW_a^{(0)} - (1-Y_e)W_b^{(0)},$$

where $W_i^{(k)}$ is the probability of β processes of the type i for $k = 0, 1$. Four β processes labeled with a', b', a, and b are spelled out as follows:

$$a':\ \nu + n \to e^- + p; \quad b':\ \bar\nu + p \to e^+ + n; \qquad (12)$$
$$a:\ e^- + p \to \nu + n; \quad b:\ e^+ + n \to \bar\nu + p.$$

In the ultrarelativistic approximation, this list obviously exhausts the entire variety of β processes involving free nucleons since the ordinary β decay of a neutron and the inverse three-particle β process have relatively small probabilities $W_i^{(k)}$, which are integrals within finite limits of about m_ec^2 (see below).[4] In accordance with (12), it is not difficult to understand why negative signs for the β processes b' and b appear in (11) instead of positive signs for the same processes in (10). Indeed, the emergence of positrons (b') reduces the quantity Y_e, while the disappearance of positrons (b), on the contrary, increases it. This corresponds to negative signs of P and Q if one considers that the quantity Q has a negative sign in Eq. (8). It is more straightforward to understand positive signs in relations (10), since H is associated with the heating of matter in the β process b', while C is associated with the cooling of matter in the β process b [see the corresponding signs in (7)]. Similar arguments applied to electrons in the β processes a' and a explain the corresponding signs in (11) and (10) and in (8) and (7). It can also be seen from (12) that the β processes a and a' are mutually inverse, and so are the β processes b and b'.

Further, we present the probabilities $W_i^{(k)}$, which are quantities integrated over the spectra of ν and $\bar\nu$ and which are proportional to the same matrix element for two free nucleons n and p that is expressed in terms of the free-neutron half-life—that is, in terms of $(ft)_{np}$. Specifically, we have

$$W_{a'}^{(k)} = W_0(r)\frac{\ln 2}{(ft)_{np}}\left(\frac{T_{\nu\mathrm{eff}}}{m_ec^2}\right)^5 \qquad (13)$$
$$\times \int_0^\infty \frac{x^{4+k}e^{-x}}{e^{-x} + e^{-\psi_{\nu\mathrm{eff}}}}\frac{1 + e^{-x\Delta_T + \psi}}{1 + e^{-x\Delta_T + \varphi}}dx,$$

$$W_{b'}^{(k)} = W_0(r)\frac{\ln 2}{(ft)_{np}}\left(\frac{T_{\nu\mathrm{eff}}}{m_ec^2}\right)^5$$
$$\times \int_0^\infty \frac{x^{4+k}e^{-x}}{e^{-x} + e^{\psi_{\nu\mathrm{eff}}}}\frac{1 + e^{-x\Delta_T - \psi}}{1 + e^{-x\Delta_T - \varphi}}dx;$$

[3] For the inelastic scattering of ν and $\bar\nu$ on e^- and e^+, there are well-known cross sections and even the mean energy transfer to degenerate ultrarelativistic electrons (see data in [5] and references therein). It can be shown that the ratio of the mean energy transfer in scattering processes to the energy transfer in absorption processes is less than 1/16 for all neutrino energies (here, the contribution of e^+ is disregarded against the contribution of e^-). Nevertheless, the inclusion of scattering processes in the description of neutrino radiation within a PNS and in the semitransparent CPNS layer is a problem of importance if the number of nuclides in the CPNS is sizable (compare with [9]). However, the inclusion of such processes would entail the violation of the condition $\psi_{\bar\nu\mathrm{eff}} = -\psi_{\nu\mathrm{eff}}$ since the chemical potentials of ν and $\bar\nu$ would then become independent parameters of the neutrinosphere [20], and this would render the problem in question more involved.

[4] All possible neutrino interactions with the matter of collapsing star cores were presented, for example, in the classic monograph of Fowler and Hoyle [21]. However, the emissivities of these processes were determined in [22]; this led to the conclusion that, under the physical conditions (characteristic temperatures and densities) of the collapse of star cores, URCA processes have much higher emissivities than all the remaining processes (see also [5]): $T > 10^9$ K and $\rho > 10^7$ g/cm^3. Although the additional condition that all β processes are in kinetic equilibrium (in going over to URCA processes) in matter transparent to neutrinos was adopted in those calculations, they can also be used to obtain rough estimates in the case where there is no such equilibrium. Upon taking into account Kirchhoff's law [11], a similar dominance is then obtained for the absorption of neutrino radiation in β processes. If necessary, specific corrections can be found upon solving the problem of the CPNS structure.

$$W_a^{(k)} = \frac{\ln 2}{(ft)_{np}}\left(\frac{T}{m_e c^2}\right)^5 \int_0^\infty \frac{x^{4+k}e^{-x}}{e^{-x}+e^{-\varphi}}dx, \quad (14)$$

$$W_b^{(k)} = \frac{\ln 2}{(ft)_{np}}\left(\frac{T}{m_e c^2}\right)^5 \int_0^\infty \frac{x^{4+k}e^{-x}}{e^{-x}+e^{\varphi}}dx.$$

The integral terms on the right-hand side of (13) include, in addition to the parameters $T_{\nu\text{eff}}$ and $\psi_{\nu\text{eff}}$ of neutrino radiation from the neutrinosphere, which are already known from (3), the dimensionless ratio $\Delta_T = T_{\nu\text{eff}}/T$, where T is the matter temperature at the point having the radius value of r, as well as ψ and φ, the dimensionless chemical potentials for neutrinos (ν) and electrons (e^-) at the same point; they are given by $\varphi = \mu_{e^-}/T$ and $\psi = \mu_\nu/T$ (analogously to the definition of $\psi_{\nu\text{eff}}$). From the condition of thermodynamic equilibrium for β processes [23], it follows that, in the ultrarelativistic approximation [24], the chemical potential ψ is related to the chemical potential for free nuclides by the simple equation

$$\psi = \varphi - \ln\left(\frac{1-Y_e}{Y_e}\right); \quad (15)$$

that is, it is unambiguously determined by the values of φ and Y_e at this point. It should be emphasized that relation (15) is valid for any nonequilibrium distribution of neutrino radiation (with respect to energies and with respect to angles), and this is a special feature of a CPNS. As a matter of fact, this statement identically reproduces the known conclusions from Kirchhoff's law in the case of nonequilibrium photon radiation [23]. The only difference is that, in the integrals on the right-hand side of (13), the quantity ψ arises owing to the effect of induced absorption caused by Fermi–Dirac statistics; in contrast, the Bose–Einstein statistics of photons leads to the effect of induced radiation (see the derivation below).

In the integral terms in (14), there remains only one function, φ, of the aforementioned local functions Δ_T, ψ, and φ, since they do not involve the effect of induced neutrino absorption [see (12)]; moreover, the properties of the neutrinosphere are immaterial here.

Finally, the additional factor $W_0(r)$ appears in relations (13) since, for the corresponding β processes a' and b' in (12), there is the effect of dilution of neutrino radiation from the neutrinosphere, which covers, at the point r, not the full solid angle of 4π but its part equal to $W_0(r)$ [for $r \to 0$, $W_0(r) \to 1/2$],

$$W_0(r) = \frac{1}{2}\left[1 - \left(1 - \frac{r_{\nu 0}^2}{r^2}\right)^{1/2}\right]. \quad (16)$$

The function $W_0(r)$ in (16) is referred to as the dilution factor. It takes into account an anisotropic (nonequilibrium) character of radiation from the neutrinosphere for $r > r_{\nu 0}$.

In order to explain the physical meaning of the integrands in (13), it is necessary to introduce the Fermi–Dirac intensities that characterize neutrino radiation for ν and $\bar\nu$ and which are in equilibrium with respect to the particle energies $\varepsilon_{\nu,\bar\nu}$ (this is an analog of the Planck intensity of photon radiation [11, 23] for the conditions of the neutrinosphere):

$$I_{\nu\text{eff}} = c\left(\frac{T_{\nu\text{eff}}}{ch}\right)^3 \frac{x^3}{1+\exp(x-\psi_{\nu\text{eff}})}, \quad (17)$$

$$I_{\bar\nu\text{eff}} = c\left(\frac{T_{\nu\text{eff}}}{ch}\right)^3 \frac{x^3}{1+\exp(x+\psi_{\nu\text{eff}})}.$$

Here, $x = \varepsilon_{\nu,\bar\nu}/T_{\nu\text{eff}}$ stands for the dimensionless ν, $\bar\nu$ energies, while $\psi_{\bar\nu\text{eff}} = -\psi_{\nu\text{eff}}$, as was indicated for relation (3), which is obtained from relations (17) on the basis of the general definition of the density of the radiation-energy flux; that is,

$$F_{\nu\bar\nu} = 2\pi \int_0^1 \mu d\mu \int_0^\infty (I_{\nu\text{eff}}d\varepsilon_\nu + I_{\bar\nu\text{eff}}d\varepsilon_{\bar\nu}) \quad (18)$$

$$= \pi T_{\nu\text{eff}} \int_0^\infty (I_{\nu\text{eff}} + I_{\bar\nu\text{eff}})dx$$

$$= \frac{\pi c}{(ch)^3} T_{\nu\text{eff}}^4 [F_3(\psi_{\nu\text{eff}}) + F_3(-\psi_{\nu\text{eff}})],$$

where the third-order Fermi–Dirac functions appear in the bracketed expression. According to [25], the sum of these functions can be expressed in terms of elementary algebraic functions as

$$F_3(y) + F_3(-y) = \frac{1}{4}\left(y^4 + 2\pi^2 y^2 + \frac{7\pi^4}{15}\right). \quad (19)$$

As might have been expected, relation (3) is obtained upon the substitution of (19) into (18). This is a corollary of Fermi–Dirac statistics, but with allowance for the helicities of the particles ν and $\bar\nu$. This is the reason why the original expressions (17) for the intensity do not involve the factor of 2, which appears in the Planck expression for the photon intensity upon taking into account two states of photon polarization.

Further, it is obvious that, with the aid of expressions (17), one can similarly calculate the specific power of heating of matter or the neutrino-energy deposition H from (7) at any CPNS point having a radius value in the region $r > r_{\nu 0}$, provided that the semitransparency condition is satisfied, which means that the losses of this energy are rather small. To do this, each of the intensities $I_{\nu\text{eff}}$ and $I_{\bar\nu\text{eff}}$ must be multiplied by the corresponding linear coefficient of absorption, $\tilde k_\nu$ or $\tilde k_{\bar\nu}$, and by the dilution factor $W_0(r)$

from (16) and divided by the matter density ρ. The result is

$$H = W_0(r)\frac{1}{\rho}\int_0^\infty (\tilde{k}_\nu I_{\nu\text{eff}}\, d\varepsilon_\nu + \tilde{k}_{\bar\nu} I_{\bar\nu\text{eff}}\, d\varepsilon_{\bar\nu}) \qquad (20)$$
$$= H_{a'} + H_{b'},$$

where the notation for the quantity H is introduced for the processes a' and b' in (12) individually.

Below, we will derive an expression for the probability $W_{a'}^{(1)}$ in (13) for the β process a' (the derivation of the corresponding expression for $W_{b'}^{(1)}$ is similar). Prior to doing this, we recast the expressions for the coefficients $\tilde{k}_\nu$ and $\tilde{k}_{\bar\nu}$ into a form corrected for the induced-absorption effect, a consequence of the Fermi–Dirac statistics of ν and $\bar\nu$ [11, 23] (the tilde labels over the symbols for the "atomic" coefficients k_ν and $k_{\bar\nu}$ denote the presence of these corrections):

$$\tilde{k}_\nu = k_\nu[1+\exp(\psi - \Delta_T x)], \qquad (21)$$
$$\tilde{k}_{\bar\nu} = k_{\bar\nu}[1+\exp(-\psi - \Delta_T x)].$$

Since the local equilibrium chemical potentials ν and $\bar\nu$ ($\psi_{\bar\nu} = -\psi_\nu \equiv -\psi$) appear in (21), the quantity ψ is defined in just the same way as in (15), while $\Delta_T = T_{\nu\text{eff}}/T$ and $x = \varepsilon_{\nu,\bar\nu}/T_{\nu\text{eff}}$, as was in (17). For the ensuing calculation of the quantity $H_{a'}$, we use the coefficient $\tilde{k}_\nu$ from (21).

The atomic coefficient k_ν is borrowed from the derivation of the equivalent neutrino range with respect to the absorption process a' in [11] for an arbitrary set of nuclides (a more detailed validation is given in [26], but it relies only on the elementary Fermi theory of β processes [27]):

$$k_\nu = l_\nu^{-1} = \frac{\sigma_0}{m_0}\frac{\rho\theta}{1+\theta}\frac{\varepsilon_\nu^2}{(m_e c^2)^2} \qquad (22)$$
$$\times\left[1 - \frac{1}{1+\exp(-\varphi + \Delta_T x)}\right].$$

$$\sigma_0 = \frac{1}{4\pi c}\left(\frac{h}{m_e c}\right)^3 \frac{\ln 2}{(ft)_{np}}.$$

Here, the bracketed expression also involves the enhancement factor for the range l_ν; it arises upon taking into account the Pauli exclusion principle for electrons originating from the process a'. Substituting the coefficient $\tilde{k}_\nu$ specified by Eqs. (21) and (22) and the intensity $I_{\nu\text{eff}}$ from (17) and taking into account (9), we obtain, after some simple algebra, the following expression for $H_{a'}$ from (20):

$$H_{a'} = W_0(r)(1-Y_e)\frac{T_{\nu\text{eff}}}{m_0}\left(\frac{T_{\nu\text{eff}}}{m_e c^2}\right)^5 \frac{\ln 2}{(ft)_{np}}$$
$$\times\int_0^\infty \frac{x^5\exp(-x)}{\exp(-x)+\exp(-\psi_{\nu\text{eff}})}\frac{1+\exp(-\Delta_T x+\psi)}{1+\exp(-\Delta_T x+\varphi)}dx.$$

Apart from a change in the notation in the exponentials, this is just the first term in (10) with $W_{a'}^{(1)}$ from (13) for the case of $k=1$. From the above derivation, it is clear that, if we make the substitutions $n_n \to n_p$, $\nu \to \bar\nu$, and $e^- \to e^+$ for the process b', we obtain precisely the second term, $H_{b'}$, in (10), since the only difference between this formula and the last expression for $H_{a'}$ is that the signs of the chemical potentials $\psi_{\nu\text{eff}}$, ψ, and φ are reversed. Thus, the derivation of the formula including all contributions to the quantity H from Eq. (10) is completed.

Further, we consider relations (14) for the quantities $W_a^{(1)}$ and $W_b^{(1)}$ appearing in the expression for the specific power of cooling C from (10). The expression for C can be obtained by means of a simple generalization of the known Fermi formulas for the β decay of a neutron [27], but without the inclusion of the Coulomb factors in the case of free nucleons {see a compilation of such expressions for arbitrary nuclides (A, Z) in [5]}. It can easily be shown that, upon going over to the ultrarelativistic approximation for e^- and e^+, simple integral expressions for C_a and C_b can be derived from (14) by using the representation $C = C_a + C_b$ in (10).

It only remains to derive explicit expressions for P and Q from (11). They can be obtained by substituting the expressions for $W_i^{(0)}$ from (13) and (14) into (11). First, we express the specific lepton charge Y_e in terms of the difference of the concentrations of e^- and e^+ [23] in the ultrarelativistic case as well; in doing this, we consider that the difference of the second-order Fermi–Dirac functions satisfies the identity [25]

$$F_2(y) - F_2(-y) = \frac{1}{3}(y^3 + \pi^2 y). \qquad (23)$$

For the specific lepton charge, we then obtain

$$Y_e = \frac{m_0}{\rho}\frac{8\pi T^3}{(ch)^3} \qquad (24)$$
$$\times\left[\int_0^\infty \frac{x^2 dx}{1+\exp(x-\varphi)} - \frac{x^2 dx}{1+\exp(x+\varphi)}\right]$$
$$= \frac{8\pi m_0}{(ch)^3}\frac{T^3}{\rho}[F_2(\varphi) - F_2(-\varphi)]$$
$$= \frac{8\pi m_0}{3(ch)^3}\frac{T^3}{\rho}(\varphi^3 + \pi\varphi).$$

In deriving the expression for $W_i^{(0)}$, it is necessary, in accordance with the definition of the quantity Y_e

in (24), to reduce the power of the factor x by unity in all integrands previously appearing in expression (20) for H and in C (see above)—that is, to go over from $W_i^{(1)}$ to $W_i^{(0)}$—and to multiply these preceding expressions by the dimensional factors $m_0/T_{\nu\text{eff}}$ and m_0/T in the case of H and C, respectively. We then obtain precisely the required explicit expressions for P and Q from (11) if we take into account the reversal of the signs of their terms, which was explained above.

Thus, the set of Eqs. (5)–(8) of neutrino hydrodynamics and relations (10) and (11) for its integral terms, together with their explicit expressions (13) and (14), have been completely derived. They are supplemented with relations (15), (16), and (24), so that the problem of the CPNS structure reduces to determining four independent functions of the radius r—for example, ρ, v, T, and φ—by numerically solving the four Eqs. (5)–(8). However, we rely here on the well-known fact that all thermodynamic quantities, including pressure (p) and the internal-energy density (E), can be unambiguously expressed in terms of three thermodynamic functions ρ, T, and φ mentioned above. It should be noted that, in contrast to the usual case of thermodynamics for systems involving a constant number of particles, we apply here thermodynamics for a variable number of particles [23]—specifically, for the case where the lepton charge is variable [28]. In the next section, we choose equations of state.

4. EQUATIONS OF STATE OF MATTER IN A CPNS

In the Boltzmann approximation (nondegenerate and nonrelativistic) chosen here for the gas of free nucleons and the ultrarelativistic approximation for the Fermi–Dirac gases of electrons and positrons, we can immediately write the corresponding expressions for the quantities p and E as the sums of the aforementioned components:

$$E = E_{\text{nucl}} + E_{\text{urel}}, \quad p = \frac{2}{3}E_{\text{nucl}} + \frac{1}{3}E_{\text{urel}}, \quad (25)$$

$$E_{\text{nucl}} = \frac{3}{2}\frac{\rho_0}{m_0}T,$$

$$E_{\text{urel}} = \frac{2\pi T^4}{(ch)^3}\left(\varphi^4 + 2\pi^2\varphi^2 + \frac{11\pi^4}{15}\right).$$

The simplicity of the equation of state for nucleons (E_{nucl} and p_{nucl}) requires no comments (maybe, it is only reasonable to indicate that, in this expression, we neglect the difference of the n and p masses, which is slightly above 1%). For the lepton component of matter (E_{urel}, p_{urel}), we used identity (19) and took into account the additive correction arising owing to the contribution of equilibrium photon radiation. This is the term $4\pi^4/15$ in the parenthetical expression appearing in the formula for E_{urel}. As might have been expected, one does indeed have

$$E_\gamma = \Delta E_{\text{urel}} = \frac{2\pi T^4}{(ch)^3}\frac{4\pi^4}{15} = \frac{8\pi^5}{15(ch)^3}T^4 = a^*T^4,$$

where $a^* = 4\sigma^*_{\text{SB}}/c$ is the known radiation constant [see Eq. (4)]. It should be noted that, upon the subtraction of the correction E_γ, these formulas naturally coincide in form with the corresponding formulas for neutrino radiation, the chemical potentials being of course different, as well as the effects of photon polarization and neutrino helicities (see Section 6 below) [24].

Of particular importance among thermodynamic functions for matter is entropy, for which we present, without a detailed derivation, an expression in the form of the specific entropy density

$$S = S_n + S_p + S_{e^-} + S_{e^+} + S_\gamma, \quad (26)$$

which, by definition, is an additive quantity for a mixture of ideal gases. Here, the sum

$$S_n + S_p = \frac{k_{\text{B}}}{m_0}\left(\frac{5}{2} + \ln\left[\frac{2m_0}{\rho}\left(\frac{2\pi m_0 T}{h^2}\right)^{3/2}\right]\right) \quad (27)$$

$$- \frac{k_{\text{B}}}{m_0}[Y_e \ln Y_e + (1 - Y_e)\ln(1 - Y_e)]$$

is the total entropy of free nucleons, which includes an additional term owing to a nonequilibrium mixture of n and p [with allowance for (9)], and

$$S_{e^-} + S_{e^+} + S_\gamma = \frac{8\pi}{3}\frac{k_{\text{B}}}{(ch)^3}\frac{T^3}{\rho}\left(\pi^2\varphi^2 + \frac{11\pi^4}{15}\right). \quad (28)$$

Expression (28) has a rather simple form owing to the use of the identities in (19) and (23).

It can be shown that the specific entropy density S satisfies the thermodynamic identity

$$TdS = dE - \frac{p}{\rho^2}d\rho + \frac{T}{m_0}\left[\ln\left(\frac{1 - Y_e}{Y_e}\right) - \varphi\right]dY_e, \quad (29)$$

which is of crucial importance in statistical physics and which involves the quantities E and p from (25) and the quantity Y_e from (24). The point is that only if the identity in (29) is valid are the equations of state correct [23]. It should be recalled that only the first two terms appear on the right-hand side of (29) for the thermodynamics of systems involving a constant number of particles. Obviously, the physical meaning of the identity in question is the following: the quantity obtained by dividing the sum of the three terms on its right-hand side by temperature is the total differential

of a function—it is referred to as the differential of the specific entropy density.

5. EXTERNAL BOUNDARY CONDITIONS: CHOICE OF BOUNDARY CONDITIONS FOR A CPNS

The formulation of boundary conditions for the set of Eqs. (5)–(8), which describes the CPNS structure in the form of the spherical layer $r_{\nu 0} \le r \le r_{\rm sw}$, is of paramount importance. Qualitatively, such boundary conditions have already been outlined in Section 2 as some features of the spherical ASW front of radius $r_{\rm sw}$ from the exterior and of the PNS surface of given radius $r_{\nu 0}$ from the interor. The formulation of boundary conditions that is given below is not the only possibility for the problem of the CPNS structure, but it is at least mathematically correct and physically justified. We will show from the outset that the radius $r_{\rm sw}$, which is the only free parameter, must be determined in solving the boundary-value problem in question.

Indeed, the well-known Hugoniot conditions at the ASW front, which is immobile in a stationary problem, reduce, in a spherically symmetric coordinate frame, to four algebraic equations (conservation laws for the mass-, momentum-, energy-, and lepton-charge-flux densities) for determining four unknown quantities, $\rho_{\rm sw}$, $T_{\rm sw}$, $\varphi_{\rm sw}$, and $v_{\rm sw}$, according to the definitions of v_0 and ρ_0 in relations (1) and (2), respectively, provided that the ASW radius $r = r_{\rm sw}$ is specified. The quantities behind the shock-wave front are equipped with the index "sw." This means that the set of ordinary first-order differential Eqs. (5)–(8) is unambiguously solved for all four functions ρ, v, T, and φ of the radius, which have already been chosen with allowance for (25). At the internal boundary—that is, at a preset radius $r_{\nu 0}$—all of the above functions will then take uniquely defined values $\rho_{\nu 0}$, $v_{\nu 0}$, $T_{\nu 0}$, and $\varphi_{\nu 0}$. On the other hand, all these physical quantities at the neutrinosphere must be, strictly speaking, continuously matched with the corresponding PNS quantities. The point is that the only change in the equations of state for PNS matter in relation to expressions (25) is that the additive contributions of the neutrino equilibrium components are taken into account in the terms $P_{\rm urel}$ and $E_{\rm urel}$,

$$\Delta E_{\rm urel} = \frac{\pi}{(ch)^3} T_{\nu 0}^4 \left(\psi_{\nu 0}^4 + 2\pi^2 \psi_{\nu 0}^2 + \frac{7\pi^4}{15} \right),$$

$$\Delta P_{\rm urel} = \frac{1}{3} \Delta E_{\rm urel},$$

but, as a rule, $\Delta E_{\rm urel}$ is considerably less than the quantity $E_{\rm urel}$ from (25) [7, 24]; therefore, they can be disregarded in practical calculations. Among the necessary continuity conditions for four physical quantities at $r = r_{\nu 0}$, preference should be given, on the basis of physical considerations, to the continuity condition for the temperature $T_{\nu 0}$, since the ν, $\bar{\nu}$ energy flux $F_{\nu,\bar{\nu}}$ (3), which was actually taken into account in the integral terms H and P from (10) and (11), respectively, exhibits the strongest dependence precisely on the temperature at the neutrinosphere. It is this continuity condition that will be treated in the following as the main internal boundary condition, the only one at $r = r_{\nu 0}$; it can be satisfied by appropriately choosing the ASW radius $r_{\rm sw}$. In view of this, the quantity $r_{\rm sw}$ is assigned here the mathematical meaning of an eigenvalue of the problem of the CPNS structure.

We now proceed to formulate a specific external boundary condition—that is, the Hugoniot conditions at the ASW front. As was mentioned in the Introduction, the shock waves involved are assumed to be hydrodynamically strong; therefore, the quantities v_0 and ρ_0 are sufficient for determining the mass-, momentum-, and energy-flux densities. In (1) and (2), these quantities are preset in the approximation of a free (steady-state) fall of matter consisting of nuclides of the iron peak of elements. It should also be noted that a rigorous solution to the problem of the accretion of a cold iron gas (with allowance for back pressure) yields velocities of fall near the PNS surface that are less than the free-fall velocity (1) only by a few percent [29]. Thus, the quantities v_0 and ρ_0 are taken to be specified by relations (1) and (2) at constant parameters M_0 and $\dot{M}_0$ (see Section 1) and the parameter $r_{\rm sw}$ treated as an eigenvalue of the problem.

One may dispense with considering a formidable chain of nuclear reactions resulting in the dissociation of iron-peak nuclides into free nucleons, assuming that these reactions proceed, as was indicated in Section 2, within the internal structure of the ASW front, whose width, as is known, is disregarded in the Hugoniot conditions [13]. These conditions must include a constant value of the specific energy of dissociation of iron-peak nuclides into free nucleons. If the most typical nuclide $^{56}_{26}$Fe is taken for some averaged nuclide of the iron peak, this energy is $\varepsilon_0 = 8.80$ MeV $= 1.28 \times 10^{-5}$ erg per nucleon. According to the arguments presented in Section 2, the specific lepton charge in front of the ASW front—it is obviously $Y_{e0} = 26/56 = 0.464$—will have the same value behind the front, $Y_{e\rm sw} = Y_{e0}$. It should be emphasized that, although the above assumptions on nuclear processes within the ASW front seem rather rough, they do not lead to sizable quantitative errors in the problem of the CPNS structure.

Finally, we write all four Hugoniot conditions (relations) [13] in a form that is convenient for a further consideration. We have

$$v_{\rm sw} = v_0 \frac{\rho_0}{\rho_{\rm sw}}, \tag{30}$$

$$T_{\rm sw} = \frac{m_0}{3} v_0^2 \left[\left(1 - \frac{\rho_0}{\rho_{\rm sw}}\right)\left(7\frac{\rho_0}{\rho_{\rm sw}} - 1\right) + \frac{2\varepsilon_0}{m_0 v_0^2} \right], \tag{31}$$

$$\frac{2}{3} E_{\rm nucl\,sw} + \frac{1}{3} E_{\rm urel\,sw} = \rho_0 v_0^2 \left(1 - \frac{\rho_0}{\rho_{\rm sw}}\right), \tag{32}$$

$$Y_{e\rm sw} = Y_{e0}, \tag{33}$$

where $E_{\rm nucl\,sw} \equiv E_{\rm nucl}(r_{\rm sw})$, $E_{\rm urel\,sw} \equiv E_{\rm urel}(r_{\rm sw})$, $T_{\rm sw} \equiv T(r_{\rm sw})$, and $\rho_{\rm sw} \equiv \rho(r_{\rm sw})$. It should be noted that the equations of state (25) were used in relations (31) and (32); in addition, $Y_{e\,\rm sw} \equiv Y_e(r_{\rm sw})$ in (33) and $v_{\rm sw} \equiv v(r_{\rm sw})$ in (30). The set of algebraic Eqs. (30)–(33) is indeed necessary and sufficient for determining the quantities $\rho_{\rm sw}$, $T_{\rm sw}$, $\varphi_{\rm sw}$, and $v_{\rm sw}$ if we take into account the equations of state (25) and the definition of the specific lepton charge in (24). It should be noted that, in fact, relation (31) is a combination of the first three Hugoniot conditions (according to the above listing) such that the temperature $T_{\rm sw}$ is explicitly expressed only in terms of the density $\rho_{\rm sw}$ [apart from the constants m_0 and ε_0 (see above) and the quantities v_0 and ρ_0 from (1) and (2) in front of the ASW front]. In what is concerned with relations (32) and (33), we can additionally state that, together with the condition for the density of the baryon-mass flux (30), they serve as the Hugoniot conditions for the densities of the momentum flux and the specific-lepton-charge flux.

6. INTERNAL BOUNDARY CONDITIONS FOR A CPNS

The neutrinosphere temperature $T_{\nu 0}$ can be unambiguously expressed in terms of the effective neutrino-radiation temperature $T_{\nu\rm eff}$, because the relation between these temperatures must satisfy the mixed boundary condition at the external PNS boundary [11]. This condition also includes the corresponding neutrino-radiation chemical potentials $\psi_{\nu 0}$ and $\psi_{\nu\rm eff}$. In turn, $T_{\nu\rm eff}$ and $\psi_{\nu\rm eff}$ completely determine the intensity of neutrino radiation from the PNS surface [see Eq. (17)] and the energy-flux density $F_{\nu\bar\nu}$ from (3). The physical meaning of the above boundary condition is that it requires the vanishing of the densities of the unidirectional fluxes of the ν and $\bar\nu$ energy and lepton charge from outside to the neutrinosphere, while the boundary condition itself is a generalization of the well-known mixed boundary condition for radiation hydrodynamics at the boundary with a vacuum, the latter being of crucial importance in the traditional hydrodynamic theory of supernova explosions [5] and in the theory of controlled thermonuclear fusion [30]. According to [11, 26], the conditions in question for neutrinos are given by

$$-\frac{c}{4} U_{\nu\bar\nu} + \frac{1}{2} F_{\nu\bar\nu} = 0, \quad -\frac{c}{4} n_{\nu\bar\nu} + \frac{1}{2} \Lambda_{\nu\bar\nu} = 0, \tag{34}$$

where $U_{\nu\bar\nu}$ is the ν, $\bar\nu$ energy density; $n_{\nu\bar\nu}$ is the ν, $\bar\nu$ lepton-charge density; and $F_{\nu\bar\nu}$ and $\Lambda_{\nu\bar\nu}$ are, respectively, the neutrino-energy-flux density [see Eq. (3)] and the density of the flux of ν, $\bar\nu$ lepton charge. The first two quantities involved, $U_{\nu\bar\nu}$ and $n_{\nu\bar\nu}$, are obviously expressed in terms of the local neutrino-radiation intensities $I_{\nu 0}$ and $I_{\bar\nu 0}$ [which are analogous to those in (17)] as

$$\begin{aligned} U_{\nu\bar\nu} &= \frac{2\pi}{c} \int\limits_{-1}^{1} d\mu \int\limits_{0}^{\infty} (I_{\nu 0} d\varepsilon_\nu + I_{\bar\nu 0} d\varepsilon_{\bar\nu}) \\ &= \frac{4\pi T_{\nu 0}^4}{(ch)^3} [F_3(\psi_{\nu 0}) + F_3(-\psi_{\nu 0})] \\ &= \frac{\pi T_{\nu 0}^4}{(ch)^3} \left(\psi_{\nu 0}^4 + 2\pi^2 \psi_{\nu 0}^2 + \frac{7\pi^4}{15}\right), \end{aligned} \tag{35}$$

$$\begin{aligned} n_{\nu\bar\nu} &= 2\pi \int\limits_{-1}^{1} d\mu \int\limits_{0}^{\infty} \left(\frac{I_{\nu 0}}{\varepsilon_\nu} d\varepsilon_\nu - \frac{I_{\bar\nu 0}}{\varepsilon_{\bar\nu}} d\varepsilon_{\bar\nu}\right) \\ &= \frac{4\pi T_{\nu 0}^3}{(ch)^3} [F_2(\psi_{\nu 0}) - F_2(-\psi_{\nu 0})] \\ &= \frac{4\pi T_{\nu 0}^4}{3(ch)^3} (\psi_{\nu 0}^3 + \pi^2 \psi_{\nu 0}). \end{aligned} \tag{36}$$

The derivation of formulas (35) and (36) involved, in addition to substituting the local temperature $T_{\nu 0}$ and the local chemical potential $\psi_{\nu 0}$ [formally instead of $T_{\nu\rm eff}$ and $\psi_{\nu\rm eff}$ in expressions (17)] into the expressions for the local ($r = r_{\nu 0}$) equilibrium neutrino-radiation intensities $I_{\nu 0}$ and $I_{\bar\nu 0}$, using identities (19) and (23). It should be noted that the local intensities $I_{\nu 0}$ and $I_{\bar\nu 0}$ also include diffusion corrections of order μ, which are generally not small at the PNS boundary, but which vanish upon integration over a full solid angle [see integration with respect to μ in (35) and (36)] [26]. The other two quantities appearing in the boundary conditions (34), $F_{\nu\bar\nu}$ and $\Lambda_{\nu\bar\nu}$, are expressed, on the contrary, in terms of the effective values $T_{\nu\rm eff}$ and $\psi_{\nu\rm eff}$, as was done in (3) for $F_{\nu\bar\nu}$. Similarly to $F_{\nu\bar\nu}$, the flux $\Lambda_{\nu\bar\nu}$ can be expressed in

terms of the intensities $I_{\nu\mathrm{eff}}$ and $I_{\bar{\nu}\mathrm{eff}}$ from (17) as

$$\Lambda_{\nu\bar{\nu}} = 2\pi \int_0^1 \mu d\mu \int_0^\infty \left(\frac{I_{\nu\mathrm{eff}}}{\varepsilon_\nu} d\varepsilon_\nu - \frac{I_{\bar{\nu}\mathrm{eff}}}{\varepsilon_{\bar{\nu}}} d\varepsilon_{\bar{\nu}} \right)$$

and is further calculated in the same way as $n_{\nu\bar{\nu}}$ in (36). As a result, we obtain [for the sake of completeness, we also reproduce formula (3) for $F_{\nu\bar{\nu}}$]

$$F_{\nu\bar{\nu}} = \frac{\pi}{4} \frac{c}{(ch)^3} T_{\nu\mathrm{eff}}^4 \left(\psi_{\nu\mathrm{eff}}^4 + 2\pi^2 \psi_{\nu\mathrm{eff}}^2 + \frac{7\pi^4}{15} \right),$$

$$\Lambda_{\nu\bar{\nu}} = \frac{\pi}{3} \frac{c}{(ch)^3} T_{\nu\mathrm{eff}}^3 (\psi_{\nu\mathrm{eff}}^3 + \pi^2 \psi_{\nu\mathrm{eff}}). \qquad (37)$$

Upon substituting formulas (35) and (3) into the first boundary condition in (34) and formulas (36) and (37) into the second boundary condition there, we derive the explicit expressions for the internal boundary condition (34); that is,

$$T_{\nu 0}^4 \left(\psi_{\nu 0}^4 + 2\pi^2 \psi_{\nu 0}^2 + \frac{7\pi^4}{15} \right) \qquad (38)$$

$$= \frac{1}{2} T_{\nu\mathrm{eff}}^4 \left(\psi_{\nu\mathrm{eff}}^4 + 2\pi^2 \psi_{\nu\mathrm{eff}}^2 + \frac{7\pi^4}{15} \right),$$

$$T_{\nu 0}^3 (\psi_{\nu 0}^3 + \pi^2 \psi_{\nu 0}) = \frac{1}{2} T_{\nu\mathrm{eff}}^3 (\psi_{\nu\mathrm{eff}}^3 + \pi^2 \psi_{\nu\mathrm{eff}}).$$

This set of two algebraic equations can be solved for the temperature $T_{\nu 0}$ (since the ratio $\xi = \psi_{\nu 0}/\psi_{\nu\mathrm{eff}}$ of the chemical potentials depends only on the potential $\psi_{\nu\mathrm{eff}} \equiv \eta$) according to the equation

$$\frac{\xi^4 \eta^4 + 2\pi^2 \xi^2 \eta^2 + \frac{7\pi^4}{15}}{\xi^4 \left(1 + \frac{\pi^2}{\xi^2 \eta^2} \right)^{4/3}} = 2^{1/3} \frac{\eta^4 + 2\pi^2 \eta^2 + \frac{7\pi^4}{15}}{\left(1 + \frac{\pi^2}{\eta^2} \right)^{4/3}}. \qquad (39)$$

The only positive root of Eq. (39) has the following typical values: $\xi = 0.84$ at $|\eta| = 0$, $\xi = 0.79$ at $|\eta| = 1$, and $\xi(|\eta|) = 4.1/|\eta|$ for $|\eta| \to \infty$ (at $|\eta| \geq 10$). For this root of Eq. (39), the dependence $\xi(|\eta|)$ is refined by numerically solving this equation. Thus, the internal boundary condition literally corresponding to the first relation in (38) has the form

$$T_{\nu 0}^4 = \frac{T_{\nu\mathrm{eff}}^4}{2} \left(1 + \frac{30}{7\pi^2} \psi_{\nu\mathrm{eff}}^2 + \frac{15}{7\pi^4} \psi_{\nu\mathrm{eff}}^4 \right) \qquad (40)$$

$$\times \left(1 + \frac{30}{7\pi^2} \xi^2 \psi_{\nu\mathrm{eff}}^2 + \frac{15}{7\pi^4} \xi^4 \psi_{\nu\mathrm{eff}}^4 \right)^{-1},$$

which involves the chemical-potential ratio ξ equal to the above root of Eq. (39), $\xi = \xi(|\psi_{\nu\mathrm{eff}}|) \equiv \xi(|\eta|)$. From (40), it can be seen that, at $\psi_{\nu\mathrm{eff}} = 0$, $T_{\nu 0} = 2^{-1/4} T_{\nu\mathrm{eff}}$, which is the well-known result arising in radiation hydrodynamics if use is made of a mixed boundary condition of the type in (34). It is interesting to note that the above relation between the local and the effective temperature is valid both for photons and for neutrinos despite the distinction between the equilibrium energy fluxes, which was highlighted in discussing formula (3) and which is due to the difference in statistics they obey (this is reflected in the coefficient 7/8 for neutrinos). It is straightforward to verify that the same coefficient also appears in the expression for the equilibrium energy density $U_{\nu\bar{\nu}}$ from (35). This occurs because, in the first condition in (34)—it directly leads to (40)—the two terms involved have the same coefficient (according to the aforesaid). In the general case of $\psi_{\nu\mathrm{eff}} \neq 0$, the temperature ratio $T_{\nu 0}/T_{\nu\mathrm{eff}}$ increases monotonically up to unity at $|\eta| \simeq 5$, formally becoming indefinitely large for $|\eta| \to \infty$. Nevertheless, only moderately small values of $|\psi_{\nu\mathrm{eff}}| \lesssim 1$ (see Section 2) are of interest for the theory of PNSs; therefore, the effect of changes in this ratio proves to be insignificant—at $|\psi_{\nu\mathrm{eff}}| = 1$, the coefficient 0.57 appears on the right-hand side of the internal boundary condition (40) instead of 0.5. However, it should be emphasized that, in the general case of $|\psi_{\nu\mathrm{eff}}| \neq 0$, the effect of the Fermi–Dirac statistics of ν, $\bar{\nu}$ radiation is consistently taken into account in this condition [and in Eq. (39) as well].

As to the mixed boundary condition (34), which leads to condition (40) we are interested in, the following comment is strictly speaking in order. In accordance with the physical meaning of (34), effects of intrinsic neutrino radiation are disregarded in this formulation of the problem. Such effects seem small in view of the smallness of the CPNS optical thickness, but an analysis of similar problems in radiation hydrodynamics reveals [30] that the problem associated with disregarding them is nontrivial. It is possible to validate the absence of the self-absorption of intrinsic radiation in the semitransparent layer [this was actually used in Eqs. (7) and (8)], but effects associated with the heating of the nontransparent sphere by intrinsic neutrino radiation can become sizable. With allowance for the comprehensible dependence on the smallness of the optical thickness of the layer, it would be straightforward to include these feedback effects in our consideration quantitatively—in particular, by substituting, into the expression on the right-hand side of the first condition in (34), the term $\Delta F_{\nu\bar{\nu}}$ representing the additional (inverse) heating for the density of the unidirectional energy flux; that is,

$$\Delta F_{\nu\bar{\nu}} = -\frac{1}{r_{\nu 0}^2} \int_{r_{\nu 0}}^{r_{\mathrm{sw}}} \rho(r) C(r) W_0(r) r^2 dr, \qquad (41)$$

where the specific radiation power $C(r) \equiv C$ is defined in (10) [it also appears in (7)], the dilution factor

$W_0(r)$ is defined in (16), and integration is performed over the entire thickness of the CPNS. It is obvious that, quantitatively, the smallness of the effects being discussed would imply $(2\Delta F_{\nu\bar{\nu}}/F_{\nu\bar{\nu}}) \ll 1$, which can be verified in solving the problem of the CPNS structure. However, the inclusion of effects like those that are specified by Eq. (41) would break down the basic strategies adopted in formulating the problem in question, which were outlined in Sections 1 and 2 and which were based on disregarding any feedback CPNS effects on the interior PNS and on the exterior accreting flux of the iron gas from the remnants of the iron core of a star. All such feedback CPNS effects, including both those that were mentioned above (effects of a finite CPNS mass and of the mass influx to the PNS or an additional heating of the PNS neutrinosphere) and those that were not mentioned (for example, CPNS-induced distortions of the blackbody spectrum of the neutrinosphere), can be properly taken into account only within the complete nonstationary multidimensional problem of neutrino hydrodynamics, where it is of course meaningless to isolate the problem of a CPNS.

The above investigation of the internal boundary condition at the PNS neutrinosphere can be briefly summarized as follows. In contrast to what occurs in the complete hydrodynamic problem, where all physical quantities are continuous everywhere (with the exception of shock-wave fronts)—that is, at any value of the radius r—the stationary (quasistationary) model of a CPNS is formulated here in such a way that the neutrino-hydrodynamics Eqs. (5)–(8) themselves dictate the necessary and sufficient set of boundary conditions, which includes the only internal boundary condition (40); for this, we have taken here the condition of continuity of the matter temperature in the layer at the neutrinosphere, $T(r_{\nu 0}) \equiv T_{\nu 0}$, where $T_{\nu 0}$ is the local temperature of this surface—it is unambiguously related to the neutrino-radiation parameters $T_{\nu\mathrm{eff}}$ and $\psi_{\nu\mathrm{eff}}$ according to the mixed boundary condition (34). In turn, these parameters are determined by the neutrino emissivity $L_{\nu\bar{\nu}} = 4\pi r_{\nu 0}^2 F_{\nu\bar{\nu}}$ and the radius $r_{\nu 0}$ of a PSN, which are its global properties.

7. CONCLUSION

Thus, the physicomathematical model constructed here for the neutrino crown of a protoneutron star (CPNS) includes the set of ordinary differential Eqs. (5)–(8); the additional relations (10), (11), (13), and (14), which specify integral terms representing the interaction of matter with neutrino radiation; and the auxiliary relations (15), (16), and (24), which express the quantities ψ, W_0, and Y_e in terms of the functions ρ, v, T, and φ taken to be basic features of the problem being considered. Of course, the equations of state of CPNS matter, which are given by relations (25), must be taken into account in this formulation of the problem. For the boundary conditions adopted here, which were formulated, at the external boundary (ASW front), on the basis of the Hugoniot conditions (30)–(33) and, at the internal boundary (surface of the PNS neutrinosphere), on the basis of the condition of continuity for temperature [see Eq. (40)] with allowance for Eq. (39), the problem of the CPNS structure must have an unambiguous numerical solution. These boundary conditions are necessary and sufficient for the numerical solution in question to be dependent only on the preset parameters M_0, $\dot{M}_0$, $T_{\nu\mathrm{eff}}$, $\psi_{\nu\mathrm{eff}}$, and $r_{\nu 0}$. The ASW radius r_{sw} is an eigenvalue of the problem and is found in solving this problem. It should also be emphasized that the solution exists in a specific region of the aforementioned parameters of the problem.

Some simplifications made in the physical formulation of the problem were critically discussed in the main body of the article. Of these, many can easily be verified upon obtaining a numerical solution to the problem. But one of them, that which consisted in adopting the ultrarelativistic approximation for the lepton component, calls for a dedicated consideration. As was seen in Section 2 from estimates of about 5 MeV for characteristic CPNS temperatures, the accuracy of this approximation is not high since we neglect $(m_n - m_p)c^2 \simeq 1.3$ MeV against this value. Moreover, temperatures lower than the above estimate may actually arise in the solution itself, especially in the vicinity of the ASW front. In order to validate the approximation adopted here, we therefore derived more detailed equations and relations for the problem in question that are exact for the (e^-, e^+) component in the nonrelativistic limit as well. By solving this cumbersome problem, along with the problem in the above physical formulation, it proved to be possible to find a rough criterion of applicability of the ultrarelativistic approximation—more specifically, nonrelativistic corrections to all quantities characterizing the CPNS structure are within a few percent if $T_{\mathrm{sw}} \gtrsim 0.3 T_{\nu\mathrm{eff}} \simeq 1.5$ MeV. Here, we imply a rather wide region of two basic parameters of the problem, which, for a numerical solution, were taken to be $\dot{M}_0$ and $L_{\nu\bar{\nu}} \propto r_{\nu_0^2}$ since M_0, $T_{\nu\mathrm{eff}}$, and $\psi_{\nu\mathrm{eff}}$ were assumed to be constant. This region can be specified by the inequalities

$$0.1 \lesssim \frac{\dot{M}_0}{M_\odot/\mathrm{s}} \lesssim 10, \quad 1 \lesssim \frac{L_{\nu\bar{\nu}}}{10^{52}\ \mathrm{erg/s}} \lesssim 100. \quad (42)$$

Of these, the first was considered in Section 2, but the two inequalities, taken together, are motivated by the hydrodynamic theory of collapse [7, 9]. It would

hardly be appropriate to refrain from mentioning the fact that the smallness of nonrelativistic corrections is due to some cancellations in the intricate functions involved in the nonlinear solution being discussed. This especially concerns the Hugoniot conditions, where such an unexpected smallness of corrections was revealed previously in [31] and where the lowest temperatures are actually obtained.

As was mentioned above, astrophysical applications of the aforementioned solution to the stationary problem of the CPNS structure are associated with the following circumstances. On one hand, this spherical layer of a PNS plays an important (maybe, even a crucial) role in the ensuing evolution of an ASW—the question to be answered in this connection is that of whether it will become an explosion shock wave (that is, an explosion of a collapsing supernova) or whether it will be gradually attenuated, which will be accompanied by a decrease in the neutrino emissivity and in the accretion rate (that is, the conditions of a "quiet" collapse will be realized in this case). On the other hand, a physical validation of results in the vicinity of the neutrinosphere—this is a region that is semitransparent to neutrino radiation—is the weakest point in hydrodynamic theory. In particular, it is of interest to clarify, over the entire range (42) of the basic parameters of the problem, the question of whether a convective instability may develop in the structure under consideration. A criterion of convective instability within a CPNS is of course derived within the thermodynamics of systems containing a variable number of particles, and this was consistently taken into account in our formulation of the problem. The role of the lepton component of matter in the development of convective instability is obviously significant, and the specific lepton charge in a CPNS is determined by nonequilibrium neutrino radiation according to Eq. (8) and relations (9). In the case of a nonlinear development of convective instability, it affects strongly the state of an ASW [14–16, 32] and can also entail other important astrophysical processes under the conditions of a quiet collapse.

The neutronization of the baryon component of matter in a CPNS—that is, a considerable increase in the ratio of the neutron and the proton concentration, up to values of $\theta \gg 1.154$—is a remarkable property of the crown and is a clear manifestation of extreme physical conditions in the problem under consideration, since it is well known [4] that the implementation of nuclear reactions of neutronization under terrestrial conditions involves formidable experimental difficulties.

ACKNOWLEDGMENTS

First of all, I am indebted to Yu.G. Abov, whose keen interest in neutrino processes in collapsing stars greatly contributed to the appearance of this article. I am also deeply grateful to I.Yu. Litvinova, whose numerical calculations made it possible to obtain, in the present study, a criterion of applicability of the ultrarelativistic approximation and to pinpoint the region (42) of the parameters involved where the solution to the problem in question has indeed been found. (I hope to present this solution in a forthcoming publication). Special thanks are due to D.K. Nadyozhin for valuable advice and a long-term collaboration in developing neutrino hydrodynamics. The generous assistance of N.A. Bobrova in preparing the manuscript of this article is gratefully acknowledged.

REFERENCES

1. S. A. Golgate and R. H. White, Astrophys. J. **143**, 626 (1966).
2. L. N. Ivanova, V. S. Imshennik, and D. K. Nadezhin, Nauchn. Inf. Astrosoveta Akad. Nauk SSSR **13**, 3 (1969).
3. S. W. Bruenn, Astrophys. J., Suppl. Ser. **58**, 771 (1985).
4. V. S. Imshennik, Yad. Fiz. **58**, 888 (1995) [Phys. At. Nucl. **58**, 823 (1995)].
5. V. S. Imshennik and D. K. Nadyozhin, Itogi Nauki Tekh., Ser. Astron. **21**, 63 (1982); V. S. Imshennik and D. K. Nadyozhin, Sov. Sci. Rev., Sect. E **2**, 75 (1983).
6. V. S. Imshennik, in *The Astrophysics on the Threshold of the 21st Centure,* Ed. by N. S. Kardashev (Gordon and Breach, Philadelphia, 1992), p. 167.
7. D. K. Nadyozhin, Astrophys. Space Sci. **51**, 283 (1977); **53**, 131 (1978).
8. S. I. Blinnikov, V. S. Imshennik, and D. K. Nadyozhin, Astrophys. Space Sci. **150**, 273 (1988).
9. A. Burrows and J. Goshy, Astrophys. J. **416**, L75 (1993).
10. A. Burrows, in *Proceedings of the IAU Colloquium No. 145, Xian, China, 1993* (Cambridge Univ. Press, Cambridge, 1996), p. 99.
11. V. S. Imshennik and D. K. Nadezhin, Zh. Éksp. Teor. Fiz. **63**, 1548 (1972) [Sov. Phys. JETP **36**, 821 (1973)].
12. Ya. B. Zel'dovich and I. D. Novikov, *Gravitation Theory and Star Evolutions* (Nauka, Moscow, 1971).
13. L. D. Landau and E. M. Lifshitz, *Course of Theoretical Physics,* Vol. 6: *Fluid Mechanics* (Nauka, Moscow, 1986; Pergamon, Oxford, 1987).
14. M. Herant, W. Benz, and S. A. Colgate, Astrophys. J. **395**, 642 (1992).
15. H.-T. Janka and E. Muller, Astron. Astrophys. **290**, 496 (1994).
16. A. Burrows, J. Hayes, and B. A. Fryxell, Astrophys. J. **450**, 830 (1995).
17. S. Weinberg, Rev. Mod. Phys. **46**, 255 (1974); V. S. Kaftanov, Astrophys. Space Sci. **78**, 105 (1981).
18. A. Mezzacappa and S. W. Sruenn, Astrophys. J. **405**, 637 (1993).
19. A. G. Aksenov and D. K. Nadezhin, Pis'ma Astron. Zh. **24**, 813 (1998) [Astron. Lett. **24**, 703 (1998)].

20. V. S. Imshennik and D. K. Nadyozhin, Astrophys. Space Sci. **62**, 309 (1979).
21. W. Fowler and F. Hoyle, *Neutrino Processes and Pair Formation in Massive Stars and Supernovae* (Univ. of Chicago Press, Chicago, 1965; Mir, Moscow, 1967).
22. D. K. Nadezhin and V. M. Chechetkin, Astron. Zh. **46**, 270 (1969) [Sov. Astron. **13**, 213 (1969)].
23. L. D. Landau and E. M. Lifshitz, *Course of Theoretical Physics,* Vol. 5: *Statistical Physics* (Nauka, Moscow, 1976; Pergamon, Oxford, 1980), Part 1.
24. V. S. Imshennik and M. V. Murzina, Pis'ma Astron. Zh. **16**, 745 (1990) [Sov. Astron. Lett. **16**, 322 (1990)].
25. P. Rhodes, Proc. R. Soc. London, Ser. A **204**, 396 (1950).
26. V. S. Imshennik and D. K. Nadyozhin, Preprint No. 18, Inst. Prikl. Mat. Akad. Nauk SSSR (Inst. of Applied Mathematics, Academy of Sciences of USSR, Moscow, 1971).
27. D. A. Frank-Kamenetsky, *Physical Processes in Stars* (Fizmatgiz, Moscow, 1959).
28. V. S. Imshennik and V. M. Chechetkin, Astron. Zh. **47**, 929 (1970) [Sov. Astron. **14**, 747 (1971)].
29. V. S. Imshennik and M. S. Popov, Pis'ma Astron. Zh. **27**, 101 (2001) [Astron. Lett. **27**, 81 (2001)].
30. V. S. Imshennik, Vopr. At. Nauki Tekh., Ser.: Metod. Program. Chisl. Reshen. Zadach Mat. Fiz., No. 1, 29 (1987).
31. M. V. Murzina, Preprint No. 47, ITÉF (Inst. of Theoretical and Experimental Physics, Moscow, 1990).
32. A. Burrows, Nucl. Phys. A **606**, 151 (1996).

Translated by A. Isaakyan

Physics of Atomic Nuclei, Vol. 65, No. 11, 2002, pp. 2092–2099. Translated from Yadernaya Fizika, Vol. 65, No. 11, 2002, pp. 2153–2160.

ELEMENTARY PARTICLES AND FIELDS

Violation of Isotopic Invariance in Strong Interactions and Mass Spectrum of the $1/2^+$ Baryon Octet

V. K. Grigoriev*, O. N. Erofeeva, and V. N. Luzin

Institute of Theoretical and Experimental Physics, Bol'shaya Cheremushkinskaya ul. 25, Moscow, 117259 Russia

Received March 11, 2002

Abstract—The ideas developed by Gell-Mann and Okubo in studying violation of unitary symmetry are used to describe violation of isototic invariance in strong interactions. The present consideration is performed for the example of the mass spectrum of the octet formed by baryons of spin–parity $1/2^+$: only for this family are the widths of its particles much less than the scale of the effects being investigated, their masses being known from experiments to a fairly high precision. The Gell-Mann–Okubo formula is generalized in such a way that relations both for the splitting between the isomultiplets of the octet and for the mass splitting within these isomultiplets follow from the new formula. Moreover, a relation between masses that describes their electromagnetic splitting and which coincides in form with the Coleman–Glashow relation also follows from this formula. The relations obtained for the masses of the baryons belonging to the octet in question are satisfied to a precision not poorer than 3%. © *2002 MAIK "Nauka/Interperiodica"*.

1. INTRODUCTION

In the early 1960s, Gell-Mann and Okubo [1, 2] applied the theory of $SU(3)$ symmetry to elementary-particle physics. This made it possible to formulate a particle systematics according to which a fairly large number of particles known at that time were distributed among various multiplets (baryon octet and decouplet, 0^- and 1^- meson octets, etc.) and to obtain relations for the masses of particles entering into isomultiplets. In addition, some other important results were also obtained.

The fact that impressed the physics community most deeply was the discovery of the Ω^- hyperon, whose existence and whose properties (mass, charge, spin, parity, strangeness) were predicted by the model based on $SU(3)$ symmetry.

In order to describe the mass spectrum, Gell-Mann and Okubo assumed that the strong-interaction Hamiltonian consists of two parts; that is,

$$H = H_0 + H_1. \qquad (1)$$

This Hamiltonian is dominated by the term H_0, which is a scalar in unitary-spin space. The interaction that violates unitary symmetry—it is represented by the term H_1—was referred to as a moderately strong interaction. The form of the term H_1 was determined from the condition requiring that this hypothetical interaction conserve isospin and hypercharge; therefore, H_1 must transform as the eighth component in the space of $SU(3)$ flavors.

The present study is devoted to analyzing the mass structure of the $J^P = 1/2^+$ baryon octet, which contains the N, Λ, Σ, and Ξ isomultiplets. For the masses of the baryon isomultiplets, the theory of broken $SU(3)$ symmetry as applied to this multiplet predicts the expressions

$$M_i = M_0 + m_1 Y_i + a(I_i(I_i+1) - Y_i^2/4), \qquad (2)$$

where Y_i is the hypercharge; I_i is the isospin of the corresponding isomultiplet; M_0, m_1, and a are parameters; and the subscript i specifies the N, Λ, Σ, and Ξ isomultiplets.

The physical meaning of formula (2) can easily be understood on the basis of the quark model. The constant m_1 is the excess of the s-quark mass over the u- and d-quark masses, which are assumed to be equal in the approximation adopted here. The third term represents the contribution of the moderately strong interaction. The binding energy generated by this interaction depends on the isospin state of the u and d quarks. The mass difference between the Σ^0 and the Λ hyperon is determined by this term exclusively.

For baryons that enter into the same isomultiplet, formula (2) yields identical mass values. Eliminating the parameters M_0, m_1, and a from the set of Eqs. (2), we arrive at the sum rule

$$\frac{M_\Xi + M_N}{2} = \frac{3M_\Lambda + M_\Sigma}{4}, \qquad (3)$$

*e-mail: grigorvk@vitep1.itep.ru

which was obtained by Gell-Mann and Okubo. By the symbol M, one implies, in Eq. (3), the mean values of relevant multiplets.

In the present study, we will consider both the fine splitting of the octet masses, which is described by the Gell-Mann–Okubo formula, and hyperfine splitting. Here, we imply, by the term "fine splitting," the distinction between isomultiplet masses and, by the term "hyperfine splitting," the distinction between the masses of particles entering into the same isomultiplet. In order to apply formula (3), which describes fine splitting, to hyperfine splitting, we rewrite this formula as a difference rule that can be represented in the form of the following chain of equalities:

$$\frac{M_\Xi - M_N}{2} = \frac{3(M_\Xi - M_\Lambda) + M_\Xi - M_\Sigma}{4} = \frac{3(M_\Lambda - M_N) + M_\Sigma - M_N}{4}. \quad (4)$$

Substituting the tabular values of the isomultiplet masses into (4), we find that the left-hand side, the central part, and the right-hand side in the chain of equalities (4) are, respectively, 187, 181, and 193 MeV. Thus, the Gell-Mann–Okubo formula is satisfied to within 4%.

A further development of the ideas based on the $SU(3)$ symmetry of flavors led to the quark model and, eventually, to quantum chromodynamics (QCD). In turn, QCD has yielded a large number of predictions confirmed by experimental data.

In the course of the development of QCD, it became clear that there is no moderately strong interaction. From the present-day point of view, violation of isotopic invariance is due to a number of factors, including the distinctions between the masses of the u and d quarks and between their condensates; the interaction with instantons, which proves to be dependent on the quark flavors; and electromagnetic interaction. In view of this, it became common practice to believe that the good agreement between the elementary Gell-Mann–Okubo formula and experimental results is purely coincidental.

Nonetheless, some authors who relied on QCD [3–7], but who employed different computational procedures, obtained results that reproduce relation (3). Moreover, it turned out that, when the results obtained in the aforementioned studies coincide with the conclusions following from $SU(3)$ symmetry, they provide a much closer description of experimental data than what would be expected on the basis of preliminary estimates. From this fact, it was deduced in [4] that the Gell-Mann–Okubo formula is not of an accidental character, but that it has a profound physical meaning.

In the present study, the ideas underlying the Gell-Mann–Okubo model of unitary-symmetry violation are extended to the case of hyperfine splitting. This approach is demonstrated for the example of the octet formed by baryons of spin–parity $1/2^+$. Only for this family are the intrinsic widths of the particles much less than the scale of the effects being considered, and only for the particles entering into are the experimental mass values known to a precision sufficient for our purpose (even in this case, however, it would be desirable that the errors in the measured masses of the cascade hyperons Ξ^- and Ξ^0 be much smaller). It will be shown that, to a considerable extent, the violation of unitary symmetry and the violation of isotopic symmetry have a common origin and that these two phenomena can be described within a unified framework. Far back in 1966, it was noticed [8] that hyperfine splitting satisfies a difference rule that has the same form as the equalities in (4):

$$\frac{M_{\Sigma^-} - M_{\Sigma^+}}{2} = \frac{3(M_{\Sigma^-} - M_{\Sigma^0}) + M_n - M_p}{4} = \frac{3(M_{\Sigma^0} - M_{\Sigma^+}) + M_{\Xi^-} - M_{\Xi^0}}{4}. \quad (5)$$

Upon the substitution of the mass values from the tables presented by the Particle Data Group [9] into (5), the three parts of this double equality from left to right become, respectively, 4.04 ± 0.04, 3.93 ± 0.03, and 4.05 ± 0.15 MeV. It can be seen that the difference rule (5) is satisfied to the same degree of precision and is of the same form as that in (4).

In our study, we propose a formula that describes the mass spectrum of the $1/2^+$ baryon octet. This formula is a generalization of that in (2), but, in contrast to the latter, the former yields a mass value for each member of the octet. From this formula, one can deduce the equalities in (5), the Gell-Mann–Okubo difference rules in (4), and the relation

$$M_{\Sigma^-} - M_{\Sigma^+} = M_{\Xi^-} - M_{\Xi^0} + M_n - M_p \quad (6)$$

between the masses, which is coincident in form with the Coleman–Glashow formula [10] for the electromagnetic mass splitting in the octet being considered.

In our treatment, we avoid introducing a moderately strong interaction. Instead, we assume that two mechanisms are responsible for the generation of the mass spectrum, that which is associated with the distinctions between the constituent mass of the u and d quarks and the constituent mass of the s quark and that which is associated with the Pauli exclusion principle.

Formally, fulfillment of the Pauli exclusion principle is achieved by requiring that, for fermions, the product of wave functions of all types (spatial, spin, and isospin ones) be asymmetric under the permutations of particle pairs. Our assumption is that it is not the usual isospin, whose orientation is fixed by the u and d quarks, but an isospin associated

with some linear combinations of baryon fields that appears in the isospin part of the above product. As a result, relations (5) will be obtained; concurrently, the parameter θ whose value determines baryon-mixing coefficients will be expressed in terms of the masses of the particles entering into the octet being considered.

The ensuing exposition is organized as follows. In Section 2, we present a brief survey devoted to an analysis of isotopic-invariance violation within QCD. The role of the Pauli exclusion principle in the formation of the mass spectrum of the baryon octet is discussed in Section 3. In Section 4, this approach is generalized to describe hyperfine splitting. The mixing of the Λ and Σ^0 hyperons is considered in Section 5. The Conclusion (Section 6) is devoted to discussing various mechanisms of baryon mixing.

2. TAKING INTO ACCOUNT ISOTOPIC-INVARIANCE VIOLATION WITHIN QCD

Possible mechanisms of isotopic-invariance violation that lead to mass splitting within isomultiplets have been discussed in various studies. The mechanisms considered there are associated with various factors, including the distinction between the u- and d-quark masses; the distinction between the vacuum expectation values for different quarks; and the electromagnetic interaction of quarks, which is difficult to take into account because of the effect of strong interaction.

In analyzing effects violating isotopic invariance, use was made of various quark models, QCD sum rules, and lattice calculations. As examples of calculations on the basis of the relativistic bag model, we can quote those in [11, 12]. One-gluon exchanges were additionally taken into account in [13].

Instanton effects and the role of the quark condensate were studied in [14]. It was shown there that these effects are of importance in calculating the masses of the Σ and Ξ hyperons. It follows that the quark-flavor dependence of the masses manifests itself upon taking into account instanton effects. The role of instanton effects was also indicated in [15]. Specific calculations of the masses of the $1/2^+$ baryon octet and of some other isomultiplets were performed in [16], and good agreement between the results of the calculations and experimental data was obtained, the distinction being not greater than 0.1 MeV for all isotopic mass differences with the exception of Ξ hyperons, for which it is 0.5 MeV.

In some studies, isotopic-invariance violation was taken into account with the aid of QCD sum rules [17]. By way of example, we would like to indicate the study of Adami *et al.* [18], who showed that isotopic-invariance violation is due to the distinction between the masses of the u and d quarks and to the distinctions between their condensate densities (these parameters were calculated in [18]).

3. STRUCTURE OF THE BARYON-OCTET MASSES AND PAULI EXCLUSION PRINCIPLE

The present study is aimed primarily at modifying the last term in (2) in such a way as to arrive at a unified description of both fine and hyperfine splitting. In order to implement this idea, it is necessary, first of all, to impart a specific physical meaning to this term.

We assume that this term describes the action of the Pauli exclusion principle on the u and d quarks. Let us consider the mass difference between the Λ and Σ^0 hyperons. This pair of baryons is the most convenient for analyzing the role of the last term in (2), since the two particles being considered have the same quark content, so that the mass difference between the Λ and Σ^0 hyperons is determined by this term exclusively. The total wave function, which, in the present case, is the product of the spatial, the spin, and the isospin component,

$$\varphi_{\text{all}} = \varphi_R \cdot \varphi_S \cdot \varphi_I, \tag{7}$$

must be symmetric (here, we can disregard the color component since all hadrons are color-singlet objects—that is, the symmetry of the color component is fixed in such a way that this component is always antisymmetric). The isospin component has different symmetries for the Λ and Σ^0 hyperons because their isospins are different. It follows that, for these hyperons, the product of the spatial and the spin component has different symmetries, and this is the fact that eventually leads to the distinction between the masses. The same argument applies to other members of the octet.

In order to describe the structure of the mass spectrum of all octet members, it is sufficient to assume, first, that the masses of the isomultiplets are determined by the symmetry of the u- and d-quark state and are independent of the quantum state of the s quarks and, second, that the s-quark mass is different from the light-quark mass. The fact that the s quark, on one hand, and the u and d quarks, on the other hand, behave differently may be due to the distinctions between the masses of the quarks and between the values of their condensates.

In other words, the formation of the mass spectrum is determined by two factors—specifically, by the Pauli exclusion principle, which controls the set of possible states of u and d quarks, and by the s-quark mass (the masses of the light quarks are assumed to be identical). By the s-quark mass, we will henceforth mean the coefficient of the hypercharge Y_i on the

right-hand side of (2). This choice is justified by the proximity of this coefficient to the current mass of the s quark. However, we do not rule out the presence of other physical effects that may contribute to this coefficient. The same comment also concerns the u and d quarks, whose masses will not be taken to be identical in discussing mass splitting within isotopic multiplets. These two assumptions lead to the Gell-Mann–Okubo relation (3).

From the aforesaid, it becomes clear why the different methods of the calculations performed in [3–7] yield a mass structure that is consistent with the Gell-Mann–Okubo prediction specified by Eq. (3). The point is that the Pauli exclusion principle was taken into account in all those studies. The reason behind the agreement is that the factors that are disregarded within the QCD approaches adopted in [3–7] are small (about 4%).

4. GENERALIZATION OF THE MECHANISM OF FINE-SPLITTING GENERATION TO THE CASE OF HYPERFINE SPLITTING

The idea of our unified approach to fine and hyperfine splitting consists in assuming that it is not the usual on-shell baryons but their linear combinations that possess isospin symmetry. Owing to this, there arises an additional mechanism violating isospin conservation in strong interactions. This means that, for actual baryons, the term that is responsible for isotopic symmetry possesses mixed symmetry. Since, however, the total product in (7) must possess a specific type of symmetry, the remaining part of the product of the wave functions also possesses mixed symmetry. It is precisely this circumstance that leads to an additional change in the baryon mass.

The simplest way to implement this idea is to recast formula (2) into the alternative form

$$M = M_1 + (m_1/3)\mathrm{tr}(B\lambda_8\bar{B} - \bar{B}\lambda_8 B) + (a/2)\mathrm{tr}(B\lambda_8\bar{B} + \bar{B}\lambda_8 B), \quad (8)$$

which can be used to calculate the masses M of the particles entering into the baryon octet being considered and which can also be reduced to the Gell-Mann–Okubo relation (3). The matrices λ_8 and λ_3 appearing in Eq. (8) (we will need the matrix λ_3 below) are given by

$$\lambda_8 = 1/\sqrt{3}\begin{pmatrix} 1 & & \\ & 1 & \\ & & -2 \end{pmatrix}, \quad \lambda_3 = \begin{pmatrix} 1 & & \\ & -1 & \\ & & 0 \end{pmatrix},$$

Table

Baryon	k_1	k_2	k_3	k_4
n	-1	1	1/2	1/2
p	-1	0	1/2	2
Λ	0	0	0	2
Σ^-	0	1	2	1/2
Σ^0	0	0	2	0
Σ^+	0	-1	2	1/2
Ξ^-	1	0	1/2	2
Ξ^0	1	-1	1/2	1/2

while the matrix B can be represented as

$$B = \begin{pmatrix} \Lambda/\sqrt{6} + \Sigma^0/\sqrt{2} & \Sigma^+ & p \\ \Sigma^- & \Lambda/\sqrt{6} - \Sigma^0/\sqrt{2} & n \\ \Xi^- & \Xi^0 & -\sqrt{2/3}\Lambda \end{pmatrix}.$$

At the chosen values of the coefficients, the parameters m_1 and a in (2) and (8) coincide. Let us rearrange expression (8) in such a way that it would describe both fine and hyperfine splitting. In order to take into account the mass difference between the u and d quarks, it is sufficient to include, in our consideration, the term $(m_2/3)\mathrm{tr}(B\lambda_{8V}\bar{B} - \bar{B}\lambda_{8V}B)$, where m_2 is a new parameter and

$$\lambda_{8V} = 1/\sqrt{3}\begin{pmatrix} 1 & & \\ & -2 & \\ & & 1 \end{pmatrix} = \cos 60^\circ \lambda_3 - \sin 60^\circ \lambda_8.$$

This matrix plays the same role for the V-spin subgroup as the matrix λ_8 for the isospin subgroup. Instead of λ_{8V}, one could use here the matrix λ_3 with the same result, but, in describing the effect of the Pauli exclusion principle, it would hardly be possible to dispense with the concept of V spin. In order to obtain a unified description of fine and hyperfine splitting, we prefer to employ the matrices of the V subgroup in the present case as well.

In the third term on the right-hand side of (8), we replace particles in the matrices B and $\bar{B}$ by the linear combinations

$$\begin{aligned} p_C &= p\cos\theta + \Sigma^+\sin\theta, \quad \Sigma_C^+ = \Sigma^+\cos\theta - p\sin\theta, \\ \Lambda_C &= \Lambda\cos\theta + \Sigma^0\sin\theta, \quad \Sigma_C^0 = \Sigma^0\cos\theta - \Lambda\sin\theta, \\ n_C &= n\cos\theta + \Xi^0\sin\theta, \quad \Xi_C^0 = \Xi^0\cos\theta - n\sin\theta, \\ \Sigma_C^- &= \Sigma^-\cos\theta + \Xi^-\sin\theta, \end{aligned} \quad (9)$$

$$\Xi_C^- = \Xi^- \cos\theta - \Sigma^- \sin\theta;$$

that is, the corresponding linear combinations appear in the matrices instead of individual particles, and the matrices B and $\bar{B}$ go over to B_C and $\bar{B}_C$.

With allowance for the above transformations, formula (8) takes the form

$$M = M_1 + (m_1/3)\mathrm{tr}(B\lambda_8\bar{B} - \bar{B}\lambda_8 B) + (m_2/3)\mathrm{tr}(B\lambda_{8V}\bar{B} - \bar{B}\lambda_{8V}B) + (a/2)\mathrm{tr}(B_C\lambda_8\bar{B}_C + \bar{B}_C\lambda_8 B_C). \quad (10)$$

With the aid of formula (10), the mass of each baryon entering into the octet can be expressed in terms of the parameters M_1, m_1, m_2, a, and θ and the coefficients k_1, k_2, k_3, and k_4 as

$$M = M_1 + k_1 m_1 + k_2 m_2 + a(k_3\cos^2\theta + k_4\sin^2\theta). \quad (11)$$

For each baryon, the coefficients calculated with the aid of formula (10) are given in the table.

From expressions that have been obtained for the baryon masses with the aid of formula (11) and data presented in the table, we further eliminate the parameters M_1, m_1, m_2, a, and θ. As a result, we arrive at the difference rules in (5) and at the following relations between the masses of the baryon-octet members:

$$\frac{M_{\Xi^-} - M_p}{2} = \frac{3(M_{\Xi^-} - M_\Lambda) + M_{\Xi^0} - M_{\Sigma^+}}{4} = \frac{3(M_\Lambda - M_p) + M_{\Sigma^-} - M_n}{4}. \quad (12)$$

The last expression in (12) is an analog of formula (4), but it now involves the particle masses rather than the isomultiplet masses. The numerical values of the expressions appearing in the left-hand, central, and right-hand parts of the equalities in (12) are 191.6, 197.6, and 185.6 MeV, respectively. One of the four equalities in (5) and (12) is not linearly independent. Indeed, there are eight masses that are described by five parameters (M_1, m_1, m_2, a, θ).

By means of formula (11), the parameter θ can be expressed in terms of the masses of the baryons entering into the octet. Since the problem is overdetermined (there are eight equations and five sought parameters), there arise a few possible solutions. We will first consider m_1 as a function of $a\cos^2\theta$ and m_2 as a function of $a\sin^2\theta$.

Figure 1 displays the parameter m_1 as a function of $a\cos^2\theta$. There are four such dependences. All of them are linear and differ from one another in that they are determined by the mass difference in different baryon pairs. If the formulas proposed here had described the mass spectrum exactly, all four straight lines representing these dependences would have intersected at one point. This is not so, however, and, instead, we have four different solutions. Thus, the symmetry being considered is violated. As follows from Fig. 1, this violation has a regular character: to a high degree of precision (a few tenths of MeV), one pair of solutions has the same abscissa, while the other has the same ordinate. This can be so provided that the following condition is satisfied:

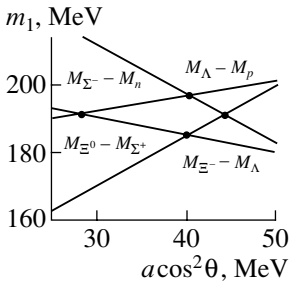

Fig. 1. Parameter m_1 as a function of $a\cos^2\theta$. The errors in the mass measurements are commensurate with the line thickness. Four solutions obtained as the points of intersection of the corresponding straight lines are indicated by small closed circles.

$$M_{\Xi^-} - M_p = M_{\Xi^0} - M_{\Sigma^+} + M_{\Sigma^-} - M_n. \quad (13)$$

The left-hand side of this relation is 383.04 MeV, while its right-hand side is equal to 383.35 MeV. Formula (13) is obtained from relations (12) by summing the central and the right-hand part and by taking half of the result, whereby the mass of the Λ hyperon is eliminated.

An analog of relation (13) was obtained as far back as the early 1960s in the study of Coleman and Glashow [10], who analyzed the effect of electromagnetic interaction on the masses of the baryons forming the octet being considered and arrived at the conclusion that, under the most general assumptions on the action of electromagnetic interaction, relation (6) must be satisfied. The left-hand side of this relation amounts to 8.08 ± 0.04 MeV, while its right-hand side is 7.92 ± 0.12 MeV. Obviously, formulas (6) and (13) are obtained from each other by a rearrangement of the terms involved.

Figure 2 displays the parameter m_2 as a function of $a\sin^2\theta$. In this case, the experimental errors in the mass difference between the cascade Ξ^- and Ξ^0 hyperons are commensurate with the distances between the intersections of the corresponding straight lines. Therefore, it is possible to single out clearly only two intersections, which are shown by ovals in the figure.

Two circumstances are worthy of special note in comparing Figs. 1 and 2. First, the relative positions of the two solutions in Fig. 2 and the relative positions of the corresponding solutions in Fig. 1 for Cabibbo-conjugate particles are identical. [By

Cabibbo-conjugate particles, we mean baryons going over to each other upon the replacement of an s quark by a d quark, and vice versa (Σ^- and Ξ^-, Λ and Σ^0, etc.).] This coincidence of the relative positions of the intersection points may suggest that the same mechanism is responsible for fine and for hyperfine splitting. This conjecture can be proved or disproved upon improving the accuracy in measurements of the cascade-hyperon masses by a factor of 3 to 5. The second circumstance is that the relative scale of fine-splitting violation is more than two times as great as the relative scale of hyperfine-splitting violation—it is noteworthy because one would rather expect an inverse relationship.

The Coleman–Glashow relation (6) also follows from formula (5) for hyperfine splitting. It should be noted that, in contrast to the Coleman–Glashow approach, our approach takes no account of electromagnetic interaction. Thus, formula (6) is obtained by two totally independent methods. Obviously, this explains the fact that the difference rules in (5) are satisfied to within 0.1 MeV. However, the role of electromagnetic interaction in the formation of the mass spectrum cannot be reduced to that which is described by formula (6). To be convinced of this, it would suffice to notice that the Σ^0-hyperon mass is absent from this formula. Thus, electromagnetic interaction was not taken into account completely. The approximate character of the proposed formulas may be partly due to this circumstance.

From the ratio of $a\sin^2\theta$ and $a\cos^2\theta$, $\tan\theta$ can be deduced in a few different ways:

$$\tan\theta \qquad (14)$$
$$= \begin{cases} \sqrt{\dfrac{(M_{\Sigma^-}-M_{\Sigma^0})-(M_{\Sigma^0}-M_{\Sigma^+})}{(M_{\Xi^-}-M_\Lambda)-(M_\Lambda-M_p)}} = 0.23, \\ \sqrt{\dfrac{(M_{\Sigma^-}-M_{\Sigma^0})-(M_n-M_p)}{(M_{\Xi^-}-M_\Lambda)-(M_{\Xi^0}-M_{\Sigma^+})}} = 0.21, \\ \sqrt{\dfrac{(M_{\Xi^-}-M_{\Xi^0})-(M_n-M_p)}{(M_{\Sigma^-}-M_n)-(M_{\Xi^0}-M_{\Sigma^+})}} = 0.20, \\ \sqrt{\dfrac{(M_{\Xi^-}-M_{\Xi^0})-(M_{\Sigma^0}-M_{\Sigma^+})}{(M_{\Sigma^-}-M_n)-(M_\Lambda-M_p)}} = 0.20. \end{cases}$$

The reason behind the distinctions between the numerical values in (14) is not that which is associated with the experimental errors in determining the particle masses, but that which is associated with the approximate description of fine splitting by relations (12).

Formula (10) is the main result of the present study. Formula (12), which is an analog of the Gell-Mann–Okubo sum rule; the Coleman–Glashow formula (6); and the difference rule in (5) for hyperfine splitting follow from it. This analog of the Gell-Mann–Okubo sum rule is somewhat different from its original form: instead of the isomultiplet masses, it involves the particle masses. This distinction did not lead to the improvement of the accuracy to which the sum rule in question is satisfied, but it enabled us to establish links between the Gell-Mann–Okubo and the Coleman–Glashow relation.

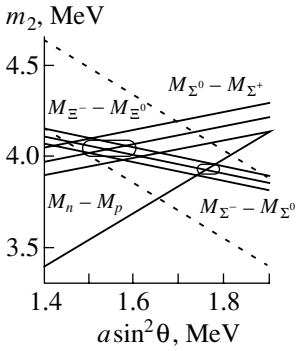

Fig. 2. Parameter m_2 as a function of $a\sin^2\theta$. The experimental errors correspond to the widths of the bands. Two solutions that are the most precise of those that have been obtained are indicated by ovals.

The high accuracy to which these relations are satisfied is worthy of special note. The Coleman–Glashow formula is accurate to within the experimental errors; the accuracy to which the Gell-Mann–Okubo sum rule is satisfied is about 3%; and the rules for hyperfine splitting are satisfied to a somewhat higher precision (about 1.5%). In the last case, however, the experimental errors are of the same scale. There is every reason to believe that, upon an experimental refinement of the baryon masses, there will emerge a clear-cut discrepancy between experimental data and the predictions of formula (10). Indeed, simple phenomenological formulas cannot yield precise mass values. Such results would rather be expected from a further development of QCD. At present, the accuracy in calculating the mass differences between isomultiplet members (and not only for the baryon octet) that has been achieved within QCD is commensurate with experimental errors [16].

In formula (10), the term that describes the effect of the Pauli exclusion principle on the mass structure of the baryon octet considered here is represented as the sum of two traces: $\mathrm{tr}(B_C\lambda_8\bar{B}_C + \bar{B}_C\lambda_8 B_C)$. This is not a unique form. The same relations between the masses appearing in expressions (5) and (12) and the same values of θ as those that follow from (14) can be obtained by using only $\mathrm{tr}(B\lambda_8\bar{B})$ or $\mathrm{tr}(\bar{B}\lambda_8\bar{B})$. This would change only the parameters M_1, m_1, and m_2. In each of the versions being considered, we can avoid mixing, according to formulas (9), one of the pairs of baryons entering into the octet.

In the version chosen here, we can avoid mixing Ξ_0 and n. If use is made of the form $\mathrm{tr}(\bar{B}_C\lambda_8 B_C)$ or of the form $\mathrm{tr}(B_C\lambda_8\bar{B}_C)$, the pair that is not mixed is that of Σ^+ and p or that of Σ^- and Ξ^-, respectively.

5. MIXING OF Λ AND Σ^0 HYPERONS

In contrast to the other six octet members, the Λ and Σ^0 hyperons consist of three different quarks (u, d, s). As a result, these particles possess an additional degree of freedom: no conservation law impedes their mixing. If isospin had been conserved exactly, the Λ hyperon would have been an isotopic singlet, while Σ^0 would have been the neutral component of the isotopic triplet.

In considering unitary-symmetry violation, Gell-Mann and Okubo disregarded isospin nonconservation. But if one considers mass splitting within the isomultiplets, it is illegitimate to neglect isotopic-invariance violation. Concurrently, the Λ and Σ^0 hyperons can no longer be considered as pure isotopic states. In order to study the problem of the mixing of Λ and Σ^0, it is convenient to modify the last term in expression (10) as

$$(a/2)\mathrm{tr}(\bar{B}(\lambda_8\cos^2\theta+\lambda_{8V}\sin^2\theta)B + B(\lambda_8\cos^2\theta+\lambda_{8V}\sin^2\theta)\bar{B}). \quad (15)$$

This expression determines that part of the mass whose emergence is associated with the action of the Pauli exclusion principle.

In expression (10), the generalization of formula (4) to the case of hyperfine splitting was implemented via a field transformation. In the present case, the generalization is performed by recasting the operator λ_8 into the form $\lambda_8\cos^2\theta+\lambda_{8V}\sin^2\theta$. In this version, there is no difference in the representation of the Hamiltonian itself from the situation where, following the strategies of the original proposal of Gell-Mann and Okubo, one would introduce, along with a moderately strong interaction that is responsible for fine splitting, a moderately weak interaction whose direction in the $SU(3)$ space would be determined by the matrix λ_{8V}. The distinction consists in that the Λ and Σ^0 states are mixed differently in these two approaches.

If one assumes that there are two interactions such that one transforms as λ_8, while the other transforms as λ_{8V}, it is sufficient to diagonalize the corresponding matrix in order to determine mixing. This yields not only the angle α of mixing of the Λ and Σ^0 hyperons but also the masses of these particles:

$$\tan\alpha=\frac{-2+3\sin^2\theta\pm2\sqrt{1-3\sin^2\theta\cos^2\theta}}{\sqrt{3}\sin^2\theta}, \quad (16)$$

$$M_{\Sigma^0,\Lambda}=M_1+a(1\pm\sqrt{1-3\sin^2\theta\cos^2\theta}). \quad (17)$$

The Σ^0 mass calculated by this formula differs from the tabular value by a few standard deviations.

A different result is obtained if the calculation of the mixing angle is based on the assumptions put forth in the present study. According to our basic hypothesis, the Pauli exclusion principle acts on the linear combinations (9) of baryons. It can easily be seen that, at the quark level, this corresponds to the mixing of the d and s quarks. These quarks go over to the linear combinations $d_C=d\cos\theta+s\sin\theta$ and $s_C=s\cos\theta-d\sin\theta$. In the case being considered, it is convenient to reformulate our assumptions as follows: the isospin-conservation law refers to the u quark and to the linear combination d_C. The mixing of the Λ and Σ^0 particles occurs in such a way that the symmetry of the states of this pair would be maximal. In order to obtain a quantitative result, we introduce the symmetry function

$$F=\cos\theta\cos\alpha+\sin\theta\cos(30^\circ-\alpha). \quad (18)$$

The angle α characterizes the mixing of the Λ and Σ^0 particles. The factor $\cos\alpha$ in the first term in this function takes into account the degree of symmetry violation for the u and d quarks, while the factor $\cos(30^\circ-\alpha)$ in the second term plays the same role for the u and s quarks. The functions of the angle θ in (18) consider that, according to our hypothesis, the Pauli exclusion principle acts on specific linear combinations of the quarks rather than on the quarks themselves. The α value at which the function F attains a maximum at a given value of θ represents the sought solution. Differentiating the function F and equating the derivative to zero, we find that α and θ are related as

$$\cot\alpha=2\cot\theta+\sqrt{3}. \quad (19)$$

At this value of the mixing angle, we obtain the following expression for the masses of the Λ and Σ^0 baryons:

$$M_{\Sigma^0,\Lambda}=M_1+a(1\pm\cos2\theta). \quad (20)$$

This expression for the Λ and Σ^0 masses coincides with the corresponding formulas given by (11), although the mixing of the Λ and Σ^0 particles was not taken explicitly into account in deriving (11).

6. CONCLUSION

To conclude the above analysis, we would like to highlight the following intriguing circumstance. It can easily be seen that baryon-field mixing implemented via formulas (9) is nothing but the mixing of the d and s quarks that occurs in the Cabibbo sector of the Cabibbo–Kobayashi–Maskawa matrix [19,

20]. Moreover, the θ value obtained from (14) complies with the Cabibbo angle to within about 1°. However, quark mixing that is generated by the Cabibbo–Kobayashi–Maskawa matrix is operative only in the sector of weak interactions, which cannot lead to mass differences of about a few MeV—the mass scale characteristic of them is a few orders of magnitude smaller. One cannot rule out the possibility that the similarity between the baryon-field transformations applied in the present study and the Cabibbo transformation and the proximity of the angle θ to the Cabibbo angle are not accidental. A conceivable explanation of why this occurred is that the quarks involved in weak interactions are more fundamental that the quarks involved in strong interactions. The point is that the Pauli exclusion principle applies to those linear combinations of the quarks that enter into weak-interaction charged current. The mixing of the quarks may be due either to the distinction between the u- and d-quark condensates or to the distinctions between the electric charges of the u and d quarks.

That the scale of isotopic-invariance violation and the square of the Cabibbo angle are close to each other was repeatedly highlighted by many authors (see, for example, [21, 22]). Attempts were made in [23, 24] to express the ratio of the d- and s-quark masses in terms of the Cabibbo angle. It is possible that, in the mass spectrum of the octet being considered, we also meet with an unusual relationship between the Cabibbo angle and the baryon masses.

ACKNOWLEDGMENTS

We are grateful to V.V. Vladimirsky, M.I. Krivoruchenko, A.E. Kudryavtsev, and E.P. Shabalin for enlightening comments. We tenderly nourish recollections of our discussions with M.V. Terent'ev before his untimely death on the problems considered in the present article.

This work was supported by the Russian Foundation for Basic Research (project nos. 02-02-16623 and 00-15-96545).

REFERENCES

1. M. Gell-Mann, CIT Report, CTSL-20 (1961).
2. S. Okubo, Prog. Theor. Phys. **27**, 949 (1962).
3. E. V. Shuryak and J. Rosner, Phys. Lett. B **218**, 72 (1989).
4. R. Dashen, E. Jenkins, and A. V. Manohar, Phys. Rev. D **49**, 4713 (1994).
5. C. Carone, H. Georgi, and S. Osofsky, Phys. Lett. B **322**, 227 (1994).
6. Phuoc Ha and Loyal Durand, Phys. Rev. D **59**, 076001 (1999).
7. Yongseok Oh and W. Weise, Eur. Phys. J. A **4**, 353 (1999).
8. V. K. Grigor'ev, Preprint No. 469, ITÉF (Institute of Theoretical and Experimental Physics, Moscow, 1966).
9. Particle Data Group, Eur. Phys. J. C **3**, 1 (1998).
10. S. Coleman and S. L. Glashow, Phys. Rev. Lett. **6**, 423 (1961).
11. P. N. Bogoliubov, Ann. Inst. Henri Poincaré **8**, 163 (1967).
12. A. Chodos, R. L. Jaffe, K. Johnson, and C. B. Thorn, Phys. Rev. D **10**, 2599 (1974).
13. R. P. Bickerstaff and A. W. Thomas, Phys. Rev. D **25**, 1869 (1982).
14. A. E. Dorokhov and N. I. Kochelev, Z. Phys. C **37**, 377 (1988).
15. L. R. Varner, W. J. Thompson, T. L. McAbee, *et al.*, Phys. Rep. **201**, 57 (1991).
16. A. E. Dorokhov, Nucl. Phys. A **581**, 654 (1995).
17. M. A. Shifman, A. I. Vainstein, and V. I. Zakharov, Nucl. Phys. B **147**, 385 (1979).
18. C. Adami, E. G. Drukarev, and B. L. Ioffe, Phys. Rev. D **48**, 2304 (1993).
19. N. Cabibbo, Phys. Rev. Lett. **10**, 531 (1963).
20. M. Kobayashi and T. Maskawa, Prog. Theor. Phys. **49**, 652 (1973).
21. R. J. Oakes, Phys. Lett. B **29B**, 683 (1969).
22. M. K. Volkov and D. Ebert, Yad. Fiz. **31**, 520 (1980) [Sov. J. Nucl. Phys. **31**, 271 (1980)].
23. S. Weinberg, Trans. N. Y. Acad. Sci. **38**, 185 (1977).
24. S. Onedo and Y. Koide, Preprint no. RIFP-704, Yukawa Hall Kioto (Kioto, 1987).

Translated by A. Isaakyan